UNIVERSITY OF CALIFORNIA,
IRVINE

Quantification and Reduction of Uncertainties Associated with Carbon Cycle–Climate System Feedbacks

DISSERTATION

submitted in partial satisfaction of the requirements
for the degree of

DOCTOR OF PHILOSOPHY

in Earth System Science

by

Forrest McCoy Hoffman

Dissertation Committee:
Professor James T. Randerson, Chair
Professor Michael L. Goulden
Professor Jefferson Keith Moore

2015

DEDICATION

This work is dedicated first and foremost to Joan, Nate, and Bjørn for their unbounded love, perpetual inspiration, fortifying allegiance, and beneficent sacrifice; and second to those people, places, characters, and things that have engendered my curiosity and love of science, including Benjamin Franklin, the Atari 800, Carl E. Sagan, Mauna Kea, Sir Karl R. Popper, Thomas S. Kuhn, Mauna Loa, Unix, Spock, C, Richard P. Feynman, Commander Data, and Linux.

TABLE OF CONTENTS

LIST OF FIGURES

LIST OF TABLES

ACKNOWLEDGMENTS

Funding for this research was provided in part by the Climate and Environmental Sciences Division (CESD) of the Biological and Environmental Research (BER) Program in the U.S. Department of Energy Office of Science. I am extremely grateful for the continuous support I have received for my research through BER-sponsored research projects and Scientific Focus Areas (SFAs). Having obtained a rarely granted sabbatical from Oak Ridge National Laboratory (ORNL) to attend the University of California, Irvine (UCI), during 2010, I would like to thank ORNL leadership for their enabling support and continuous encouragement over the last five years. I would especially like to acknowledge the championing I received throughout this journey from David C. Bader, John B. Drake, James J. Hack, Arthur B. (Barney) Maccabe and Jeffrey A. Nichols.

It has been an honor and a privilege to have James T. Randerson as my Ph.D. advisor. Jim is the quintessential scholar, a polymath and extraordinary researcher, who is captivated by science and who engenders a sense of wonder and curiosity in those around him. His incessant search for mechanistic understanding, meticulous approach to analysis, and selfless attention to student scholarship all serve to make Jim an inspirational professor and remarkable human being. Jim's reassuring manner and unflagging support have impelled my research and rekindled my enthusiasm for science. It has been a pleasure to work under his tutelage, and I anticipate many years of continued collaboration.

I would like to thank my Ph.D. committee members Michael L. Goulden and J. Keith Moore for fostering my research interests, offering motivational assistance, and providing insightful comments on my papers, presentations, and dissertation. I am grateful for thoughtful advice from James S. Famiglietti during the first few years of my Ph.D. research. I wish to personally thank the scientists who encouraged and supported my quest for this Ph.D., many of whom provided letters of recommendation or advocated for my admission to the Department of Earth System Science, including Gordon B. Bonan, John B. Drake, James S. Famiglietti, Inez Y. Fung, William W. Hargrove, Geoffrey M. Henebry, Paul F. Hessburg, Atul K. Jain, Natalie M. Mahowald, Wilfred M. Post, Steven W. Running, Susan E. Trumbore, and Warren M. Washington.

I gratefully acknowledge the contributions of the following co-authors to the published form of Chapter 2, which appeared in the February 2014 edition of the *Journal of Geophysical Research – Biogeosciences*: James T. Randerson, Vivek K. Arora, Qing Bao, Patricia Cadule, Duoying Ji, Chris D. Jones, Michio Kawamiya, Samar Khatiwala, Keith Lindsay, Atsushi Obata, Elena Shevliakova, Katharina D. Six, Jerry F. Tjiputra, Evgeny M. Volodin, and Tongwen Wu. I gratefully acknowledge the contributions of the following co-authors to the published form of Chapter 3, which appears in the October 2013 edition of *Landscape Ecology*: Jitendra Kumar, Richard Tran Mills, and William Walter Hargrove, Jr. I gratefully acknowledge the contributions of Jitendra Kumar, Damian M. Maddalena, and William W. Hargrove to the global forest representativeness analysis and figure contained in Chapter 5.

I want to thank my colleagues, co-authors, and co-workers for their encouragement and support, and for filling in for me when I was busy performing this research and preparing this dissertation, especially, Nathaniel Collier, David J. Erickson III, Lianhong Gu, William W. Hargrove, Jitendra Kumar, Yiqi Luo, Salil Mahajan, Richard Tran Mills, Richard J. Norby, William J. Riley, Peter E. Thornton, Yingping Wang, Stanley D. Wullschleger, and Min Xu. I further wish to thank my colleagues who were students, interns, and post-doctoral fellows working with me at ORNL during my Ph.D. pursuit, notably, Rahul Barman, Yasemin Ergüner Baytok, Wenting Fu, Wesley J. Kendall, Zachary L. Langford, Damian M. Maddalena, Shijie Shu, Xia Song, Shivakar S. Vulli, and Cheng-En Yang. I would also like to thank my cohort of Earth System Science graduate students, and those of the prior and subsequent years, who accepted me into their group and supported me in completing course work and research at UCI, most especially, George "Determined Moose" Azzari, Alysha "Compassionate Squirrel" Coppola, Mackenzie Greiman, Colene "Amusing Fox" Haffke, Collin "Righteous Koala" Lawrence, Anne Kelly, Zhao Liu, Shirley Mims, Gergana Mouteva, Sasha "Benevolent Dolphin" Richey, Brendan "Kooky Bear" Rogers, Alys "Lively Puma" Thomas, Kathe Todd-Brown, and Mike Tosca.

Finally, and most of all, I want to thank my wife, Joan, and the boys we raised, Nate and Bjørn, as well as Aimée and Tony and his family. They were my inspiration. In addition, I offer special thanks to Louie-Louie, Mr. Feynman, Fern, Snooker, Mary McCoy, Pinkie, Manapua, and Xavier for their unique, late-night approach to supporting the fulfillment of my research goals.

CURRICULUM VITAE

Forrest McCoy Hoffman

EDUCATION

Doctor of Philosophy in Earth System Science — **June 2015**
University of California — Irvine, California

Masters of Science in Earth System Sciences — **December 2012**
University of California — Irvine, California

Masters of Science in Physics — **December 2004**
University of Tennessee — Knoxville, Tennessee

Bachelor of Science in Physics — **August 1991**
University of Tennessee — Knoxville, Tennessee

PROFESSIONAL EXPERIENCE

Senior Computational Climate Scientist — **May 2014–present**
Climate Change Science Institute (CCSI) and Computational Earth Sciences Group,
Computer Science & Mathematics Division

Computational Climate Scientist — **October 2003–May 2014**
Climate Change Science Institute (CCSI) and Computational Earth Sciences Group,
Computer Science & Mathematics Division

Environmental Modeler — **November 1993–October 2003**
Environmental Sciences Division
Oak Ridge National Laboratory (ORNL) — Oak Ridge, Tennessee

Contributing Editor and Columnist — **January 2002–October 2006**
"Extreme Linux" column for *Linux Magazine*

Scientific Programmer/Analyst — **July 1992–November 1993**
Department of Geological Sciences, University of Tennessee, Knoxville, for
Oak Ridge National Laboratory (ORNL) — Oak Ridge, Tennessee

Knowledge Engineer — **May 1989–June 1992**
Automated Sciences Group, Inc., for
Oak Ridge National Laboratory (ORNL) — Oak Ridge, Tennessee

Research Intern — **September 1988–May 1989**
Oak Ridge Associated Universities (ORAU), for
Oak Ridge National Laboratory (ORNL) — Oak Ridge, Tennessee

Observer/Telescope Operator **1987–September 1988**
High Altitude Observatory, National Center for Atmospheric Research
Mauna Loa Solar Observatory Hilo, Hawai'i

SYNERGISTIC ACTIVITIES

- Laboratory Research Manager (Lead PI) for the multi-Institutional U.S. Department of Energy (DOE) Scientific Focus Area, *Quantifying Feedbacks and Uncertainties of Biogeochemical Processes in Earth System Models*, 2014–present.
- Lead PI for the multi-Institutional U.S. Department of Energy (DOE) Project, *Quantification and Reduction of Critical Uncertainties Associated with Carbon Cycle–Climate System Feedbacks*, 2013–2014.
- Lead PI for the multi-Institutional U.S. Department of Energy (DOE) Scientific Discovery through Advanced Computing (SciDAC-3) Project, *Applying Computationally Efficient Schemes for BioGeochemical Cycles (ACES4BGC)*, 2012–2015.
- Lead for the Earth System Modeling (ESM) Theme within the ORNL Climate Change Science Institute (CCSI), 2012–present.
- Co-organizer of the International Land Model Benchmarking (ILAMB) Project, 2010–present.
- ORNL Site PI for the multi-Laboratory Scientific Discovery through Advanced Computing (SciDAC-2) Project, *A Scalable and Extensible Earth System Model for Climate Change Science*, 2010–2011.
- U.S. Department of Energy (DOE) Laboratory lead for the Carbon-Land Model Intercomparison Project (C-LAMP).

HONORS AND AWARDS

- **Significant Event Award** for contributions to development of the Next Generation Ecosystem Experiments (NGEE) Tropics Project. Oak Ridge National Laboratory/UT-Battelle LLC, April 2015.
- **Significant Event Award** for contributions to development of the Accelerated Climate Model for Energy (ACME) Scientific Focus Area (SFA). Oak Ridge National Laboratory/UT-Battelle LLC, October 2014.
- **Employee of the Quarter** in the Computer Science & Mathematics Division. Oak Ridge National Laboratory/UT-Battelle LLC, July–September 2014.
- **Outstanding Paper in Landscape Ecology** for "Representativeness-based sampling network design for the State of Alaska" awarded by the U.S. Regional Association of the International Association of Landscape Ecology (US-IALE), May 2014.
- **Significant Event Award** for contributions to Intergovernmental Panel on Climate Change & National Climate Assessment Work. Oak Ridge National Laboratory/UT-Battelle LLC, May 2014.
- **2013 Chief's Honor Award** from Thomas L. Tidwell, Chief, U.S. Department of Agriculture Forest Service. Co-recipient for ORNL contribution to the *ForWarn* Forest

Disturbance Monitoring Project with the U.S. Department of Agriculture Forest Service, NASA Stennis Space Center, and the U.S. Geological Survey EROS Data Center, March 2014.

- **2013 Southern Research Station Director's Award for Partnerships** from Dr. Robert Doudrick, Station Director of the U.S. Department of Agriculture Forest Service, Southern Research Station. Co-recipient for ORNL contribution to the *ForWarn* Forest Disturbance Monitoring Project with the U.S. Department of Agriculture Forest Service, NASA Stennis Space Center, and the U.S. Geological Survey EROS Data Center, December 2013.
- **Group Achievement Award** from Charles Bolden, Administrator of the National Aeronautics and Space Administration (NASA). Co-recipient for ORNL contribution to the *ForWarn* Forest Disturbance Monitoring Project with the U.S. Department of Agriculture Forest Service, NASA Stennis Space Center, and the U.S. Geological Survey EROS Data Center, August 2013.
- **2013 Interagency Partnership Award** from the Federal Laboratory Consortium (FLC) for Technology Transfer. Co-recipient for ORNL contribution to the *ForWarn* Forest Disturbance Monitoring Project with the U.S. Department of Agriculture Forest Service, NASA Stennis Space Center, and the U.S. Geological Survey EROS Data Center (plus congratulatory letters from Secretary of Energy Ernest Moniz and Secretary of Agriculture Thomas Vilsack), April 2013.
- **2012 Partnership Award** from the Federal Laboratory Consortium (FLC) for Technology Transfer, Southeastern Region. Co-recipient for ORNL contribution to the *ForWarn* Forest Disturbance Monitoring Project with the U.S. Department of Agriculture Forest Service, NASA Stennis Space Center, and the U.S. Geological Survey EROS Data Center, March 2013.
- **Most Distinguished Scientific or Technical Contribution Award** from Dr. Barney Maccabe, Director of the ORNL Computer Science & Mathematics Division, for the ORNL contribution to the *ForWarn* Forest Disturbance Monitoring Project, December 2012.
- **2012 Southern Research Station Director's Science Delivery Award** from Dr. Robert Doudrick, Station Director of the U.S. Department of Agriculture Forest Service, Southern Research Station. Co-recipient for ORNL contribution to the *ForWarn* Forest Disturbance Monitoring Project with the U.S. Department of Agriculture Forest Service, NASA Stennis Space Center, and the U.S. Geological Survey EROS Data Center, October 2012.
- **Distinguished Employee Award** from the ORNL Computing and Computational Science Directorate, May 2012.
- 1st Place, **People's Choice Poster Award** for *A Cluster Analysis Approach to Comparing Atmospheric Radiation Measurement (ARM) Data with Global Climate Model (GCM) Results*, by Forrest M. Hoffman, Salil Mahajan, William W. Hargrove, Richard T. Mills, and Anthony Del Genio. The U.S. Department of Energy, Atmospheric Radiation Measurement (ARM) Program, at the 18th Annual ARM Science Team Meeting in Norfolk, Virginia, March 10–14, 2008.
- ORNL **Outstanding Mentor Award**. The U.S. Department of Energy, Oak Ridge National Laboratory, and Oak Ridge Associated Universities, February 2008.

- **Significant Event Award** for contribution to NSF's National Ecological Observatory Network (NEON) Design Committee. Oak Ridge National Laboratory/UT-Battelle LLC, March 2006.
- **Outstanding Paper in the Discipline of Landscape Ecology Award**. W. W. Hargrove, F. M. Hoffman and P. M. Schwartz, "A fractal landscape realizer for generating synthetic maps," *Cons. Ecol.* 6(1):2 (2002). Awarded by the International Association for Landscape Ecology (IALE), U. S. Regional Chapter, April 2004.
- **World-Class Teamwork Award** for building and using the Stone SouperComputer, the first Beowulf-style supercomputer at ORNL. Oak Ridge National Laboratory Values Committee, October 19, 1999.
- **President's Award for Continuous Improvement**. Oak Ridge National Laboratory/Lockheed Martin Energy Research Corp., November 1997.
- ORNL **Technical Achievement Award**. Oak Ridge National Laboratory/Lockheed Martin Energy Research Corp., 1996.
- **Distinguished Achievement Award for Operational Support**. Oak Ridge National Laboratory, Environmental Sciences Division, August 1995.
- **Significant Event Award**. Oak Ridge National Laboratory/Martin Marietta Energy Systems, June 1995.

PROFESSIONAL ORGANIZATIONS

- American Association for the Advancement of Science (AAAS), 2007–present.
- American Geophysical Union (AGU), 1996–present.
- American Meteorological Society (AMS), 2011–present. AMS Smoky Mountain Chapter, 1998–present; Chapter President, 2005.
- Ecological Society of America (ESA), 2015–present.
- International Association for Landscape Ecology, U.S. Regional Association (US-IALE), 2014–present.
- Institute of Electrical and Electronics Engineers (IEEE) Computer Society, 1998–present.
- National Speleological Society (NSS), 2013–present.
- Sigma Pi Sigma (SPS), Physics Honor Society, 1995–present.

REFEREED JOURNAL PUBLICATIONS

J. T. Randerson, K. Lindsay, E. Munoz, W. Fu, J. K. Moore, **F. M. Hoffman**, N. M. Mahowald, and S. C. Doney (2015), Multi-century changes in ocean and land contributions to climate–carbon feedbacks, *Global Biogeochem. Cycles*, in press, doi:10.1002/2014GB005079.

K. J. Anderson-Teixeira, S. J. Davies, A. C. Bennett, E. B. Gonzalez-Akre, H. C. Muller-Landau, S. J. Wright, K. Abu Salim, A. M. Almeyda Zambrano, A. Alonso, J. L. Baltzer, Y. Basset, N. A. Bourg, E. N. Broadbent, W. Y. Brockelman, S. Bunyavejchewin, D. F. R. P. Burslem, N. Butt, M. Cao, D. Cardenas, G. B. Chuyong, K. Clay, S. Cordell, H.

S. Dattaraja, X. Deng, M. Detto, X. Du, A. Duque, D. L. Erikson, C. E. N. Ewango, G. A. Fischer, C. Fletcher, R. B. Foster, C. P. Giardina, G. S. Gilbert, N. Gunatilleke, S. Gunatilleke, Z. Hao, W. W. Hargrove, T. B. Hart, B. C. H. Hau, F. He, **F. M. Hoffman**, R. W. Howe, S. P. Hubbell, F. M. Inman-Narahari, P. A. Jansen, M. Jiang, D. J. Johnson, M. Kanzaki, A. R. Kassim, D. Kenfack, S. Kibet, M. F. Kinnaird, L. Korte, K. Kral, J. Kumar, A. J. Larson, Y. Li, X. Li, S. Liu, S. K. Y. Lum, J. A. Lutz, K. Ma, D. M. Maddalena, J.-R. Makana, Y. Malhi, T. Marthews, R. Mat Serudin, S. M. McMahon, W. J. McShea, H. R. Memiaghe, X. Mi, T. Mizuno, M. Morecroft, J. A. Myers, V. Novotny, A. A. de Oliveira, P. S. Ong, D. A. Orwig, R. Ostertag, J. den Ouden, G. G. Parker, R. P. Phillips, L. Sack, M. N. Sainge, W. Sang, K. Sri-ngernyuang, R. Sukumar, I.-F. Sun, W. Sungpalee, H. S. Suresh, S. Tan, S. C. Thomas, D. W. Thomas, J. Thompson, B. L. Turner, M. Uriarte, R. Valencia, M. I. Vallejo, A. Vicentini, T. Vrška, X. Wang, X. Wang, G. Weiblen, A. Wolf, H. Xu, S. Yap, and J. Zimmerman (2015), CTFS-ForestGEO: A worldwide network monitoring forests in an era of global change, *Global Change Biol.*, 21(2):528–549, doi:10.1111/gcb.12712.

K. Lindsay, G. B. Bonan, S. C. Doney, **F. M. Hoffman**, D. M. Lawrence, M. C. Long, N. M. Mahowald, J. K. Moore, J. T. Randerson, and P. E. Thornton (2014), Preindustrial-control and twentieth-century carbon cycle experiments with the Earth system model CESM1(BGC), *J. Clim.*, 27(24):8981–9005, doi:10.1175/JCLI-D-12-00565.1.

Y. Sun, L. Gu, R. E. Dickinson, R. J. Norby, S. G. Pallardy, and **F. M. Hoffman** (2014), Impact of mesophyll diffusion on estimated global land CO_2 fertilization, *Proc. Nat. Acad. Sci.*, 111(44):15774–15779, doi:10.1073/pnas.1418075111.

Y. P. Wang, B. C. Chen, W. R. Wieder, M. Leite, B. E. Medlyn, M. Rasmussen, M. J. Smith, F. B. Agusto, **F. M. Hoffman**, and Y. Q. Luo (2014), Oscillatory behavior of two nonlinear microbial models of soil carbon decomposition, *Biogeosci.*, 11(7):1817–1831, doi:10.5194/bg-11-1817-2014.

F. M. Hoffman, J. T. Randerson, V. K. Arora, Q. Bao, P. Cadule, D. Ji, C. D. Jones, M. Kawamiya, S. Khatiwala, K. Lindsay, A. Obata, E. Shevliakova, K. D. Six, J. F. Tjiputra, E. M. Volodin, and T. Wu (2014), Causes and implications of persistent atmospheric carbon dioxide biases in Earth system models, *J. Geophys. Res. Biogeosci.*, 119(2):141–162, doi:10.1002/2013JG002381.

F. M. Hoffman, J. Kumar, R. T. Mills, and W. W. Hargrove (2013), Representativeness-based sampling network design for the State of Alaska, *Landscape Ecol.*, 28(8):1567–1586, doi:10.1007/s10980-013-9902-0.

G. Keppel-Aleks, J. T. Randerson, K. Lindsay, B. B. Stephens, J. K. Moore, S. C. Doney, P. E. Thornton, N. M. Mahowald, **F. M. Hoffman**, C. Sweeney, P. P. Tans, P. O. Wennberg, and S. C. Wofsy (2013), Atmospheric carbon dioxide variability in the Com-

munity Earth System Model: Evaluation and transient dynamics during the twentieth and twenty-first centuries, *J. Clim.*, 26(13):4447–4475, doi:10.1175/JCLI-D-12-00589.1.

J. Mao, X. Shi, P. E. Thornton, **F. M. Hoffman**, Z. Zhu, and R. B. Myneni (2013), Global latitudinal-asymmetric vegetation growth trends and their driving mechanisms: 1982–2009, *Remote Sens.*, 5(3):1484–1497, doi:10.3390/rs5031484.

K. E. O. Todd-Brown, J. T. Randerson, W. M. Post, **F. M. Hoffman**, C. Tarnocai, E. A. G. Schuur, and S. D. Allison (2013), Causes of variation in soil carbon simulations from CMIP5 Earth system models and comparison with observations, *Biogeosci.*, 10(3):1717–1736, doi:10.5194/bg-10-1717-2013.

Y. Q. Luo, J. T. Randerson, G. Abramowitz, C. Bacour, E. Blyth, N. Carvalhais, P. Ciais, D. Dalmonech, J. B. Fisher, R. Fisher, P. Friedlingstein, K. Hibbard, **F. Hoffman**, D. Huntzinger, C. D. Jones, C. Koven, D. Lawrence, D. J. Li, M. Mahecha, S. L. Niu, R. Norby, S. L. Piao, X. Qi, P. Peylin, I. C. Prentice, W. Riley, M. Reichstein, C. Schwalm, Y. P. Wang, J. Y. Xia, S. Zaehle, and X. H. Zhou (2012), A framework for benchmarking land models, *Biogeosci.*, 9(10):3857–3874, doi:10.5194/bg-9-3857-2012.

W. L. Bauerle, R. Oren, D. A. Way, S. S. Qian, P. C. Stoy, P. E. Thornton, J. D. Bowden, **F. M. Hoffman**, and R. F. Reynolds (2012), Photoperiodic regulation of the seasonal pattern of photosynthetic capacity and the implications for carbon cycling, *Proc. Nat. Acad. Sci.*, 109(22):8612–8617, doi:10.1073/pnas.1119131109.

D. N. Huntzinger, W. M. Post, Y. Wei, A. M. Michalak, T. O. West, A. R. Jacobson, I. T. Baker, J. M. Chen, K. J. Davis, D. J. Hayes, **F. M. Hoffman**, A. K. Jain, S. Liu, A. D. McGuire, R. P. Neilson, C. Potter, B. Poulter, D. Price, B. M. Raczka, H. Q. Tian, P. Thornton, E. Tomelleri, N. Viovy, J. Xiao, W. Yuan, N. Zeng, M. Zhao, and R. Cook (2012), North American Carbon Program (NACP) regional interim synthesis: Terrestrial biospheric model intercomparison, *Ecol. Model.*, 232:144–157, doi:10.1016/j.ecolmodel.2012.02.004.

X. Shi, J. Mao, P. E. Thornton, **F. M. Hoffman**, and W. M. Post (2011), The impact of climate, CO_2, nitrogen deposition, and land use change on simulated contemporary global river flow, *Geophys. Res. Lett.*, 38(8):L08704, doi:10.1029/2011GL046773.

G. A. Alexandrov, D. Ames, G. Bellocchi, M. Bruen, N. Crout, M. Erechtchoukova, A. Hildebrandt, **F. Hoffman**, C. Jackisch, P. Khaiter, G. Mannina, T. Matsunaga, S. T. Purucker, M. Rivington, and L. Samaniego (2011), Technical assessment and evaluation of environmental models and software: Letter to the editor, *Environ. Modell. Softw.*, 26(3):328–336, doi:10.1016/j.envsoft.2010.08.004.

N. M. Mahowald, S. Kloster, S. Engelstaedter, J. K. Moore, S. Mukhopadhyay, J. R. McConnell, S. Albani, S. C. Doney, A. Bhattacharya, M. A. J. Curran, M. G. Flanner, **F. M. Hoffman**, D. M. Lawrence, K. Lindsay, P. A. Mayewski, J. Neff, D. Rothenberg, E. Thomas, P. E. Thornton, and C. S. Zender (2010), Observed 20$^{\text{th}}$ century desert dust variability: Impact on climate and biogeochemistry, *Atmos. Chem. Phys.*, 10(22):10875–10893, doi:10.5194/acp-10-10875-2010.

S. Kloster, N. M. Mahowald, J. T. Randerson, P. E. Thornton, **F. M. Hoffman**, S. Levis, P. J. Lawrence, J. J. Feddema, K. W. Oleson, and D. M. Lawrence (2010), Fire dynamics during the 20$^{\text{th}}$ century simulated by the Community Land Model, *Biogeosci.*, 7(6):1877–1902, doi:10.5194/bg-7-1877-2010.

B. Baker, H. Diaz, W. Hargrove, and **F. Hoffman** (2010), Use of the Köppen-Trewartha climate classification to evaluate climatic refugia in statistically derived ecoregions for the People's Republic of China, *Clim. Change*, 98(1):113–131, doi:10.1007/s10584-009-9622-2.

J. T. Randerson, **F. M. Hoffman**, P. E. Thornton, N. M. Mahowald, K. Lindsay, Y.-H. Lee, C. D. Nevison, S. C. Doney, G. Bonan, R. Stöckli, C. Covey, S. W. Running, and I. Y. Fung (2009), Systematic assessment of terrestrial biogeochemistry in coupled climate-carbon models, *Global Change Biol.*, 15(10):2462–2484, doi:10.1111/j.1365-2486.2009.01912.x.

W. W. Hargrove, J. P. Spruce, G. E. Gasser, and **F. M. Hoffman** (2009), Toward a national early warning system for forest disturbances using remotely sensed phenology, *Photogramm. Eng. Rem. Sens.*, 75(10):1150–1156.

M. Keller, D. Schimel, W. Hargrove, and **F. Hoffman** (2008), A continental strategy for the National Ecological Observatory Network, *Front. Ecol. Environ.*, 6(5):282–284, doi:10.1890/1540-9295(2008)6[282:ACSFTN]2.0.CO;2.

D. J. Erickson III, R. T. Mills, J. Gregg, T. J. Blasing, **F. M. Hoffman**, R. J. Andres, M. Devries, Z. Zhu, and S. R. Kawa (2008), An estimate of monthly global emissions of anthropogenic CO_2: Impact on the seasonal cycle of atmospheric CO_2, *J. Geophys. Res.*, 113(G1):G01023, doi:10.1029/2007JG000435.

J. V. Pittman, E. M. Weinstock, R. J. Oglesby, D. S. Sayres, J. B. Smith, J. G. Anderson, O. R. Cooper, S. C. Wofsy, I. Xueref, C. Gerbig, B. C. Daube, E. C. Richard, B. A. Ridley, A. J. Weinheimer, M. Loewenstein, H.-J. Jost, J. P. Lopez, M. J. Mahoney, T. L. Thompson, W. W. Hargrove, and **F. M. Hoffman** (2007), Transport in the subtropical lowermost stratosphere during the Cirrus Regional Study of Tropical Anvils and Cirrus Layers-Florida Area Cirrus Experiment, *J. Geophys. Res.*, 112(D8):D08304, doi:10.1029/2006JD007851.

D. Schimel, W. Hargrove, **F. Hoffman**, and J. McMahon (2007), NEON: A hierarchically designed national ecological network, *Front. Ecol. Environ.*, 5(2):59, doi:10.1890/1540-9295(2007)5[59:NAHDNE]2.0.CO;2.

W. W. Hargrove, **F. M. Hoffman**, and P. F. Hessburg (2006), Mapcurves: A quantitative method for comparing categorical maps, *J. Geograph. Syst.*, 8(2):187–208, doi:10.1007/s10109-006-0025-x.

R. E. Dickinson, K. W. Oleson, G. Bonan, **F. Hoffman**, P. Thornton, M. Vertenstein, Z.-L. Yang, and X. Zeng (2006), The Community Land Model and its climate statistics as a component of the Community Climate System Model, *J. Clim.*, 19(11):2302–2324, doi:10.1175/JCLI3742.1.

F. M. Hoffman, W. W. Hargrove, D. J. Erickson, and R. J. Oglesby (2005), Using clustered climate regimes to analyze and compare predictions from fully coupled general circulation models, *Earth Interact.*, 9(10):1–27, doi:10.1175/EI110.1.

F. M. Hoffman, M. Vertenstein, H. Kitabata, and J. B. White III (2005), Vectorizing the Community Land Model (CLM), *Int. J. High Perf. Comput. Appl.*, 19(3):247–260, doi:10.1177/1094342005056113.

W. W. Hargrove, **F. M. Hoffman**, and R. A. Efroymson (2005), A practical map-analysis tool for detecting potential dispersal corridors, *Landscape Ecol.*, 20(4):361–373, doi:10.1007/s10980-004-3162-y.

M. A. White, **F. Hoffman**, W. W. Hargrove, and R. R. Nemani (2005), A global framework for monitoring phenological responses to climate change, *Geophys. Res. Lett.*, 32(4):L04705, doi:10.1029/2004GL021961.

E. Saxon, B. Baker, W. Hargrove, **F. Hoffman**, and C. Zganjar (2005), Mapping environments at risk under different global climate change scenarios, *Ecol. Lett.*, 8(1):53–60, doi:10.1111/j.1461-0248.2004.00694.x.

W. W. Hargrove and **F. M. Hoffman** (2004), Potential of multivariate quantitative methods for delineation and visualization of ecoregions, *Environ. Manage.*, 34(Supplement 1):S39–S60, doi:10.1007/s00267-003-1084-0.

W. W. Hargrove, **F. M. Hoffman**, and B. E. Law (2003), New analysis reveals representativeness of the AmeriFlux Network. *Eos Trans. AGU*, 84(48):529, 535, doi:10.1029/2003EO480001.

W. W. Hargrove, **F. M. Hoffman**, and P. M. Schwartz (2002), A fractal landscape realizer for generating synthetic maps, *Conserv. Ecol.*, 6(1):2.

J.-P. Gwo, E. F. D'Azevedo, H. Frenzel, M. Mayes, G.-T. Yeh, P. M. Jardine, K. M. Salvage, and **F. M. Hoffman** (2001), HBGC123D: A high performance computer model of coupled hydrogeological and biogeochemical processes, *Comput. Geosci.*, 27(10):1231–1242, doi:10.1016/S0098-3004(01)00027-9.

W. W. Hargrove, **F. M. Hoffman**, and T. Sterling (2001), The do-it-yourself supercomputer, *Sci. Am.*, 265(2):72–79.

W. W. Hargrove and **F. M. Hoffman** (1999), Using multivariate clustering to characterize ecoregion borders, *Comput. Sci. Eng.*, 1(4):18–25, doi:10.1109/5992.774837.

F. M. Hoffman and V. S. Tripathi (1993), A geochemical expert system prototype using object-oriented knowledge representation and a production rule system, *Comput. Geosci.*, 19(1):53–60, doi:10.1016/0098-3004(93)90042-4.

REFEREED CONFERENCE PUBLICATIONS

W. M. Christie, W. W. Hargrove, S. P. Norman, J. P. Spruce, J. Kumar, **F. Hoffman**, and S. W. Schroeder (2013), *ForWarn* forest change detection system provides a weekly snapshot of US forest contribtions to aid forest managers, In *Proceedings of the 9th Southern Forestry and Natural Resource Management GIS Conference*, Athens, Georgia, USA.

R. T. Mills, J. Kumar, **F. M. Hoffman**, W. W. Hargrove, J. P. Spruce, and S. P. Norman (2013), Identification and visualization of dominant patterns and anomalies in remotely sensed vegetation phenology using a parallel tool for principal components analysis, *Procedia Comput. Sci.*, 18:2396–2405, doi:10.1016/j.procs.2013.05.411.

R. Sisneros, J. Huang, G. Ostrouchov, and **F. Hoffman** (2011), Visualizing life zone boundary sensitivities across climate models and temporal spans, In M. Sato, S. Matsuoka, P. M. Sloot, G. D. van Albada, and J. Dongarra, editors, Proceedings of the International Conference on Computational Science (ICCS 2011), *Procedia Comput. Sci.*, 4:1582–1591, doi:10.1016/j.procs.2011.04.171.

R. T. Mills, **F. M. Hoffman**, J. Kumar, and W. W. Hargrove (2011), Cluster analysis-based approaches for geospatiotemporal data mining of massive data sets for identification of forest threats, In M. Sato, S. Matsuoka, P. M. Sloot, G. D. van Albada, and J. Dongarra, editors, Proceedings of the International Conference on Computational Science (ICCS 2011), *Procedia Comput. Sci.*, 4:1612–1621, doi:10.1016/j.procs.2011.04.174.

J. Kumar, R. T. Mills, **F. M. Hoffman**, and W. W. Hargrove (2011), Parallel k-means clustering for quantitative ecoregion delineation using large data sets, In M. Sato, S. Matsuoka, P. M. Sloot, G. D. van Albada, and J. Dongarra, editors, Proceedings of the International Conference on Computational Science (ICCS 2011), *Procedia Comput. Sci.*, 4:1602–1611, doi:10.1016/j.procs.2011.04.173.

F. M. Hoffman, J. W. Larson, R. T. Mills, B.-G. J. Brooks, A. R. Ganguly, W. W. Hargrove, J. Huang, J. Kumar, and R. R. Vatsavai (2011), Data Mining in Earth System Science (DMESS 2011), In M. Sato, S. Matsuoka, P. M. Sloot, G. D. van Albada, and J. Dongarra, editors, Proceedings of the International Conference on Computational Science (ICCS 2011), *Procedia Comput. Sci.*, 4:1450–1455, doi:10.1016/j.procs.2011.04.157.

F. M. Hoffman, R. T. Mills, J. Kumar, S. S. Vulli, and W. W. Hargrove (2010), Geospatiotemporal data mining in an early warning system for forest threats in the United States, In *Proceedings of the 2010 IEEE International Geoscience and Remote Sensing Symposium (IGARSS 2010)*, pages 170–173, doi:10.1109/IGARSS.2010.5653935.

C. R. Johnson, M. Glatter, W. Kendall, J. Huang, and **F. M. Hoffman** (2009), Querying for feature extraction and visualization in climate modeling, In G. Allen, J. Nabrzyski, E. Seidel, G. D. van Albada, J. Dongarra, and P. M. Sloot, editors, Proceedings of the 9th International Conference on Computational Science (ICCS 2009), *Lecture Notes in Computer Science (LNCS)*, 5545:416–425, doi:10.1007/978-3-642-01973-9_46.

Y. Xue, **F. M. Hoffman**, and D. Liu (2009), GeoComputation 2009, In G. Allen, J. Nabrzyski, E. Seidel, G. D. van Albada, J. Dongarra, and P. M. Sloot, editors, Proceedings of the 9th International Conference on Computational Science (ICCS 2009), *Lecture Notes in Computer Science (LNCS)*, 5545:345–348, doi:10.1007/978-3-642-01973-9_38.

R. T. Mills, **F. M. Hoffman**, P. H. Worley, K. S. Perumalla, A. Mirin, G. E. Hammond, and B. F. Smith (2009), Coping at the user-level with resource limitations in the Cray Message Passing Toolkit MPI at scale: How not to spend your summer vacation, In *Proceedings of the 2009 Cray User Group (CUG) Conference*.

R. Sisneros, M. Glatter, B. Langley, J. Huang, **F. Hoffman**, and D. J. Erickson III (2008), Time-varying multivariate visualization for understanding terrestrial biogeochemistry, *J. Phys.: Conf. Ser.*, 125(1):012093, doi:10.1088/1742-6596/125/1/012093.

F. M. Hoffman, W. W. Hargrove, R. T. Mills, S. Mahajan, D. J. Erickson, and R. J. Oglesby (2008), Multivariate Spatio-Temporal Clustering (MSTC) as a data mining tool for environmental applications, In M. Sànchez-Marrè, J. Béjar, J. Comas, A. E. Rizzoli, and G. Guariso, editors, *Proceedings of the iEMSs Fourth Biennial Meeting: International Congress on Environmental Modelling and Software Society (iEMSs 2008)*, pages 1774–1781, ISBN 978-84-7653-074-0.

F. M. Hoffman, J. T. Randerson, I. Y. Fung, P. E. Thornton, Y.-H. J. Lee, C. C. Covey, G. B. Bonan, and S. W. Running (2008), The Carbon-Land Model Intercomparison Project (C-LAMP): A protocol and evaluation metrics for global terrestrial biogeochemistry models, In M. Sànchez-Marrè, J. Béjar, J. Comas, A. E. Rizzoli, and G. Guariso, editors, *Proceedings of the iEMSs Fourth Biennial Meeting: International Congress on Environmental Modelling and Software Society (iEMSs 2008)*, pages 1039–1046, ISBN 978-84-7653-074-0.

W. Kendall, M. Glatter, J. Huang, **F. Hoffman**, and D. E. Bernholdt (2008), Web enabled collaborative climate visualization in the earth system grid, In *Proceedings of the International Symposium on Collaborative Technologies and Systems 2008 (CTS 2008)*, pages 212–220, doi:10.1109/CTS.2008.4543934.

F. M. Hoffman, C. C. Covey, I. Y. Fung, J. T. Randerson, P. E. Thornton, Y.-H. Lee, N. A. Rosenbloom, R. C. Stöckli, S. W. Running, D. E. Bernholdt, and D. N. Williams (2007), Results from the Carbon-Land Model Intercomparison Project (C-LAMP) and availability of the data on the Earth System Grid (ESG), *J. Phys.: Conf. Ser.*, 78(1):012026, doi:10.1088/1742-6596/78/1/012026.

F. M. Hoffman, I. Fung, J. Randerson, P. Thornton, J. Foley, C. Covey, J. John, S. Levis, W. M. Post, M. Vertenstein, R. Stöckli, S. Running, F. A. Heinsch, D. Erickson, and J. Drake (2006), Terrestrial biogeochemistry in the Community Climate System Model (CCSM), *J. Phys.: Conf. Ser.*, 46(1):363–369, doi:10.1088/1742-6596/46/1/051.

G. R. Carr, M. J. Cordery, J. B. Drake, M. W. Ham, **F. M. Hoffman**, and P. H. Worley (2005), Porting and performance of the Community Climate System Model (CCSM3) on the Cray X1, In *Proceedings of the 2005 Cray Users Group (CUG) Conference*.

F. M. Hoffman, M. Vertenstein, H. Kitabata, J. B. White, P. Worley, J. Drake, and M. Cordery (2004), Adventures in vectorizing the Community Land Model, In *Proceedings of the 2004 Cray Users Group (CUG) Conference*.

W. W. Hargrove and **F. M. Hoffman** (2000), An analytical assessment tool for predicting changes in a species distribution map following changes in environmental conditions, In B. O. Parks, K. M. Clarke, and M. P. Crane, editors, *Proceedings of the Fourth International Conference on Integrating GIS and Environmental Modeling (GIS/EM4): Problems, Prospects and Research Needs*, Boulder, Colorado, University of Colorado, Cooperative Institute for Research in Environmental Sciences (CIRES), ISBN 0-9743307-0-1.

J.-P. Gwo, **F. M. Hoffman**, and W. W. Hargrove (2000), Mechanistic-based genetic algorithm search on a Beowulf cluster of Linux PCs, In *Proceedings of the High Performance Computing 2000 (HPC2000) Conference*.

G. Mahinthakumar, **F. M. Hoffman**, W. W. Hargrove, and N. T. Karonis (1999), Multivariate geographic clustering in a metacomputing environment using Globus, In *Supercomputing '99: Proceedings of the 1999 ACM/IEEE conference on Supercomputing (CDROM)*, Supercomputing '99, New York, NY, USA, doi:10.1145/331532.331537.

F. M. Hoffman and W. W. Hargrove (1999), Multivariate geographic clustering using a Beowulf-style parallel computer, In H. R. Arabnia, editor, *Proceedings of the International Conference on Parallel and Distributed Processing Techniques and Applications (PDPTA '99)*, volume III, pages 1292–1298.

TECHNICAL REPORTS

K. W. Oleson, D. M. Lawrence, G. B. Bonan, M. G. Flanner, E. Kluzek, P. J. Lawrence, S. Levis, S. C. Swenson, P. E. Thornton, A. Dai, M. Decker, R. Dickinson, J. Feddema, C. Heald, **F. Hoffman**, J.-F. Lamarque, N. Mahowald, G.-Y. Niu, T. Qian, J. Randerson, S. Running, K. Sakaguchi, A. Slater, R. Stöckli, A. Wang, Z.-L. Yang, X. Zeng, and X. Zeng (2010), Technical description of version 4.0 of the Community Land Model (CLM), Technical Note NCAR/TN-478+STR, National Center for Atmospheric Research, Boulder, Colorado, USA.

C. Ehlschlaeger, J. Westervelt, H. Balbach, H. R. Akcakaya, T. Hoctor, C. Goodison, W. W. Hargrove, **F. M. Hoffman**, W. Rose, and R. C. Lozar (2006), Habitat fragmentation handbook for installation planners. Technical Report ERDC/CERL TR-06-36, U.S. Army Corps of Engineers, Engineer Research and Development Center.

R. C. Lozar, W. Hargrove, and **F. Hoffman**. Use of the Corridor Tool in support of threatened and endangered species habitat fragmentation. Technical Report ERDC/CERL TR-05-23, U.S. Army Corps of Engineers, Engineer Research and Development Center.

M. Vertenstein, K. Oleson, S. Levis, and **F. Hoffman** (2004), Community Land Model version 3.0 (CLM3.0) user's guide. Technical report, National Center for Atmospheric Research, Boulder, Colorado, USA.

F. Hoffman, M. Vertenstein, P. Thornton, K. Oleson, and S. Levis (2004), Community Land Model version 3.0 (CLM3.0) developer's guide. Technical Memorandum ORNL/TM-2004/119, Oak Ridge National Laboratory, Oak Ridge, Tennessee, USA.

W. W. Hargrove and **F. M. Hoffman** (2004), A flux atlas for representativeness and statistical extrapolation of the AmeriFlux network, Technical Memorandum ORNL/TM-2004/112, Oak Ridge National Laboratory, Oak Ridge, Tennessee, USA.

K. W. Oleson, Y. Dai, G. Bonan, M. Bosilovich, R. Dickinson, P. Dirmeyer, **F. Hoffman**, P. Houser, S. Levis, G.-Y. Niu, P. Thornton, M. Vertenstein, Z.-L. Yange, and X. Zeng

(2004), Technical description of the Community Land Model, Technical Note NCAR/TN-461+STR, National Center for Atmospheric Research, Boulder, Colorado, USA.

DATA

Map data for the State of Alaska doi: 10.5440/1108686
Data from: **F. M. Hoffman**, J. Kumar, R. T. Mills, and W. W. Hargrove (2013), Representativeness-based sampling network design for the State of Alaska, *Landscape Ecol.*, 28(8):1567–1586, doi:10.1007/s10980-013-9902-0.

ABSTRACT OF THE DISSERTATION

Quantification and Reduction of Uncertainties Associated with Carbon Cycle–Climate System Feedbacks

By

Forrest McCoy Hoffman

Doctor of Philosophy in Earth System Science

University of California, Irvine, 2015

Professor James T. Randerson, Chair

Anthropogenic perturbation of global biogeochemical cycles, particularly through emissions of radiatively active greenhouse gases into the atmosphere—chiefly carbon dioxide (CO_2), methane (CH_4), and nitrous oxide (N_2O)—is altering the Earth's climate and inducing feedbacks from the terrestrial biosphere and oceans on future CO_2 levels and the climate system. Identifying and quantifying these feedbacks and quantifying and reducing uncertainties associated with them in process-rich Earth system models (ESMs) are important for advancing our understanding of the Earth system, predicting future atmospheric CO_2 levels, informing carbon management and energy policies, and fostering the future of life on Earth. This dissertation presents three studies designed to advance our understanding of biogeochemical processes and their interactions with climate under conditions of increasing atmospheric CO_2 and to offer an approach for understanding observational representativeness and for scaling up measurements.

In the first investigation, I analyzed emission-driven simulations of ESMs from the fifth phase of the Coupled Model Intercomparison Project (CMIP5) in which atmospheric CO_2 levels were computed prognostically. Comparison of ESM prognostic atmospheric CO_2 over the historical period with observations indicated that ESMs, on average, had a small positive bias

in predictions of contemporary atmospheric CO_2, due in part to weak ocean carbon uptake. I found a significant linear relationship between contemporary atmospheric CO_2 biases and future CO_2 levels for the multimodel ensemble, and used this emergent constraint to create a contemporary CO_2 tuned model (CCTM) to estimate an atmospheric CO_2 trajectory for the 21^{st} century for the Representative Concentration Pathway (RCP) 8.5. The CCTM yielded CO_2 estimates of 600 ± 14 ppm at 2060 and 947 ± 35 ppm at 2100, which were 21 ppm and 32 ppm below the multi-model mean during these two time periods, respectively. This analysis indicated that much of the model-to-model variation in projected CO_2 during the 21^{st} century was tied to biases that existed during the observational era and that model differences in the representation of concentration–carbon feedbacks and other slowly varying carbon cycle processes appear to be the primary driver of this variability.

In the second study, I extended a quantitative methodology for stratifying sampling domains and understanding the representativeness of measurements, measurement sites, and observational networks. Multivariate spatiotemporal clustering was applied to down-scaled general circulation model results and data for the State of Alaska at 4 km^2 resolution to define multiple sets of ecoregions across two decadal time periods and to identify optimal sampling locations for those ecoregions. I developed a representativeness metric and used it to characterize environmental dissimilarity between potential sampling sites. This analysis provided insights into optimal sampling strategies and offered a framework for up-scaling measurements that can be applied at different spatial and temporal scales to meet the needs of individual measurement campaigns.

In the third investigation, I applied a feedback analysis framework to three sets of long-term climate change simulations from the Community Earth System Model version 1.0 (CESM1(BGC)) to quantify drivers of nonlinear terrestrial and ocean responses of carbon uptake. In the biogeochemically coupled simulation (BGC), the effects of CO_2 fertilization and nitrogen deposition were expressed in the biosphere. In the radiatively coupled sim-

ulation (RAD), the effects of rising temperature and circulation changes due to radiative forcing from CO_2, other greenhouse gases, and aerosols were expressed in the atmosphere. In the third, fully coupled simulation (FC), both the bigoeochemical and radiative coupling effects acted simultaneously. I found that climate–carbon sensitivities derived from RAD simulations produced a net ocean carbon storage climate sensitivity that is weaker and a net land carbon storage climate sensitivity that is stronger than those diagnosed from the FC and BGC simulations. For the ocean, this nonlinearity was associated with warming-induced weakening of ocean circulation and mixing that limited exchange of dissolved inorganic carbon between surface and deeper water masses. For the land, this nonlinearity was associated with strong gains in vegetation productivity in the FC simulation that were driven by enhancements in the hydrological cycle and increased nutrient availability. I developed and applied a nonlinearity metric for individual model variables to rank nonlinear responses and drivers. For these simulations, the overall climate–carbon cycle feedback gain at 2300 was 28% lower when estimated from climate–carbon sensitivities derived from the RAD simulation than when derived from the difference between the FC and BGC simulations. The gain estimated from compatible emissions calculations corresponded well with the gain estimated from FC − BGC climate–carbon sensitivity parameters, confirming the validity of the larger gain. This difference has direct implications for carbon management and energy policies because underestimating the climate–carbon cycle feedback gain would result in allowable emissions estimates that would be too low to meet climate change targets.

In these studies, I have shown that 1) we can reduce uncertainties in future climate projections by improving models to more closely match the long-term time series of observed atmospheric CO_2; 2) we can reduce sampling biases and partition important environmental gradients to design an optimized network of sampling sites at desired scales; and 3) we can reduce uncertainties in the assessment of climate–carbon cycle feedbacks due to nonlinear terrestrial and marine responses by deriving climate–carbon sensitivities from fully coupled and biogeochemically coupled simulations.

Chapter 1

Introduction

Anthropogenic emissions of radiatively active greenhouse gases into the atmosphere—chiefly carbon dioxide (CO_2), methane (CH_4), and nitrous oxide (N_2O)—combined with changes in aerosol loading and land use change, are rapidly accelerating global biogeochemical cycles, increasing radiative forcing, and altering Earth's climate (*IPCC*, 2013). The perturbation of the global carbon cycle is expected to induce feedbacks between terrestrial and marine ecosystems and the climate system, affecting future atmospheric CO_2 levels; temperatures; precipitation; rates of permafrost thaw; sea level rise; ocean acidification; frequency, extent, and severity of extreme events; water availability and quality; crop and fishery yields; and energy production and consumption. Most induced climate–carbon cycle feedbacks are highly uncertain, difficult to predict, and potentially large (*Ciais et al.*, 2013a). Identifying and quantifying feedbacks between biogeochemical cycles and the climate system, and quantifying and reducing uncertainties associated with those feedbacks in process-rich Earth system models (ESMs), are important for understanding the behavior of the Earth system, predicting future atmospheric CO_2 levels, and informing carbon management and energy policies.

Contemporary ESMs represent human, ecosystem, and climate processes and attempt to capture the complex interactions, responses, and feedbacks between all of these dynamic systems, operating on different temporal and spatial scales. Scenarios characterizing alternative future socioeconomic, technological, and environmental conditions, along with attendant energy resource options and consequent demand, are used to generate a consistent set of biological, chemical, and land use inputs to drive ESMs (*Moss et al.*, 2010). Results from these ESMs are subsequently analyzed to gauge the potential success of mitigation efforts required to stabilize CO_2 levels in the atmosphere or to diagnose the climate impacts of energy and agricultural policies and practices, taking into account carbon cycle responses and feedbacks.

1.1 Feedback Analysis Framework

Friedlingstein et al. (2003, 2006) developed a formulation for analysis of climate–carbon cycle feedbacks and applied it to the analysis of 11 coupled atmosphere–ocean general circulation models with coupled carbon cycles for the Coupled Climate–Carbon Cycle Model Intercomparison Project (C^4MIP). The C^4MIP experimental protocol specified a biogeochemically coupled and radiatively uncoupled run (BGC), in which the radiative effects of increasing atmospheric CO_2 were turned off, and a fully coupled run (FC), in which all processes experienced the effects of increasing atmospheric CO_2. *Friedlingstein et al.* (2006) defined the effect of climate-induced changes in the global carbon budget due to an increase of atmospheric CO_2 as

$$\Delta C_A^{\mathrm{FC}} = \frac{1}{(1-g)} \Delta C_A^{\mathrm{BGC}}, \tag{1.1}$$

where ΔC_A^{FC} is the change in atmospheric CO_2 in the fully coupled run, $\Delta C_A^{\mathrm{BGC}}$ is the

corresponding change in CO_2 in the biogeochemically coupled or radiatively uncoupled run, and g is the gain of the climate–carbon cycle feedback as defined by *Hansen et al.* (1984). To separate the influences of climate and CO_2 on land and ocean carbon uptake, they defined the land and ocean carbon storage as

$$\Delta C_L^{\mathrm{FC}} = \beta_L \Delta C_A^{\mathrm{FC}} + \gamma_L \Delta T^{\mathrm{FC}}, \tag{1.2}$$

$$\Delta C_O^{\mathrm{FC}} = \beta_O \Delta C_A^{\mathrm{FC}} + \gamma_O \Delta T^{\mathrm{FC}}, \tag{1.3}$$

where ΔC_L^{FC} and ΔC_O^{FC} are the changes in land and ocean carbon storage (in units of $\mathrm{Pg\,C}$) in the fully coupled simulation arising from an increase in atmospheric CO_2 mole fraction of ΔC_A^{FC} (ppm) and a temperature increase of ΔT^{FC} (K). Here β_L and β_O are the land and ocean concentration–carbon sensitivities in units of $\mathrm{Pg\,C\,ppm^{-1}}$, and γ_L and γ_O are the land and ocean climate–carbon sensitivities in units of $\mathrm{Pg\,C\,K^{-1}}$. *Friedlingstein et al.* (2006) assumed all the climate change effects could be effectively represented by the temperature change, ΔT^{FC}.

The strengths of these sensitivities were found by first solving for β_O and β_L from a radiatively uncoupled simulation forced with a trajectory of carbon emissions to the atmosphere,

$$\beta_O^{\mathrm{BGC}} = \frac{\Delta C_O^{\mathrm{BGC}}}{\Delta \mathrm{CO}_2^{\mathrm{BGC}}}, \tag{1.4}$$

$$\beta_L^{\mathrm{BGC}} = \frac{\Delta C_L^{\mathrm{BGC}}}{\Delta \mathrm{CO}_2^{\mathrm{BGC}}}, \tag{1.5}$$

then solving for γ_O and γ_L from the fully coupled simulation as follows,

$$\gamma_O^{\mathrm{FC-BGC}} = \frac{\Delta C_O^{\mathrm{FC}} - \beta_O \Delta \mathrm{CO}_2^{\mathrm{FC}}}{\Delta T^{\mathrm{FC}}}, \tag{1.6}$$

$$\gamma_L^{\mathrm{FC-BGC}} = \frac{\Delta C_L^{\mathrm{FC}} - \beta_L \Delta \mathrm{CO}_2^{\mathrm{FC}}}{\Delta T^{\mathrm{FC}}}. \tag{1.7}$$

The effect of changing CO_2 on the global mean temperature was approximated as

$$\Delta T^{\mathrm{FC}} = \alpha \Delta C_A^{\mathrm{FC}}, \tag{1.8}$$

where α is the linear transient climate sensitivity to CO_2 in units of $\mathrm{K\,ppm^{-1}}$.

Gregory et al. (2009) extended the carbon cycle feedback methodology and described ways to estimate feedback sensitivity parameters from different model experiments, including calculating the climate–carbon feedback parameters directly from model experiments that were biogeochemically uncoupled and radiatively coupled, herein called RAD simulations. *Arora et al.* (2013) analyzed the idealized 1% $\mathrm{y^{-1}}$ increasing CO_2 simulations from the fifth phase of the Coupled Model Intercomparison Project (CMIP5) using this framework. Following from *Friedlingstein et al.* (2006) and *Arora et al.* (2013), the overall climate–carbon feedback gain, g, can be related to these feedback sensitivity parameters through the following equation,

$$g = \frac{-\alpha\left(\gamma_O + \gamma_L\right)}{\left(m + \beta_O + \beta_L\right)}, \tag{1.9}$$

where m is a constant (2.12 $\mathrm{Pg\,C\,ppm^{-1}}$). The gain of the carbon cycle is larger for stronger effective climate–carbon sensitivities (i.e., for more negative values of γ_L and γ_O). Conversely, the gain of the carbon cycle is weaker if ocean and land uptake respond positively to increasing atmospheric CO_2 (i.e., larger positive values of β_L and β_O). Nonlinear and inter-

active aspects of the climate–carbon cycle feedback were neglected in the original derivation. Subsequent work has shown that for the ocean, γ_O is different when estimated using RAD or FC − BGC simulations (*Schwinger et al.*, 2014). In addition, since β_L is non-linear with respect to changes in atmospheric CO_2 mole fractions, γ_L derived from emissions-forced model experiments is different than when derived from concentration-forced simulations (*Zickfeld et al.*, 2011). Here, I show that γ_L is also sensitive to the manner in which it is estimated from a given set of simulations.

1.2 Quantifying Feedbacks and Reducing Biases

As ESMs become increasingly complex, there is a growing need for comprehensive, multi-faceted, and rigorous evaluation, analysis, and diagnosis of model results. In addition, resource and logistical constraints limit the frequency and extent of environmental observations available for developing, parameterizing, or evaluating models, resulting in unquantified sampling biases and necessitating a systematic sampling strategy to maximize coverage and objectively represent environmental variability at desired scales. To advance our understanding of biogeochemical processes and their interactions with climate under conditions of increasing atmospheric CO_2, and to offer an approach for understanding observational representativeness and up-scaling measurements, I conducted a series of studies to 1) identify and quantify persistent atmospheric CO_2 biases in a suite of the world's leading ESMs; 2) develop a quantitative and systematic methodology for stratifying sampling domains, informing measurement site selection, and determining the representativeness of observational sites and networks; and 3) characterize nonlinear responses of terrestrial ecosystems and ocean processes in long-term climate change simulations.

In the first of these investigations, I analyzed emission-driven simulations—in which atmospheric CO_2 levels were computed prognostically—for historical (1850–2005) and future

periods (Representative Concentration Pathway (RCP) 8.5 for 2006–2100) produced by 15 ESMs for the fifth phase of the Coupled Model Intercomparison Project (CMIP5). Comparison of ESM prognostic atmospheric CO_2 over the historical period with observations indicated that ESMs, on average, had a small positive bias in predictions of contemporary atmospheric CO_2. Weak ocean carbon uptake in many ESMs contributed to this bias, based on comparisons with observations of ocean and atmospheric anthropogenic carbon inventories. A significant linear relationship between contemporary atmospheric CO_2 biases and future CO_2 levels found for the multimodel ensemble (i.e., an emergent constraint) was used to create a contemporary CO_2 tuned model (CCTM) estimate of the atmospheric CO_2 trajectory for the 21st century. This analysis provided evidence that much of the model-to-model variation in projected CO_2 during the 21st century was tied to biases that existed during the observational era and that model differences in the representation of concentration–carbon feedbacks and other slowly varying carbon cycle processes appear to be the primary driver of this variability. By improving models to more closely match the long-term time series of CO_2 from Mauna Loa, our analysis suggests that uncertainties in future climate projections can be reduced. This paper is published as

F. M. Hoffman, J. T. Randerson, V. K. Arora, Q. Bao, P. Cadule, D. Ji, C. D. Jones, M. Kawamiya, S. Khatiwala, K. Lindsay, A. Obata, E. Shevliakova, K. D. Six, J. F. Tjiputra, E. M. Volodin, and T. Wu (2014), Causes and implications of persistent atmospheric carbon dioxide biases in Earth system models, *J. Geophys. Res. Biogeosci.*, 119(2):141–162, doi:10.1002/2013JG002381.

In the second study, I further developed a quantitative methodology for stratifying sampling domains and understanding the representativeness of measurements, measurement sites, and observational networks. Because making environmental measurements can be difficult, dangerous, and expensive, a systematic sampling strategy is needed to minimize sampling biases and represent important environmental gradients at desired spatial and temporal scales.

Multivariate spatiotemporal clustering was applied to down-scaled general circulation model results and data for the State of Alaska at 4 km^2 resolution to define multiple sets of ecoregions across two decadal time periods. Maps of ecoregions for the present (2000–2009) and future (2090–2099) were produced, showing how combinations of 37 characteristics are distributed and how they may shift in the future. Representative sampling locations were identified on present and future ecoregion maps. A representativeness metric was developed, and representativeness maps for eight candidate sampling locations were produced. This metric was used to characterize the environmental similarity or dissimilarity of each site. The analysis provided model-inspired insights into optimal sampling strategies, provided a framework for up-scaling measurements, and could inform a down-scaling approach for integration of models and measurements. The techniques described here can be applied at different spatial and temporal scales to meet the needs of individual measurement campaigns. This paper is published as

F. M. Hoffman, J. Kumar, R. T. Mills, and W. W. Hargrove (2013), Representativeness-based sampling network design for the State of Alaska, *Landscape Ecol.*, 28(8):1567–1586, doi:10.1007/s10980-013-9902-0.

In the third investigation, I used three sets of long-term climate change simulations; consisting of historical (1850–2005), RCP 8.5 (2006–2100), and extended-RCP 8.5 (2101–2300) simulations from the Community Earth System Model version 1.0 (CESM1(BGC)); to quantify drivers of terrestrial and ocean carbon and water cycle changes. In two simulations, called BGC and RAD, the effects of CO_2 fertilization and nitrogen (N) deposition in the biosphere (biogeochemically coupled) and the effects of rising temperature and circulation changes due to radiative forcing from CO_2, other greenhouse gases, and aerosols (radiatively coupled), respectively, were isolated. In a third fully coupled simulation, called FC, the radiative and biogeochemical couplings were combined to investigate the net effect of CO_2 and N fertilization and climate change on terrestrial and marine ecosystems. The feedback anal-

ysis framework, described above, was applied to these simulation experiments to quantify the concentration–carbon, β, and climate–carbon, γ, feedback sensitivities in two different ways out to year 2300. I found that γ_L was weaker when estimated as the reduction in land carbon from the BGC and FC simulations, as compared to γ_L derived directly from the RAD simulation, indicating a strong nonlinearity in the response of the biosphere to the combined effects of increasing atmospheric CO_2 and rising temperatures. Meanwhile, γ_O exhibited the opposite nonlinear behavior. The nonlinearity in terrestrial climate–carbon cycle feedbacks was attributed to differences in gross primary production (GPP) between the BGC and FC simulations because climate-induced GPP reductions were buffered by nonlinear changes in the hydrological cycle and N mineralization. These results suggest that employing RAD simulations to estimate carbon–climate feedbacks results in an underestimate in the increase of land carbon uptake and an overestimate in the increase of ocean carbon uptake under the combined conditions of increased temperature and elevated atmospheric CO_2. The imbalance of these opposing estimate biases will lead to allowable emissions estimates that are too low or too high to maintain a given CO_2 level or temperature target.

Chapter 2

Causes and Implications of Persistent Atmospheric Carbon Dioxide Biases in Earth System Models

2.1 Introduction

Anthropogenic emissions of radiatively active greenhouse gases into the atmosphere, especially carbon dioxide (CO_2), are rapidly increasing the burden of these gases and altering the Earth's climate (*IPCC*, 2007; *Raupach and Canadell*, 2010). This perturbation of the global carbon cycle is expected to induce feedbacks from the terrestrial biosphere and oceans on future CO_2 concentrations and the climate system. These climate–carbon cycle feedbacks are highly uncertain, difficult to predict, and potentially large (*Denman et al.*, 2007). Understanding and predicting the strength and direction of feedbacks is critically important for estimating future atmospheric CO_2 concentrations and, therefore, accurately predicting the effects and extent of climate change.

Models of Earth's climate system are used to predict responses to human and natural forcings into the future, while hind-casts are used to judge the ability of individual models to reproduce observed patterns. Current generation Earth System Models (ESMs) attempt to capture the complex interactions and feedbacks between climate, terrestrial and ocean ecosystems, and human activities. Scenarios describing alternative prospective future socioeconomic, technological, and environmental conditions are used to generate a consistent set of chemical, biological, and land use data to drive ESMs (*Moss et al.*, 2010). The results from such ESM simulations are valuable for diagnosing the magnitude of mitigation efforts required to stabilize CO_2 levels in the atmosphere under various scenarios, taking into account carbon cycle responses and feedbacks. Traditionally, such models were provided with a trajectory of CO_2 and other greenhouse gases consistent with scenario assumptions about population, energy resources and consumption, and agricultural policies and practices. Recently, as improvements to the representation of biogeochemical processes on land and in the ocean and better atmospheric chemistry have been added to ESMs, scenario-derived emissions of radiatively active gases, consistent with plausible natural and anthropogenic influences, are used to force ESMs. Concentration-driven simulation results are frequently analyzed to evaluate the mean carbon stocks and fluxes and to constrain biosphere processes and feedbacks in land and ocean models (*Friedlingstein et al.*, 2006; *Arora et al.*, 2013; *Anav et al.*, 2013). They also provide the opportunity to estimate emissions scenarios consistent with a specific trajectory of atmospheric CO_2 (*Jones et al.*, 2013). Emission-driven simulations, in contrast, provide the opportunity to assess the implications of biases resulting from uncertainties associated with ecosystem processes and feedbacks as the effects of those uncertainties propagate through the coupled ESM.

Friedlingstein et al. (2003, 2006) developed a framework for analysis of climate–carbon cycle feedbacks and applied it to 11 coupled climate–carbon cycle atmosphere–ocean general circulation models for the Coupled Climate–Carbon Cycle Model Intercomparison Project (C^4MIP). *Friedlingstein et al.* (2006) introduced model sensitivities of land and ocean carbon

sinks to climate (γ_L and γ_O, respectively) and to atmospheric CO_2 concentration (β_L and β_O, respectively) as metrics of climate–carbon and concentration–carbon feedbacks, respectively, to complement the overall climate sensitivity to atmospheric CO_2 parameter, α, in common use. In their study, *Friedlingstein et al.* (2006) found that the model sensitivities of the land carbon sinks to climate (γ_L) varied by almost a factor of 9 and to concentration (β_L) by almost a factor of 14. Moreover, the models varied by a factor of almost 8 in their gain (g) of the climate–carbon cycle feedback. *Arora et al.* (2013) performed a similar analysis for nine ESMs participating in the Fifth Phase of the Coupled Model Intercomparison Project (CMIP5) (*Taylor et al.*, 2012) and found that γ_L varied by almost a factor of 6, β_L varied by almost a factor of 7, and the emissions-derived gain (g_E) varied by more than a factor of 6. The emissions-derived gain (g_E) is analogous to the *Friedlingstein et al.* (2006) gain (g) for concentration-forced simulations. The multi-model mean feedback parameters, and their standard deviations, were lower in the nine CMIP5 models than in the C^4MIP models, with γ_L being 26% weaker and β_L being 32% weaker. These differences may be partially explained by differences in the future emissions scenarios used in the two studies. Nevertheless, these results point to very large uncertainties in the response of terrestrial biosphere models to climate change and rising CO_2 concentrations, and in the overall strength of the feedbacks they predict. While the framework developed by *Friedlingstein et al.* (2006) is useful for evaluating the overall strength of feedback responses within a given model and for comparing concentration and climate sensitivities between models, it provides no indication about the likelihood of any model being correct. In addition, multiple factors contribute to the apparent strength of the β_L, β_O, γ_L, and γ_O sensitivities, and the concentration and climate sensitivities interact with each other non-linearly through biological and chemical processes (*Gregory et al.*, 2009).

In the studies described above characterizing carbon cycle feedback processes, no comparisons were made to observations. This is the next crucial step for reducing uncertainties associated with future scenarios of global climate change. Recent research has made initial

steps in this direction. *Cox et al.* (2013) used the observed relationship between the growth rate of atmospheric CO_2 and tropical temperature as a constraint to reduce predicted uncertainty in the land carbon storage sensitivity to climate change (γ_L) in the tropics in C^{4}MIP models. Similarly, *Gillett et al.* (2013) used the ratio of warming to cumulative emissions of CO_2 to estimate a transient response to cumulative emissions (TRCE) from observations for comparison with 12 CMIP5 models. Such innovative use of contemporary measurements to constrain carbon cycle responses to climate change is important for reducing the range of uncertainty in future climate change projections (*Randerson*, 2013). Moreover, comparisons with data sets derived from the synthesis of measurements collected over a wide geospatial range can provide constraints on individual processes and on carbon cycle responses that are sensitive to initial conditions. *Todd-Brown et al.* (2013) compared soil carbon stocks from 11 CMIP5 models with the Harmonized World Soil Database (HWSD) and the Northern Circumpolar Soil Carbon Database (NCSC). Despite reasonable global-scale agreement with these observations, most ESMs failed to reproduce grid-scale soil carbon variations, suggesting that key processes may be missing in the majority of ESMs.

The goal of this paper is to identify long-term CO_2 biases in emission-driven simulation results produced by ESMs participating in CMIP5 and describe the causes and implications of those biases for future climate projections during the middle and latter half of the 21st century. In our analysis, we developed a new approach using contemporary inventory observations and structural information about feedbacks within the CMIP5 models to constrain future CO_2 predictions and to reduce uncertainties associated with the range of possible CO_2 mole fractions consistent with the RCP 8.5 emissions scenario.

2.2 Methods

2.2.1 Model descriptions

We analyzed historical and future emission-driven simulation results produced using ESMs for CMIP5. The historical simulations, referred to as experiment 5.2 or esmHistorical (*Taylor et al.*, 2012), were forced with spatially distributed CO_2 emissions reconstructed from fossil fuel consumption estimates (*Andres et al.*, 2011) for the period 1850–2005. The future simulations, referred to as experiment 5.3 or esmrcp85 (*Taylor et al.*, 2012), were forced with projected CO_2 emissions for the period 2006–2100, following the scenario described by the Representative Concentration Pathway (RCP) 8.5 (*Moss et al.*, 2010). Model output was obtained primarily from the Earth System Grid Federation (ESGF), an international network of distributed climate data servers (*Williams et al.*, 2011).

Simulation results were produced by fully coupled ESMs with interactive terrestrial and marine biogeochemistry models, which feature climate–carbon cycle feedback mechanisms. Since the simulations were forced with CO_2 emissions, these models prognostically computed global atmospheric CO_2 mole fractions, which represent an integration of physical, chemical, and biological processes on Earth and their interactions and feedbacks with the climate system. The ESMs employed different aerosol emissions, land use change processes, and process parameterizations, leading to a range of different aerosol and greenhouse gas concentrations, radiative forcings, and climate interactions. The ability of models to accurately reproduce the observed atmospheric CO_2 mole fraction trajectory over the historical period provides a broad indication of model fidelity, a necessary but not sufficient condition for credible ESM performance. Each of the models that generated output used in this study is listed in Table 2.1.

Table 2.1: Models that generated output used in this study.

Model	Modeling Center (or Group)	Component Models and Resolutions			
		Atmosphere	Land	Ocean	Sea Ice
BCC-CSM1.1 (*Wu et al.*, 2013)	Beijing Climate Center, China Meteorological Administration, CHINA	AGCM2.1 ($2.875^\circ \times 2.875^\circ$, L26)	BCC_AVIM1.0 ($2.875^\circ \times 2.875^\circ$)	MOM4_L40 ($1^\circ \times (1–\frac{1}{3})^\circ$, L40)	SIS ($1^\circ \times (1–\frac{1}{3})^\circ$)
BCC-CSM1.1(m) (*Wu et al.*, 2013)	Beijing Climate Center, China Meteorological Administration, CHINA	AGCM2.2 ($1.125^\circ \times 1.125^\circ$, L26)	BCC_AVIM1.0 ($1.125^\circ \times 1.125^\circ$)	MOM4_L40 ($1^\circ \times (1–\frac{1}{3})^\circ$, L40)	SIS ($1^\circ \times (1–\frac{1}{3})^\circ$)
BNU-ESM[†f] (*Dai et al.*, 2003, 2004; *College of Global Change and Earth System Science*, 2012)	Beijing Normal University, CHINA	CAM3.5 ($2.875^\circ \times 2.875^\circ$, L26)	CoLM3 & BNUDGVM (C/N) ($2.875^\circ \times 2.875^\circ$, L10)	MOM4p1 & IBGC ($1^\circ \times (1–\frac{1}{3})^\circ$, L50)	CICE4.1 ($1^\circ \times (1–\frac{1}{3})^\circ$)
CanESM2[‡] (*Arora et al.*, 2011)	Canadian Centre for Climate Modelling and Analysis, CANADA	CanAM4 ($2.81^\circ \times 2.81^\circ$, L35)	CLASS2.7 & CTEM1 ($2.81^\circ \times 2.81^\circ$)	CanOM4 & CMOC1.2 ($1.5^\circ \times 1^\circ$, L40)	CanSIM1 ($2.81^\circ \times 2.81^\circ$)
CESM1-BGC[f] (*Hurrell et al.*, in press; *Keppel-Aleks et al.*, 2013; *Lindsay et al.*, 2014)	Community Earth System Model Contributors, NSF-DOE-NCAR, USA	CAM4 ($0.9^\circ \times 1.25^\circ$, L30)	CLM4 ($0.9^\circ \times 1.25^\circ$)	POP2 & NPZD ($1^\circ \times (1–\frac{1}{3})^\circ$, L60)	CICE4 ($1^\circ \times (1–\frac{1}{3})^\circ$)
FGOALS-s2.0[a] (*Bao et al.*, 2013; *Liu et al.*, 2012; *Lin et al.*, 2013)	LASG, Institute of Atmospheric Physics, CAS, CHINA	SAMIL2.4.7 ($1.67^\circ \times 2.81^\circ$, L26)	CLM3 & VEGAS2.0 ($1.67^\circ \times 2.81^\circ$)	LICOM2.0 ($1^\circ \times (1–\frac{1}{2})^\circ$, L30)	CSIM5 ($1^\circ \times (1–\frac{1}{2})^\circ$)
GFDL-ESM2g, GFDL-ESM2m[b] (*Dunne et al.*, 2012, 2013)	NOAA Geophysical Fluid Dynamics Laboratory, USA	AM2 ($2^\circ \times 2.5^\circ$, L24)	LM3 ($2^\circ \times 2.5^\circ$)	MOM4 ($1^\circ \times (1–\frac{1}{3})^\circ$, L50)	SIS ($1^\circ \times (1–\frac{1}{3})^\circ$)
HadGEM2-ES[c] (*Collins et al.*, 2011; *Jones et al.*, 2011)	Met Office Hadley Centre, UNITED KINGDOM	HadGAM2 & UKCA ($1.25^\circ \times 1.875^\circ$, L38)	MOSES2 & TRIFFID ($1.25^\circ \times 1.875^\circ$)	HadGOM2 & diat-HadOCC ($1^\circ \times (1–\frac{1}{3})^\circ$, L40)	HadGOM2 ($1^\circ \times (1–\frac{1}{3})^\circ$)
INM-CM4[†‡] (*Volodin et al.*, 2010)	Institute for Numerical Mathematics, RUSSIA	($2^\circ \times 1.5^\circ$, L21)	($2^\circ \times 1.5^\circ$)	($1^\circ \times 0.5^\circ$, L40)	($1^\circ \times 0.5^\circ$)
IPSL-CM5A-LR[d] (*Dufresne et al.*, 2013)	Institut Pierre-Simon Laplace, FRANCE	LMDZ4 ($3.75^\circ \times 1.9^\circ$, L39)	ORCHIDEE ($3.75^\circ \times 1.9^\circ$)	ORCA2 & PISCES ($2^\circ \times (2–\frac{1}{2})^\circ$, L31)	LIM2 ($2^\circ \times (2–\frac{1}{2})^\circ$)
MIROC-ESM[f] (*Watanabe et al.*, 2011; *Oschlies*, 2001)	Japan Agency for Marine-Earth Science and Technology, Atmosphere and Ocean Research Institute (University of Tokyo), and National Institute for Environmental Studies, JAPAN	MIROC-AGCM & SPRINTARS ($2.875^\circ \times 2.875^\circ$, L80)	MATSIRO & SEIB-DGVM ($2.875^\circ \times 2.875^\circ$, L6)	COCO3.4 & NPZD ($1.5^\circ \times 1^\circ$, L44)	COCO3.4 ($1.5^\circ \times 1^\circ$)
MPI-ESM-LR[ef] (*Maier-Reimer et al.*, 2005; *Raddatz et al.*, 2007; *Brovkin et al.*, 2009)	Max Planck Institute for Meteorology, GERMANY	ECHAM6 ($2.81^\circ \times 2.81^\circ$, L47)	JSBACH ($2.81^\circ \times 2.81^\circ$)	MPIOM & HAMOCC ($1.5^\circ \times 1.5^\circ$, L40)	MPIOM ($1.5^\circ \times 1.5^\circ$)
MRI-ESM1 (*Yukimoto et al.*, 2011; *Nakano et al.*, 2011; *Yukimoto et al.*, 2012; *Obata and Shibata*, 2012)	Meteorological Research Institute, JAPAN	GSMUV ($0.75^\circ \times 0.75^\circ$, L48)	HAL & MRI-LCCM2 ($0.75^\circ \times 0.75^\circ$)	MRI.COM3 ($1^\circ \times 0.5^\circ$, L51)	MRI.COM3 ($1^\circ \times 0.5^\circ$)
NorESM1-ME (*Bentsen et al.*, 2013; *Iversen et al.*, 2013; *Tjiputra et al.*, 2013)	Norwegian Climate Centre, NORWAY	CAM4-Oslo ($1.9^\circ \times 2.5^\circ$, L26)	CLM4 ($1.9^\circ \times 2.5^\circ$)	MICOM & HAMOCC ($1^\circ \times (1–\frac{1}{3})^\circ$, L53)	CICE4 ($1^\circ \times (1–\frac{1}{3})^\circ$)

[†]Atmospheric CO_2 required unit correction.

[‡]Ocean carbon flux required unit correction.

[a]FGOALS-s2 model provided no ocean carbon fluxes.

[b]GFDL-ESM2g and GFDL-ESM2m output available beginning January 1861.

[c]HadGEM2-ES output available for December 1859 through November 2099; annual atmospheric CO_2 obtained directly from Hadley Centre.

[d]IPSL-CM5A-LR monthly atmospheric CO_2 obtained directly from IPSL.

[e]MPI-ESM-LR provided three *esmHistorical* realizations and one *esmrcp85* realization.

[f]Atmospheric CO_2 mole fraction was computed from 3-dimensional output.

2.2.2 Model output

Monthly output of prognostic atmospheric CO_2 and surface ocean CO_2 flux from emission-driven ESM simulations were analyzed to evaluate the evolution of the carbon cycle over the 20th and 21st centuries. Atmospheric CO_2 was obtained either as the total atmospheric mass of CO_2 and converted to mole fraction, or as the atmospheric CO_2 mole fraction at every atmosphere model layer. In the latter case, the global mole fraction was calculated as the area-weighted mean of CO_2 in the lowest atmosphere level. Surface ocean CO_2 flux was integrated spatially to determine global carbon uptake and further integrated over time to estimate the global change in ocean carbon inventory. While the net terrestrial CO_2 flux was available for some models in the form of net biospheric productivity, here, annual land carbon uptake was calculated as the difference between the prescribed annual anthropogenic emissions and the sum of the annual change in atmosphere and ocean carbon inventories. Therefore, the change in land carbon storage for a given year was estimated as

$$\Delta C_L = \sum_i F_i - \Delta C_A - \Delta C_O, \tag{2.1}$$

where F_i was the total anthropogenic fossil carbon emissions from all sources i (fossil fuel burning and cement production) for that year, ΔC_A was the change in atmospheric carbon storage for that year, and ΔC_O was the change in ocean carbon storage for that year. A single trajectory of annual anthropogenic carbon emissions, derived from the experimental forcing, was used in calculations for all model results. Carbon fluxes due to land use change were included implicitly in ΔC_L and were not included explicitly in total fossil carbon emissions $\sum_i F_i$. We assumed F_i in each model followed the historical and RCP 8.5 time series on the Potsdam Institute for Climate Impact Research site (`http://www.pik-potsdam.de/~mmalte/rcps/index.htm`). We also assumed the individual ESMs were at steady state at the beginning of the historical simulation (*i.e.*, that drift in the control simulation was

minimal).

2.2.3 Comparing CMIP5 ESMs with long-term carbon cycle observations

Atmospheric CO_2 mole fraction observations used for comparison with model projections of atmospheric CO_2 over the historical period were the same as those used to force the corresponding concentration-driven simulations, which were not analyzed here. Compiled by Tom Wigley and Malte Meinshausen, these "end-of-year CO_2 concentrations" consist of a combination of 75-y smoothed Law Dome ice core data (*Etheridge et al.*, 1996) up to 1832; 20-y smoothed Law Dome ice core data for 1823–1958; the Keeling Mauna Loa record, with 0.59 ppm subtracted (which is the Mauna Loa mean minus the NOAA global mean over 1982–1986) for 1959–1981; and the NOAA global mean value for 1982–2008 (*Conway et al.*, 1994). Development of these and related forcing data for pre-industrial control, 20^{th} century, and RCP simulations are described by *Meinshausen et al.* (2011).

Sabine et al. (2004) used inorganic carbon measurements from the World Ocean Circulation Experiment (WOCE) and the Joint Global Ocean Flux Study (JGOFS), both conducted in the 1990s, and the tracer-based ΔC^* separation technique to estimate the global oceanic anthropogenic CO_2 sink for the period 1800–1994. Their ocean inventory estimate of 118 ± 19 Pg C accounts for approximately 48% of the total emissions from fossil fuel burning and cement production. They subtracted this ocean inventory estimate and the change in atmospheric inventory over the same period of 165 ± 4 Pg C from the estimate of cumulative emissions of 244 ± 20 Pg C to obtain a cumulative terrestrial biosphere source of 39 ± 28 Pg C.

More recently, *Khatiwala et al.* (2009) applied a Green's function model for ocean tracer transport, estimated from tracer and salinity data using a maximum entropy deconvolution technique, to simulate the time evolution of the ocean inventory and uptake rate of

anthropogenic CO_2 for the period 1765–2008. They estimated the ocean inventory and uptake rate in 2008 to be 140 ± 25 Pg C and 2.3 ± 0.6 Pg C y^{-1}, respectively. When they adjusted the estimate to include the Arctic Ocean and marginal seas not represented in the GLobal Ocean Data Analysis Project (GLODAP) database, the global inventory increased by approximately 11 Pg C. Using annual estimates of anthropogenic emissions and the atmospheric inventory, including uncertainties, they produced a trajectory for the terrestrial carbon budget, indicating that the terrestrial biosphere was a source of anthropogenic CO_2 until the 1940s, after which it became a sink. *Tans* (2009) performed a similar mass balance calculation using an empirical pulse response function constrained by the integrated ocean uptake in 1994 (*Sabine et al.*, 2004), the 1993–2002 uptake rate centered on late 1997 from atmospheric oxygen measurements (*Manning and Keeling*, 2006), and the 1995–2000 uptake rate estimate from an ocean inverse model (*Gruber et al.*, 2009). Deriving net terrestrial emissions as a residual, instead of including land use emissions explicitly due to their large uncertainty, *Tans* (2009) also found that net terrestrial emissions were positive before 1940 and were negative thereafter, making their cumulative contribution in 2008 small.

Khatiwala et al. (2013) produced a newly updated global ocean anthropogenic carbon sink trajectory through 2010 using the Green's function model. A cumulative sum of this ocean uptake provided an ocean anthropogenic carbon inventory estimate for 2010 of 150 ± 26 Pg C. Adding a partial estimate for accumulation in marginal seas and coastal areas from *Lee et al.* (2011) of 8.6 ± 0.6 Pg C yielded a more spatially comprehensive estimate of 160 ± 26 Pg C. Since the *Lee et al.* (2011) estimate was a lower bound, the upper bound was constrained using multiple Community Climate System Model (CCSM)-based simulations, resulting in a range for the inventory outside the GLODAP region of 9–14 Pg C. However, *Khatiwala et al.* (2013) ultimately computed a "best estimate" inventory for the GLODAP region in 2010 of 143 Pg C by averaging results from three different inversion methods, including the Green's function model. Using the above range for marginal seas and coastal areas, they provide a 2010 global best estimate inventory of 152–157 Pg C. Selecting the mid-point value yields a

final estimate of 155 Pg C with an uncertainty of ±20%. Here we scaled the Green's function time series to obtain the 155 Pg C best estimate for 2010 and to account for marginal seas and coastal areas.

The *Sabine et al.* (2004) and *Khatiwala et al.* (2013) data-based estimates with uncertainties provide valuable global constraints on model carbon cycle processes and feedbacks. However, these inventory estimates must be further adjusted to the 1850 equilibrium starting date of model simulations. The *Sabine et al.* (2004) ocean inventory estimate for 1994 was adjusted by subtracting the difference between the 1850 and 1800 ocean inventory estimates from the scaled *Khatiwala et al.* (2013) 1765–2010 time series, yielding 109 ± 19 Pg C. Similarly, the scaled *Khatiwala et al.* (2013) ocean inventory best estimate for 2010 was adjusted by subtracting the 1850 value, yielding 141 ± 38 Pg C. Using the adjusted trajectory of ocean uptake and applying Equation 2.1 on the time series through 2010, we calculated total carbon accumulation in the ocean and on land from 1850–2010 with their uncertainties based on *Khatiwala et al.* (2013) uncertainty estimates (Figure 2.1). Land and ocean carbon sinks computed using this approach were consistent with combined estimates reported by *Ballantyne et al.* (2012); however, here the net land flux included land use emissions.

2.2.4 A framework for constraining future trends

One approach for reducing uncertainties using contemporary observations is to identify relationships between contemporary variability and future trends within the models and constrain the contemporary variability using observations. This strategy was employed by *Hall and Qu* (2006), who evaluated the strength of the springtime snow albedo feedback ($\Delta\alpha_S/\Delta T_S$) from 17 models used for the IPCC Fourth Assessment Report and compared them with the observed springtime snow albedo feedback from the International Satellite Cloud Climatology Project (ISCCP) and ERA-40 reanalysis data. They found a linear re-

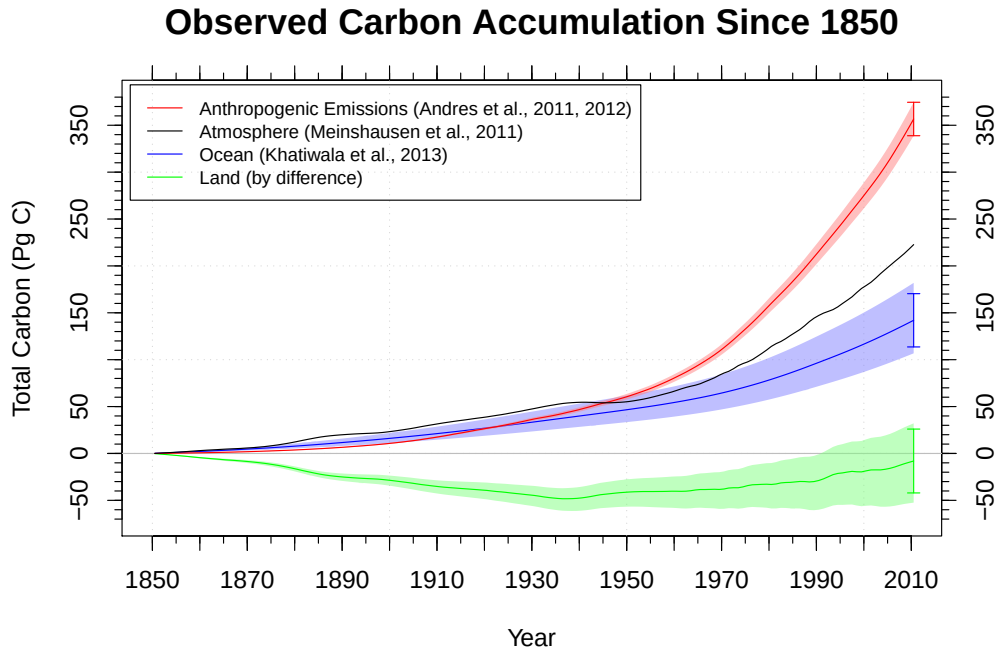

Figure 2.1: Observational estimates of anthropogenic carbon emissions (excluding land use change) and accumulation in the atmosphere, ocean, and land reservoirs are shown for 1850 to 2010. Land carbon accumulation/loss and its uncertainty was calculated from mass balance using an adjusted ocean carbon accumulation time series with uncertainty from *Khatiwala et al.* (2013).

lationship between model predictions of seasonal and 21st century snow albedo feedbacks. *Hall and Qu* (2006) assumed this relationship, which represents consistency in the structure of these models, accurately reflects functional behavior in nature, and used observational estimates of the contemporary seasonal cycle snow albedo feedback to constrain the longer-term snow albedo feedback that occurs in the models during the 21st century. More recently, this approach was applied by *Cox et al.* (2013) to the carbon cycle. In this latter study, the authors were able to show that the long-term climate sensitivity of tropical carbon fluxes was related to this same sensitivity on interannual timescales. By using contemporary observations, they were able to narrow the likely range of future model scenarios, showing that the likelihood of forest dieback was probably overestimated in earlier work.

As described below, we found a similar linear relationship over decadal timescales between contemporary and future atmospheric CO_2 mole fractions in CMIP5 emission-driven simulations. Specifically, models that had higher positive biases in atmospheric CO_2 mole fraction by the end of the observational era in 2010 tended to predict higher atmospheric CO_2 levels during the 21st century for the RCP 8.5 scenario than models that more closely matched the observations. We used this relationship, and implicitly the collection of CMIP5 models, to construct a hypothetical model that was tuned to contemporary observations, hereafter referred to as the contemporary CO_2 tuned model, or CCTM.

The CCTM estimate was obtained using the following approach. First, we computed a linear regression between atmospheric CO_2 at each future year (y-axis) and atmospheric CO_2 during 2010 (x-axis), defined as the 5-y mean for 2006–2010. In particular, we repeatedly applied the regression formula,

$$y_i = \beta_0 + \beta_1 x_i + \epsilon_i \tag{2.2}$$

where x_i was the 2010 CO_2 mole fraction, y_i was the future CO_2 mole fraction, and ϵ_i was an error term for every model $i = 1, \ldots, n$. β_0 and β_1 were two parameters, representing the y-intercept and the slope of the resulting line, respectively. Here, $n = 17$, representing the 17 separate simulations from 15 models from the CMIP5 collection. For every future interval, the error term ϵ_i was minimized using ordinary least squares to yield a linear regression model,

$$\hat{y}_i = \hat{\beta}_0 + \hat{\beta}_1 x_i, \tag{2.3}$$

where $\hat{y}_i$ was the predicted future CO_2 mole fraction from the linear regression model that

minimizes the residual, $e_i = y_i - \hat{y}_i$. The least squares estimates for the parameters were calculated using a standard algebraic approach. As shown in the results section below, these regressions were statistically significant through 2100, although uncertainties increased through time. Second, we estimated the intersection of this regression with a vertical line representing NOAA Global Monitoring Division (GMD) observations in 2010 (384.6 ± 0.5 ppm; a 5-y mean centered on 2008) (*Conway et al.*, 1994). This intercept at each time interval and the 95% confidence limits on the intercept comprised our CCTM estimate.

The CCTM estimate allowed us to inquire what might be the impact of tuning ESMs to capture the observed recent trajectory of global atmospheric CO_2. This approach takes advantage of the collection of CMIP5 models—including the wide range of sensitivities of gross land and ocean carbon fluxes to elevated CO_2 and climate changes, residence time distributions of carbon in ocean and land reservoirs, and feedbacks—to create an estimate with a zero bias at the end of the observed record. As such, it can be thought of as a "black box" approach to representing the carbon cycle. It was useful in developing approaches for analyzing ESM uncertainties because of the long-term bias persistence observed for this set of models.

We also developed a similar multi-model constraint on the evolution of ocean and land cumulative flux (inventory) time series to better understand why atmospheric CO_2 biases were so persistent. As described in the results, observational uncertainties were considerably higher for the ocean and land inventories, and, as a consequence, it was not possible to reduce uncertainties in future estimates by the same amount as for atmospheric carbon dioxide.

2.2.5 Calculating climate implications of CO_2 biases

Individual models directly calculate radiative forcing and surface temperature responses to anthropogenic CO_2, and therefore have different climate sensitivities (α). For our analysis,

we chose to use a standard method for approximating radiative forcing and subsequent temperature changes to equitably assess the climate implications of CO_2 biases across all models. We adopted the method described by *Boucher and Reddy* (2008), who employed an impulse response function (IRF) to describe the evolution of atmospheric CO_2 and global surface temperature. The IRF was derived from a HadCM3 climate model simulation in which the global atmospheric CO_2 mole fraction was abruptly ramped up to 4 times the pre-industrial levels and subsequently held constant. As described by *Boucher and Reddy* (2008), global surface temperature change may be estimated as

$$\delta T(t) = \sum_i \frac{c_i}{d_i} e^{\frac{-t}{d_i}}, \tag{2.4}$$

where the coefficients c_i (in units of $\mathrm{K\,(W\,m^{-2})^{-1}}$) and d_i (in units of y) are in Table A1 of *Boucher and Reddy* (2008). Next, this IRF was used to estimate the global surface temperature change at a time period horizon, P, from a radiative forcing profile, $\mathrm{RF}(t)$, as

$$\Delta T_s(t, P) = \int_{t_0}^{t_0+P} \mathrm{RF}(t)\, \delta T(t_0 + P - t)\, dt. \tag{2.5}$$

We reduced the c_1 and d_1 coefficients from the Hadley model by 10.5%, by multiplying by 0.895, to obtain a transient climate response of 1.9 K, the same as the mean of ESMs reported by *Gillett et al.* (2013).

First, we followed *Ramaswamy et al.* (2001) to approximate radiative forcing due to anthropogenic CO_2 at time t as

$$\mathrm{RF}(t) = m \ln\left(\frac{[\mathrm{CO_2}](t)}{[\mathrm{CO_2}](t_0)}\right), \tag{2.6}$$

where m was set equal to 5.35 $\mathrm{W\,m^{-2}}$ and $[\mathrm{CO_2}](t_0)$ was defined as 284 ppm in the year 1850. Second, we calculated CO_2-corrected predictions of future surface temperature following the method of *Boucher and Reddy* (2008, their Appendix A). This method approximates the delayed response of surface temperature to radiative forcing as a sum of two exponentials with adjustment times of 8.4 and 410 years. Coefficients c_1 and d_1 in the exponentials (*Boucher and Reddy*, 2008, Appendix A) were multiplied by 0.895 to obtain a transient climate response of 1.9 K per doubling of CO_2 as reported by *Gillett et al.* (2013) for the mean of the CMIP5 ESMs. While using the IRF from another ESM might alter the mean temperature change per unit of radiative forcing presented here, it would not change the order among models. We note that this calculated temperature change accounts only for CO_2-driven climate change and does not include observed cooling due to aerosols or contributions from other greenhouse gases like methane (CH_4), nitrous oxide (N_2O), and chlorofluorocarbons (CFCs).

2.2.6 Quantifying uncertainty

Sabine et al. (2004) provided uncertainty estimates for their estimate of the ocean anthropogenic carbon inventory. *Khatiwala et al.* (2013) used the GLODAP/WOA05 databases to generate global estimates of historical anthropogenic CO_2 ocean uptake, and they propagated uncertainties from these databases through their Green's function model to provide uncertainties for these uptake estimates. We used these uncertainties in quadrature to provide an uncertainty range for the *Khatiwala et al.* (2013) inventory and propagated them through Equation 2.1 to provide estimates of uncertainty for land carbon accumulation. For

the linear regression models used here to construct the CCTM estimate, 95% confidence intervals were calculated and propagated into estimates of atmospheric CO_2, radiative forcing, and temperature change. For purposes of uncertainty comparison, the 95% confidence interval ranges for the CCTM were compared with the 95^{th} percentile of the range for the multi-model distribution, assuming a normal distribution.

2.3 Results

2.3.1 Contemporary biases

Comparison of ESM prognostic atmospheric CO_2 mole fraction over the historical period with observations indicated that ESMs, on average, had a high bias in their predictions of contemporary atmospheric CO_2 (Figure 2.2(a)). For the multi-model mean, this high bias was persistent from 1946 throughout the 20^{th} century (Figure 2.2(b)). By the end of the historical model simulation period (2005), the multi-model mean was 5.6 ppm above observations and the models ranged from 21.7 ppm below to 26.2 ppm above the observed CO_2 mole fraction of 378.8 ppm. Of the 19 historical simulations from 15 ESMs included in this analysis, only two predicted a CO_2 mole fraction well below observations in 2005. By 2010, near the end of the observational record, the multi-model mean was 7.9 ppm higher than the global mean CO_2 mole fraction reported by NOAA GMD (*Conway et al.*, 1994). This bias was probably a conservative estimate of the true multi-model mean bias because fossil fuel emissions from the RCP 8.5 scenario during 2006–2010 (8.6 $\mathrm{Pg\,C\,y^{-1}}$) were slightly lower than the observed emissions (8.7 $\mathrm{Pg\,C\,y^{-1}}$) (*Peters et al.*, 2013; *Le Quéré et al.*, 2013).

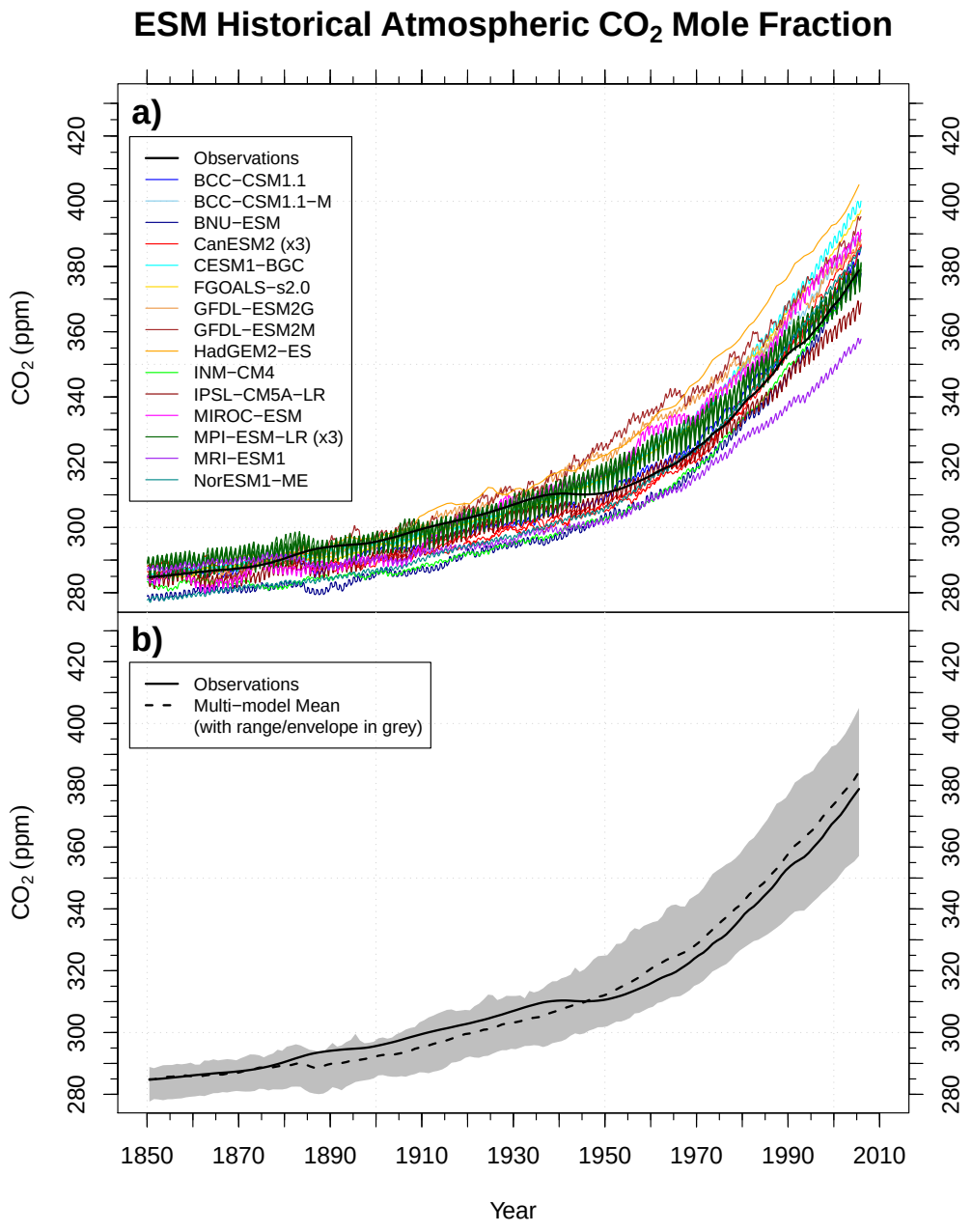

Figure 2.2: (a) Most ESMs exhibit a high bias in atmospheric carbon dioxide (CO_2) mole fraction. The predicted atmospheric CO_2 mole fraction for the 19 historical simulations shown here ranges from 357–405 ppm at the end of the CMIP5 historical period (1850–2005). (b) The multi-model mean is biased high from 1946 throughout the remainder of the 20^{th} century, ending 5.6 ppm above observations in 2005.

2.3.2 Causes of the contemporary bias

Most ESMs exhibited a small or moderate low bias in ocean carbon accumulation from 1870–1930 when compared with adjusted estimates from *Khatiwala et al.* (2013), but most ESMs were contained within the envelope of observational uncertainty after 1930 (Figure 2.3(a)). Ocean carbon accumulation ranged from 88–261 Pg C, with a multi-model mean of 145 Pg C, as compared with observational estimates of 142 ± 38 Pg C through year 2010. Excluding the two outlier models that had unlikely land contemporary sink estimates (FGOALS-s2.0 and MRI-ESM1), the range of ocean carbon accumulation was reduced to 101–210 Pg C with a mean of 141 Pg C at 2010, a better match with observations. However, most ocean models achieved this correspondence with observational estimates primarily as a consequence of high biases in atmospheric CO_2 mole fraction. Normalizing ocean carbon accumulation with atmospheric accumulation $\left(\frac{\Delta C_O}{\Delta C_A}\right)$ provided a measure of the strength of ocean carbon storage in emissions-forced simulations that partially accounted for atmospheric CO_2 biases. Performing this normalization and comparing with adjusted ocean inventories from *Sabine et al.* (2004) for 1994 (Figure 2.4) and from *Khatiwala et al.* (2013) for 2010 (Figure 2.5) indicated that the majority of models were near or below the observed ratio. Across the different models, the ocean/atmosphere ratio ranged from 0.42–0.99, with a multi-model mean of 0.61, which compared well with the observational estimate of 0.64 ± 0.15 in 2010. Excluding the same two outlier models (FGOALS-s2.0 and MRI-ESM1), the range of the ocean/atmosphere ratio was reduced to 0.42–0.91, with a mean of 0.58.

Terrestrial biosphere models within ESMs also had a wide range of responses, with both positive and negative net carbon accumulation throughout the 20^{th} century (Figures 2.4 and 2.5). Terrestrial and ocean carbon accumulation compensated for one another ($R = -0.91$, Figure 2.6), reducing the bias in predicted atmospheric CO_2. This compensation effect was exemplified by the INM-CM4 model, which had the correct atmospheric CO_2 in 2005, but had strong ocean uptake that was balanced by weak land carbon uptake. During the second

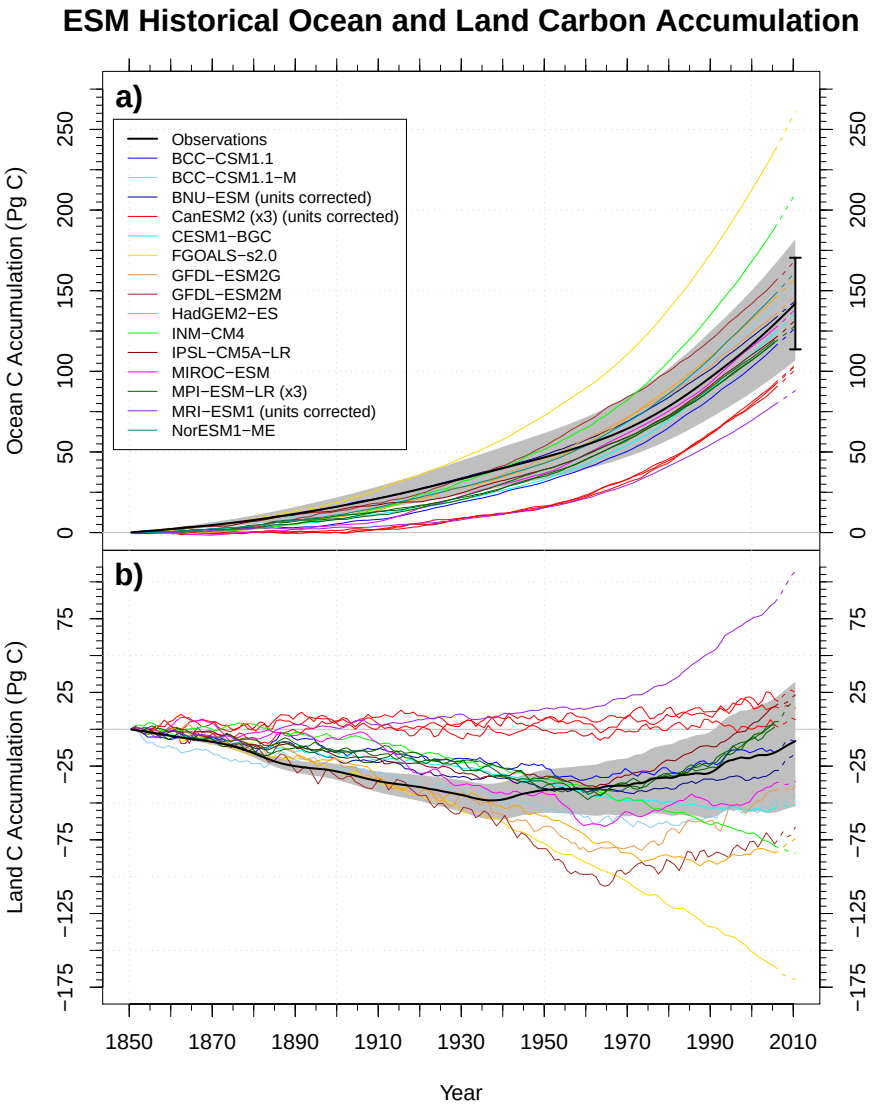

Figure 2.3: (a) Ocean and (b) land anthropogenic carbon inventories from CMIP5 models compared to estimates from *Khatiwala et al.* (2013). Most ESMs exhibit a low bias in ocean anthropogenic carbon accumulation from 1870–1930 as compared with adjusted estimates from *Khatiwala et al.* (2013). While some models enter the envelope of observational uncertainty later in the 20$^{\text{th}}$ century, this was often a consequence of the increasing high bias in atmospheric CO_2 mole fractions. ESMs had a wide range of land carbon accumulation responses to increasing atmospheric CO_2 and land use change, ranging from a cumulative source of 170 Pg C to a cumulative sink of 107 Pg C in 2010. In these figures, solid colored lines represent historical simulation results and the extending dashed line segments represent the first 5 years of the RCP 8.5 simulations. The shaded polygon represents the uncertainties surrounding the adjusted observational estimates of ocean and land carbon accumulation, and the error bars correspond to the ±20% uncertainty in the *Khatiwala et al.* (2013) best estimate of ocean carbon accumulation for 2010.

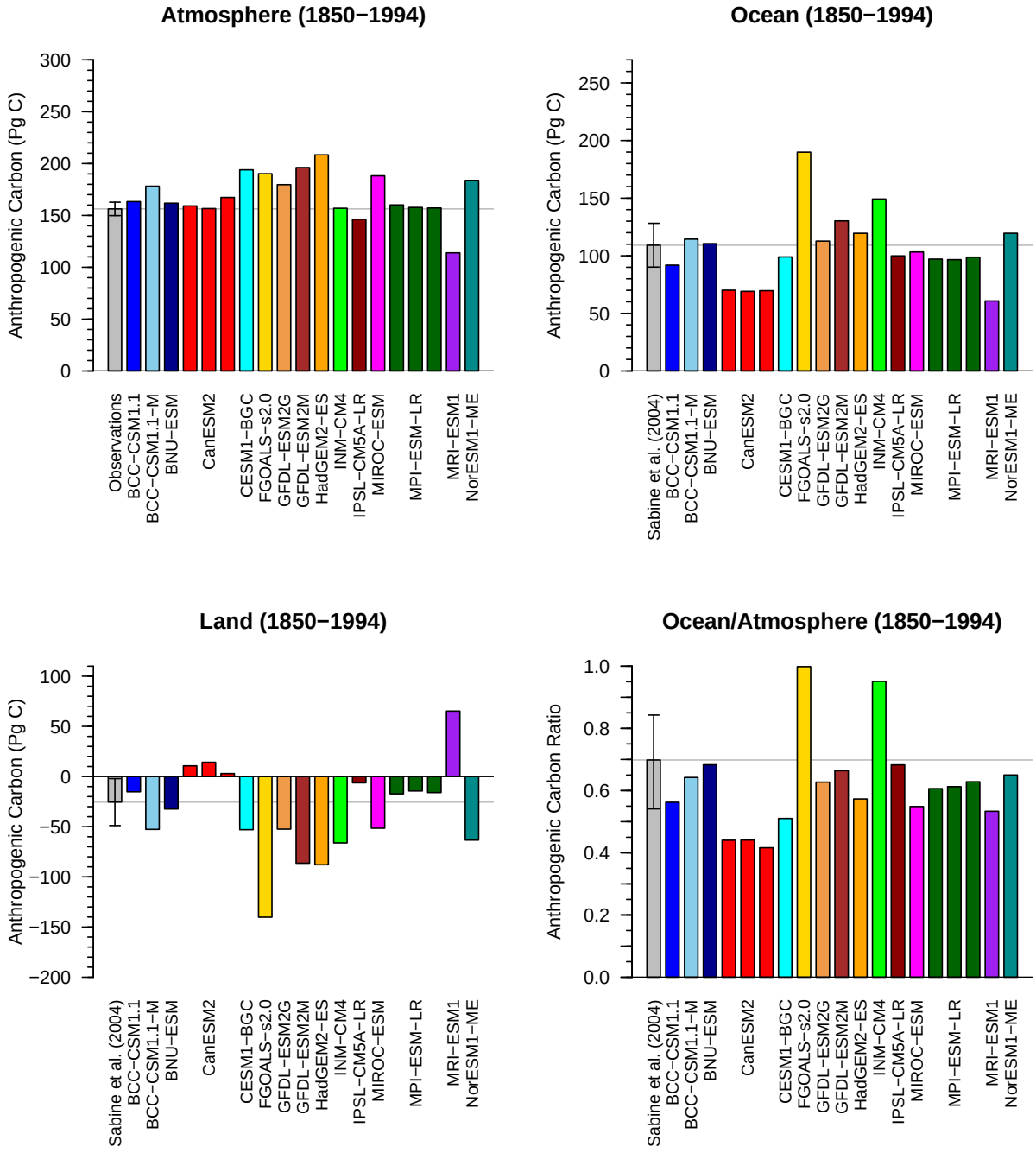

Figure 2.4: Reconstructed atmospheric CO_2 levels and observationally based estimates of carbon uptake from *Sabine et al.* (2004) provide powerful constraints on carbon inventories in the atmosphere and ocean as well as on land. While ocean carbon accumulation appears adequate in some model results, ocean carbon accumulation in most ESMs show a low bias once normalized by atmospheric accumulation (lower right panel).

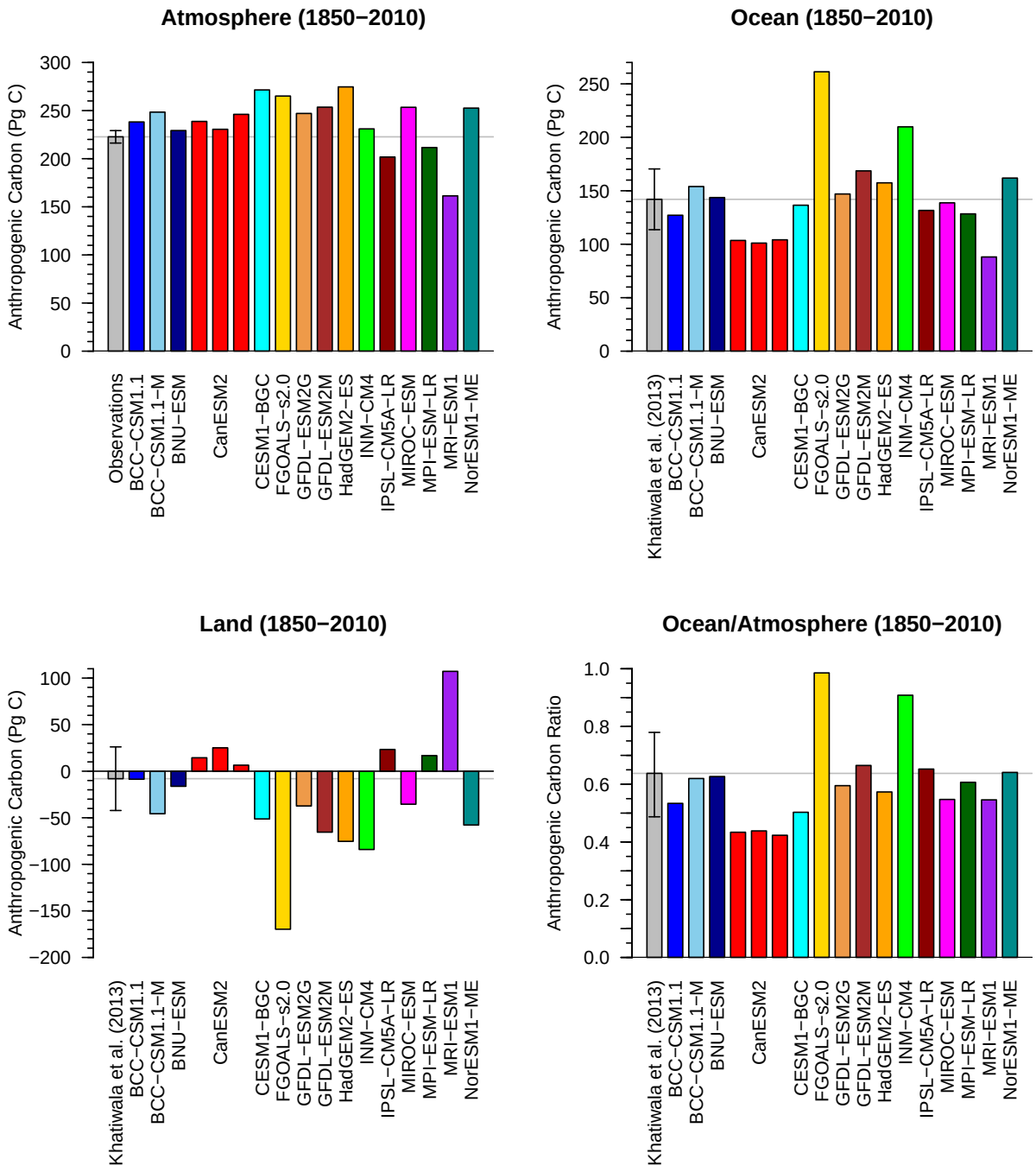

Figure 2.5: Reconstructed atmospheric CO_2 levels and observationally based estimates of ocean carbon uptake from *Khatiwala et al.* (2013) provide constraints on carbon inventories in the ocean, and on land when combined with fossil fuel and atmospheric CO_2 observations. While ocean carbon accumulation appears adequate in some model results, ocean carbon accumulation in most ESMs show a low bias once normalized by atmospheric accumulation (lower right panel).

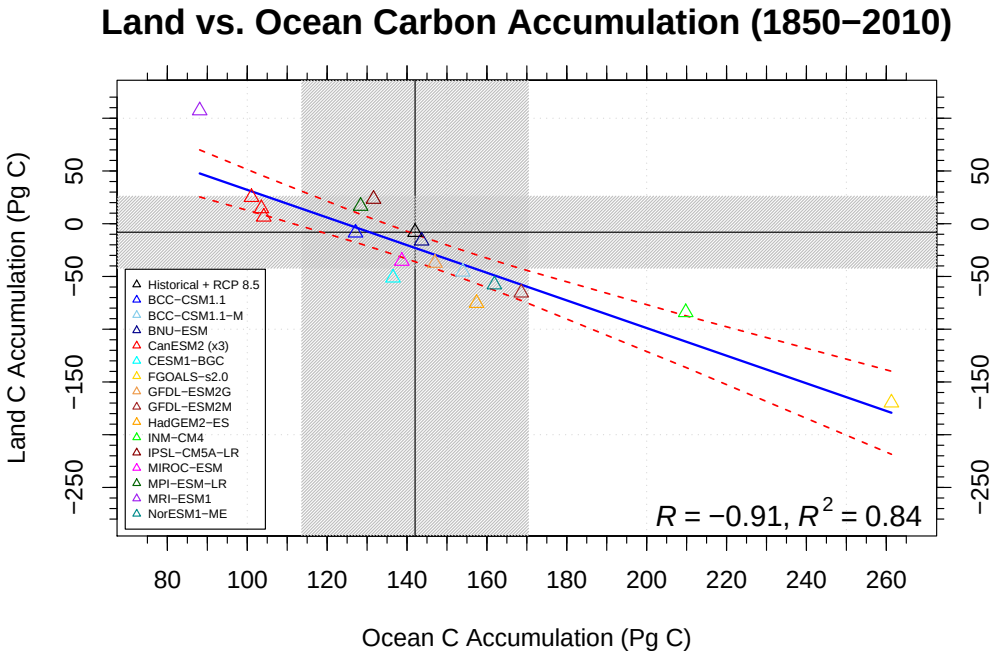

Figure 2.6: Land versus ocean carbon accumulation for all CMIP5 models in 2010. Terrestrial and ocean carbon accumulation compensated for one another ($R = -0.91$) reducing the bias in predicted atmospheric CO_2.

half of the 20$^{\text{th}}$ century, the land carbon sink was persistent with high rates during the 1990s and 2000s (Table 2.2). Thought to be due to changes in human land use (*i.e.*, reduced deforestation, new afforestation, and secondary re-growth of previously cleared land), wildfire suppression (*Girod et al.*, 2007; *Hurtt et al.*, 2002), and enhanced forest growth due to rising atmospheric CO_2 levels and higher rates of nitrogen deposition (*Pan et al.*, 2011; *Phillips et al.*, 2009), this growing land sink reinforced rising ocean uptake rates and resulted in a doubling of global carbon uptake between 1960 and 2010 (*Ballantyne et al.*, 2012). Although the multi-model mean distribution of land sinks closely matched the observations, individual model estimates varied widely. BCC-CSM1.1-M, CESM1-BGC, FGOALS-s2.0, GFDL-ESM2M, HadGEM2-ES, INM-CM4, and NorESM1-ME tended to underestimate land sinks, whereas CanESM2 and MRI-ESM1 tended to overestimate them (Figure 2.3(b)).

Table 2.2: Comparison of observationally based estimates of decadal atmosphere, ocean, and land uptake rates of anthropogenic CO_2 with CMIP5 model predictions. Only models that provided both atmospheric CO_2 and ocean carbon fluxes are included in the multi-model means. Positive values represent additions to the atmosphere, ocean, or land reservoirs, and negative values represent losses. All units are $\mathrm{Pg\,C\,y^{-1}}$.

Model	1960–1969				1970–1979				1980–1989				1990–1999				2000–2010			
	FFE	**Atm**	**Ocn**	**Lnd**	**FFE**	**Atm**	**Ocn**	**Lnd**	**FFE**	**Atm**	**Ocn**	**Lnd**	**FFE**	**Atm**	**Ocn**	**Lnd**	**FFE**	**Atm**	**Ocn**	**Lnd**
Observations	3.0	1.8	1.0	0.2	4.6	2.7	1.4	0.6	5.5	3.4	1.8	0.3	6.2	3.2	2.0	1.0	7.7	4.3	2.4	1.1
Multi-model Mean		1.7	1.3	0.0		2.8	1.5	0.3		3.3	1.9	0.2		3.5	2.2	0.6		4.4	2.5	0.8
BCC-CSM1.1		1.2	1.0	0.8		3.1	1.4	0.0		3.4	1.8	0.3		3.5	2.0	0.8		4.7	2.3	0.7
BCC-CSM1.1-M		1.8	1.3	−0.2		3.0	1.7	−0.1		3.1	2.0	0.4		3.6	2.2	0.4		4.3	2.6	0.8
BNU-ESM		1.8	1.1	−0.0		2.8	1.5	0.3		3.2	1.7	0.6		4.3	2.0	−0.1		4.0	2.1	1.7
CanESM2 r1		1.5	1.0	0.4		3.2	1.3	0.2		4.0	1.6	−0.1		3.6	1.7	0.9		5.7	2.3	−0.3
CanESM2 r2		2.1	0.9	−0.1		2.7	1.2	0.7		3.9	1.7	−0.2		3.5	1.7	1.0		5.3	2.2	0.3
CanESM2 r3		1.7	1.0	0.3		3.4	1.1	0.1		3.1	1.6	0.8		4.9	2.0	−0.7		4.9	2.2	0.6
CESM1-BGC		2.4	1.2	−0.6		3.2	1.5	−0.1		4.0	1.9	−0.4		4.2	2.2	−0.2		4.9	2.4	0.3
FGOALS-s2.0		2.1	2.1	−1.3		3.5	2.8	−1.6		3.6	3.4	−1.5		3.9	4.0	−1.6		4.9	4.6	−1.8
GFDL-ESM2G		1.7	1.4	−0.1		2.1	1.4	1.0		3.0	1.7	0.8		3.3	2.1	0.9		4.1	2.2	1.4
GFDL-ESM2M		1.4	1.5	−0.0		2.0	1.6	1.0		3.4	1.9	0.2		3.0	2.2	1.0		4.3	2.5	0.9
HadGEM2-ES		2.7	1.6	−1.3		2.9	1.8	−0.1		3.8	2.0	−0.4		3.5	2.3	0.4		4.3	2.4	1.0
INM-CM4		2.1	1.7	−0.8		3.1	2.4	−0.9		3.5	2.8	−0.9		3.6	3.3	−0.7		5.0	4.0	−1.2
IPSL-CM5A-LR		1.2	1.1	0.6		2.3	1.3	1.0		2.7	1.8	1.0		3.0	1.9	1.3		3.8	2.0	1.9
MIROC-ESM		0.7	1.3	1.0		2.9	1.4	0.4		3.4	1.7	0.4		4.0	2.2	−0.1		4.2	2.2	1.3
MPI-ESM-LR r1		1.3	1.2	0.5		2.7	1.4	0.6		3.0	1.7	0.8		2.7	1.9	1.6		3.5	2.0	2.2
MPI-ESM-LR r2		1.6	1.2	0.1		2.2	1.3	1.0		3.3	1.7	0.4		2.5	1.9	1.8		—	—	—
MPI-ESM-LR r3		1.0	1.1	0.9		2.8	1.3	0.5		3.2	1.7	0.6		2.4	1.9	2.0		—	—	—
MRI-ESM1		1.4	0.8	0.7		2.4	1.2	1.0		2.1	1.3	2.0		2.4	1.5	2.3		2.9	1.8	3.0
NorESM1-ME		2.0	1.4	−0.5		3.0	1.7	−0.2		3.6	2.1	−0.3		4.0	2.5	−0.3		4.4	2.7	0.9

2.3.3 Implications of contemporary atmospheric CO_2 biases in CMIP5 models

High atmospheric CO_2 biases produced radiative forcing during the latter half of the 20th century that was too large in the affected ESMs (Table 2.3). For the year 2010, the multi-model mean atmospheric CO_2 mole fraction was 7.9 ppm above observations, corresponding to a radiative forcing that was 0.10 $\mathrm{W\,m^{-2}}$ higher than that obtained from the observed atmospheric CO_2 mole fraction. The integrated effect of the radiative forcing bias from the multi-model mean during the 19th and 20th centuries led to CO_2-induced temperature change that was 0.06°C higher by 2010 than an estimate derived from the observed CO_2 trajectory. Across all ESMs, the temperature change bias for 2010 ranged from −0.20°C to 0.24°C. Because land and ocean carbon uptake rates are likely to be reduced with climate warming (negative γ_L and γ_O), these temperature biases have the potential to further reinforce atmospheric CO_2 biases in the 21st century, leading to persistent and divergent biases into the future for many aspects of the climate system, unless compensated for by biases in concentration–carbon feedbacks (β_L and β_O) or climate sensitivities (α). Atmospheric CO_2 mole fraction projections out to 2100 under the RCP 8.5 scenario for all ESMs are shown in Figure 2.7. Corresponding anthropogenic carbon inventories for the ocean and land out to 2100 are shown in Figure 2.8.

2.3.4 Persistence of biases into the future

To explore the persistence of atmospheric CO_2 biases beyond the present, we examined the relationship between 5-y mean contemporary and future atmospheric CO_2 mole fractions from ESMs. Figure 2.9(a) reveals a strong linear relationship between the predicted sizes of contemporary and future atmospheric CO_2 biases in 2060 with a coefficient of determination $R^2 = 0.70$. This correlation declined to $R^2 = 0.54$ in 2100 (Figure 2.9(b)) probably as

Table 2.3: Atmospheric CO_2 mole fraction, radiative forcing, and resulting temperature changes for each of the CMIP5 ESMs, the multi-model mean, the CCTM estimate, and the combination of observed and RCP 8.5 projection for the years 2010, 2060, and 2100. Values are 5-y means for the time periods 2006–2010, 2056–2060, and 2096–2100.

	CO_2 Mole Fraction (ppm)			**Radiative Forcing ($W\,m^{-2}$)**			**Cumulative ΔT (°C)**			**ΔT Bias (°C)**		
Model	**2010**	**2060**	**2100**	**2010**	**2060**	**2100**	**2010**	**2060**	**2100**	**2010**	**2060**	**2100**
BCC-CSM1.1	390	603	945	1.70	4.03	6.43	0.97	2.39	4.02	0.03	0.02	−0.01
BCC-CSM1.1-M	396	619	985	1.78	4.16	6.65	1.04	2.49	4.16	0.10	0.12	0.13
BNU-ESM	382	602	963	1.59	4.02	6.53	0.90	2.33	4.07	−0.04	−0.04	0.04
CanESM2 r1	394	641	1024	1.75	4.36	6.86	0.98	2.58	4.30	0.04	0.21	0.27
CanESM2 r2	392	641	1023	1.72	4.35	6.85	0.98	2.57	4.30	0.04	0.20	0.27
CanESM2 r3	396	641	1025	1.78	4.35	6.87	1.01	2.58	4.30	0.07	0.21	0.27
CESM1-BGC	407	697	1121	1.92	4.80	7.34	1.12	2.85	4.64	0.18	0.48	0.61
FGOALS-s2.0	404	636	993	1.89	4.31	6.70	1.09	2.57	4.23	0.15	0.20	0.20
GFDL-ESM2G	395	616	967	1.77	4.14	6.56	1.04	2.49	4.12	0.10	0.12	0.09
GFDL-ESM2M	400	621	964	1.83	4.18	6.54	1.09	2.52	4.13	0.15	0.15	0.10
HadGEM2-ES	411	636	983	1.98	4.31	6.64	1.18	2.60	4.20	0.24	0.23	0.17
INM-CM4	386	591	897	1.64	3.92	6.15	0.92	2.36	3.86	−0.02	−0.01	−0.17
IPSL-CM5A-LR	375	573	908	1.48	3.75	6.22	0.86	2.21	3.87	−0.08	−0.16	−0.16
MIROC-ESM	398	658	1121	1.81	4.50	7.35	1.06	2.67	4.58	0.12	0.30	0.55
MPI-ESM-LR r1	383	590	948	1.60	3.91	6.45	0.95	2.31	4.03	0.01	−0.06	0.00
MRI-ESM1	361	516	778	1.28	3.20	5.39	0.74	1.89	3.33	−0.20	−0.48	−0.70
NorESM1-ME	391	667	1070	1.72	4.57	7.09	0.98	2.68	4.46	0.04	0.31	0.43
Multi-model Mean	392	621	980	1.72	4.18	6.63	1.00	2.48	4.17	0.06	0.11	0.14
CCTM Estimate	385	600	948	1.62	4.01	6.45	0.94	2.37	4.03	—	—	—
Historical + RCP 8.5	385	590	917	1.63	3.91	6.27	0.94	2.32	3.93	0.00	−0.05	−0.10

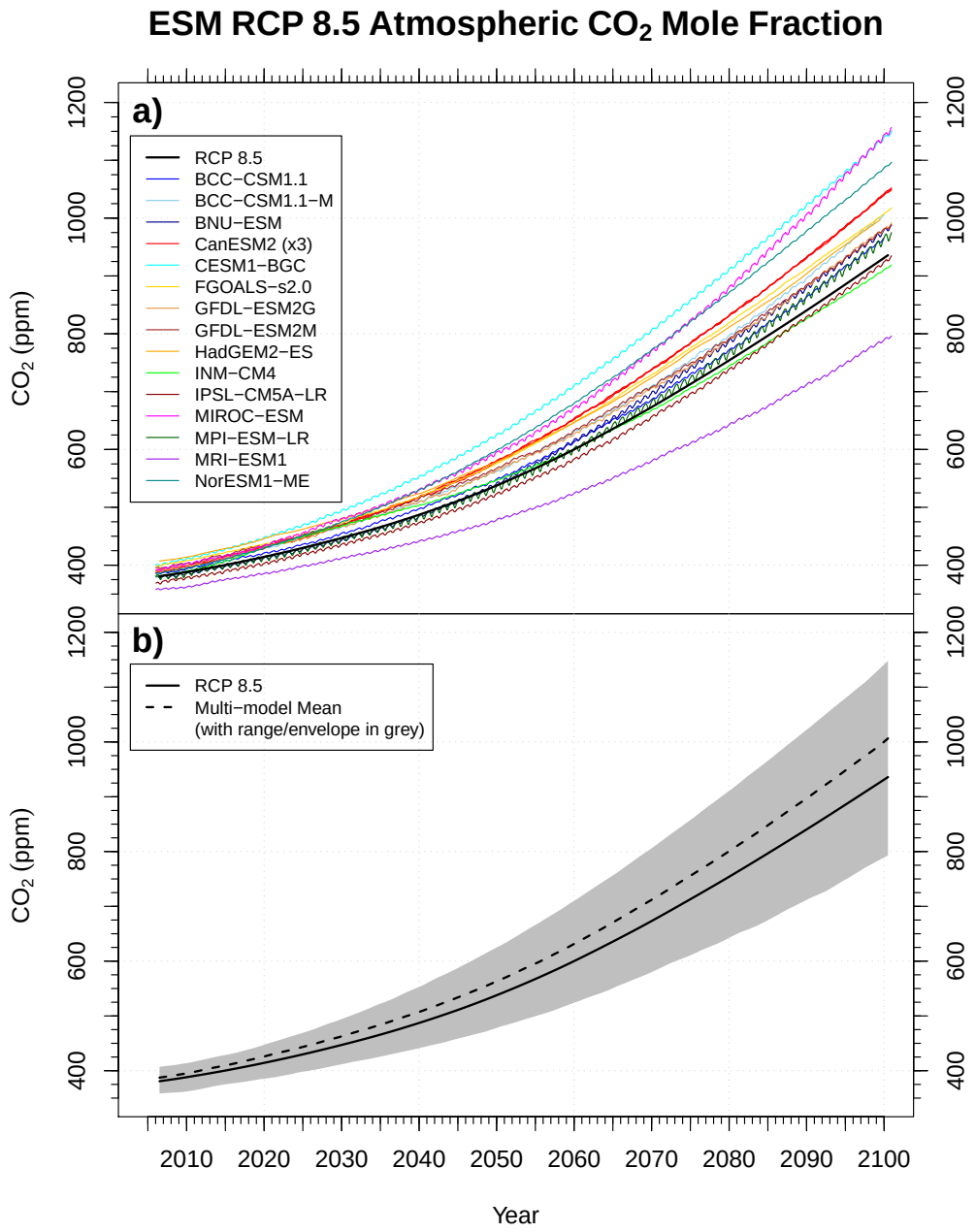

Figure 2.7: (a) ESMs had a wide range of predicted atmospheric CO_2 mole fraction by the end of the 21st century, ranging from 800 ppm to over 1150 ppm. (b) The multi-model mean is 63 ppm above the RCP 8.5 target atmospheric CO_2 mole fraction by the end of the 21st century.

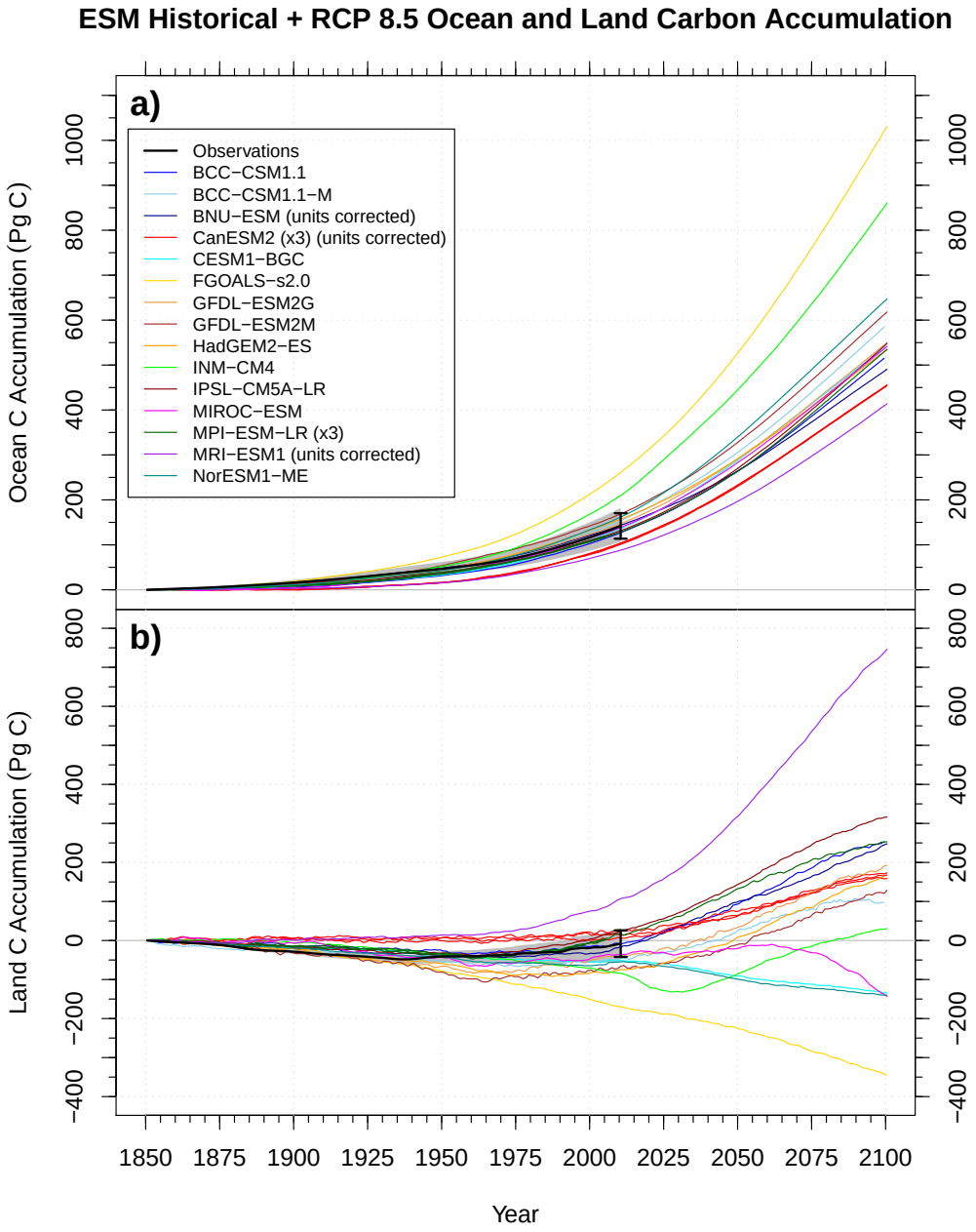

Figure 2.8: (a) Ocean and (b) land anthropogenic carbon inventories from CMIP5 models compared to estimates from *Khatiwala et al.* (2013). The spreads in model projections of ocean and land carbon accumulation grown throughout the 21st century, and trends in land model responses change sign in some models during this time. The shaded polygon represents the uncertainties surrounding the adjusted observational estimates of ocean and land carbon accumulation, and the error bars correspond to the $\pm 20\%$ uncertainty in the *Khatiwala et al.* (2013) best estimate of ocean carbon accumulation for 2010.

a consequence of varying climate–carbon cycle feedbacks taking effect in different models. Because model biases in atmospheric CO_2 mole fraction are persistent, biases at year 1850 affect biases at year 2010. To investigate the impact of different model baselines, we also examined the relationship between the 5-y mean contemporary and future anthropogenic atmospheric carbon inventory in 2060 (Figure 2.10(a)) and 2100 (Figure 2.10(b)), taking into account uncertainties from measurements of 19^{th} century CO_2 and fossil emissions. This alternative metric slightly changed the ordering of models and strengthened the coefficient of determination, further confirming the robustness of the bias persistence relationship. To explore the value of a tuned model with no CO_2 bias at the end of the historical period, we compared the CCTM estimate described in the Methods with the set of CMIP5 model predictions and the RCP 8.5 CO_2 mole fraction trajectory. Figure 2.11 shows the coefficients of determination (R^2) of the CCTM atmospheric CO_2 mole fraction trajectory, as well as for the trajectories for ocean and land carbon accumulation when the same method is applied for those reservoirs. All of the coefficients of determination peak at one for the contemporary tuning year (2008, the center of the 2006–2010 averaging period), as expected, and decreases on either side, into the past and future. Statistical significance ($p < 0.05$) was maintained with $N = 17$ model results for R^2 values above 0.23 (*i.e.*, after about 1910 and through 2100 for atmospheric CO_2). The resulting atmospheric CO_2 trajectory for 1850–2100 is shown as the red line in Figure 2.12.

The CCTM estimate suggests that for a tuned model, future atmospheric CO_2 in 2060 under the RCP 8.5 scenario would be 600 ± 14 ppm (including the 95% confidence interval of the estimate). In contrast, the multi-model mean atmospheric CO_2 mole fraction in 2060 was 621 ± 80 ppm, which was above and outside the confidence interval for the CCTM estimate (Figure 2.13(a)). Individual model predictions spanned a range from 516–697 ppm in 2060. The spread of the CCTM was considerably smaller than that of the multi-model 95^{th} percentile distribution spread. In 2100, the CCTM estimate yielded an atmospheric CO_2 mole fraction of 948 ± 35 ppm, while the multi-model mean prediction was 980 ± 161 ppm

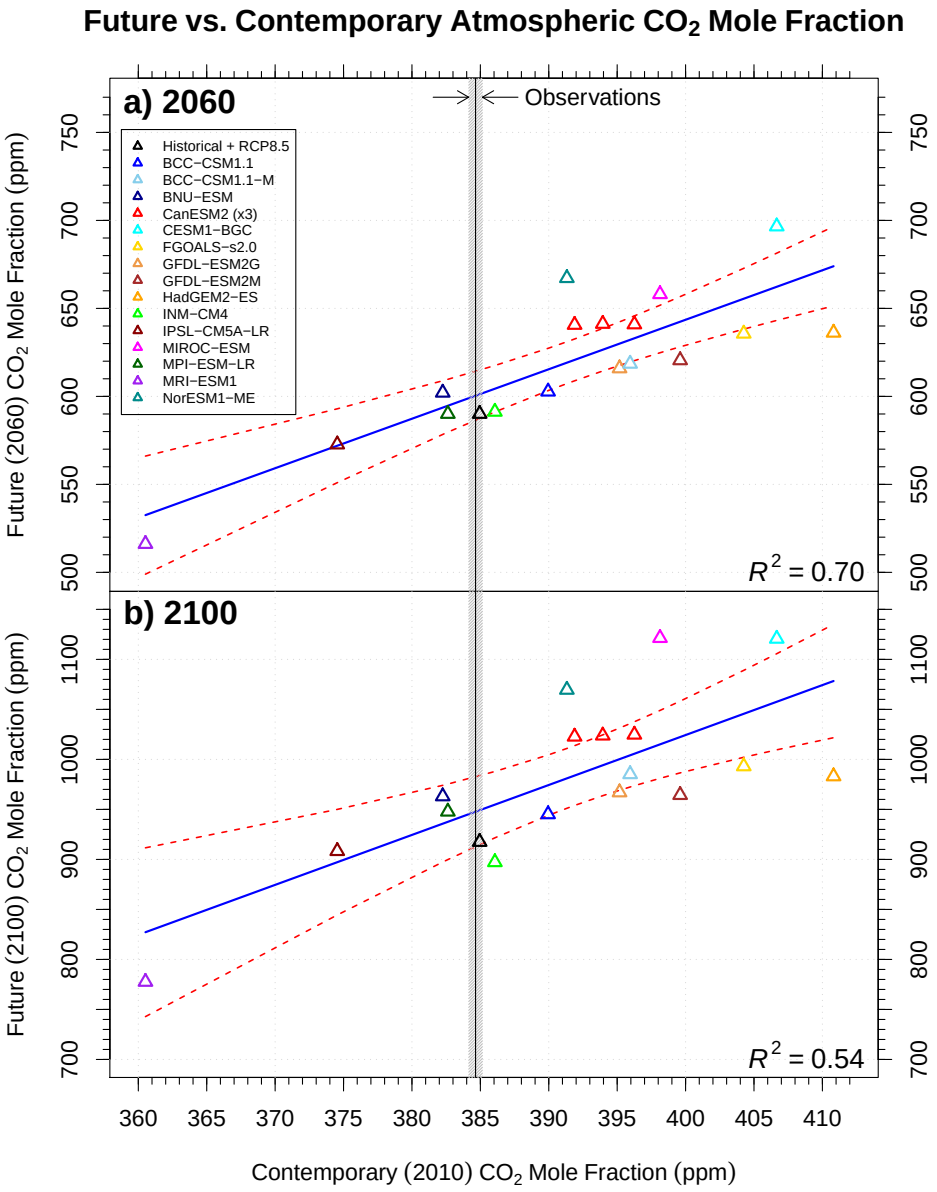

Figure 2.9: (a) Future (2060) vs. contemporary (2010) atmospheric CO_2 mole fraction fit for CMIP5 emissions-forced simulations of RCP 8.5, and (b) Future (2100) vs. contemporary (2010) atmospheric CO_2 mole fraction for the same set of model simulations. The observed atmospheric CO_2 mole fraction is represented by the vertical line at 384.6 ppm with an uncertainty range ($\pm$0.5 ppm) shown in gray. The linear regression model is represented by the blue line surrounded by red dashed lines indicating a 95% confidence interval. While a point is plotted for the historical observed atmospheric CO_2 and the RCP 8.5 concentration trajectory derived from a reduced form model without explicit feedbacks, that point is not included in the linear regression.

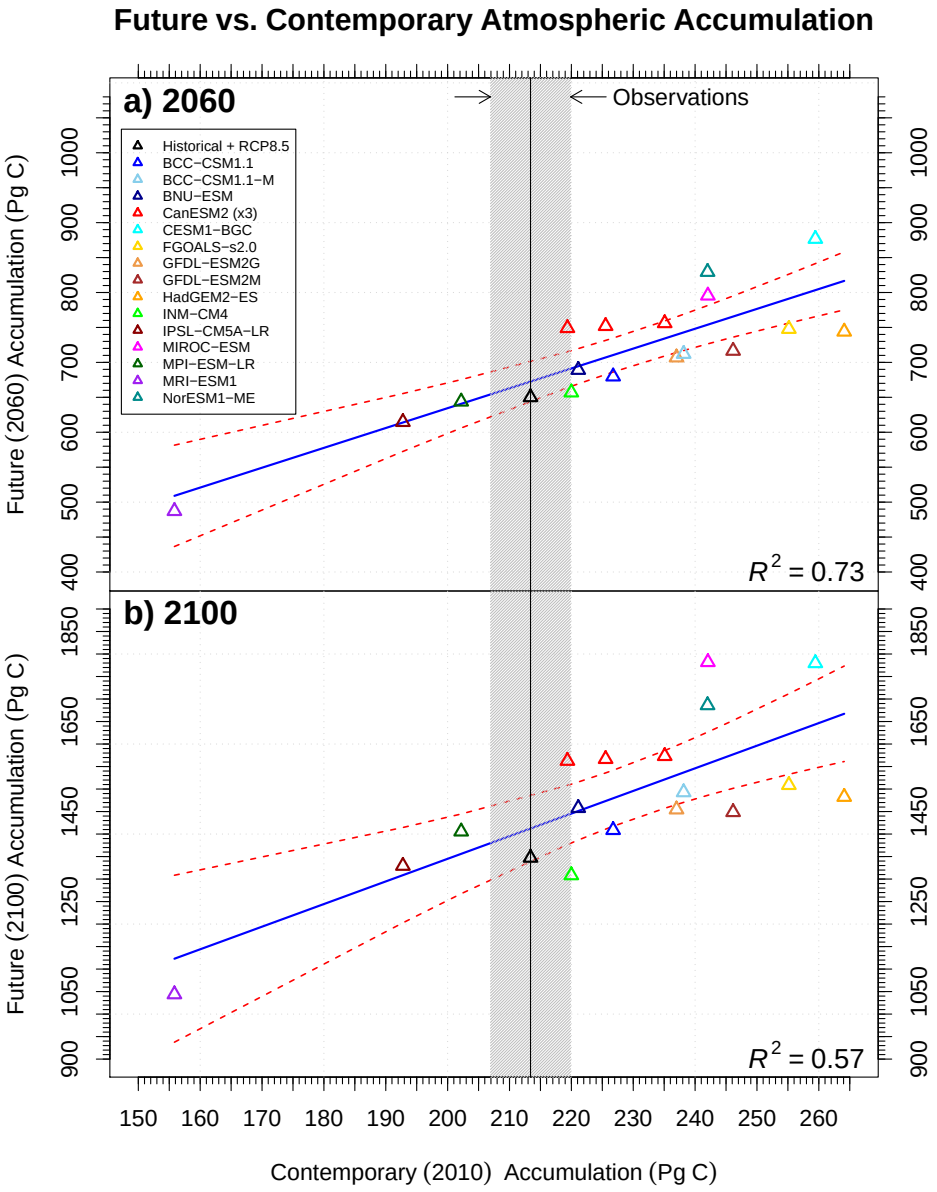

Figure 2.10: (a) Future (2060) vs. contemporary (2010) anthropogenic atmospheric carbon accumulation fit for CMIP5 emissions-forced simulations of RCP 8.5, and (b) Future (2100) vs. contemporary (2010) anthropogenic atmospheric carbon accumulation for the same set of model simulations. The observed atmospheric carbon accumulation is represented by the vertical line at 213.4 Pg C with an uncertainty range (±6.5 Pg C) shown in gray. The linear regression model is represented by the blue line surrounded by red dashed lines indicating a 95% confidence interval. Adding uncertainties from fossil fuel emissions increased the uncertainty range to ±12.7 Pg C. Even with this larger range, only 6 of 17 simulations were consistent with the available inventory observations. While a point is plotted for the historical observed atmospheric carbon accumulation and the RCP 8.5 accumulation derived from a reduced form model without explicit feedbacks, that point is not included in the linear regression.

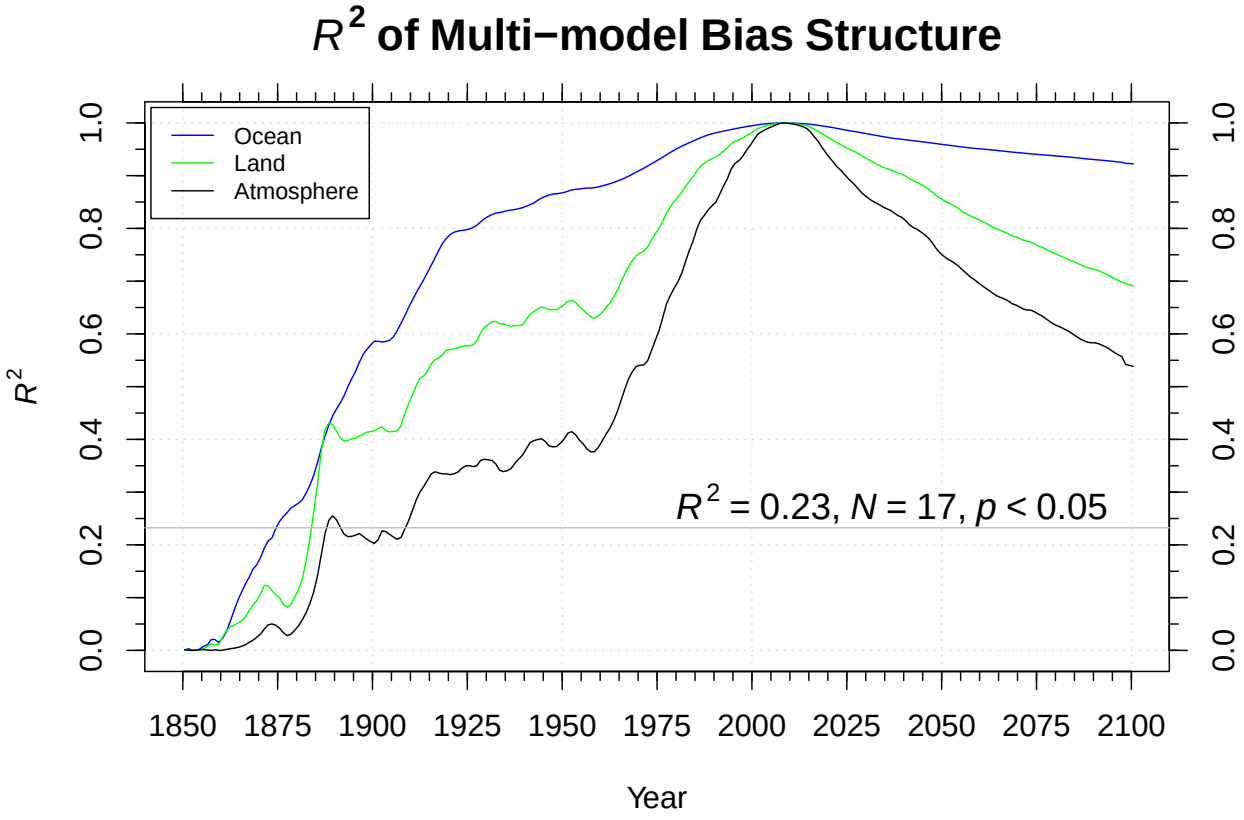

Figure 2.11: The coefficients of determination (R^2) for the multi-model bias structure, from which the contemporary CO_2 tuned model (CCTM) was derived, relative to the set of CMIP5 model atmospheric CO_2 mole fractions (black) and oceanic (blue) and land (green) anthropogenic carbon inventories in 2010, defined as the 5-y mean for the period 2006–2010.

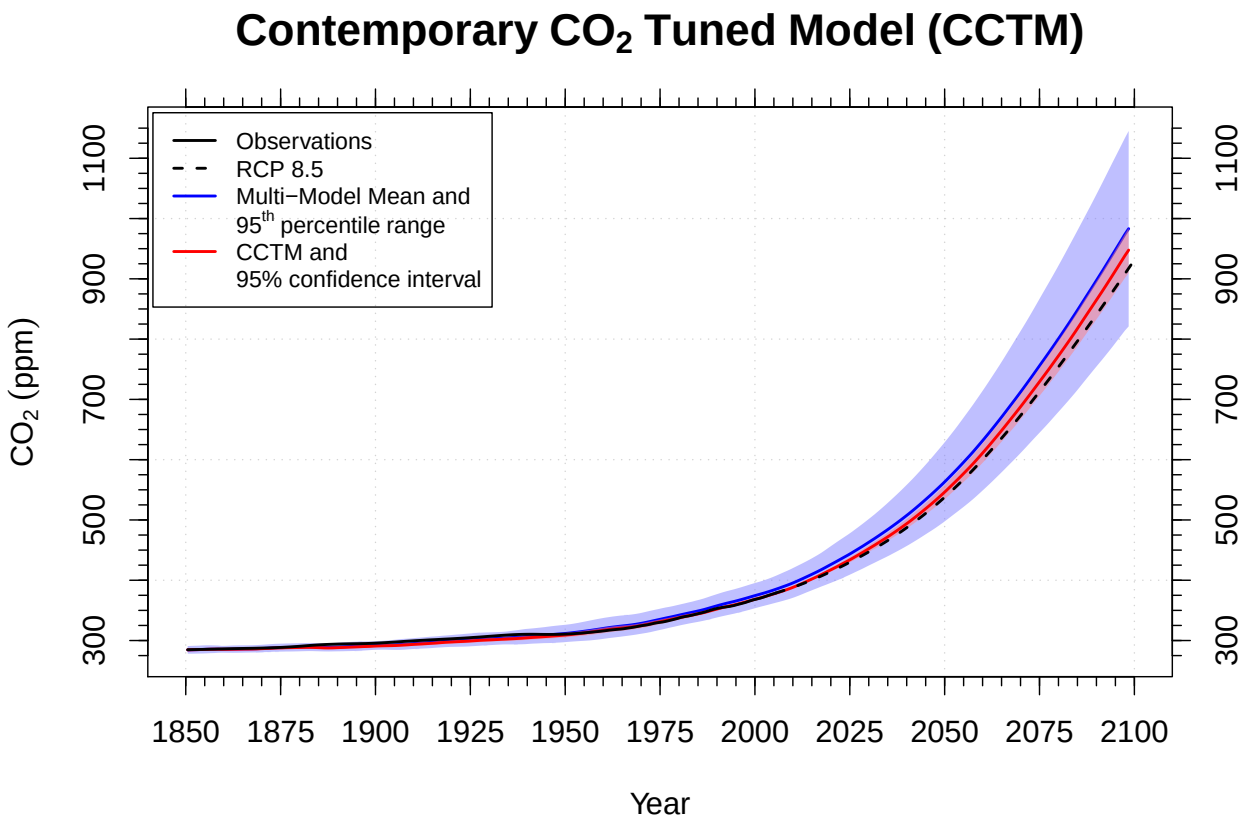

Figure 2.12: The contemporary CO_2 tuned model (CCTM) atmospheric CO_2 mole fraction estimate compared to the CMIP5 multi-model mean trajectory. The pink range surrounding the CCTM represents the 95% confidence interval from the linear model around the contemporary observation projected onto the y-axis of historical or future CO_2 mole fractions for every year. The blue line represents the multi-model mean CO_2 trajectory and the blue range indicates the 95^{th} percentile of the range for the multi-model standard deviation, assuming a normal distribution ($1.96\,\sigma$).

(Figure 2.13(b)). The CanESM2, CESM1-BGC, MIROC-ESM, and NorESM1-ME models predicted atmospheric CO_2 mole fractions greater than 1000 ppm by 2100. In terms of anthropogenic atmospheric carbon accumulation, the CCTM estimate in 2060 under the RCP 8.5 scenario was 672 ± 28 Pg C (including the 95% confidence interval of the estimate). The multi-model mean anthropogenic atmospheric carbon accumulation in 2060 was 715 ± 173 Pg C, which was above and outside the confidence interval for the CCTM estimate (Figure 2.14(a)). In 2100, the CCTM estimate yielded an anthropogenic atmospheric carbon accumulation of 1412 ± 72 Pg C, while the multi-model mean prediction was 1488 ± 347 Pg C (Figure 2.14(b)).

To assess the mechanisms causing the strong relationship between contemporary and future atmospheric CO_2 levels among the models, we also developed CCTM-like estimates for the individual ocean and land inventories (Figure 2.15). This analysis revealed that the ordering of ocean inventories among the models was more persistent into the future than for land inventories, but, for both components, statistically significant multi-model relationships existed between contemporary (2010) and future values through the end of the 21st century (Figure 2.11). However, because uncertainties in ocean and land inventories were larger, constraints offered by contemporary observations were considerably weaker than for atmospheric CO_2, in terms of the future evolution of these inventory components (Figure 2.16).

2.3.5 Implications of a persistent atmospheric CO_2 bias

To explore the climate implications of the persistent atmospheric CO_2 biases described above, we compared the radiative forcing (Equation 2.6) and the resulting temperature change (Equations S1 and S2) for the CCTM estimate and the set of CMIP5 model predictions. Figure 2.17(a) shows the radiative forcing due only to CO_2 calculated for each of the CMIP5 models. The model range was 5.4–7.4 W m^{-2} at year 2100 for RCP 8.5. Figure 2.17(b)

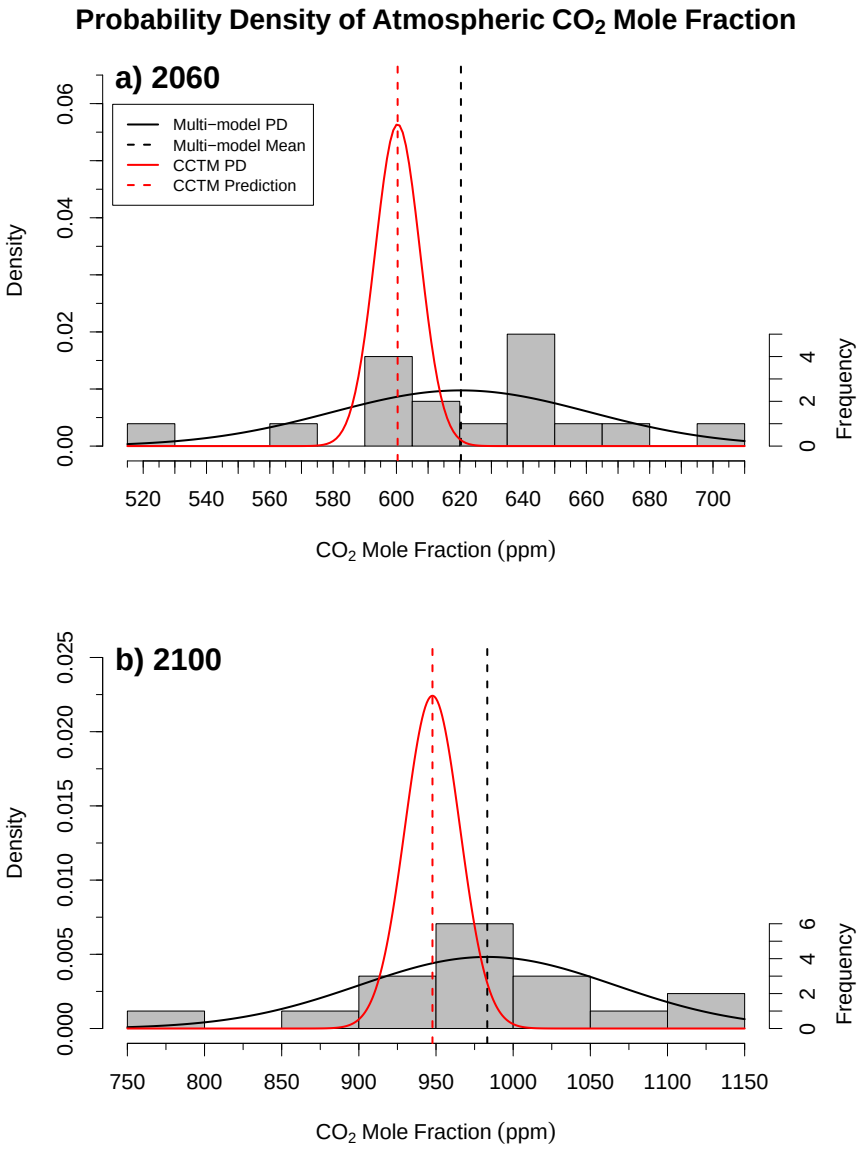

Figure 2.13: The probability density of CO_2 mole fraction predictions from the CCTM peaks lower than the probability density for multi-model mean for (a) 2060 and (b) 2100. In addition, the width of the probability density is much smaller for the CCTM, by almost a factor of 6 at 2060 and almost a factor of 5 at 2100, indicating a significant reduction in the range of uncertainty for the CCTM prediction.

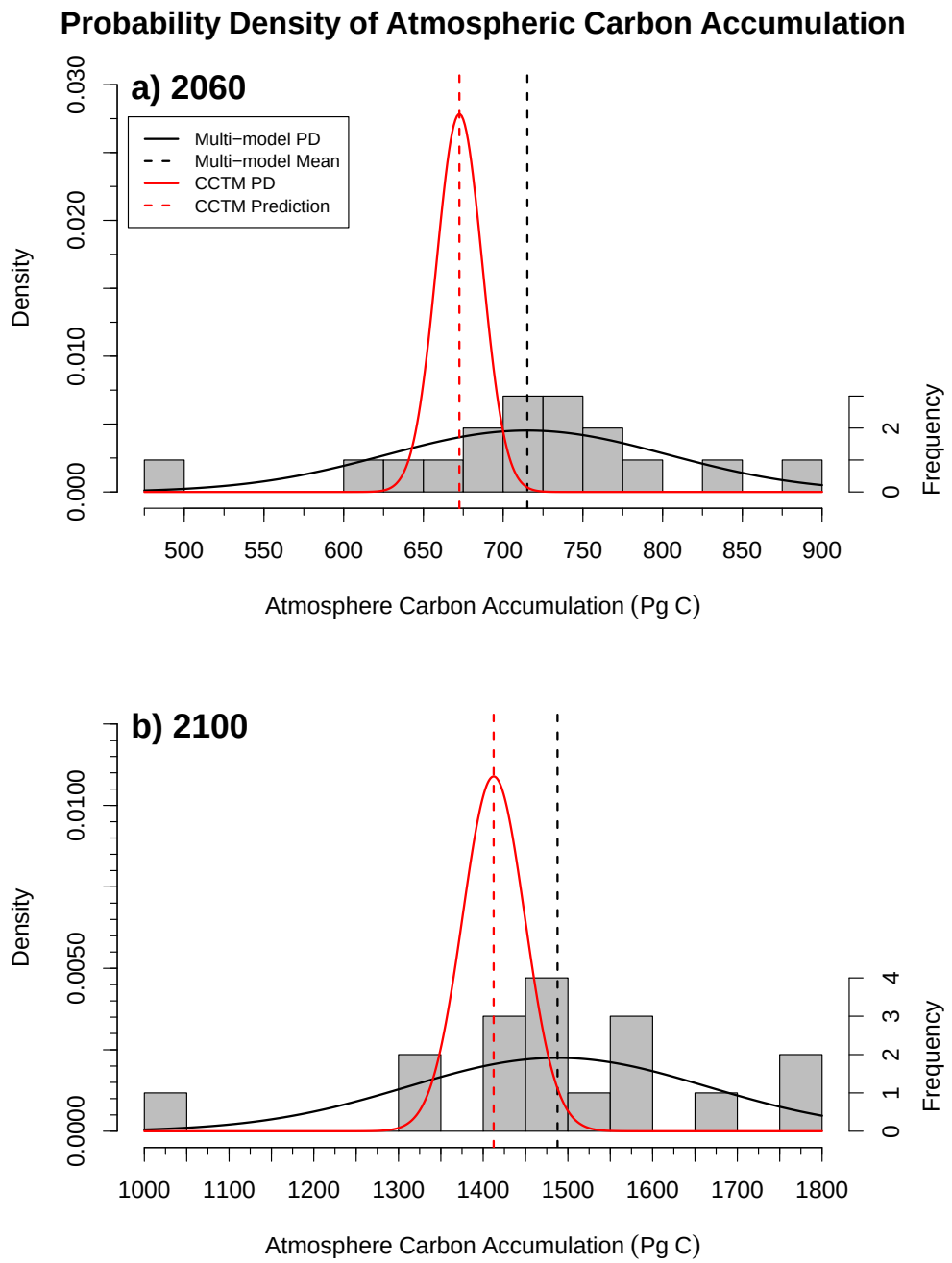

Figure 2.14: The probability density of anthropogenic atmospheric carbon accumulation predictions from the CCTM peaks lower than the probability density for the multi-model mean for (a) 2060 and (b) 2100. In addition, the width of the probability density is much smaller for the CCTM, by more than a factor of 6 at 2060 and almost a factor of 5 at 2100, indicating a significant reduction in the range of uncertainty for the CCTM prediction.

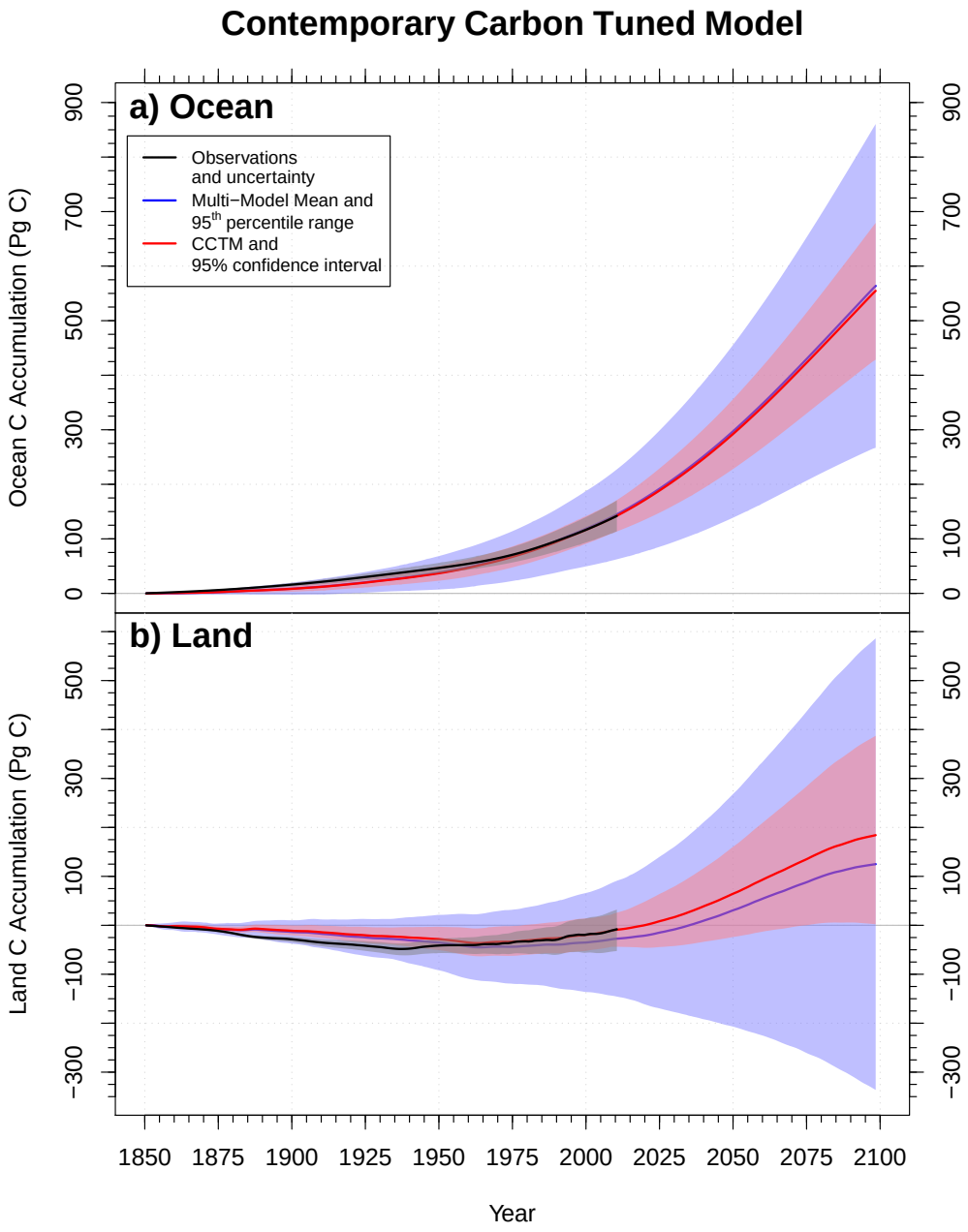

Figure 2.15: CCTM-like analyses were performed for (a) ocean and (b) land carbon accumulated fluxes. Trajectories for these inventories, including uncertainties, were projected out to year 2100.

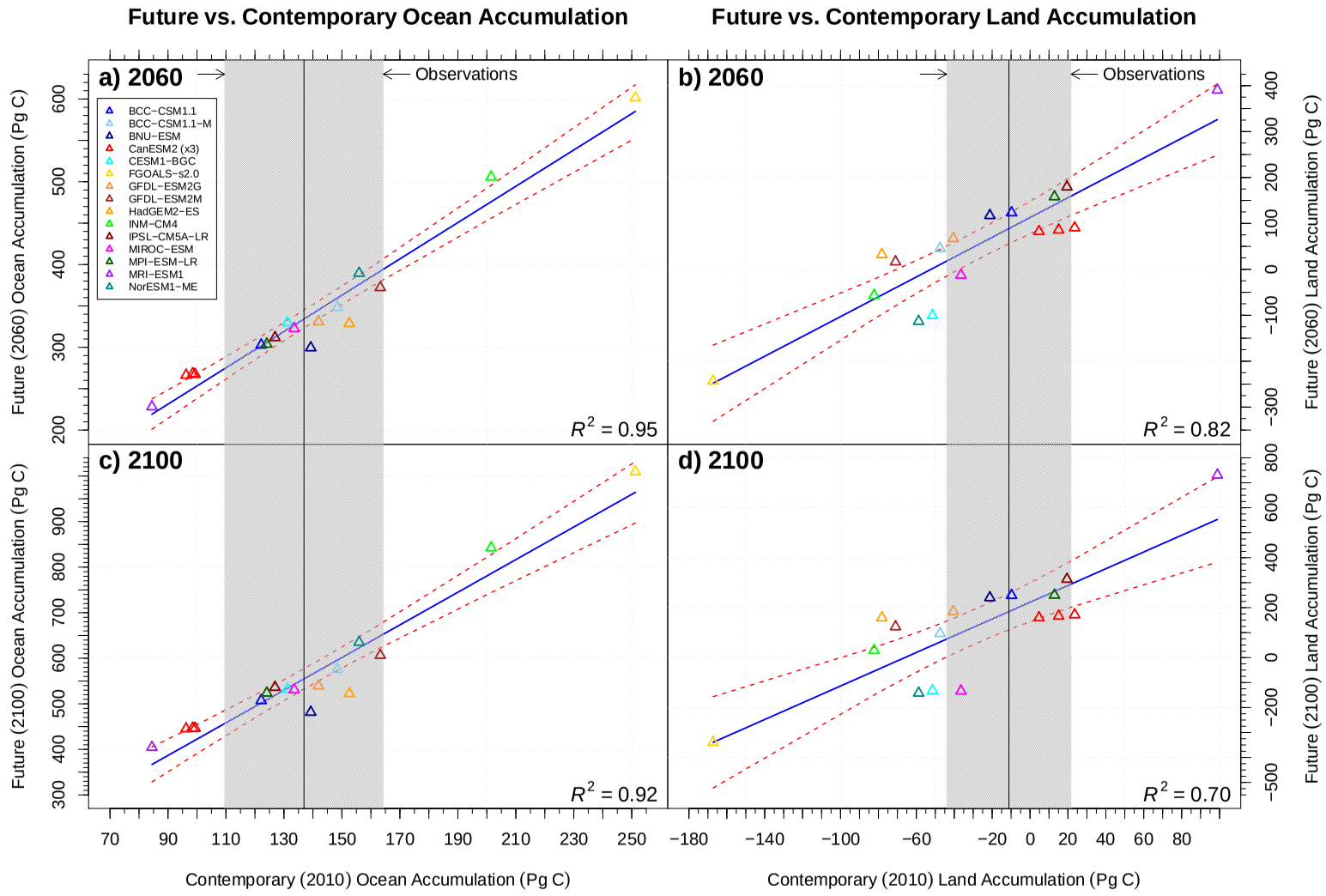

Figure 2.16: Future ((a) 2060 and (c) 2100) vs. contemporary (2010) ocean carbon accumulation for CMIP5 emissions-forced simulations of RCP 8.5, and corresponding plots for land carbon accumulation for the same periods ((b) and (d), respectively). Observed contemporary accumulation estimates are shown as vertical lines with an uncertainty range shown in gray. The linear regression model is represented by the blue line surrounded by red dashed lines indicating a 95% confidence interval.

shows the multi-model mean radiative forcing compared to the radiative forcing for the CCTM estimate. As with the CO_2 comparison described above, the spread of the CCTM was considerably smaller than that of the multi-model 95th percentile distribution spread. In 2100, the CCTM estimate yielded a radiative forcing of 6.4 ± 0.2 W m^{-2}, while the multi-model mean prediction was 6.6 ± 0.9 W m^{-2}. Figure 2.17(c) shows the corresponding cumulative temperature change due to this CO_2 radiative forcing for each of the CMIP5 models. The temperature increase for the models ranged from 3.3°C to 4.6°C. Figure 2.17(d) shows the corresponding multi-model mean cumulative temperature change compared to the CCTM estimate. In 2100, the CCTM estimate yielded a cumulative temperature increase from the CO_2-induced radiative forcing of 4.0 ± 0.1°C, while the multi-model mean prediction was 4.2 ± 0.6°C.

The CO_2 mole fraction, CO_2-induced radiative forcing, and CO_2-induced cumulative temperature change for each of the CMIP5 models are shown in Table 2.3 for the years 2010, 2060, and 2100. In addition, the last three columns of the table show the temperature change bias between the models and the CCTM estimate. In 2010 the temperature bias of the multi-model mean was 0.06°C (ranging from −0.20°C to 0.24°C), and this bias increased to 0.11°C in 2060. Individual model results showed that some biases increased, some decreased, and others remained the same between 2010 to 2060. The MRI-ESM1 and CESM1-BGC models had the largest temperature biases in 2060, at −0.48°C and 0.48°C, respectively, while the INM-CM4 and MPI-ESM-LR models had the smallest temperature biases in 2060, at −0.02°C and 0.01°C, respectively. By 2100, the multi-model mean temperature bias had increased to 0.14°C. The MRI-ESM1 and CESM1-BGC models had the largest temperature biases in 2100, at −0.70°C and 0.61°C, respectively. The temperature biases for individual models were significant and increased with time during the 21st century. The original RCP 8.5 atmospheric CO_2 mole fraction trajectory resulted in a −31 ppm mole fraction bias and a −0.10°C temperature bias from the CCTM estimate at 2100. This result suggests a small inconsistency between the RCP 8.5 specification of the CO_2 mole fraction trajectory

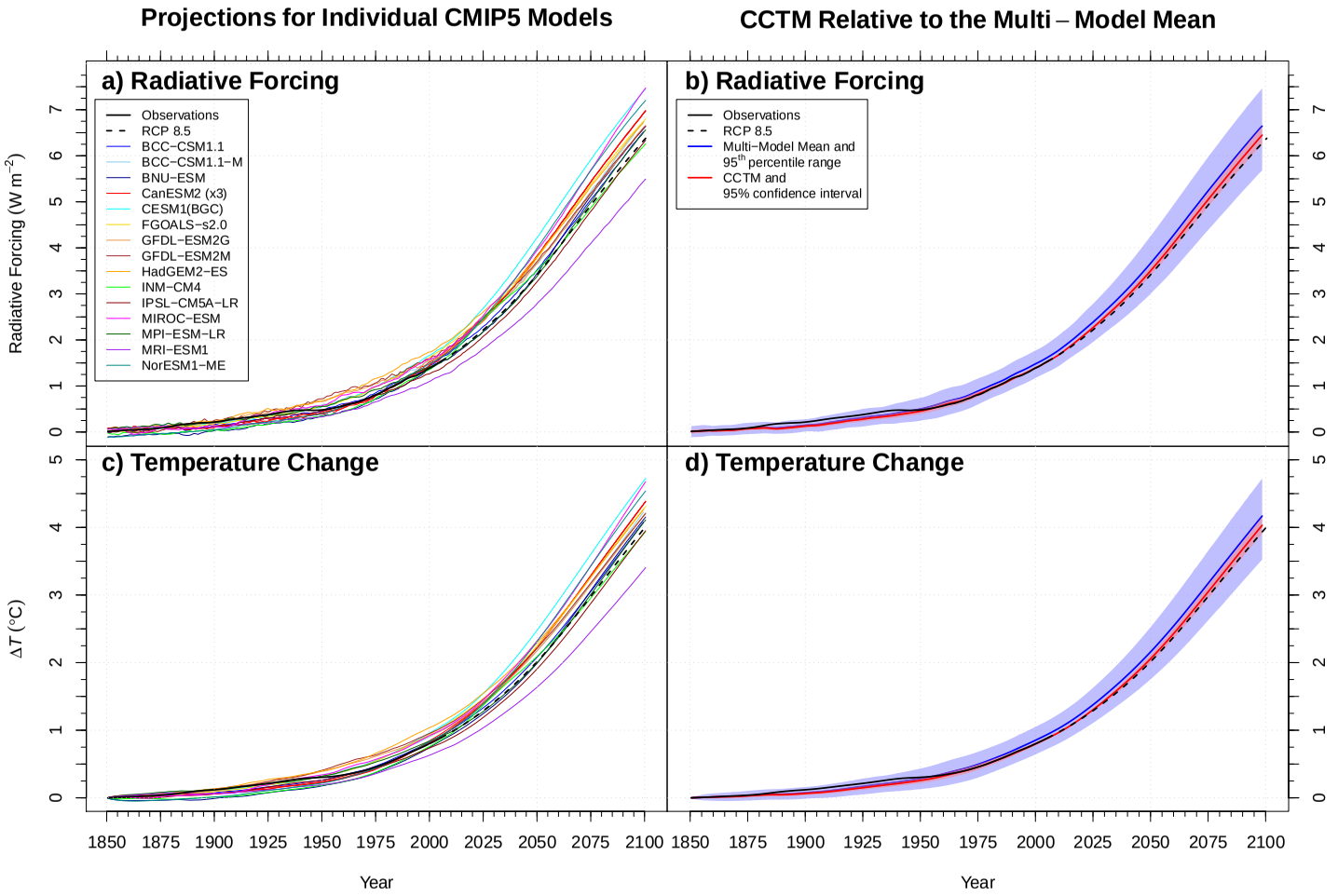

Figure 2.17: (a) and (c) CO_2-induced radiative forcing and temperature change computed from the prognostic atmospheric CO_2 mole fraction for each of the CMIP5 models. (b) and (d) Corresponding radiative forcing and temperature change for the multi-model mean and contemporary CO_2 tuned model (CCTM). The pink range surrounding the CCTM represents the uncertainty propagated from the 95% confidence interval from the linear model for the CCTM atmospheric CO_2 trajectory. The blue range surrounding the multi-model mean represents the uncertainty propagated from the 95th percentile of the range for the standard deviation of the multi-model mean atmospheric CO_2 trajectory.

and the corresponding fossil fuel emissions trajectory. The RCP 8.5 trajectory was derived from the MESSAGE-MACRO integrated assessment model (*Riahi et al.*, 2011), which incorporates the MAGICC/SCENGEN (version 4.1) coupled gas-cycle/climate model (*Wigley*, 2003) that includes a net positive carbon cycle feedback, but lacks explicit representation of many ecosystem processes that influence climate–carbon and concentration–carbon feedbacks. Prior to its use in deriving the RCP 8.5 trajectory, parameters in the carbon cycle model of MAGICC/SCENGEN (version 5.3) (*Wigley*, 2008) were changed to give concentration projections consistent with the results from the C^4MIP activity (*Friedlingstein et al.*, 2006).

It is important to note in the context of the results described above that model-to-model variations in atmospheric CO_2 trajectories documented here contributed to only a small amount of the model-to-model variation in surface air temperature changes. This is because many of the models in the ensemble had different representations of aerosol processes, including forcings and feedbacks, and because the models had widely varying climate sensitivities (*e.g.*, *Gillett et al.* (2013)). Specifically, the multi-model mean estimate of temperature change from the beginning of the simulations was 3.1 ± 1.3°C at 2060 and 5.1 ± 2.2° at 2100. When we adjusted each model temperature estimate for the impact of CO_2 biases using the CO_2-induced temperature biases shown in Table 2.3, the multi-model mean changed slightly to 3.0 ± 1.2°C at 2060 and 5.0 ± 1.9°C at 2100.

2.4 Discussion

2.4.1 Why do carbon cycle biases persist on decadal timescales?

In our analysis, we found that the ordering among model predictions of atmospheric CO_2 persisted for several decades. Models that had the highest positive biases near the end of the

observational record in 2010 were more likely to have higher positive biases in earlier decades, during the latter half of the 20th century (Figures 2.2 and 2.17). Similarly, this same set of models also had the highest set of future atmospheric CO_2 projections during the middle and latter half of the 21st century in response to RCP 8.5 emissions (Figure 2.9). Many structural model elements probably contributed to this bias and ordering persistence, including processes that influence the strength of concentration–carbon feedbacks. One important example includes the representation of ocean mixing processes that regulate the formation of intermediate and deep waters in the ocean. Past work from analysis of 13 simulations from the second phase of the Ocean Carbon-cycle Model Intercomparison Project (OCMIP-2) indicated that climate models often underestimate this overturning in the Southern Ocean (*Doney et al.*, 2004; *Matsumoto et al.*, 2004; *Dutay et al.*, 2002). In addition, *Russell et al.* (2006) performed an intercomparison of the Southern Ocean circulation in CMIP3 control simulations and found that the maximum wind stress in the Southern Hemisphere, nominally associated with the Antarctic Circumpolar Current (ACC), was located too far equator-ward in most models. In ESMs, such deficiencies in model structure and large scale circulation have the potential to limit CO_2 uptake by the oceans, and are likely to contribute to a persistent atmospheric CO_2 bias over time because many of the physical processes regulating mixing are unlikely to change rapidly. Biases in atmospheric CO_2 caused by this type of mechanism likely grow through time as the atmospheric CO_2 growth rate accelerates and transport of carbon out of the mixed layer becomes an increasing bottleneck to net ocean carbon uptake. Our finding that many models underestimated the ocean anthropogenic carbon inventory (Figures 2.5 and 2.4) is consistent with other studies indicating some ocean models exhibit weak meridional overturning circulation (*Downes et al.*, 2011; *Sallée et al.*, 2013). However, additional research is needed to understand the causes of model-to-model variations in ocean carbon uptake for the CMIP5 models.

On land, similar deficiencies in model structure have the potential to contribute to persistent multi-decadal biases in carbon fluxes. Key regulators of carbon uptake on land in response

to elevated levels of atmospheric CO_2 include, for example, the response of gross primary production (GPP) to CO_2 concentration, the allocation of GPP to longer lived woody pools, and subsequent increases in soil organic matter pools (*Thompson et al.*, 1996; *Luo et al.*, 2006). Carboxylation parameterizations of Rubisco often follow the form of a modified Michaelis-Menten equation (*Farquhar et al.*, 1980) and vary considerably among models. Models that have lower estimates of the maximum carboxylation rate in different biomes, in response to nitrogen limitation (*e.g.*, *Thornton et al.* (2007)) or other factors, are likely to have smaller CO_2-driven increases in GPP by the end of the 20^{th} or 21^{st} centuries. Similarly, models that have reduced allocation of GPP to wood pools will also have lower rates of carbon uptake, given the same trajectory of GPP increases. Since in many models, the maximum carboxylation rate is either held constant or unlikely to rapidly change in response to changing environmental conditions, this parameterization can induce a long-term bias in carbon fluxes. The same argument applies to allocation submodels: although many plant allocation models are dynamic (*Friedlingstein et al.*, 1999; *Arora and Boer*, 2005; *Litton et al.*, 2007) and respond to regional variations in light availability, soil moisture, and other environmental controls, many aspects of these models are unlikely to change rapidly during the 20^{th} and 21^{st} centuries, allowing flux biases to persist in response to monotonic increases in atmospheric CO_2.

Other land model structural components not associated with concentration–carbon feedbacks also can contribute to long-term flux biases. For example, land use carbon emissions are an important component of the terrestrial carbon budget and are highly uncertain (*Hansen et al.*, 2010; *Houghton et al.*, 2012; *Baccini et al.*, 2012; *Andres et al.*, 2012; *Harris et al.*, 2012). Model estimates of this flux can be biased if, for example, the representations of aboveground and belowground carbon pools within the model do not capture observed patterns. As a consequence, carbon losses for a given rate of land clearing may be too high or too low, with a bias that is persistent if rates of land clearing change gradually from one decade to the next. Similarly, climate–carbon feedbacks, including, for example, the response

of heterotrophic respiration to temperature (*Davidson and Janssens*, 2006) could also contribute to long-term biases. Nevertheless, for the CMIP5 models, their contribution during the latter half of the 20$^{\text{th}}$ century and first half of the 21$^{\text{st}}$ century might be expected to be smaller than other drivers, given that temperature and other changes in climate increase through time (*Arora et al.*, 2013).

The overall success of contemporary atmospheric CO_2 observations in constraining future CO_2 levels (*e.g.*, Figure 2.13) is probably related to several factors. First, the atmospheric anthropogenic carbon inventory is known relatively well, in contrast to the much larger uncertainties associated with the ocean and land inventories. Second, concentration–carbon feedbacks appear to contribute more to the inter-model variations of future (2100) atmospheric CO_2 level projections than climate–carbon feedbacks (*Arora et al.*, 2013). In this context, the rapid rise of atmospheric CO_2 observed over the last few decades provides an important direct test of the combined set of ocean and land concentration–carbon mechanisms operating within the models, and, as described above, any biases today are likely amplified as the growth rate of CO_2 accelerates. Although temperature and other climate changes also occurred during this period, the magnitude of these changes was much smaller as compared to what is expected during the middle and latter part of the 21$^{\text{st}}$ century. As a consequence, the variations in atmospheric CO_2 estimates among models resulting from climate–carbon feedbacks were likely relatively small for the contemporary period (*e.g.*, *Arora et al.* (2013)). The growing importance of climate–carbon feedbacks probably contributes to the increasing uncertainty in our CCTM estimate during the latter part of the 21$^{\text{st}}$ century (Figure 2.12).

2.4.2 What is the value of improving carbon cycle processes to match contemporary CO_2?

One of the goals of the integrated assessment modeling community in developing the different representative concentration pathways (RCPs) was to enable ESMs to compute possible emissions scenarios consistent with a particular atmospheric CO_2 trajectory (*van Vuuren et al.*, 2011). This is valuable, for example, in identifying the magnitude of required mitigation efforts to stabilize CO_2 levels in the atmosphere at a particular mole fraction, taking into account carbon cycle responses and feedbacks (*e.g.*, *Jones et al.* (2013)).

Our analysis has several implications for the interpretation of future compatible emissions time series derived from the set of ESMs participating in CMIP5. First, the compatible emissions time series derived from the multi-model mean of concentration-forced simulations during the 21st century is likely to be too low. This assertion is based on the observation that 1) fossil fuel emissions would have to be reduced below observations to eliminate the high bias found in the multi-model mean during the last few decades (Figure 2.2), and 2) our finding that biases observed today were significantly correlated with future atmospheric CO_2 projections because of parameterizations of slowly changing carbon cycle processes.

Second, the range of variation in compatible emission estimates among individual models during the remainder of the 21st century has a large component that can be avoided for any given concentration-forced scenario by reducing or eliminating biases in contemporary atmospheric CO_2. Specifically, if each model were individually optimized to eliminate biases in atmospheric CO_2 during the last few decades, the range of compatible emissions projections during the 21st century would be considerably compressed. In our analysis, we investigated the potential magnitude of this uncertainty reduction by using the entire set of CMIP5 ESMs to construct a tuned model (CCTM). Projections from the CCTM provided almost a 6-fold reduction in uncertainty of atmospheric CO_2 levels at 2060, and nearly a 5-

fold reduction at 2100. As previously noted the range of model projections diverges through time during the 21st century, as climate–carbon cycle feedbacks strengthen. However, even by the end of the century, a significant component of the variation among models can be attributed to biases that exist today. This result is consistent with results from *Arora et al.* (2013) that show much of the model-to-model variation in carbon cycle estimates is driven by concentration–carbon feedbacks, and only to a lesser degree by variation in climate–carbon feedbacks.

Considering the carbon cycle a "black box" from the perspective of climate change impacts on other aspects of the Earth system, there is significant value in model development efforts to eliminate biases in atmospheric CO_2 that occur by the end of the observational record. By doing so for the set of simulations evaluated here, high biases in radiative forcing and global temperature increases could be reduced in many of the models (Figure 2.17). Improved estimates of CO_2-induced climate change, in turn, would reduce uncertainties related to rates of snow and ice melt (*Flanner et al.*, 2009) and other processes contributing to climate feedbacks (*Hall and Qu*, 2006; *Davidson and Janssens*, 2006; *Zaehle et al.*, 2010; *Koven et al.*, 2011). Benefits would also exist for developing more precise estimates of changes in ocean surface chemistry (*Caldeira and Wickett*, 2003; *Doney et al.*, 2009a) and ocean circulation (*Downes et al.*, 2011; *Sallée et al.*, 2013), and better estimates of climate change impacts on agriculture and other aspects of human society (*Lobell et al.*, 2011).

An interesting question then emerges regarding how best to reduce these biases within individual models and for the set of ESMs as a whole contributing to future climate assessments. Many structural elements of the models may be improved through extensive comparison of ESMs with observations and the development of community-wide benchmarking and evaluation systems such as the International Land Model Benchmarking (ILAMB) project (*Luo et al.*, 2012) and equivalent ocean projects (*Doney et al.*, 2009b). These efforts are underway, and significant advances are expected over the next several years. Biases also may be reduced

by having closer coordination among different ESM development teams and allocating more time to evaluating coupled transient ESM simulations during the 19^{th} and 20^{th} centuries. More specifically, given that constraints on some long-term flux components are uncertain, modeling teams may need to optimize several sets of parameters to achieve a more realistic integrated carbon simulation. For example, adjustments to parameterizations of sub-grid scale mesoscale eddy mixing can improve many aspects of physical ocean system (*Gent and McWilliams*, 1990; *Danabasoglu and Marshall*, 2007; *Danabasoglu et al.*, 2008; *Gent*, 2011), but may have unintended consequences for ocean carbon uptake. At a minimum, more quantification and analysis of these trade-offs is needed, and ocean carbon benchmarks need to be fully considered when modifications are made to ocean model physics.

On land, uncertainties in land use histories and responses of carbon storage to elevated CO_2 and other changing resources provide additional opportunities for making model adjustments that can improve the fidelity of the model's overall atmospheric CO_2 trajectory, but not conflict with available data constraints. Ecosystem manipulation experiments and observations also are needed to improve our understanding of ecosystem processes and their representation in models. In addition, a robust set of Earth system observations are needed to quantify climate change impacts on terrestrial carbon sinks and carbon dynamics associated with land use change.

2.5 Conclusions

The trajectories of atmospheric CO_2 mole fraction for 19 historical and 17 future emission-driven simulation results produced for CMIP5 by 15 fully coupled ESMs were analyzed. Comparison of ESM prognostic atmospheric CO_2 over the historical period with observations indicated that ESMs, on average, had a high bias in their predictions of contemporary CO_2 levels. Comparison with observationally based estimates of anthropogenic carbon inventories

in the ocean indicated that this bias was driven by weak to nominal ocean carbon uptake in many ESMs, and that terrestrial and ocean carbon accumulation often compensated for one another within individual models, reducing the bias in predicted atmospheric CO_2. We found a linear relationship over decadal timescales between contemporary and future atmospheric CO_2 mole fractions, and used this relationship to construct a model of the atmospheric CO_2 trajectory tuned to contemporary observations, which we called the CCTM. CCTM estimates of atmospheric CO_2 were 21 ppm lower than the multi-model mean at 2060 and 32 ppm lower at 2100. Using an impulse response function, we approximated radiative forcing and temperature changes resulting from ESM, CCTM, and observed CO_2 trajectories. Comparison of temperature changes from ESMs with the CCTM estimate indicated a small positive multi-model mean bias during the 21st century. Individual model results exhibited a much larger range of CO_2-induced temperature change, from 1.9°C to 2.9°C in 2060 and from 3.3°C to 4.6°C in 2100, demonstrating the net effect and significant climate implications associated with the large model spread in carbon accumulation in ocean and land reservoirs.

Atmospheric CO_2 biases persist in models for decades because parameterizations of biological and physical processes related to carbon accumulation on land and in the ocean do not allow the system to change rapidly. Many of the biases associated with concentration–carbon feedbacks (*i.e.*, *Arora et al.* (2013)) likely increase through time in the RCP 8.5 scenario as the atmospheric CO_2 growth rate accelerates. Because of the high atmospheric CO_2 bias exhibited by ESMs for the contemporary period, future fossil fuel emissions trajectories designed to stabilize atmospheric CO_2 levels, sometimes called "allowable" emissions, would be too low if estimated from the multi-model mean. We have shown that a significant component of the variation of atmospheric CO_2 levels among models during the 21st century was linked to biases in their predictions of contemporary atmospheric CO_2. This suggests improving the agreement of individual models with the contemporary atmospheric CO_2 record could reduce the magnitude of future CO_2 biases in many models and narrow the range of predicted radiative forcing and CO_2-induced global temperature increases. To reduce

biases in individual models, a rigorous campaign of extensive and multi-faceted evaluation—directed at improving model structure and optimizing model parameters through comparison with contemporary observations—must be performed. Community-based benchmarking and model evaluation systems, such as ILAMB, tighter coordination among ESM development teams, and optimization of model parameters using all available observational constraints have the potential to both reduce model biases and significantly decrease the multi-model spread of carbon cycle predictions for future development scenarios and mitigation.

Chapter 3

Representativeness-Based Sampling Network Design for the State of Alaska

3.1 Introduction

The Arctic contains vast amounts of frozen water in the form of sea ice, snow, glaciers, and permafrost. Extended areas of permafrost in the Arctic contain soil organic carbon that is equivalent to twice the size of the atmospheric carbon pool, and this large stabilized carbon store could be released by widespread thawing of permafrost, resulting in a positive feedback to climate warming (*Schuur et al.*, 2008). The Intergovernmental Panel on Climate Change (IPCC) Fourth Assessment Report (AR4) has documented strong evidence for warming of the Earth's climate over the last century and has attributed the increase in global temperatures primarily to the rising anthropogenic greenhouse gas burden (*IPCC*, 2007). Climate warming is projected to continue with broad implications for sensitive ecosystems

and globally important climate feedbacks (*Anisimov et al.*, 2007). Warming is projected to be especially pronounced at high latitudes and accompanied by significant regional impacts. Evidence of Arctic-wide responses are already being observed (*Hinzman et al.*, 2005). Despite these potential implications, the Arctic has a limited record of low density observations. *The Arctic Climate Impact Assessment (ACIA)* (2005) emphasized the need for studies of the complex and interacting processes of the atmosphere, sea ice, ocean, and terrestrial systems to improve the interpretation of past climate and projections of future climate. The *Committee on Designing an Arctic Observing Network* (2006) identified critical needs and gaps for observations in the Arctic. It recommended an Arctic Observing Network to satisfy current and future scientific needs and offered recommendations on key physical, biogeochemical, and human dimensions variables to monitor.

Conducting systematic and continuous field observations and long term monitoring are challenging, particularly in the Arctic. Resource and logistical constraints limit the frequency and extent of observations, necessitating the development of a systematic sampling strategy that objectively represents environmental variability at the desired spatial scale. Statistical design of the network, particularly the location of sampling sites, is critical for maximizing the representativeness of the sampled data, given a fixed number of sampling locations. A methodology that provides a quantitative framework for stratifying sampling domains, informing site selection, and determining the representativeness of measurements is required to ensure that observations are well distributed across geographic and environmental data space. This information is needed for up-scaling and extrapolating point measurements to a larger landscape with similar environmental characteristics. This study addresses these needs by developing a quantitative methodology, based on the concept of ecoregions, for objectively delineating sampling domains, identifying optimal sampling locations for these domains, and quantifying representativeness of sites and measurements. This methodology is applied at the landscape scale to inform the design of a sampling network for the U.S. Department of Energy's Next Generation Ecosystem Experiment (NGEE) Arctic project in

the State of Alaska. The National Science Foundation's (NSF's) National Ecological Observatory Network (NEON) adopted an objective, data-based methodology to define 20 optimal sampling domains across the conterminous United States (*Keller et al.*, 2008; *Schimel et al.*, 2007). An extension of that same methodology was applied both across space and through time to support identification of measurement sites and provide a framework for scaling measurements and model parameters for the NGEE Arctic project.

3.2 Quantitative Delineation of Ecoregions

3.2.1 Ecoregions

Ecoregions have been widely used to stratify geographic domains into nearly homogeneous land areas with respect to their geophysical, biological, and climatic characteristics. Since ecoregions are selected to correspond well with biome distributions and species ranges, they are frequently used as a framework for studying ecosystem structure and function. Qualitative and generalized ecoregion maps of the United States and the world have traditionally been developed by experts for studying ecosystem behavior or to define units for land management (*Omernik*, 1987; *Olson and Dinerstein*, 2002; *Bailey and Hogg*, 1986; *Bailey*, 2009). *Hargrove and Hoffman* (1999) used cluster analysis for quantitative delineation of ecoregions using a set of nine environmental characteristics for the conterminous United States at a resolution of 1 km^2, and subsequently demonstrated its application for sampling network design, environmental niche modeling, and comparison of global model predictions (*Hargrove and Hoffman*, 2004; *Hoffman et al.*, 2005). *Krohn et al.* (1999) applied clustering to create hierarchical biophysical regions for Maine at a 21 km^2 resolution. *Jensen et al.* (2001) used agglomerative clustering for hierarchical classification of sub-watersheds in the Columbia River Basin using 19 indirect biophysical variables. In this study, we used k-means cluster

analysis to delineate ecoregions having nearly equal within-region heterogeneity for two time periods: the present (2000–2009) and the future (2090–2099). While species ranges are expected to correspond well with ecoregions under equilibrium conditions, species responses to transient climate conditions underlying dynamic ecoregions are difficult to predict. Assuming the environmental changes are slow enough, that habitats are sufficiently connected to enable migration, and that significant adapations do not occur, future instantiations of ecoregions in new geographic areas are likely to support the same plant and animal communities as they do in the present.

3.2.2 Multivariate Spatiotemporal Clustering (MSTC)

The k-means algorithm (*Hartigan*, 1975) clusters a dataset of n observation vectors ($\vec{X}_1$, $\vec{X}_2$, ..., $\vec{X}_n$) into a user-selected number of groupings or clusters (k), equalizing the full multi-dimensional variance across clusters. The algorithm begins by calculating the Euclidean distance of each observation to the initial centroid vectors ($\vec{C}_1$, $\vec{C}_2$, ..., $\vec{C}_n$) and classifies or assigns each observation to its nearest centroid. Each centroid vector is recalculated as the vector mean of all observations assigned to it. This classification and re-calculation process is iteratively repeated until fewer than some fixed proportion of observations change their cluster assignment between iterations. In the algorithm used here, convergence is assumed once fewer than 0.05% of the observations change cluster assignments. The results of the k-means algorithm are sensitive to the choice of initial centroids. Various heuristics may be employed for their selection, such as choosing initial centroids to have an even distribution within data space or to be spread along the edges of the distribution of observations. In this study, a multi-stage refinement method based on the work of *Bradley and Fayyad* (1998) is employed.

For geographic or spatial stratification applications, observation vectors consist of map cells,

the dimensions of which are the biological or geophysical characteristics or variables under consideration. In this case, the k-means algorithm produces geographic regions with nearly equal heterogeneity with respect to the variance of these environmental characteristics. For spatiotemporal partitioning, observation vectors consist of map cells at different time periods, and the resulting regions maintain their equalized heterogeneity across variables for all time periods considered together. *Hoffman and Hargrove* (1999) developed a parallel version of the k-means algorithm for use on clusters of inexpensive personal computers (*Hargrove et al.*, 2001), and this code was used in a meta-computing environment to cluster data using multiple supercomputers across the Internet (*Mahinthakumar et al.*, 1999). *Hoffman et al.* (2008) later implemented improvements to accelerate convergence, handle empty cluster cases, and obtain initial centroids through a scalable implementation of the *Bradley and Fayyad* (1998) method. *Kumar et al.* (2011) extended this work to develop a fully distributed, highly scalable k-means parallel clustering tool for analysis of very large data sets, which was employed in the study presented here.

3.2.3 Input Data Layers

Selection of input data layers reflects a compromise between desirability and availability. Characteristics influencing the distribution, primary production, and reproduction of species include climate factors, topography, permafrost characteristics, edaphic or soil properties, disturbances, and community composition. Detailed and gridded data on soil factors, disturbances, and community composition is sparse or completely unavailable for the State of Alaska. However, climate is a primary driver controlling species ranges and affecting these secondary environmental factors. Therefore, we have chosen to demonstrate the utility of this analysis method using modeled climatic variables and permafrost properties and observed topography. As observations of soil properties and disturbances become available, they can easily be incorporated into future analyses as additional input data layers. This

analysis used a set of 37 environmental characteristics shown in Table 3.1, from down-scaled general circulation model (GCM) results and observational data for the State of Alaska at a nominal resolution of 2 km × 2 km. These data were used to define a collection of ecoregions at multiple levels of division across two time periods for Alaska. Model results were averaged for the present (2000–2009) and the future (2090–2099). This analysis combined temperature, precipitation, and related bio-climatic projections from a five-model composite data set of down-scaled GCM results for the A1B emissions scenario (*Nakićenović et al.*, 2000) described by *Walsh et al.* (2008); corresponding snow and permafrost projections from the Geophysical Institute Permafrost Lab (GIPL) 1.3 permafrost dynamics model forced with the composite GCM results (*Romanovsky and Marchenko*, 2009); limnicity data based on the National Hydrography Dataset (NHD), pre-processed by *Arp and Jones* (2009); and elevation from the Shuttle Radar Topography Mission 30 (SRTM30) data set. SRTM30 is a combination of data from the SRTM and U.S. Geological Survey's GTOPO30 data set. Since the SRTM mission was only able to map up to approximately 60.25°N latitude, values above this point in the SRTM30 data set are completely from GTOPO30. The same limnicity and elevation data were used for both time periods. Because the units of measurement differ between variables, all data were standardized such that each variable had a mean of zero and a standard deviation of one prior to clustering to equalize the contribution from each predictor.

3.2.4 Alaska Ecoregions

Nowacki and Brock (1995) and *Gallant et al.* (1995) produced ecoregion maps for the State of Alaska using two different expert-based methodologies, strongly focused on land form. Later, *Nowacki et al.* (2001) produced a "unified" ecoregion map—combining the two expert-based techniques—by considering limited data and in consultation with experienced ecologists, biologists, geologists, and regional experts. While useful for some purposes, such qualitative

Table 3.1: The 37 characteristics or variables, averaged for 2000–2009 and 2090–2099, used in Multivariate Spatiotemporal Clustering (MSTC) for the State of Alaska.

Description	Number or Name	Units	Source
Monthly mean air temperature	12	°C	GCM
Monthly mean precipitation	12	mm	GCM
Day of freeze	mean	day of year	GCM
	standard deviation	days	
Day of thaw	mean	day of year	GCM
	standard deviation	days	
Length of growing season	mean	days	GCM
	standard deviation	days	
Maximum active layer thickness	1	m	GIPL
Warming effect of snow	1	°C	GIPL
Mean annual ground temperature at bottom of active layer	1	°C	GIPL
Mean annual ground surface temperature	1	°C	GIPL
Thermal offset	1	°C	GIPL
Limnicity	1	%	NHD
Elevation	1	m	SRTM30

maps are based on the subjective expertise of the person or group developing them and suffer from various limitations (*Hudson*, 1992; *Zhou*, 1996). The question of whether ecoregions can or should be developed using quantitative statistical methods or should rely upon human expertise has been a matter of debate among geographers (*McMahon et al.*, 2001). In this study, Multivariate Spatiotemporal Clustering (MSTC) was applied to derive ecoregions based on climate and topographic factors for the present and the future at multiple levels of division. The climate and topographic factors discussed in §3.2.3 describe the environmental conditions of each map cell and are the most important drivers controlling vegetation and primary production. Thus, groupings or clusters of similarly characterized map cells delineated based on these variables define unique ecoregions. As demonstrated by *Hargrove and Hoffman* (2004), both present and projected future climate factors were included in the same analysis so that groups of similar cells were objectively determined across space and through time. MSTC provides a basis for comparison of environmental conditions in the future with those in the present. Ecoregions constructed through this analysis may grow or

shrink in spatial area and may shift across the landscape. At high levels of division or under extreme environmental change conditions, some present-day ecoregions may become extinct in the future (*i.e.*, shrink to zero spatial area), while others may exist only in the future (*i.e.*, have no analog in the present). This quantitative delineation of ecoregions across space and through time facilitates assessment of the magnitude of change between present and future environmental conditions and enables the evaluation of the ecological implications of climate change scenarios. From a conservation perspective, this methodology maps changing habitats and species at risk from climate change (*Saxon et al.*, 2005). From a field sampling perspective, this methodology identifies regions fostering potentially vulnerable ecosystems or supporting large and vulnerable carbon stores that may be sensitive to climate change (*McGuire et al.*, 2009; *Chapin et al.*, 2010). Such ecoregions warrant intense observation and benefit from careful, quantifiable, and defensible sampling network design strategies.

Expert-derived ecoregion maps are static and have boundaries based on subjective consideration of geographic properties and expert judgment. In contrast, statistically derived ecoregions can vary with time and are delineated in the data space or state space representing all the characteristics under consideration. Moreover, the state space resolution can be varied by selecting different values of k, the level of division in the clustering algorithm. Figures 3.1(a) and 3.1(b) contain maps of the 10 quantitatively defined, most-different Alaskan ecoregions for the present and future, respectively. The cluster centroid of each ecoregion represents the mean value of all the characteristics or state variables for that ecoregion. Tables 3.2 and 3.3 show the 10 centroid values of all 37 state variables, as well as the land area and percent land area for both the present and future time periods. Increasing the selected number of clusters in the k-means algorithm allows the definition of a larger number of more specifically defined, less generalized ecoregions. For example, Figures 3.1(c) and 3.1(d) contain maps of the 20 quantitatively defined, most-different Alaskan ecoregions for the present and future, respectively. By continuing to increase the level of division, the state space resolution can be further increased. Maps of Alaska were produced for $k = 5$, 10, 20, 50, 100, 200, 500, and

1000 ecoregions (*Hoffman et al.*, 2013). To demonstrate the additional state space resolution provided by higher levels of division, maps of 50 and 100 ecoregions for the present and future are shown in Figure 3.2. Since cluster centroids are calculated in the 37-dimensional state space, they may not actually exist in geographic space. However, the map cell closest to the calculated centroid in state space is easily identified. This cell is called the realized centroid for the ecoregion, and it best represents the combination of environmental conditions for the entire ecoregion. The location of these representative realized centroids is indicated by the blue dot in each ecoregion in Figures 3.1 and 3.2.

Ecoregions defined quantitatively may or may not correspond well to expert-derived ecoregions (*Hargrove et al.*, 2006). Table 3.4 shows the spatial overlap or correspondence between the 10 quantitatively defined MSTC Ecoregions and the eight dominantly associated Level 2 ecological groups consisting of the 32 ecoregions defined by *Nowacki et al.* (2001). As expected, strongly distinctive or orographically constrained ecoregions, like Arctic Tundra, have a high degree of correspondence. As shown in Table 3.4, nearly 96% of MSTC Ecoregion 3 overlaps with the Arctic Tundra Level 2 ecological group defined by *Nowacki et al.* (2001), and 93% of their Arctic Tundra group overlaps with MSTC Ecoregion 3. Meanwhile, MSTC Ecoregion 4 intersects multiple Level 2 ecological groups but most dominantly corresponds to the Bering Taiga group with less than 48% overlap. Because 10 MSTC Ecoregions are intersected with eight Level 2 ecological groups, MSTC Ecoregions appear to subdivide two Level 2 ecological groups and the percent area overlap of MSTC Ecoregions on Level 2 ecological groups is usually larger than the percent area overlap of Level 2 ecological groups on MSTC Ecoregions. A quantitative goodness-of-fit method that explicitly accounts for the degree of spatial correspondence between categorical maps with different numbers of categories (*Hargrove et al.*, 2006) can be used to further explore this sort of correspondence analysis.

Alaska exhibits wide ranging heterogeneity in environmental conditions, which can be re-

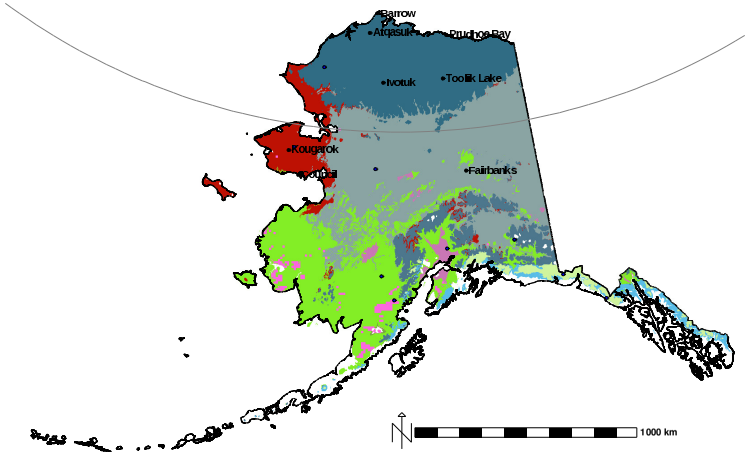

(a) 10 ecoregions, present (2000–2009)

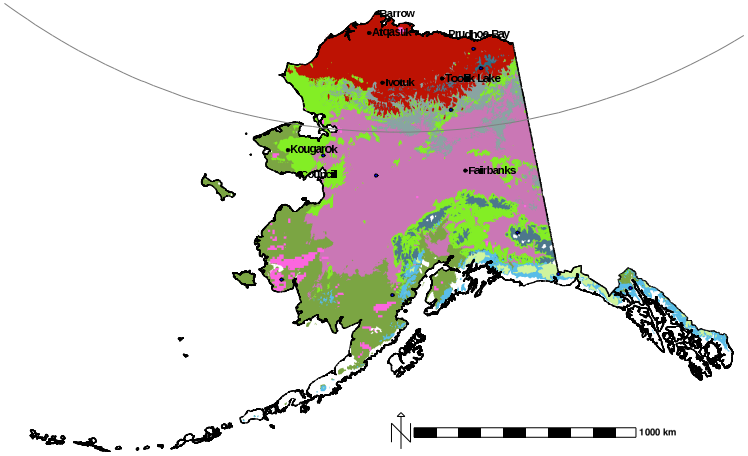

(b) 10 ecoregions, future (2090–2099)

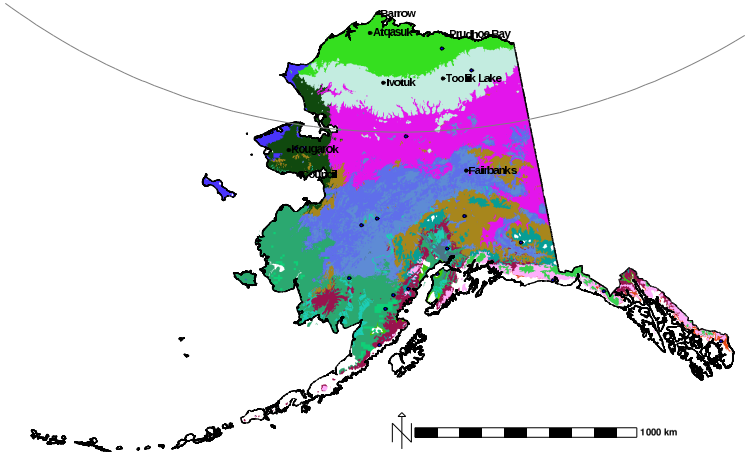

(c) 20 ecoregions, present (2000–2009)

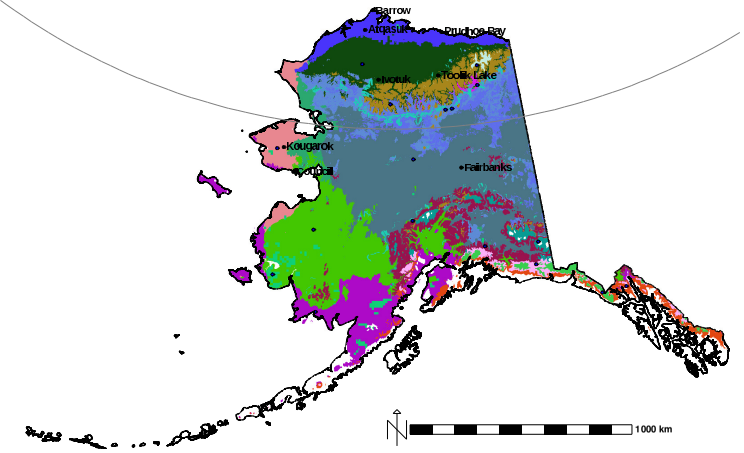

(d) 20 ecoregions, future (2090–2099)

Figure 3.1: The 10 (a and b) and 20 (c and d) most-different quantitatively defined ecoregions for the State of Alaska in the present (a and c) and future (b and d) decades were derived from 37 variables and are shown using random colors. Realized centroids, map locations most closely approximating the mean value within an ecoregion of all the 37 variables, are indicated by the blue dot in each ecoregion.

Table 3.2: 10 Alaska Ecoregions with elevation, precipitation, and temperature

		Monthly Mean Precipitation (mm)												Monthly Mean Temperature (°C)											
		Jan	Feb	Mar	Apr	May	Jun	Jul	Aug	Sep	Oct	Nov	Dec	Jan	Feb	Mar	Apr	May	Jun	Jul	Aug	Sep	Oct	Nov	Dec
1		328.42	284.15	248.03	213.67	213.59	173.93	202.24	283.41	429.71	523.36	387.81	383.70	-5.99	-4.04	-1.44	2.89	6.85	10.35	12.84	12.18	8.02	2.83	-2.42	-4.79
2		29.06	21.48	22.60	20.85	16.53	35.36	53.89	72.98	55.97	40.90	33.40	33.55	-15.50	-18.87	-16.20	-9.48	0.67	8.95	12.71	10.87	5.04	-3.57	-9.19	-13.97
3		23.79	15.13	17.31	17.14	16.84	34.64	48.53	69.06	47.68	36.91	26.46	24.55	-23.36	-25.20	-21.91	-13.14	-1.15	7.97	11.54	8.69	1.00	-10.26	-18.53	-24.92
4		52.87	45.42	43.99	36.14	41.55	66.09	87.36	116.79	98.97	75.19	56.97	54.83	-10.64	-10.70	-7.07	-0.99	6.38	11.53	14.19	12.73	7.49	-0.78	-6.59	-10.36
5		27.86	21.10	20.29	15.67	23.40	55.77	69.13	77.37	56.34	39.13	28.88	26.97	-18.89	-17.05	-11.27	-1.88	7.58	13.47	15.72	12.73	5.76	-4.72	-13.77	-18.82
6		46.02	38.39	41.14	34.36	36.75	48.58	61.56	100.36	84.54	62.36	53.71	51.05	-5.53	-6.60	-3.79	0.60	7.49	12.13	15.02	14.48	10.24	2.59	-2.12	-5.56
7		70.13	58.04	62.02	50.47	52.88	63.39	80.38	128.24	118.58	89.91	82.71	76.47	-2.66	-3.89	-1.33	2.44	8.38	12.64	15.56	15.28	11.24	3.89	0.50	-2.31
8		559.21	476.17	428.45	381.38	375.37	287.92	347.00	486.23	755.09	914.55	651.59	693.75	-11.72	-8.73	-5.78	-0.47	3.01	7.21	10.00	9.06	4.11	-1.25	-7.42	-10.43
9		115.78	102.92	99.70	77.83	83.27	143.64	182.02	206.01	215.50	180.12	119.10	126.89	-14.78	-13.36	-10.05	-3.69	1.69	6.61	9.25	7.79	2.11	-5.33	-11.44	-14.51
10		36.12	31.06	31.52	25.20	27.09	64.58	77.77	98.97	69.45	47.02	42.52	43.39	-12.10	-10.56	-5.20	2.92	11.11	15.91	18.05	15.93	9.81	-0.11	-6.68	-10.07

Table 3.3: 10 Alaska Ecoregions with elevation, other environmental factors, and area

		Freeze Day (d)		Thaw Day (d)		GS Length (d)		Max AL	ΔT_{sn}	MAGT	MAGST	Thermal	Limnicity	Elevation	Present (2000–2009)		Future (2090–2099)	
		mean	stdev	mean	stdev	mean	stdev	Thick (m)	(°C)	ALB (°C)	(°C)	Offset (°C)	(%)	(m)	Area (km^2)	% Area	Area (km^2)	% Area
1		312.43	8.38	76.71	14.73	235.71	20.48	-0.23	1.07	3.82	4.07	-0.25	0.91	911.04	33424	2.45	48356	3.54
2		279.34	5.80	133.42	3.11	145.91	6.51	0.74	2.77	-1.87	-1.32	-0.55	3.61	395.02	93860	6.87	227188	16.63
3		262.53	1.62	138.98	2.76	123.55	2.83	0.62	3.63	-5.84	-5.38	-0.45	3.62	543.53	295596	21.63	2316	0.17
4		289.40	4.45	107.53	6.30	181.87	9.82	-0.44	1.70	1.28	2.00	-0.72	3.33	440.21	302024	22.10	204408	14.96
5		276.72	2.11	110.36	4.29	166.36	5.32	0.63	1.97	-1.48	-0.66	-0.83	1.49	412.60	486504	35.61	88952	6.51
6		311.55	9.96	92.86	15.41	218.69	24.00	-0.22	1.02	3.51	4.06	-0.55	52.78	37.88	16708	1.22	26308	1.93
7		329.34	17.32	70.29	31.07	259.05	42.78	-0.21	0.52	4.96	5.23	-0.27	5.45	189.60	1404	0.10	243244	17.80
8		283.29	4.86	110.22	7.53	173.38	10.28	0.01	1.80	0.36	0.74	-0.38	0.20	1429.68	26352	1.93	22392	1.64
9		267.14	3.52	126.13	6.38	142.03	7.35	0.53	2.12	-2.01	-1.70	-0.31	0.27	1587.51	92088	6.74	39512	2.89
10		291.63	5.32	93.33	8.27	198.30	12.38	-0.51	0.99	2.53	3.27	-0.74	1.47	315.57	18412	1.35	463696	33.94

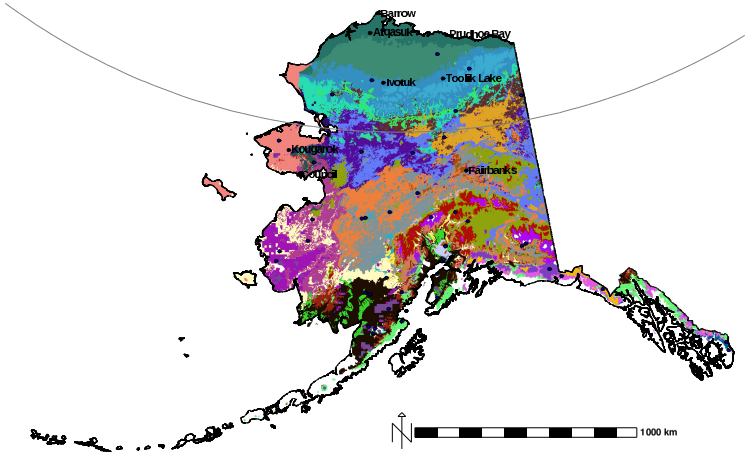

(a) 50 ecoregions, present (2000–2009)

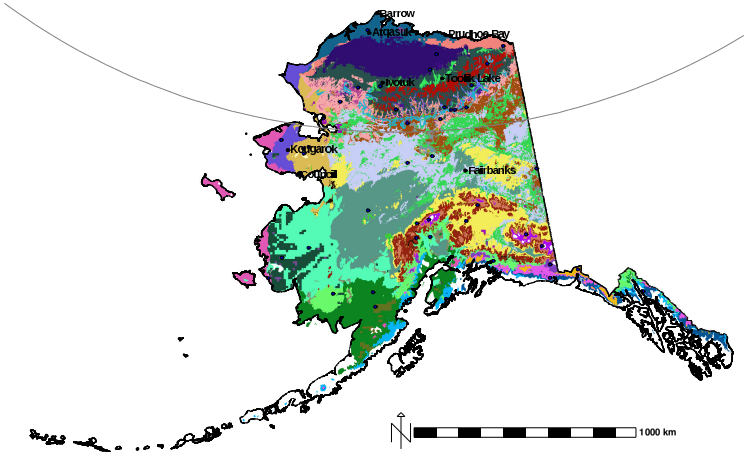

(b) 50 ecoregions, future (2090–2099)

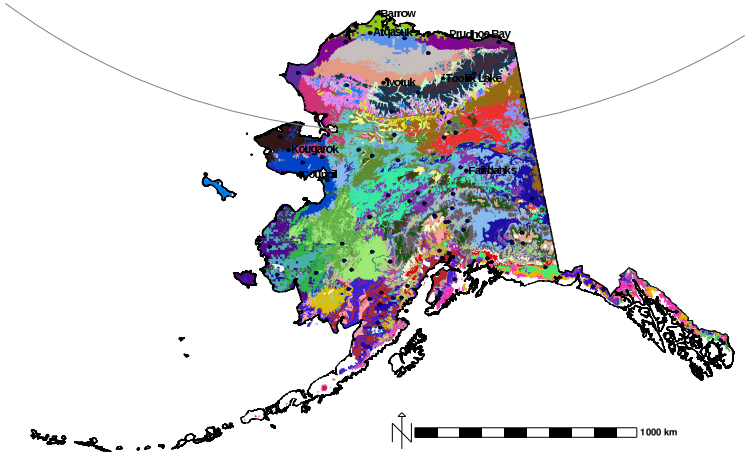

(c) 100 ecoregions, present (2000–2009)

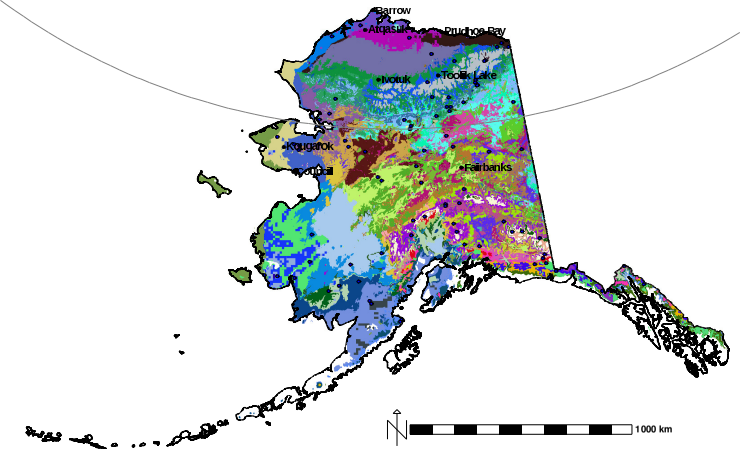

(d) 100 ecoregions, future (2090–2099)

Figure 3.2: The 50 (a and b) and 100 (c and d) most-different quantitatively defined ecoregions for the State of Alaska in the present (a and c) and future (b and d) decades were derived from 37 variables and are shown using random colors. Realized centroids, map locations most closely approximating the mean value within an ecoregion of all the 37 variables, are indicated by the blue dot in each ecoregion.

Table 3.4: Spatial correspondence between the 10 quantitatively defined MSTC Ecoregions and the eight dominantly associated Level 2 ecological groups consisting of the 32 ecoregions defined by *Nowacki et al.* (2001).

MSTC Ecoregion	**Nowacki Level 2 Ecological Group**	**% area overlap of MSTC on Nowacki**	**% area overlap of Nowacki on MSTC**
1	Coastal Rainforests	85.62	30.83
2	Bering Tundra	58.69	78.77
3	Arctic Tundra	95.75	93.44
4	Bering Taiga	47.66	70.63
5	Intermontane Boreal	78.70	81.58
6	Aleutian Mountains	41.31	22.23
7	Aleutian Mountains	64.18	2.94
8	Coastal Rainforests	96.56	27.46
9	Alaska Range Transition	59.99	35.23
10	Alaska Range Transition	64.38	9.19

solved by selecting larger numbers of clusters in the MSTC algorithm. While MSTC is a non-hierarchical procedure, inherently hierarchical relationships within the combinations of state variables automatically emerge when increasing the level of division. For example, at a level of division of $k = 10$, the North Slope of Alaska is represented by a single ecoregion (#3) corresponding to the Arctic Tundra Level 2 ecological group (Figure 3.3(a)). The North Slope is divided into two ecoregions (#5 and #13) corresponding to the Brooks Range and Beaufort Coastal Plains ecoregions defined by *Nowacki et al.* (2001) at a level of division of $k = 20$ (Figure 3.3(b)). By further increasing the level of division to $k = 50$, the North Slope is divided into five different ecoregions (#32, 33, 34, 35, and 40) corresponding to the Intermontane Boreal ecological group, high- and low-elevation Brooks Range, Brooks Foothills, and Beaufort Coastal Plains ecoregions defined by *Nowacki et al.* (2001) (Figure 3.3(c)). Even more specialized ecoregions can be resolved by further increasing the desired level of division in the MSTC algorithm (Figure 3.2).

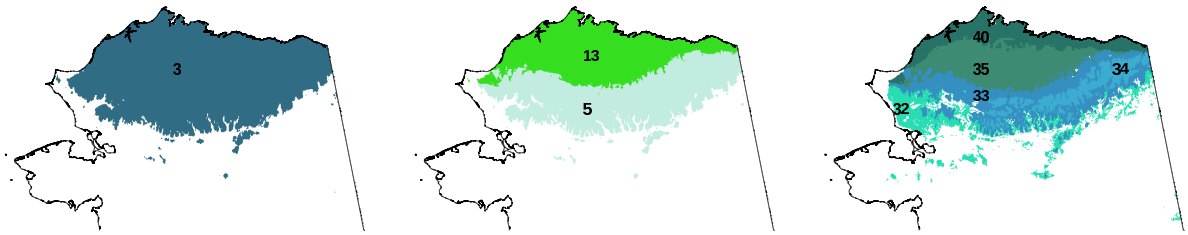

(a) At $k = 10$, the North Slope is occupied by MSTC Ecoregion #3, which corresponds to the Arctic Tundra Level 2 ecological group.

(b) At $k = 20$, the North Slope is occupied by MSTC Ecoregion #5, corresponding to the Brooks Range ecoregion; and MSTC Ecoregion #13, corresponding to the Beaufort Coastal Plains ecoregion.

(c) At $k = 50$, the North Slope is occupied by MSTC Ecoregion #32, corresponding to the Intermontane Boreal ecological group; MSTC Ecoregions #33 and #34, corresponding to low- and high-elevation subsets of the Brooks Range ecoregion; MSTC Ecoregion #35, which corresponds to the Brooks Foothills ecoregion; and MSTC Ecoregion #40, which corresponds to the Beaufort Coastal Plains ecoregion.

Figure 3.3: A hierarchy of increasingly specific ecoregions for the North Slope of Alaska emerge by increasing the level of division in the MSTC algorithm. MSTC cluster numbers are shown and the spatially corresponding Level 2 ecological group or ecoregion defined by *Nowacki et al.* (2001) is identified.

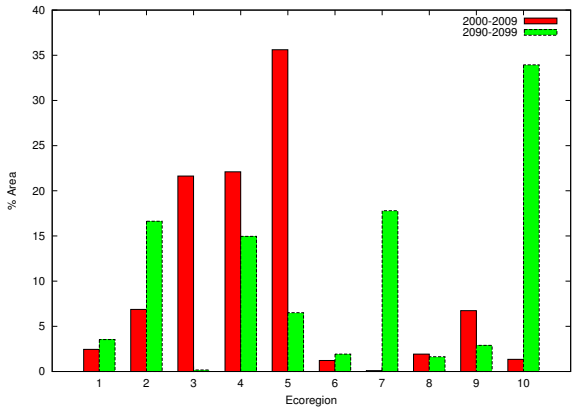

(a) Percent area distribution of 10 ecoregions during the present (2000–2009) and future (2090–2099) periods.

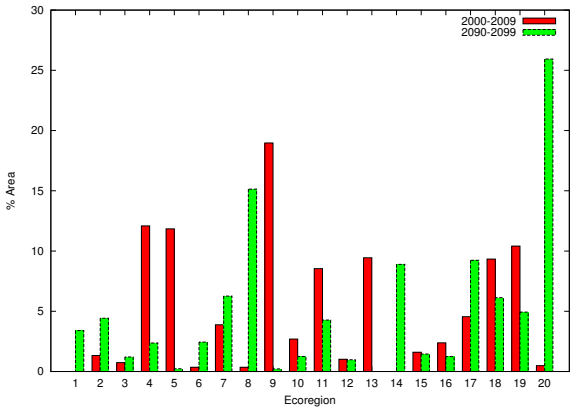

(b) Percent area distribution of 20 ecoregions during the present (2000–2009) and future (2090–2099) periods.

Figure 3.4: Percent area distribution of (a) 10 and (b) 20 ecoregions during the present (2000–2009) and future (2090–2099) periods. Mean values for the state variables for the 10 ecoregions are contained in Tables 3.2 and 3.3.

3.3 Mapping Sensitive Environments

Evidence of environmental change in the Arctic and resulting impacts on aquatic productivity and biodiversity, terrestrial ecosystems, and local economies were highlighted by *Anisimov et al.* (2007). Increased shrub abundance has been observed in Alaska (*Sturm et al.*, 2001, 2005; *Tape et al.*, 2006). During the last 50 years, the tree line along the Arctic to sub-Arctic boundary has moved 10 km northward and 2% of Alaskan tundra on the Seward Peninsula has been replaced by forests. Ecoregions derived for the present and future (Figure 3.1) show a similar northward shift, indicating a dramatic change in environmental conditions due to a warming climate by the end of this century, as projected by models using the A1B emissions scenario (*Nakićenović et al.*, 2000). By tracking changes in the spatial area and migration of ecoregions statistically derived from a hypervolume of environmental gradients (*Hutchinson*, 1957), this objective approach for mapping landscapes undergoing environmental change can be applied to predict shifts in species ranges and constrain estimates of changes in the carbon balance of sensitive environments.

Figure 3.4(a) shows the percent area distribution of each ecoregion, at the $k = 10$ level of division, for the present and future time periods. Correspondence between these MSTC Ecoregions and *Nowacki et al.* (2001) Level 2 ecological groups is shown in Table 3.4. A significant decrease in the area of Ecoregion #3, representing most of the North Slope of Alaska as shown in Figure 3.3(a), is observed. This contemporary Arctic Tundra environment is predicted to be reduced to about 0.78% of its present area by the end of the century. About 76% of the area will be replaced by conditions typical of the warmer Bering Tundra environment (Ecoregion #2). Meanwhile, the Bering Tundra (Ecoregion #2) environment moves northward by the end of the century and more than doubles in areal extent. About 70% of its current area, especially over the Seward Peninsula, will change to conditions similar to contemporary Bering Taiga (Ecoregion #4). In the future, the Bering Taiga (Ecoregion #4) environment decreases in extent by 32% and migrates northward. Under increased temperatures and reduced permafrost conditions, the present-day Aleutian Mountains (Ecoregion #7) environmental conditions are predicted to replace 65% of Bering Taiga (Ecoregion #4), and Alaska Range Transition (Ecoregion #10) environmental conditions are expected to replace 28% of Bering Taiga (Ecoregion #4). Aleutian Mountain (Ecoregion #7) and Alaska Range Transition (Ecoregion #10) environments, which exist in the southern coastal regions of Alaska, are expected to grow in extent northward and occupy a larger portion of Alaska. Alaska Range Transition (Ecoregion #10) environmental conditions are also expected to replace about 75% of the Intermontane Boreal (Ecoregion #5) environment in the future, which will be reduced to 18% of its current area by the end of the century. While similar trends of large scale northward migrations and changes in the areal extents of the environments discussed above are observed at 20 and higher levels of divisions, these ecoregion refinements highlight the changes that are occurring in smaller, more uniquely defined environments.

Figure 3.4(b) shows the percent area distribution of $k = 20$ ecoregions for the present and future time periods. In addition to areal extent, changes and geographic redistribution of ecoregions between the present and future, at this level of division one present-day ecoregion

ceases to exist in the future (*i.e.*, becomes extinct) while another ecoregion exists only in the future (*i.e.*, is born) and has no analog in the present. Ecoregion #13 (Figure 3.5(a)), which represents the most northern portion of Arctic Tundra on the North Slope, becomes extinct in the future due to projected climate change. Ecoregions #2 and #17, which presently occupy the Seward Peninsula and nearby coasts (Figure 3.5(b)), replace Ecoregion #13 in the future (Figure 3.5(c)). Approximately 46% of the area of Ecoregion #13 is replaced by Ecoregion #2 and 53% is replaced by Ecoregion #17. Under this climate change scenario, the ecoregions replacing the extinct region in the future have characteristically higher precipitation, higher temperatures, earlier thaw dates, later freeze dates, a longer growing season, increased active layer depth, and higher ground surface temperatures. At the end of the century, much of the Seward Peninsula and nearby coasts are occupied by an entirely new combination of environmental conditions, defined by Ecoregion #1, which has no analog in the present (Figure 3.5(d)). This new ecoregion, which appears only in the future time period, represents an environment with higher precipitation and temperature, an increased growing season length, increased active layer depth, and higher soil temperatures.

As the level of division is increased in the MSTC algorithm, more specialized ecoregions are delineated. As a result, the number of present-day ecoregions that become extinct and the number of non-analog future ecoregions will both increase. Identification of regions representing new combinations of environment conditions that did not previously occur together is important for forecasting species range distributions, conservation planning, and climate change impacts on biodiversity (*Fitzpatrick and Hargrove*, 2009).

3.4 Site Selection

Selection of sampling locations for long term monitoring of ecosystem properties and processes should be guided by an objective, quantitative, systematic, and defensible methodol-

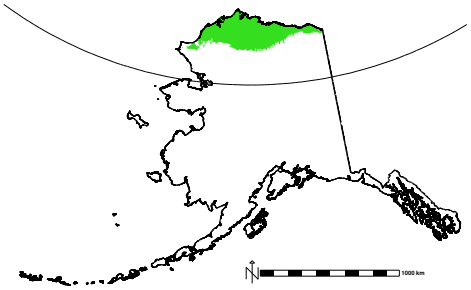

(a) Ecoregion #13 (present), the coldest Arctic Tundra on the North Slope, ceases to exist in the future.

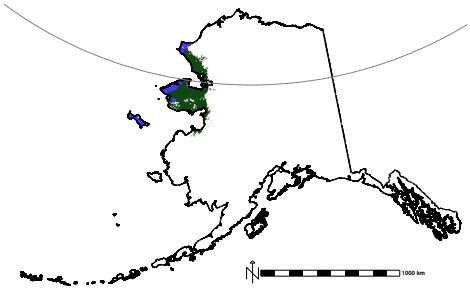

(b) Ecoregions #2 and #17 (present) are limited to the Seward Peninsula and nearby coasts.

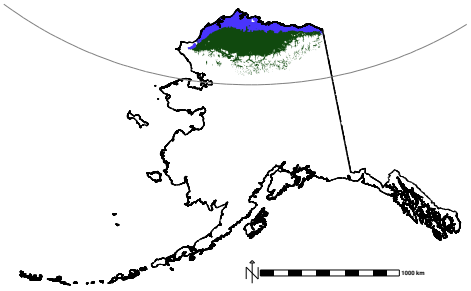

(c) Ecoregions #2 and #17 (future) have moved northward, displacing Ecoregion #13 (present) on the North Slope.

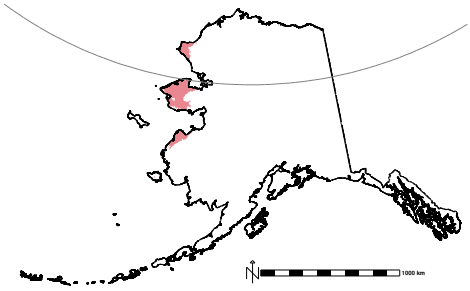

(d) A new Ecoregion #1 (future) occupies much of the Seward Peninsula and nearby coasts and has no analog in present.

Figure 3.5: At $k = 20$, MSTC Ecoregions migrate across the landscape, one becomes extinct, and one comes into existence between the present and future.

ogy. Instead, sampling locations in large-scale networks have often been established in opportunistic, political, or logistically-driven ways, resulting in unquantified representation of heterogeneity, biased sampling, uncharacterized uncertainty, and undirected network growth. Finite resources and logistical constraints limit the spatiotemporal frequency and extent of environmental observations, necessitating the development of a systematic sampling strategy to objectively represent environmental variability at the desired spatial scale. An appropriately designed observation strategy should be employed to quantitatively delineate sampling domains, sites, and frequencies. The National Science Foundation's (NSF's) National Ecological Observatory Network (NEON) adopted the objective, data-based methodology described above to define 20 optimal sampling domains across the conterminous United States (*Keller et al.*, 2008; *Schimel et al.*, 2007). Accurate characterization of the landscape and translation of data collected in the field and laboratory into useful datasets, process algorithms, and model parameters requires classification of the landscape into discrete units based on ecological, hydrological, and geological properties. In much the same way that ecologists develop ecoregions, geologists often classify landscape areas into geomorphological units based on their geophysical and hydrological features. For complex and evolving landscapes featuring interacting vegetation and geomorphological dynamics responding to changes in climate, such as in the Arctic, these stratification concepts may be unified to produce biogeomorphic units at relevant spatial scales for landscape characterization, identification of ecological and geomorphological processes, assessing the representativeness of measurements, and providing a framework for scaling measurements and model parameters to larger domains.

An important aspect of site selection and the up- and down-scaling approach to integration of models, observations, and process studies is the estimation of representativeness. The MSTC methodology described above for landscape characterization offers useful metrics for indicating the representativeness of sites, measurements, and model parameters, assuming the environmental characteristics included in the analysis covary with the measured variables. *Hargrove et al.* (2003) described this technique for understanding the representativeness of

a sampling network based on a suite of environmental gradients considered to be useful proxies for the characteristics being measured. Maps identifying poorly represented regions can be produced, suggesting where new measurements should be taken to maximize sampling network coverage. As discussed in §3.2.4, since the cluster centroid represents the mean value of all the state variables in an ecoregion, the realized centroid for an ecoregion is the location that best represents the combination of environmental conditions of the entire ecoregion. Therefore, statistically defined realized centroids, indicated by blue dots in each ecoregion in Figures 3.1 and 3.2, are the optimal sampling locations for each ecoregion. Logistical constraints—including accessibility, availability of electric power and telecommunications infrastructure, and geologic stability—may prevent establishment of sampling sites at such optimal locations, particularly in an Arctic environment. Nevertheless, the MSTC Ecoregion framework provides a means for quantifying the representativeness of measurements taken at sub-optimal locations, either within an ecoregion or across any larger domain for which the desired state variables are available.

3.5 Quantifying Representativeness

While most *in situ* field measurements are made at relatively small, individual geographic points, ecosystem processes operate at many scales. To utilize limited point measurements at larger spatial and temporal scales for input to or evaluation of process modeling or for estimating landscape-scale characteristics, the representativeness of those measurements must be quantified in the context of a heterogeneous and evolving landscape. A useful representativeness metric is one that can inform the selection of sampling locations, up-scaling of point measurements, down-scaling of remote sensing data, and extrapolation of measurements to unsampled domains. This requires that the underlying variables used to define ecoregions covary with the point measurements (*i.e.*, the surrogate variables have and maintain predictive

power). The representativeness metric described by *Hargrove et al.* (2003) provides a unitless, relative measure of the dissimilarity between the ecoregion of interest, which may contain a sampling site, and any other ecoregion. It is calculated as the Euclidean distance between two ecoregion centroids within the standardized n-dimensional state space. Ecoregions with similar combinations of environmental conditions will have centroids located near to each other in state space. Therefore, the Euclidean distance between those centroids will be small, representing a low dissimilarity or high representativeness measure. Meanwhile, ecoregions with very different combinations of environmental conditions will have centroids located far from each other in state space, resulting in a large Euclidean distance between them. Such ecoregions will have a high dissimilarity or low representativeness measure. To best capture the natural heterogeneity at the scale of interest, this ecoregion-based representativeness should be calculated using MSTC Ecoregions with a large number of divisions (*i.e*, a large value of k).

While *Hargrove et al.* (2003) calculated representativeness in the context of ecoregions, this same approach can be applied to every map cell projected individually onto the n-dimensional state space used to perform the cluster analysis that produced MSTC Ecoregions. This point-based representativeness metric captures the full range of heterogeneity in the combinations of environmental conditions, providing a continuously varying measure of dissimilarity for every map cell with respect to a map cell of interest, which may contain a sampling location. When a single ecoregion centroid or map cell of interest is considered, a map of site representativeness can be produced. However, multiple ecoregions or map cells of interest may be considered simultaneously, for instance, to provide a quantitative measure of the representativeness of an array or network of sampling sites. The result is a map of network representativeness for which the dissimilarity measure for every ecoregion centroid or map cell is the Euclidean distance between that point and the nearest ecoregion centroid or map cell of interest (*i.e.*, the minimum value from a stack of site representativeness maps, one for each ecoregion centroid or map cell containing a measurement site). This representativeness

metric, whether ecoregion- or point-based, can be calculated not only between different geographic points in space, but also between different (or the same) geographic points through time. For example, the Euclidean distance between the present combination of environmental conditions and those of the future for any single map cell represents a measure of the magnitude of environmental change over time. Therefore, with this metric it is possible to calculate not only the present-day representativeness of measurements from a site, but also the future representativeness of those present-day measurements, based on future projections of the state variables used in the analysis.

3.5.1 Site Representativeness

Due to significant logistical constraints when working in the Arctic, a set of eight potential sites were identified as candidates for measurements, long term monitoring and potential manipulative experiments for the U.S. Department of Energy's Next Generation Ecosystem Experiment (NGEE) Arctic project in the State of Alaska: Barrow, Council, Atqasuk, Ivotuk, Kougarok, Prudhoe Bay, Toolik Lake, and Fairbanks. Because of available support infrastructure, Barrow was selected as an initial location for collecting field measurements. To adequately capture the heterogeneity of environmental gradients, an ecoregion-based representativeness analysis employed ecoregion maps at the $k = 1000$ level of division. Figure 3.6(a) shows the present-day representativeness of the monitoring site at Barrow for the present period. In this map, white to light gray land areas are well-represented by the Barrow location, while dark gray to black land areas are poorly represented by Barrow. The Arctic Tundra of the North Slope is well represented by the Barrow site, but the representativeness drops rapidly at the Brooks Range, which experiences different climate conditions driven by high topography. If a field researcher were attempting to select one additional sampling location to provide optimal coverage of the environments within the state of Alaska, that next site should be chosen within the darkest land areas shown in the map. Once a new

candidate site has been selected, a new map of representativeness can be generated with simultaneous consideration of both sites. Using this relative representativeness metric, optimal sampling locations can be chosen to maximize the coverage of environmental conditions for any domain at any scale for which sufficient state variable data are available.

Since climate model projections for the future were included in the MSTC procedure, the future representativeness of the present-day Barrow-containing ecoregion can also be mapped (Figure 3.6(b)). Since the climate is projected to change significantly, the future representativeness of the present-day ecoregion is relatively lower, which is indicated by darker colors in Figure 3.6(b) as compared with Figure 3.6(a). Such changes in representativeness are especially large in the Northern Arctic Coastal Plains since this Arctic Tundra is projected to warm significantly and has been identified as a sensitive environment (§3.3). Similarly, Figures 3.7(a) and 3.7(b) contain maps of the present and future representativeness of present-day Barrow, respectively, calculated using the point-based representativeness method. As expected, the large-scale pattern of maps in Figure 3.7 is the same as that of the maps in Figure 3.6, but the maps in Figure 3.7 show more detail and are less generalized than those in Figure 3.6. Point-based site representativeness maps for each of the eight candidate sites for the present time period are shown in Figure 3.8.

Since the representativeness metric—or measure of dissimilarity—can be computed between any two map locations, a table quantitatively characterizing dissimilarity of the eight individual candidate sampling locations may be useful for site selection purposes. Table 3.5 shows point-to-point dissimilarity values for the eight candidate sampling locations for the present time period. Of those locations, Barrow and Fairbanks are the most dissimilar, having a dissimilarity value of 12.16. Atqasuk and Prudhoe Bay are the most similar of the sites. Both Atqasuk and Prudhoe Bay are near-coastal sites at the northern extent of the North Slope; therefore, the environmental conditions are expected to be similar. In addition, according to Table 3.5, the Prudhoe Bay site is most similar to Barrow, while the Council

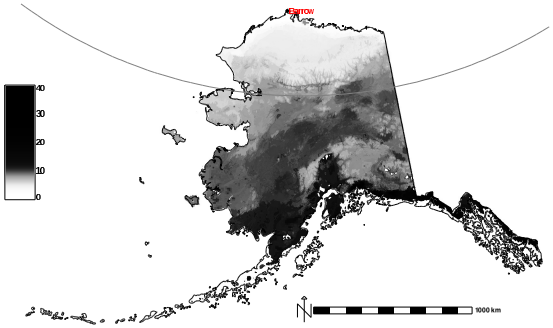

(a) Ecoregion-based representativeness of present-day Barrow for the present period (2000–2009)

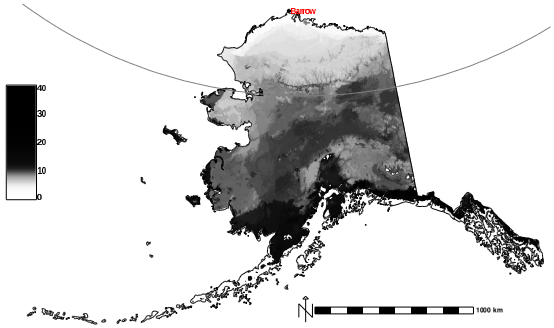

(b) Ecoregion-based representativeness of present-day Barrow for the future period (2090–2099)

Figure 3.6: Ecoregion-based representativeness maps of present-day Barrow for the present and future time periods. White to light gray land areas are well-represented by Barrow, while dark gray to black land areas are poorly represented by Barrow.

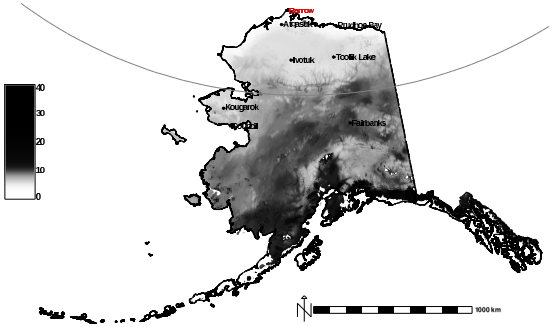

(a) Point-based representativeness of present-day Barrow for the present period (2000–2009)

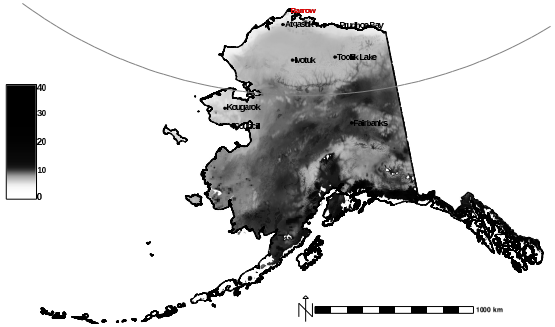

(b) Point-based representativeness of present-day Barrow for the future period (2090–2099)

Figure 3.7: Point-based representativeness maps of present-day Barrow for the present and future time periods. White to light gray land areas are well-represented by Barrow, while dark gray to black land areas are poorly represented by Barrow.

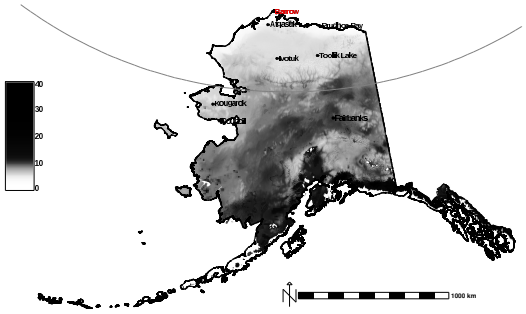

(a) Barrow

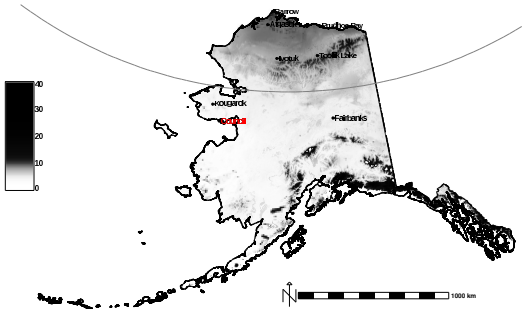

(b) Council

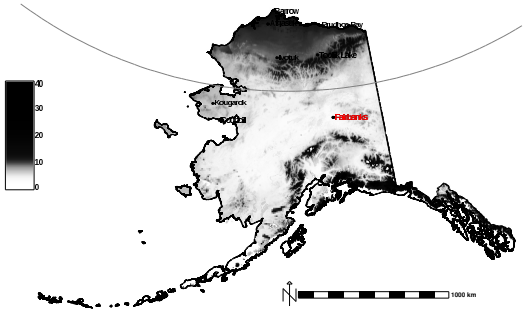

(c) Fairbanks

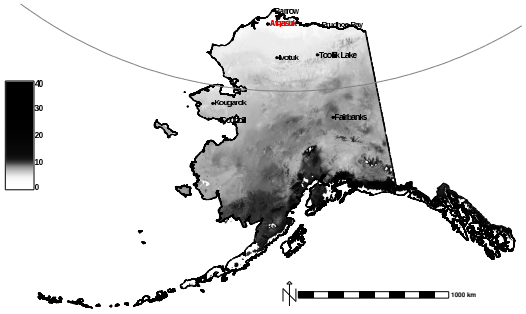

(d) Atqasuk

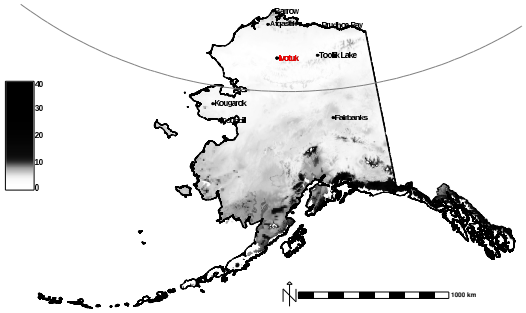

(e) Ivotuk

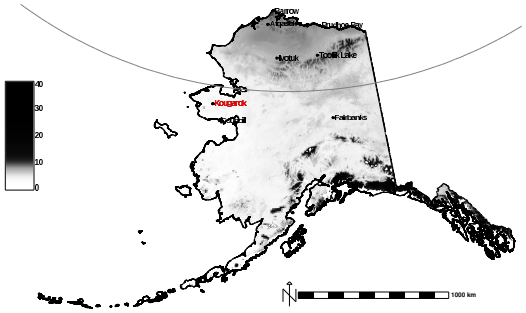

(f) Kougarok

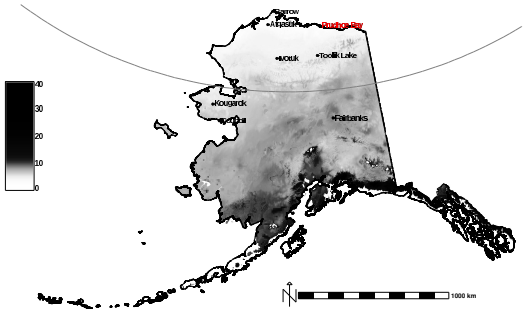

(g) Prudhoe Bay

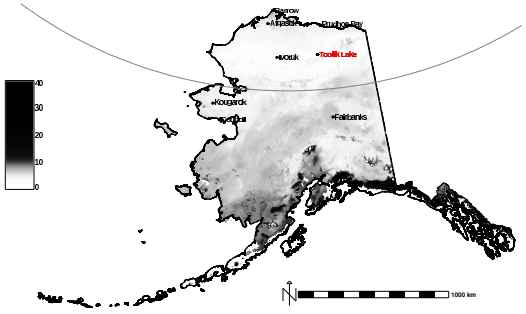

(h) Toolik Lake

Figure 3.8: Point-based representativeness for eight potential present-day NGEE Arctic sites for the present time period. White to light gray land areas are well-represented by the site, while dark gray to black land areas are poorly represented by the site.

site is the most dissimilar to Barrow, ignoring Fairbanks. This example analysis suggests that if Barrow were the first sampling site selected, Council may be a strong candidate for a second site in the northern half of the State of Alaska because of its dissimilarity to Barrow. Similarly, Table 3.6 shows point-to-point dissimilarity values for the eight candidate sampling locations for the future time period. While the dissimilarity values for the future are similar to those of the present, it is apparent that some sites become more similar while others become less similar. For example, Barrow and Council become less dissimilar in the future (*i.e.*, their dissimilarity value of 9.13 in the present changes to 8.87 in the future), indicating that the environmental conditions in Barrow and Council are more different in the present than they are projected to be in the future.

Table 3.7 shows a full matrix of point-to-point dissimilarity values for the eight candidate sites between the present and the future. This table quantifies the dissimilarity of present-day sites to those same sites in the future. For this list of widely dispersed locations, the environmental conditions for any single site in the present will be most like the environmental conditions for that same site in the future. Therefore, the smallest dissimilarity values are along the diagonal in Table 3.7. The largest value on the diagonal is for the Barrow site, indicating that environmental conditions at Barrow are projected to change more than at any other candidate site. In addition, this table shows that environmental conditions at Barrow in the future are more similar to those at Council in the present (8.38) than are the conditions at Barrow in the present to Council in the future (9.67). This result is consistent with the MSTC Ecoregion migration shown in Figure 3.5. This point-to-point analysis through time is a novel method for quantifying relationships between sampling locations and how those relationships evolve over time due to environmental change.

Table 3.5: Site state space distances for the present (2000–2009).

Sites	Council	Atqasuk	Ivotuk	Toolik Lake	Kougarok	Prudhoe Bay	Fairbanks
Barrow	9.13	4.53	5.90	5.87	7.98	3.57	12.16
Council		8.69	6.37	7.00	2.28	8.15	5.05
Atqasuk			5.18	5.23	7.79	1.74	10.66
Ivotuk				1.81	5.83	4.48	7.90
Toolik Lake					6.47	4.65	8.70
Kougarok						7.25	5.57
Prudhoe Bay							10.38

Table 3.6: Site state space distances for the future (2090–2099).

Sites	Council	Atqasuk	Ivotuk	Toolik Lake	Kougarok	Prudhoe Bay	Fairbanks
Barrow	8.87	4.89	6.88	6.94	8.04	4.18	11.95
Council		8.82	6.93	7.74	2.43	8.24	5.66
Atqasuk			5.86	5.84	8.15	2.30	10.16
Ivotuk				2.01	7.27	4.75	7.51
Toolik Lake					7.81	5.00	8.33
Kougarok						7.89	6.42
Prudhoe Bay							9.81

Table 3.7: Site state space distances between the present (2000–2009) and the future (2090–2099).

		Future (2090–2099)							
	Sites	Barrow	Council	Atqasuk	Ivotuk	Toolik Lake	Kougarok	Prudhoe Bay	Fairbanks
Present (2000–2009)	Barrow	3.31	9.67	4.63	6.05	5.75	9.02	3.69	11.67
	Council	8.38	1.65	8.10	5.91	6.87	3.10	7.45	5.38
	Atqasuk	6.01	9.33	2.42	5.46	5.26	8.97	2.63	10.13
	Ivotuk	7.06	7.17	5.83	1.53	2.05	7.25	4.87	7.40
	Toolik Lake	7.19	7.67	6.07	2.48	1.25	7.70	5.23	8.16
	Kougarok	7.29	3.05	6.92	5.57	6.31	2.51	6.54	5.75
	Prudhoe Bay	5.29	8.80	3.07	4.75	4.69	8.48	1.94	9.81
	Fairbanks	12.02	5.49	10.36	7.83	8.74	6.24	10.10	1.96

3.5.2 Network Representativeness

A monitoring network often consists of a geographically distributed constellation of measurement sites or may be locations where samples are collected for further analysis in the laboratory. Quantifying the representativeness of the network as a whole is important for optimal network design to avoid unnecessary duplication and to maximize the coverage of the monitoring network. By combining multiple maps of site representativeness for every sampling location, and calculating the minimum value for every map cell, maps of network representativeness are produced. Figures 3.9(a) and 3.9(b) contain maps of ecoregion-based network representativeness for all eight candidate sampling sites for the present and future time periods, respectively. Similarly, Figures 3.10(a) and 3.10(b) contain maps of point-based network representativeness for the same eight candidate sampling sites for the present and future time periods, respectively. White to light gray land areas are well-represented by the network of sites, while dark gray to black land areas are poorly represented by the network of sites. If the objective were to maximize the coverage of all environments in the State of Alaska, the next sampling location should be chosen within the darkest land areas shown in the map. Most of Alaska is well represented by this network of eight sampling locations.

3.6 Conclusions

Systematic sampling strategies are essential for understanding ecosystem responses to climate change and informing model development. In the harsh Arctic environment—where climate change appears to be most rapidly affecting sensitive ecosystems and vulnerable, carbon-rich permafrost—filling critical gaps in observations is expensive and technically challenging. To fully explore the regional and global implications of climate change in the Arctic, global Earth System Models must capture the important processes and feedbacks. Such models

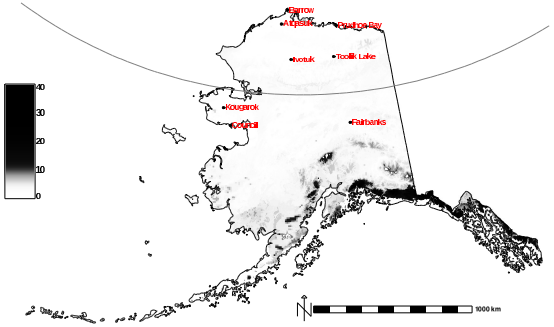

(a) Ecoregion-based network representativeness of eight sites for the present period

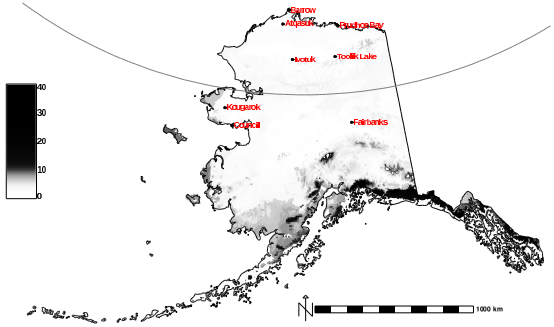

(b) Ecoregion-based network representativeness of eight sites

Figure 3.9: Ecoregion-based representativeness maps for a network of eight sites for the present and future time periods. White to light gray land areas are well-represented by the network of sites, while dark gray to black land areas are poorly represented by the network of sites.

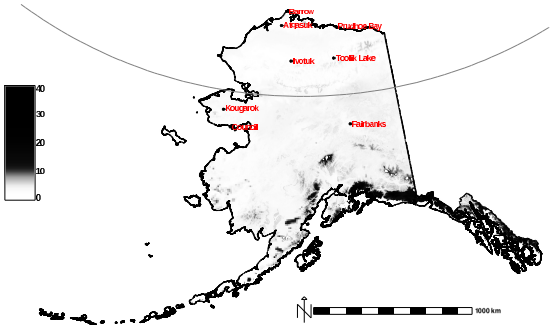

(a) Point-based network representativeness of eight sites for the present period

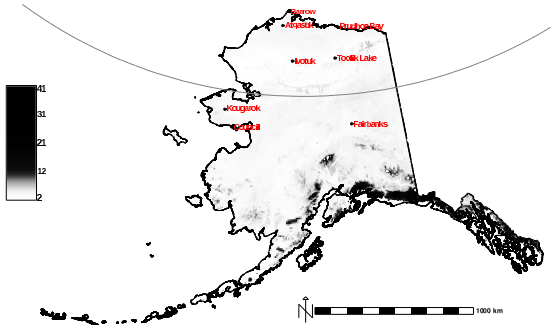

(b) Point-based network representativeness of eight sites for the future period

Figure 3.10: Point-based representativeness maps for a network of eight sites for the present and future time periods. White to light gray land areas are well-represented by the network of sites, while dark gray to black land areas are poorly represented by the network of sites.

must be developed based on a rich body of observational data as representative as possible of multiple spatial and temporal scales. Meanwhile, finite resources and logistical constraints place restrictions on the number of sampling sites, spatial extent, frequency, and types of measurements that can be collected. This study develops a quantitative, data-based methodology for stratifying sampling domains, informing site selection, and determining the representativeness of measurement sites and sampling networks.

Multivariate spatiotemporal clustering (MSTC), based on k-means cluster analysis, was applied to down-scaled general circulation model (GCM) results and observational data for the State of Alaska at a nominal resolution of 4 km^2 to define a set of ecoregions at multiple levels of division across two decadal time periods. Maps of ecoregions for the present (2000–2009) and future (2090–2099) were produced, showing how combinations of 37 environmental conditions are distributed across Alaska and how these combinations shift as a result projected climate change in the 21st century. Using this statistical approach, optimal sampling locations, called realized centroids, were identified for each ecoregion at every level of division. In addition, the resulting geographic shifts and changes in areal distribution of ecoregions suggested that some environments may disappear, many will be redistributed, and new ones will appear in the coming century. This analysis provides insights into the identification of the most sensitive and potentially vulnerable Arctic ecosystems. The Euclidean distance within the 37-dimensional state space used for MSTC provides a metric for representativeness. Gray-scale maps of representativeness, showing the similarity of every map cell to a list of eight candidate samples locations near town sites in Alaska, were produced for each site. Tables quantitatively characterizing the similarity of candidate sampling locations to each other across space and through time were generated. These tables are useful for understanding the strength of the environmental gradients between sites and how those gradients may change based on model projections of the future. Taken together, these analysis products provide model-inspired insights into optimal sampling strategies across space and through time, and these same techniques can be applied at different spatial and temporal scales to

meet the needs of individual measurement or monitoring campaigns.

The representativeness of a sampling network is best maximized during the design of the network. Even if additional "optimized" sites are added to an existing network, it will require many more additions to approach the theoretical maximum representativeness for a given number of initial sites. It is difficult, with only the sequential addition of new optimized sites, to achieve the same representativeness once some sampling sites have been established. Representativeness resulting from such network "repairs" rarely ever equal the representativeness of a network initially designed *de novo* with that same number of sampling sites. Even if the network is to be constructed in stages, it is best to design site placement using the final, ultimate complement of sites and to operate sub-optimally until the full network can be completed. Otherwise, many more sites will have to be added to the existing network to achieve the same representativeness than could otherwise have been designed in initially.

Cluster analysis and n-dimensional data space regressions offer quantitative methods for up-scaling and extrapolating measurements to land areas within and beyond the sampling domain and provide a down-scaling approach to the integration of models, observations, and process studies. The success of these methods depends upon selecting appropriate surrogate environmental characteristics that covary with the observations and parameters that will be up- or down-scaled. The accuracy of the up-scaled data will be higher for areas represented well by the monitoring network and lower for areas that are poorly represented. At a large scale, these techniques are useful for delineating distinct, broad regions and optimal measurement sites. However, this methodology can also be applied at finer spatiotemporal scales, with inclusion of other geophysical characteristics and remote sensing data, to inform measurement frequency and site selection within these broader ecoregions.

Chapter 4

Climate and Atmospheric Composition Drivers of Terrestrial and Marine Carbon Cycle Changes from 1850 to 2300

4.1 Introduction

Quantifying the strength of climate–carbon cycle feedbacks is important for understanding the long-term responses and sustainability of natural and managed ecosystems to changes in climate and for informing carbon management and energy policies. Feedback sensitivities relating the global carbon cycle and Earth's climate system are traditionally decomposed into the response of land and ocean carbon uptake to changes in atmospheric CO_2 (the concentration–carbon feedback) and changes in climate (the climate–carbon feedback), using different types of simulations and experimental designs (*Friedlingstein et al.*, 2006; *Gregory*

et al., 2009). Concentration–carbon feedback sensitivities, denoted by β_O and β_L with units of $\mathrm{Pg\,C\,ppm^{-1}}$, quantify the changes in carbon accumulation in the ocean and on land, respectively, that result from ecosystem responses to a change in the atmospheric CO_2 mole fraction. Climate–carbon feedback sensitivities, denoted by γ_O and γ_L with units of $\mathrm{Pg\,C\,K^{-1}}$, quantify the changes in carbon storage that result from ocean and land responses to all of the changes in climate, which are characterized for the purposes of analysis by the change in near-surface air temperature. Following from *Friedlingstein et al.* (2006) and *Arora et al.* (2013), the overall climate–carbon feedback gain, g, can be related to these feedback sensitivity parameters through the following equation,

$$g = \frac{-\alpha\,(\gamma_O + \gamma_L)}{(m + \beta_O + \beta_L)}, \tag{4.1}$$

where α is the sensitivity of the global mean near-surface air temperature to cumulative changes in atmospheric CO_2 (usually referred to as the climate sensitivity) in units of $\mathrm{K\,ppm^{-1}}$, m is a constant ($2.12\ \mathrm{Pg\,C\,ppm^{-1}}$), and γ_O, γ_L, β_O, and β_L are defined above.

These feedback parameters are derived from Earth system model (ESM) experiments designed to isolate the climate and atmospheric CO_2 mole fraction responses. By holding atmospheric CO_2 constant for the terrestrial biosphere while simultaneously increasing CO_2 for atmospheric radiation computations, the temperature, precipitation, and related climate changes will be manifested, and simulated physical and ecological processes will respond only to those changes. Such radiatively coupled or RAD simulations are used to directly extract the climate–carbon feedback parameter, γ. In biogeochemically coupled or BGC simulations, atmospheric CO_2 is increased for the land and ocean biosphere while being held constant for atmospheric radiation calculations, stimulating direct biogeochemical responses due to rising CO_2 partial pressure. BGC simulations are used to directly compute the concentration–carbon feedback parameter, β. Radiative and biogeochemical coupling

are combined in fully coupled or FC simulations, which exhibit responses due to the net effects of rising temperatures and elevated atmospheric CO_2. If the climate–carbon and concentration–carbon effects combine linearly, the change in any variable in the FC simulation will be the same as the change in that variable in the RAD and the BGC experiments added together, which we write as,

$$\Delta\text{FC} = \Delta\text{RAD} + \Delta\text{BGC}. \tag{4.2}$$

Using results from a previous generation of climate models with coupled carbon cycle components that contributed to the first Coupled Climate–Carbon Cycle Model Intercomparison Project (C^4MIP) experiment, *Gregory et al.* (2009) extended this feedback analysis methodology and concluded that nonlinear interactions could be exhibited by different model experiments. They argued that γ diagnosed across different scenarios would yield similar results, and that γ is less sensitive to differences in simulation design than is β. Drawing upon the findings of *Gregory et al.* (2009), *Arora et al.* (2013) chose to use the γ calculated from the RAD simulations in their analysis of idealized 1% y^{-1} increasing CO_2 simulations from the fifth phase of the Coupled Model Intercomparison Project (CMIP5). This was different from *Friedlingstein et al.* (2006), who calculated γ as the difference between the FC and the BGC results from emissions-forced simulations in C^4MIP. *Arora et al.* (2013) and *Ciais et al.* (2013b) reported that land and ocean concentration–carbon sensitivity, β, was typically four to five times larger than climate–carbon sensitivity, γ, across CMIP5 ESMs. While the land and ocean concentration–carbon responses, β, contributed nearly equally to the overall concentration–carbon response, model spread was larger for β_L than for β_O. In addition, the land climate–carbon response, γ_L, was larger than the ocean climate–carbon response, γ_O, in all models. The magnitudes and model spread of both sets of land and ocean sensitivities, β and γ, declined from C^4MIP to CMIP5 due to changes in model parameterizations and

process representations in participating ESMs. However, models with a coupled terrestrial nitrogen cycle exhibited the weakest concentration–carbon and climate–carbon sensitivities, and increased the multi-model range of these feedback parameters. *Ciais et al.* (2013b) reiterated the *Gregory et al.* (2009) conclusion that γ is much less sensitive to scenario differences than β since both global temperature and carbon uptake lag the forcing. While *Arora et al.* (2013) quantified the carbon cycle feedbacks for land and ocean for a suite of CMIP5 models, those results were not used by either *Arora et al.* (2013) or *Ciais et al.* (2013b) to investigate the magnitude of nonlinear ecosystem responses in different models.

Studies of the evolution of the global carbon cycle and the climate over long time scales usually employ Earth system models of intermediate complexity (EMICs) (*Plattner et al.*, 2008; *Zickfeld et al.*, 2011). However, the detailed interactive multi-scale process representations in fully coupled ESMs make them ideally suited for such investigations. Uncertainties regarding the sustainability of tropical forests (*Cox et al.*, 2004; *Huntingford et al.*, 2013), variable rates of permafrost thaw and deepening of the active layer (*Koven et al.*, 2015), and slowdown of the Atlantic meridional overturning circulation (*Randerson et al.*, in press) require scenario testing in simulation experiments with explicit consideration of relevant dynamics over a period of multiple centuries. For example, nutrient cycling affects ocean and land carbon uptake and is controlled by climate, ecosystem productivity, and anthropogenic perturbations that alter nutrient inputs. Terrestrial ecosystem productivity and the resulting carbon sequestration potential may be overestimated in models that do not consider nitrogen and phosphorus limitation (*Wieder et al.*, 2015). Two CMIP5 models incorporated a coupled terrestrial carbon–nitrogen cycle, and their results suggest that nutrient limitation may buffer both climate and CO_2 concentration ecosystem responses (*Arora et al.*, 2013; *Ciais et al.*, 2013b). It may be important to capture the complex interactions of physical, chemical, and biological processes, such as these, that lead to thresholds or nonlinear behaviors that may be simulated only by rigorous, process-rich ESMs.

Zickfeld et al. (2011) employed both emissions-forced and concentration-driven simulations from an EMIC, the University of Victoria Earth System Climate Model (UVic ESCM), to explore carbon cycle nonlinearities both on land and in the ocean. They found that land was responsible for about 80% of the overall nonlinearity, while the ocean accounted for the remaining 20%. They further confirmed that concentration–forced simulations are better suited for deriving comparable feedback parameters than are emissions–forced simulations. More recently, *Schwinger et al.* (2014) analyzed the nonlinearity of ocean carbon cycle feedbacks in a collection of CMIP5 models and found that climate-induced carbon uptake reductions computed from the combination of FC and BGC simulations were stronger than those inferred from the RAD experiment. This result was attributable to increased stratification between the deep ocean and the mixed layer produced by climate warming that weakened the pathway for penetration of anthropogenic atmospheric CO_2 into the ocean. Consequently, the loss of carbon in the RAD simulation emanates primarily from the upper ocean, leading to an overall ocean climate–carbon feedback that effectively underestimates the reduction of ocean carbon uptake resulting from increased temperature and elevated CO_2.

To investigate the degree of linearity of these feedbacks, we analyzed results from three long-term simulations of the Community Earth System Model version 1.0 (CESM1(BGC)) with fully coupled ocean and land biogeochemical cycles (*Lindsay et al.*, 2014). These RAD, BGC, and FC simulations followed a business-as-usual future trajectory—comprised of historical, Representative Concentration Pathway 8.5 (RCP 8.5), and Extended Concentration Pathway 8.5 (ECP 8.5) forcing (*Meinshausen et al.*, 2011)—for increases in atmospheric CO_2, other greenhouse gases, and aerosols from the pre-industrial period to the end of the 23$^{\text{rd}}$ century (1850–2300). We quantified feedback parameters, century by century, and assessed land and ocean carbon cycle responses to anthropogenic atmospheric forcing agents in the absence of land use change. Unlike what *Schwinger et al.* (2014) concluded for the ocean, we found that land climate–carbon feedback sensitivities calculated from the RAD simulation

may overestimate the reduction of land carbon uptake under the combined conditions of increased temperature and elevated CO_2. No group has similarly investigated nonlinearities of the terrestrial carbon cycle from a contemporary ESM with fully interactive physical and biogeochemical processes.

4.2 Methods

4.2.1 Model description

We performed simulations using the Community Earth System Model version 1.0 (*Gent et al.*, 2011; *Hurrell et al.*, 2013) with fully interactive biogeochemical cycles enabled (*Lindsay et al.*, 2014). The model system configuration, referred to as CESM1(BGC), consisted of the Community Atmosphere Model version 4 (CAM4) (*Neale et al.*, 2013), the Community Land Model version 4 (CLM4) (*Lawrence et al.*, 2012a) with a coupled carbon–nitrogen cycle (*Thornton et al.*, 2007), an ocean physics component based on the Parallel Ocean Program version 2 (POP2) (*Smith et al.*, 2010; *Danabasoglu et al.*, 2012) with the Biogeochemical Elemental Cycling (BEC) module (*Moore et al.*, 2013), and a dynamic sea ice model (*Jahn et al.*, 2012; *Hunke et al.*, 2013). The multi-phase procedure for spin-up of CESM1(BGC) entailed performing independent spin-up simulations for the land and ocean models using a fixed pre-industrial atmospheric CO_2 mole fraction, followed by interactive ocean-land-atmosphere-sea ice simulations in which atmospheric CO_2 was allowed to evolve as a three dimensional tracer as described by *Lindsay et al.* (2014). Model spin-up was followed by a 1000-year control simulation designed to capture only natural climate variability and for which no anthropogenic perturbation was included.

The experiments described here were branched at year 151 of the control simulation, the same year simulations performed for CMIP5 were branched. The CMIP5 simulations are

available from the Earth System Grid Federation archive. Transient land cover change and wood harvesting, using land cover information derived from observations and future scenarios (*Hurtt et al.*, 2011), were enabled in CLM4's plant functional type framework (*Lawrence et al.*, 2012b) for years 1850 through 2100 in most CMIP5 simulations and in long-term simulations described by *Randerson et al.* (in press). However, land cover distributions were held constant and wood harvesting was disabled in the simulations described here. The performance of CESM1(BGC) is described in detail by *Long et al.* (2013) for the ocean carbon cycle and chlorofluorocarbons, by *Moore et al.* (2013) for ocean ecosystem dynamics and nutrient cycling, by *Keppel-Aleks et al.* (2013) for atmospheric CO_2, and by *Lindsay et al.* (2014) for seasonal and interannual cycles of atmospheric CO_2, surface fluxes, and their responses to El Niño-Southern Oscillation.

4.2.2 Experimental design

We conducted three CESM1(BGC) simulations with different coupling configurations, as shown in Table 4.1, following the CMIP5 protocol for concentration-forced historical (1850–2005), RCP 8.5 (2006–2100), and ECP 8.5 (2101–2300) trajectories of atmospheric CO_2 mole fractions, which increased from about 285 ppm in 1850 to 1962 ppm in 2300 (Figure 4.1(a) and Table 4.2). Biogeochemical processes and interactions were enabled in the ocean and land models, and terrestrial and marine ecosystems were allowed to respond to either static pre-industrial or transient forcing agents in the absence of land use change effects. In the RAD simulation, transient atmospheric CO_2, CH_4, chlorofluorocarbons, ozone, aerosols, and aerosol deposition on snow were all radiatively coupled, but the ocean and land experienced constant pre-industrial (1850) atmospheric CO_2 and nitrogen deposition forcing. In the BGC simulation, the radiative transfer scheme experienced pre-industrial (1850) CO_2 and other greenhouse gas mole fractions and aerosols, while the ocean and land were forced with transient trajectories of atmospheric CO_2 and nitrogen deposition. In the

Table 4.1: CESM1(BGC) simulations for three different coupling configurations were analyzed and are referenced as shown in the first column throughout this paper. All three 451-y simulations followed the CMIP5 Historical, RCP 8.5, and ECP 8.5 protocol (1850–2300) and were forced with the same prescribed CO_2 mole fraction trajectory as shown in Figure 4.1(a).

	Radiative Coupling		**Biogeochemical Coupling**		
Simulation Identifier	**CO_2**	**Other GHG & aerosols**	**CO_2**	**Nitrogen deposition**	**Land use**
RAD	✓	✓	–	–	–
BGC	–	–	✓	✓	–
FC	✓	✓	✓	✓	–

✓ Transient anthropogenic forcing
– Constant pre-industrial (1850) forcing

FC simulation, forcing agents were both radiatively and biogeochemically coupled, such that all model components experienced the same transient trajectories of atmospheric CO_2, other greenhouse gases, aerosols, and nitrogen deposition. The difference in responses between the FC and RAD experiments allowed us to quantify the impact of elevated atmospheric CO_2 levels on carbon cycle processes and estimate the concentration–carbon feedback parameters over time, which were subsequently compared to those parameters calculated directly from the BGC simulation. The difference in responses between the FC and BGC simulations allowed us to assess the impact of climate change on carbon cycle processes and estimate the climate–carbon feedback parameters over time, which were subsequently compared to those parameters calculated directly from the RAD simulation.

After analyzing feedback parameters from both emissions-forced and corresponding concentration-forced simulations, *Zickfeld et al.* (2011) advised using experiments with prescribed CO_2 mole fractions rather than prescribed emissions for deriving carbon cycle feedback parameters and exploring the mechanisms for nonlinear behaviors in those feedbacks. They found that the simultaneous effect of elevated CO_2 levels and climate change acted to reduce uptake in concentration-forced simulations, whereas it acted to increase uptake in runs with specified emissions (except for the land uptake between 2180 and 2300). The reason for these differences is that carbon sinks depend on atmospheric CO_2 mole fractions and land and

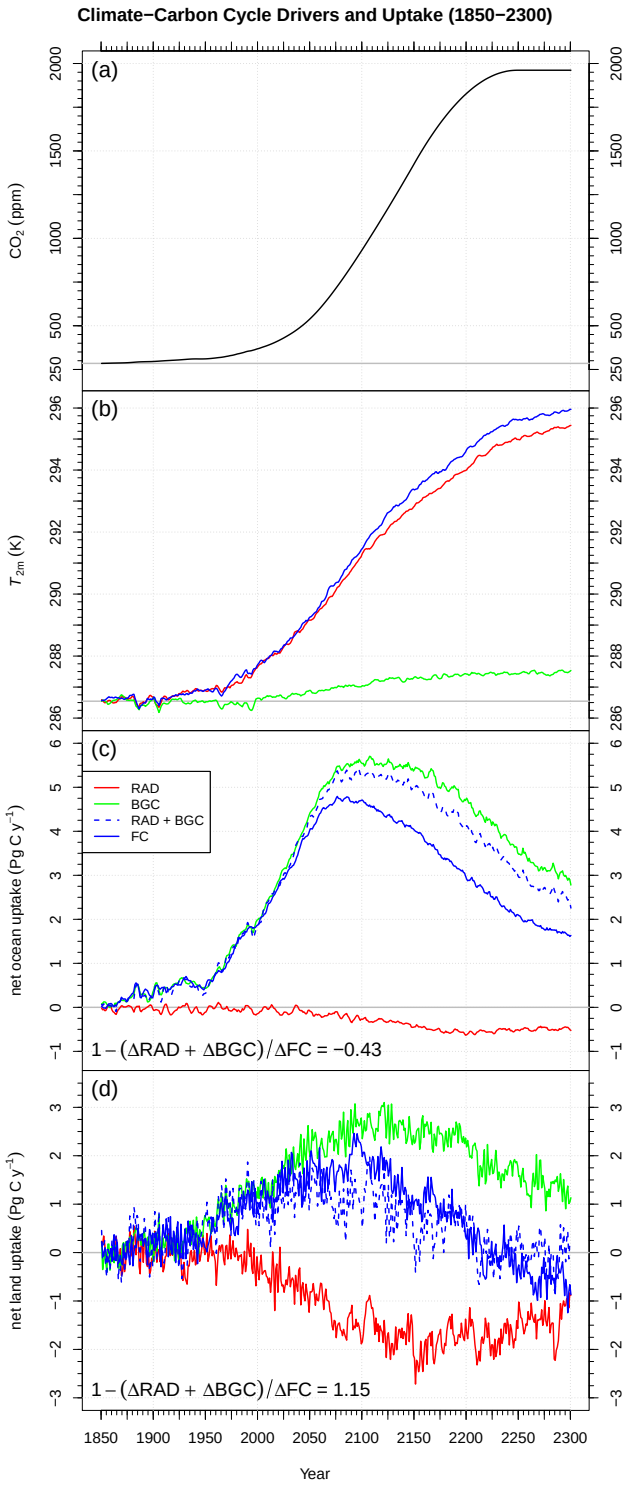

Figure 4.1: (a) The prescribed atmospheric CO_2 mole fraction was stabilized at 1962 ppm after 2225. (b) Near-surface air temperature increased in all three simulations by the end of the 23rd century. (c) Net ocean uptake decreased in the RAD simulation, but increased in the BGC and FC simulations. (d) Net land uptake was more variable than net ocean update, and it increased in the BGC and FC simulations and decreased in the RAD simulation.

Table 4.2: Cumulative carbon and temperature changes and corresponding compatible emissions were calculated for the 20th, 21st, 22nd, and 23rd centuries from the RAD, BGC, and FC simulations.

	Time (year)			
Variable	**2000**	**2100**	**2200**	**2300**
$[CO_2]_A$ (ppm)	369	936	1829	1962
	Time Period (years)			
Variable	**1850–2000**	**1850–2100**	**1850–2200**	**1850–2300**
$\Delta T_{2\,\mathrm{m}}^{\mathrm{RAD}}$ (K)	1.13	4.76	7.46	8.90
$\Delta T_{2\,\mathrm{m}}^{\mathrm{BGC}}$ (K)	0.10	0.50	0.87	0.99
$\Delta T_{2\,\mathrm{m}}^{\mathrm{FC}}$ (K)	1.19	4.92	8.11	9.41
$\Delta C_O^{\mathrm{RAD}}$ (Pg C)	−6	−19	−62	−113
$\Delta C_O^{\mathrm{BGC}}$ (Pg C)	100	519	1050	1414
ΔC_O^{FC} (Pg C)	97	475	866	1082
$\Delta C_L^{\mathrm{RAD}}$ (Pg C)	−8	−100	−275	−430
$\Delta C_L^{\mathrm{BGC}}$ (Pg C)	69	276	529	687
ΔC_L^{FC} (Pg C)	55	213	336	309
E_C^{RAD} (Pg C)	167	1265	2948	3023
E_C^{BGC} (Pg C)	349	2180	4862	5663
E_C^{FC} (Pg C)	331	2072	4486	4955

ocean uptake compensate for each other, which can lead to persistent biases in prognostic atmospheric CO_2 (*Hoffman et al.*, 2014) and result in different CO_2 trajectories across experiments. Here, we analyzed simulations forced with prescribed CO_2 mole fractions to allow for rigorous separation of feedback processes. Land use change can similarly confound analysis of carbon cycle feedbacks. *Zickfeld et al.* (2011) reported that in the absence of CO_2 fertilization, widespread replacement of forests by C_4 grasses, which are more productive than forests, reduced the negative effect of climate change on land carbon uptake. Our more-idealized experiments avoided confounding effects of land use change by enforcing a static, pre-industrial distribution of vegetation and disabling wood harvest processes.

Important hydrological and biogeochemical model output variables, listed in Table 4.3, from all three simulations were analyzed over the entire 451 y period to diagnose the climate change and increasing anthropogenic atmospheric CO_2 impacts on terrestrial and marine ecosystems as well as the hydrological cycle. Except where noted, a 5 y center-mean smoothing was applied to all variable line plots, and a gray-colored horizontal baseline is plotted at the y-axis value that represents the average of the initial 5 y means of the variable from the RAD and BGC experiments. Decadal means from the end of the simulation period were subtracted from decadal means at the beginning of the simulation period to spatially map changes in output variables. To show spatial distributions of temporal changes in variables across experiments and to diagnose nonlinear responses in those variables (i.e., where Equation (4.2) did not hold exactly), maps are shown in a 3×3 arrangement as exemplified in Figure 4.2. As in Equation (4.2), ΔFC represents the change in a variable over time from the FC simulation, ΔRAD represents the change in a variable over time from the RAD simulation, and ΔBGC represents the change in a variable over time from the BGC simulation. If the ESM responses to climate change and increasing atmospheric CO_2 levels were linear (i.e., Equation (4.2) held exactly) across the time scale of these simulations, then, in Figure 4.2, panel (f) would be a white map, panel (c) would be identical to panel (h), and panel (i) would be identical to panel (b).

Table 4.3: The energy, nitrogen, water, and carbon variables shown here were the primary drivers of hydrological and ecological changes in the RAD, BGC, and FC simulations. The change in each variable from 1850 to 2300 is shown for the RAD and BGC simulations, the sum of the RAD + BGC results, and the FC simulation. The nonlinear metric, contained in the last column, is shown in either red or green, depending on whether the RAD or the BGC coupling contributed most to change in the FC simulation. This same information is presented graphically in Figure 4.15.

Variable	Abbreviated Name	ΔRAD	ΔBGC	(ΔRAD+ ΔBGC)	ΔFC	Units	Nonlinear Metric
Energy and Nitrogen Variables							
air temperature at 2 m	T at 2m	8.85	0.95	9.80	9.33	K	−0.05
sensible heat	SH	4.46	9.38	13.84	12.66	W/m^2	−0.09
latent heat	LH	6.39	−7.57	−1.18	0.62	W/m^2	2.91
net N mineralization	N mineral	−0.03	0.29	0.26	0.29	Pg N/y	0.10
Water Variables							
precipitation	Precip	0.48	0.02	0.50	0.53	mm/d	0.06
relative humidity at 2 m	RH at 2m	−4.24	−3.63	−7.86	−6.78	%	−0.16
precipitation minus evapotranspiration	P − ET	0.26	0.28	0.54	0.51	mm/d	−0.06
evapotranspiration	ET	0.22	−0.26	−0.04	0.02	mm/d	2.83
transpiration	Transp	0.03	−0.29	−0.26	−0.17	mm/d	−0.55
soil moisture to 1 m	SMoist	0.47	2.28	2.74	2.25	mm	−0.22
total liquid runoff	Runoff	0.25	0.29	0.54	0.50	mm/d	−0.07
Carbon Variables							
gross primary production	GPP	−7.73	82.54	74.80	99.56	Pg C/y	0.25
net primary production	NPP	−8.94	24.33	15.39	19.07	Pg C/y	0.19
ecosystem respiration	ER	−6.09	81.05	74.96	99.26	Pg C/y	0.24
heterotrophic respiration	HR	−7.29	22.84	15.55	18.77	Pg C/y	0.17
total leaf area index	LAI	−0.39	1.60	1.20	1.19	unitless	−0.01
cumulative net biome production	C_L storage	−428.90	685.25	256.34	310.40	Pg C	0.17
cumulative DIC gas flux	C_O storage	−113.43	1413.99	1300.56	1081.61	Pg C	−0.20

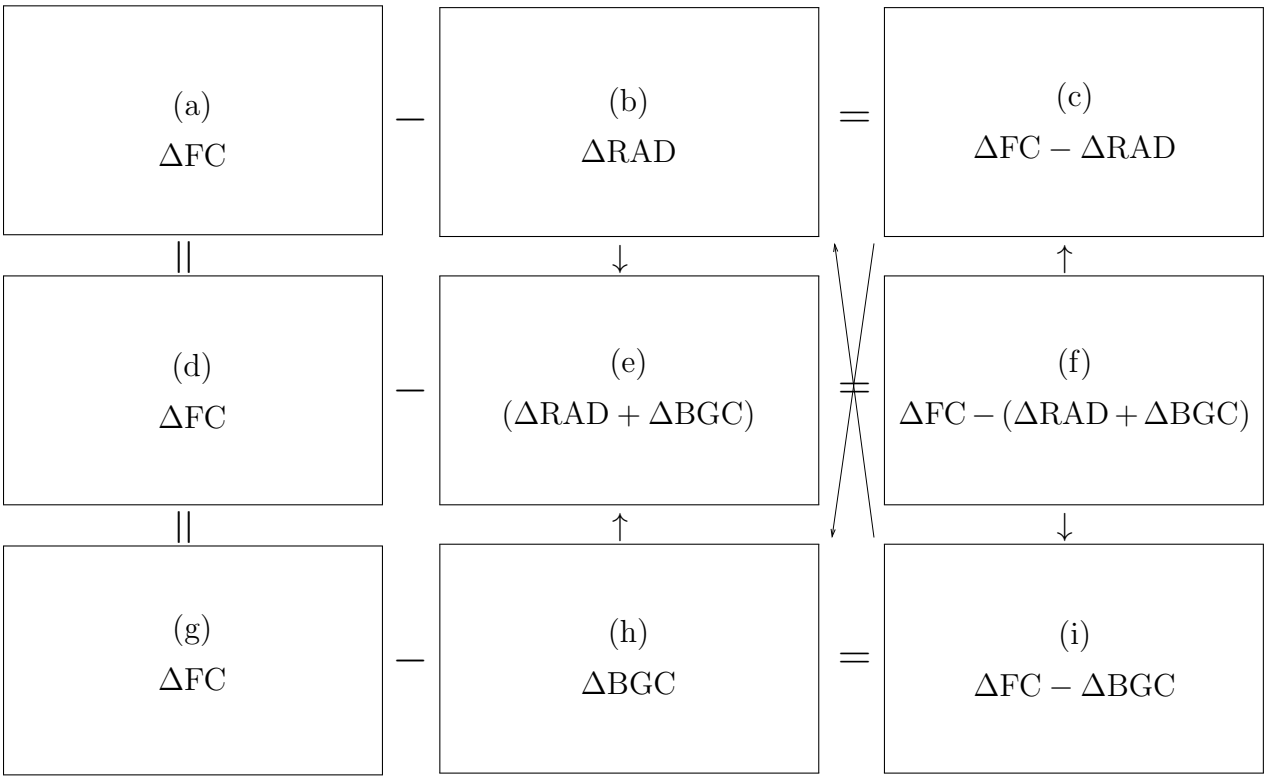

Figure 4.2: Maps comparing changes in variables across experiments are presented in three columns, where the first column (panels a, d, and g) show the (identical) change in the FC simulation, panel (b) shows the change in the RAD simulation, panel (h) shows the change in the BGC simulation, panel (e) shows the sum of the changes in the RAD plus BGC simulations, and the third column (panels c, f, and i) show the difference between the first column and the second column. If the ESM responses to climate change and increasing atmospheric CO_2 levels were linear across the simulation time scale, then panel (f) would be a white map, panel (c) would be identical to panel (h), and panel (i) would be identical to panel (b).

4.2.3 Carbon cycle feedback metrics

For C^{4}MIP, *Friedlingstein et al.* (2006) defined the overall climate–carbon cycle feedback in terms of the ratio of the changes in atmospheric CO_2 from FC and BGC simulations. The ocean and land feedback parameters were defined in terms of the influences of the atmospheric CO_2 and temperature changes in ocean and land carbon storage as follows,

$$\Delta C_O^{\mathrm{FC}} = \beta_O \Delta \mathrm{CO}_2^{\mathrm{FC}} + \gamma_O \Delta T^{\mathrm{FC}}, \tag{4.3}$$

$$\Delta C_L^{\mathrm{FC}} = \beta_L \Delta \mathrm{CO}_2^{\mathrm{FC}} + \gamma_L \Delta T^{\mathrm{FC}}, \tag{4.4}$$

where the feedback parameters (β_O, β_L, γ_O, and γ_L) are the same as defined above. The strengths of these sensitivities were found by first solving for β_O and β_L from a radiatively uncoupled simulation,

$$\beta_O^{\mathrm{BGC}} = \frac{\Delta C_O^{\mathrm{BGC}}}{\Delta \mathrm{CO}_2^{\mathrm{BGC}}}, \tag{4.5}$$

$$\beta_L^{\mathrm{BGC}} = \frac{\Delta C_L^{\mathrm{BGC}}}{\Delta \mathrm{CO}_2^{\mathrm{BGC}}}, \tag{4.6}$$

then solving for γ_O and γ_L from the fully coupled simulation as follows,

$$\gamma_O^{\mathrm{FC-BGC}} = \frac{\Delta C_O^{\mathrm{FC}} - \beta_O \Delta \mathrm{CO}_2^{\mathrm{FC}}}{\Delta T^{\mathrm{FC}}}, \tag{4.7}$$

$$\gamma_L^{\mathrm{FC-BGC}} = \frac{\Delta C_L^{\mathrm{FC}} - \beta_L \Delta \mathrm{CO}_2^{\mathrm{FC}}}{\Delta T^{\mathrm{FC}}}. \tag{4.8}$$

Gregory et al. (2009) extended the carbon cycle feedback methodology and described ways to estimate feedback sensitivity parameters from different model experiments, including cal-

culating the climate–carbon feedback parameters directly from RAD simulations as follows,

$$\gamma_O^{\mathrm{RAD}} = \frac{\Delta C_O^{\mathrm{RAD}}}{\Delta T^{\mathrm{RAD}}}, \tag{4.9}$$

$$\gamma_L^{\mathrm{RAD}} = \frac{\Delta C_L^{\mathrm{RAD}}}{\Delta T^{\mathrm{RAD}}}. \tag{4.10}$$

Arora et al. (2013, their Appendix A) outlined three approaches for estimating concentration–carbon and climate–carbon feedbacks from FC, RAD, and BGC experiments, which they derived for emission-driven and concentration-forced experiments in a companion publication (*Boer and Arora*, 2013). *Schwinger et al.* (2014, their Appendix A) derived formulas for calculating feedback parameters from a pair of model experiments, and their simplified approximations, when the temperature change in the BGC experiment is small ($\Delta T^{\mathrm{BGC}} \approx 0$) and/or the temperature change in the FC and RAD experiments are approximately equal ($\Delta T^{\mathrm{FC}} \approx \Delta T^{\mathrm{RAD}}$). For two model experiments, E1 and E2, with different trajectories of CO_2 and temperature (T) and full or partial coupling of CO_2 and temperature change in at least one of the experiments, the changes in ocean and land carbon storage are given by

$$\Delta C^{\mathrm{E1}} = \beta \Delta \mathrm{CO}_2^{\mathrm{E1}} + \gamma \Delta T^{\mathrm{E1}}, \tag{4.11}$$

$$\Delta C^{\mathrm{E2}} = \beta \Delta \mathrm{CO}_2^{\mathrm{E2}} + \gamma \Delta T^{\mathrm{E2}}. \tag{4.12}$$

Solving for the feedback parameters gives

$$\beta^{\mathrm{E1-E2}} = \frac{\left(\Delta C^{\mathrm{E1}} \Delta T^{\mathrm{E2}} - \Delta C^{\mathrm{E2}} \Delta T^{\mathrm{E1}}\right)}{\left(\Delta \mathrm{CO}_2^{\mathrm{E1}} \Delta T^{\mathrm{E2}} - \Delta \mathrm{CO}_2^{\mathrm{E2}} \Delta T^{\mathrm{E1}}\right)}, \tag{4.13}$$

$$\gamma^{\mathrm{E1-E2}} = \frac{\left(\Delta C^{\mathrm{E2}} \Delta \mathrm{CO}_2^{\mathrm{E1}} - \Delta C^{\mathrm{E1}} \Delta \mathrm{CO}_2^{\mathrm{E2}}\right)}{\left(\Delta \mathrm{CO}_2^{\mathrm{E1}} \Delta T^{\mathrm{E2}} - \Delta \mathrm{CO}_2^{\mathrm{E2}} \Delta T^{\mathrm{E1}}\right)}, \tag{4.14}$$

where the denominators for each are the same. Using this formulation, we can determine the concentration–carbon feedback parameters from the FC and RAD simulations as follows,

$$\beta^{\mathrm{FC-RAD}} = \frac{\Delta C^{\mathrm{FC}} \Delta T^{\mathrm{RAD}} - \Delta C^{\mathrm{RAD}} \Delta T^{\mathrm{FC}}}{\Delta \mathrm{CO}_2 \, \Delta T^{\mathrm{RAD}}} \approx \frac{\Delta C^{\mathrm{FC}} - \Delta C^{\mathrm{RAD}}}{\Delta \mathrm{CO}_2}, \tag{4.15}$$

where atmospheric CO_2 is constant for the RAD simulation ($\Delta \mathrm{CO}_2^{\mathrm{RAD}} = 0$) and the approximation holds when the temperature change in the FC simulation is about the same as in the RAD simulation ($\Delta T^{\mathrm{FC}} \approx \Delta T^{\mathrm{RAD}}$). Likewise, we can determine the climate–carbon feedback parameters as follows,

$$\gamma^{\mathrm{FC-BGC}} = \frac{\Delta C^{\mathrm{BGC}} - \Delta C^{\mathrm{FC}}}{\Delta T^{\mathrm{BGC}} - \Delta T^{\mathrm{FC}}} \approx \frac{\Delta C^{\mathrm{FC}} - \Delta C^{\mathrm{BGC}}}{\Delta T^{\mathrm{FC}}}, \tag{4.16}$$

where the approximation holds when the temperature change in the BGC simulation is small ($\Delta T^{\mathrm{BGC}} \approx 0$). Since the change in temperature is a surrogate for all of the effects of climate change, this condition implicitly requires that all climate change effects are negligible in the BGC simulation. Note that this approximate form is equal to the result obtained when substituting Equation (4.5) into Equation (4.7) and Equation (4.6) into Equation (4.8) since the ocean and land experience the same trajectory of anthropogenic atmospheric CO_2 in the FC and BGC simulations ($\Delta \mathrm{CO}_2^{\mathrm{FC}} = \Delta \mathrm{CO}_2^{\mathrm{BGC}}$).

To investigate the degree of nonlinearity in climate–carbon cycle feedbacks, we compared the time evolution of concentration–carbon and climate–carbon feedback parameters, derived both from partially coupled experiments and from differences with the fully coupled experiment, across the four centuries of simulation. Specifically, we compared the concentration–carbon feedback sensitivities calculated from Equations (4.5) and (4.6) with those derived from Equation (4.15), referred to as $\beta_O^{\mathrm{FC-RAD}}$ and $\beta_L^{\mathrm{FC-RAD}}$. In addition, we compared the

climate–carbon feedback sensitivities estimated from Equations (4.9) and (4.10) with those derived from Equation (4.16), referred to as $\beta_O^{\mathrm{FC-BGC}}$ and $\beta_L^{\mathrm{FC-BGC}}$. We used these feedback parameters in different combinations to calculate the overall climate–carbon cycle feedback gain, g, for each century time interval from Equation (4.1). Following the method described by *Arora et al.* (2013), we calculated trajectories of compatible emissions from the RAD, BGC, and FC experiments. We used the compatible emissions to compute the gain for the same century time intervals, following Equation (13) from *Arora et al.* (2013),

$$g = \frac{E_C^{\mathrm{BGC}} - E_C^{\mathrm{FC}}}{E_C^{\mathrm{BGC}}}, \tag{4.17}$$

and compared that gain with those obtained from combinations of simulation experiments, following Equation (4.1). Feedback parameter choices responsible for divergence among these gains indicated which experiments were the largest sources of nonlinearity and suggested whether source or sink processes were the underlying drivers in ocean and land model responses.

4.2.4 Nonlinearity metric

We developed a metric to gauge the nonlinearity of energy, carbon, nitrogen, and hydrology drivers of model responses to increasing atmospheric CO_2 and resultant climate change across the full period of simulation. This metric is defined as one minus the ratio of the sum of the output variable change in the RAD and BGC simulations from 1850–2300, divided by the corresponding change of the variable in the FC simulation, as follows:

$$M_{NL} = 1 - \frac{(\Delta\mathrm{RAD} + \Delta\mathrm{BGC})}{\Delta\mathrm{FC}}. \tag{4.18}$$

This metric considers only the beginning and end points of the analysis period for the output variable time series, and, therefore, ignores any transient nonlinear effects that may be eliminated by the end of the analysis period.

4.3 Results

4.3.1 Temperature and carbon storage changes

Global mean near-surface air temperature increased by 9.4 K between 1850 and 2300 in the fully coupled (FC) model simulation (Figure 4.1(b) and Table 4.2). Over the same period, temperature increased by 8.9 K in the radiatively coupled (RAD) simulation. Therefore, we attributed 8.9 K of the warming in the FC simulation to direct radiative effects, while the remaining 0.5 K should be attributed to the effects of increasing nitrogen deposition and rising atmospheric CO_2 on the terrestrial biosphere and marine biogeochemistry. However, in the biogeochemically coupled simulation (BGC), the temperature increased by 1.0 K, a relatively small amount, but twice that expected from subtracting the temperature change in the RAD simulation from that in the FC simulation, (ΔFC $-$ ΔRAD), following Equation (4.2). The temperature increase due to biogeochemical coupling in the FC and BGC simulations was a consequence of changes in stomatal conductance and leaf area in response to elevated atmospheric CO_2. As we will discuss below, the 0.5 K difference between the (ΔFC $-$ ΔRAD) and the ΔBGC temperatures was due to stronger gross primary production (GPP) in the FC simulation that produced enhanced leaf area over the 22$^{\text{nd}}$ and most of the 23$^{\text{rd}}$ centuries. Between 1850 and 2300, mean near-surface air temperature over land increased by 11.7 K in the FC simulation, by 10.8 K in the RAD simulation, and by 1.5 K in the BGC simulation (Figure 4.3(a)). The largest temperature increases in the FC simulation occurred at high latitudes, with some land regions exhibiting temperature changes as large as

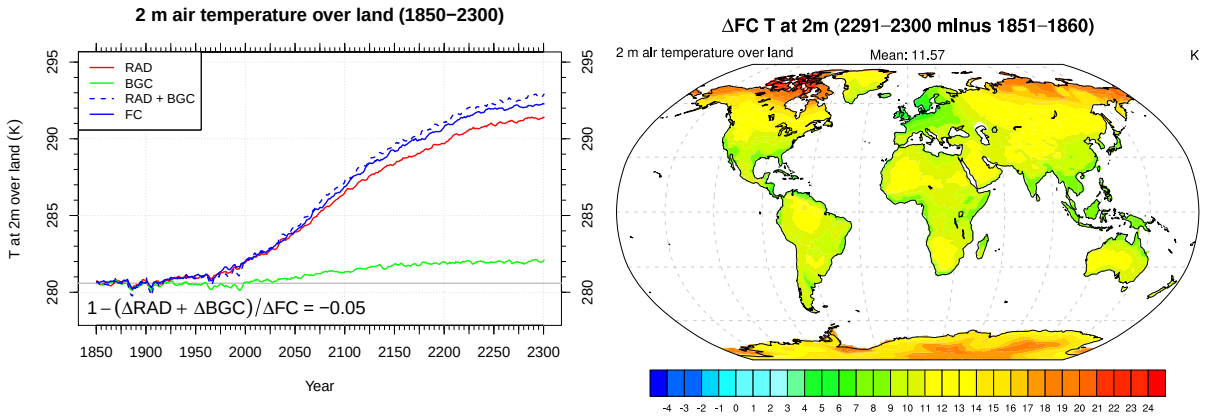

(a) Trajectories of 2 m air temperature over land for the RAD, BGC, and FC simulations

(b) Spatial distribution of change in 2 m air temperature over land in the FC simulation

Figure 4.3: The mean 2 m air temperature over land increased by 11.6 K between 1850 and 2300 under the combined effects of increased atmospheric CO_2 and consequent climate change.

25 K (Figure 4.3(b)). Northern Europe showed some of the smallest temperature increases, likely due to the slowdown of the Atlantic meridional overturning circulation (AMOC) in the 22$^{\text{nd}}$ and 23$^{\text{rd}}$ centuries (*Randerson et al.*, in press). The (ΔRAD + ΔBGC) temperature over land, which represents the combination of temperature changes from the effects of climate change simulated separately from CO_2 and N fertilization, was larger than the ΔFC temperature over land by 0.6 K. The nonlinearity metric, calculated from Equation (4.18), was -0.05, indicating that the (ΔRAD + ΔBGC) temperature increase was 5% larger than the ΔFC temperature increase at 2300.

Ocean and land rates of carbon uptake were reduced in response to climate change and the absence of elevated atmospheric CO_2. Under these conditions, ocean uptake rates dropped slowly and stabilized in the 23$^{\text{rd}}$ century, while rates of land uptake dropped rapidly after year 2000 then rose modestly during the 23$^{\text{rd}}$ century. Meanwhile, rising atmospheric CO_2 increased ocean and land uptake rates, with and without the influence of climate change, from the pre-industrial through the 21$^{\text{st}}$ century (Figure 4.1(c) and 4.1(d)). Under elevated CO_2, both ocean and land rates of uptake declined after year 2100; however, their maxima were

lower and they began declining earlier due to climate change. In response to radiative forcing and elevated CO_2, terrestrial rates of uptake declined more rapidly than in the absence of climate change. After 2100, ocean uptake rates estimated for the combination of climate change and CO_2 increase from the addition of the RAD and BGC simulation responses were larger than those produced in the FC simulation, averaging about 40–45% higher than FC uptake rates after 2150. Under elevated CO_2, the rate of land uptake declined more rapidly due to climate change than it did without radiative forcing. Moreover, it dropped below zero after 2225, when the atmospheric CO_2 mole fraction was stabilized at 1962 ppm. The net land uptake rate under climate change and elevated CO_2 estimated from the combination of RAD and BGC responses was slightly positive, approximately 0.14 $\mathrm{Pg\,C\,y^{-1}}$, while for the FC simulation it was about -0.92 $\mathrm{Pg\,C\,y^{-1}}$. The nonlinearity metric for net land uptake was 1.15, indicating that the (ΔRAD + ΔBGC) response was 15% larger than the fully coupled response.

Net ocean carbon storage, calculated as the cumulative net ocean uptake since 1850, decreased throughout the 451 y simulation period due to anthropogenic climate change in the absence of elevated atmospheric CO_2 (Figure 4.4(a) and Table 4.2). By the end of the RAD simulation, the ocean lost 113 Pg C, primarily at tropical and subtropical latitudes and from the Southern Ocean (Figure 4.4(d)). Including the ameliorating effects of increased atmospheric CO_2 with climate change, net ocean carbon storage increased throughout the simulation, with 56% of the anthropogenic carbon storage occurring after 2100. At the end of the FC simulation, the ocean accumulated 1082 Pg C, predominantly at mid- and high latitudes (Figure 4.4(c)). Without climate change, net ocean carbon storage rose more strongly than in the FC simulation after 2050 and ended 23% higher at 2300, with 1414 Pg of anthropogenic carbon accumulated. Cumulative uptake was stronger in the BGC simulation than in the FC simulation (Figure 4.4(b)). The (ΔRAD + ΔBGC) ocean carbon storage was 20% greater than the accumulation from the ΔFC simulation at 2300, indicating that marine responses to climate change and to elevated atmospheric CO_2 do not combine linearly.

When estimated from the difference between the FC and BGC simulations (ΔFC $-$ ΔBGC), the implied effect of climate change only on net ocean carbon storage was -332 Pg C, a loss nearly three times larger than that exhibited by the RAD simulation. This result is consistent with that of *Schwinger et al.* (2014), who attributed nonlinear ocean carbon cycle responses in CMIP5 models primarily to reduced carbon losses in climate change simulations as a consequence of warming-induced weakening of ocean circulation and mixing.

In response to climate change, net land carbon storage declined strongly, with 76% of the loss occurring after 2100 (Figure 4.5(a) and Table 4.2). The climate change-induced loss totaled 430 Pg C at 2300, and originated principally from tropical forests and secondarily from subtropical forests (Figure 4.5(d)). In contrast, when computed as the difference between the FC and BGC simulations (ΔFC $-$ ΔBGC), the terrestrial biosphere lost 378 Pg C as a result of increasing temperatures, suggesting the RAD simulation may overestimate land carbon losses. Under climate change and elevated CO_2, land sequestered 309 Pg of anthropogenic carbon by 2300, primarily in tropical forests and in southeast Asia, while losses occurred in northeast South America (Figure 4.5(c)) due to drying that resulted from atmospheric circulation changes, a phenomenon consistent across a majority of CMIP5 model projections (*Stocker et al.*, 2013a; *Lau and Kim*, 2015) In the absence of radiative forcing, elevated atmospheric CO_2 fueled strong land carbon accumulation, especially in tropical and subtropical forests, which reached 687 Pg C at 2300 (Figure 4.5(b)). Terrestrial biosphere responses to climate change and elevated CO_2 separately did not combine linearly, but resulted in weaker carbon accumulation on land after 2050 and ended 17% below that of the fully coupled simulation. After 2050, about 52 Pg (20%) more anthropogenic carbon was accumulated on land under the combined effects of elevated CO_2 and climate change than under the linear combination of the two. This is in contrast to the report of *Zickfeld et al.* (2011), whose EMIC results indicated that the carbon sinks on land were less efficient when exposed to the combined effects than to their linear combination, likely due primarily to conversion of forests at low latitudes to more productive C_4 grasses that are associated with higher soil

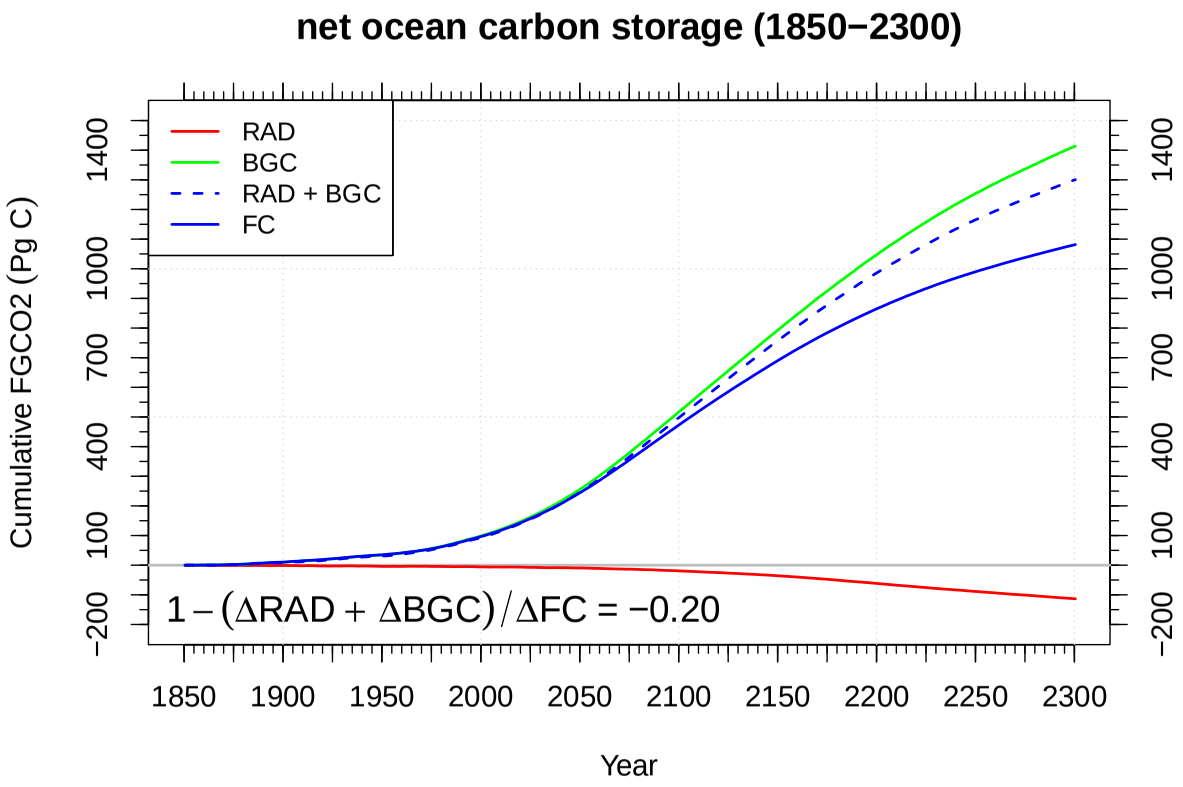

(a) Cumulative net ocean carbon storage for the simulation period (1850–2300)

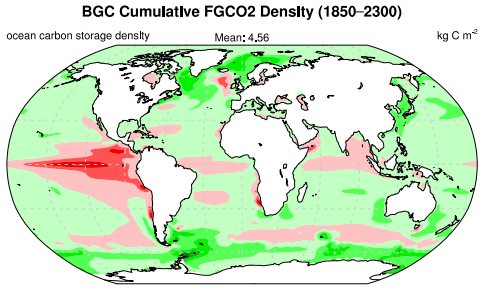

(b) Biogeochemically coupled (BGC)

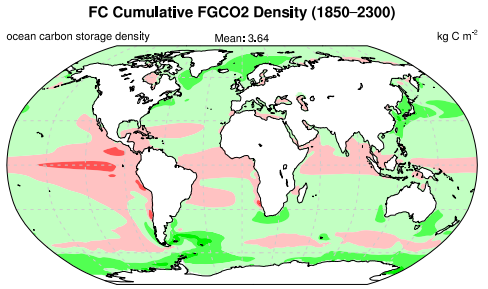

(c) Fully coupled (FC)

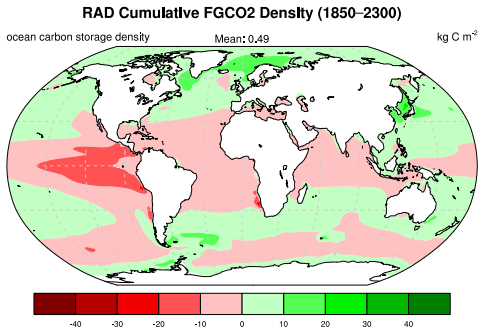

(d) Radiatively coupled (RAD)

Figure 4.4: (a) Net ocean carbon storage, calculated as the spatial integral of net ocean production, temporally integrated from 1850 to 2300 for (b) the biogeochemically coupled (BGC) simulation was 1414 Pg C, for (c) the fully coupled (FC) simulation was 1082 Pg C, and for (d) the radiatively coupled (RAD) simulation was −113 Pg C.

carbon in the *Zickfeld et al.* (2011) radiatively coupled simulations.

Carbon uptake responses to elevated CO_2 and climate change will determine anthropogenic emissions compatible with a given CO_2 concentration pathway (*Jones et al.*, 2013). The resulting diagnosed cumulative emissions may be used to evaluate the overall climate–carbon cycle feedback gain and may also be determined from feedback parameters (*Arora et al.*, 2013). Compatible emissions, E_C, diagnosed from the evolving ocean, land, and atmosphere carbon inventories, were lowest for the warming-only simulation and largest for the increasing atmospheric CO_2 simulation (Table 4.2). Under the combined conditions of warming and elevated CO_2, compatible emissions began to diverge slowly from those diagnosed for the BGC simulation and were reduced by 12% at 2300, from 5663 Pg C in the BGC simulation to 4955 Pg C in the FC simulation. Most of the reduction occurred after the atmospheric CO_2 mole fraction was stabilized around 2225.

4.3.2 Climate–carbon cycle feedback parameters

To investigate the effects of nonlinear uptake responses on the climate–carbon cycle feedback gain, we derived evolving climate–carbon and concentration–carbon feedback parameters for the ocean and land in multiple ways, using individual simulations and combinations of them as described above. The ocean concentration–carbon feedback declined during the 21st and 22nd centuries, with β_O^{BGC} decreasing from 0.80 Pg C ppm^{-1} at 2100 to 0.68 Pg C ppm^{-1} at 2200 (Figure 4.6(a) and Table 4.4), likely as a consequence of diminished buffering capacity of the oceans with increasing pCO_2, often expressed as an increasing Revelle factor (*Sabine et al.*, 2004). During the 23rd century, when atmospheric CO_2 rose slowly toward stabilization at 1962 ppm, β_O increased because ocean mixing processes had more time to adjust to rising pCO_2. The ocean concentration–carbon feedback derived from the FC and RAD simulations, $\beta_O^{\mathrm{FC-RAD}}$, exhibited a similar trajectory to β_O^{BGC}. However, $\beta_O^{\mathrm{FC-RAD}}$ declined

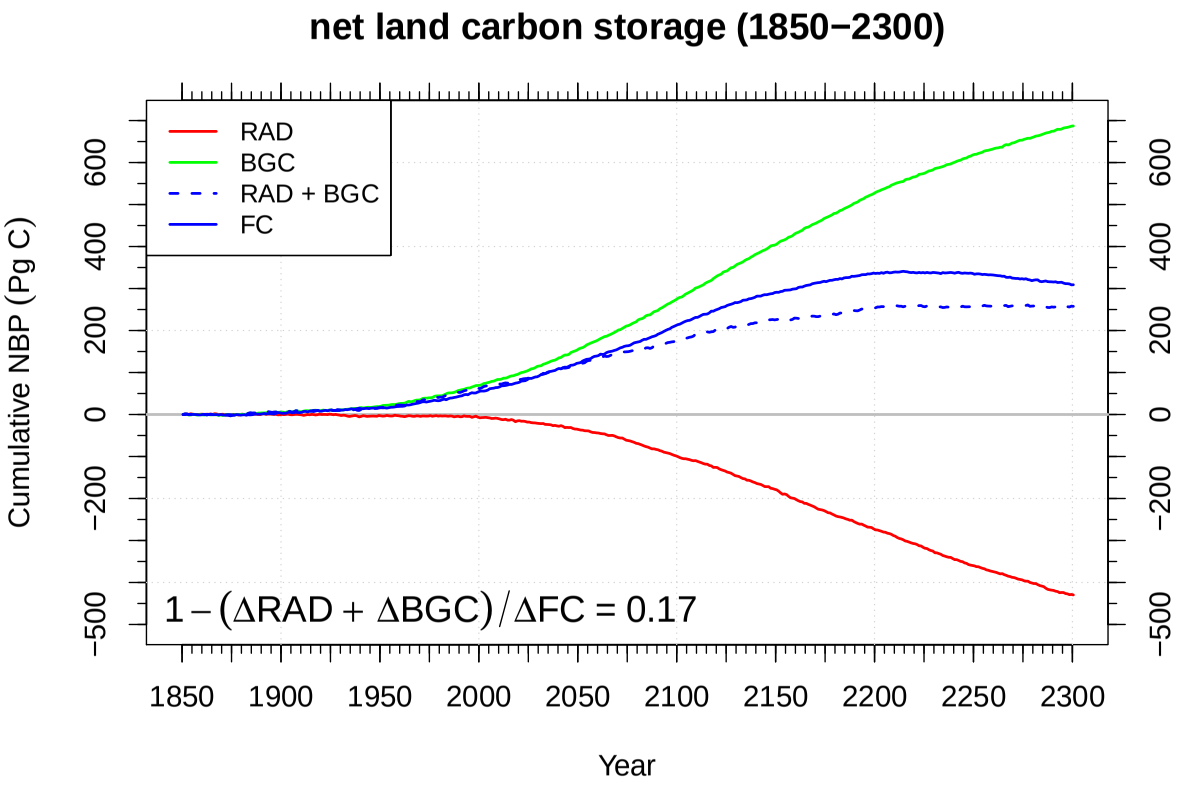

(a) Cumulative net land carbon storage for the simulation period (1850–2300)

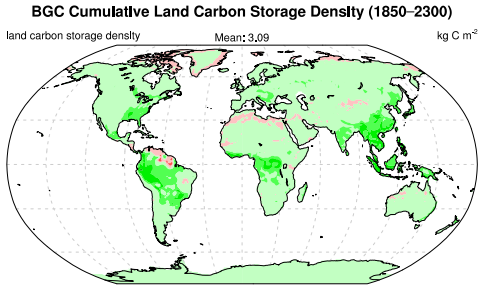

(b) Biogeochemically coupled (BGC)

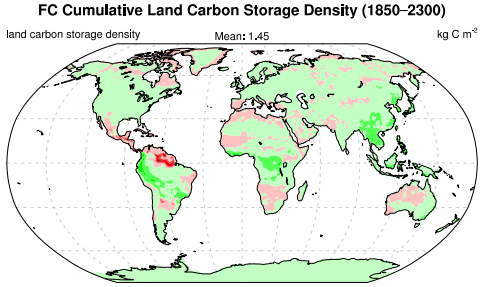

(c) Fully coupled (FC)

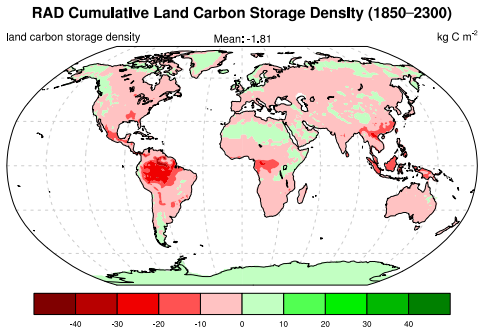

(d) Radiatively coupled (RAD)

Figure 4.5: (a) Net land carbon storage, calculated as the spatial integral of net land biosphere production, temporally integrated from 1850 to 2300 for (b) the biogeochemically coupled (BGC) simulation was 687 Pg C, for (c) the fully coupled (FC) simulation was 309 Pg C, and for (d) the radiatively coupled (RAD) simulation was −430 Pg C.

from β_O^{BGC} nearly linearly, likely as a consequence of increasing stratification that weakened the coupling between the surface waters and deeper water masses, further increasing the Revelle factor, in the warming-only simulation. Ocean regions at higher latitudes, especially the Southern Ocean, exhibited the strongest positive sensitivities to increasing $p\mathrm{CO}_2$ (Figure 4.6(c)). When calculated directly from the warming-only simulation, the sensitivity of ocean carbon uptake to temperature, γ_O^{RAD}, strengthened by a factor of 3, changing from $-4.06\ \mathrm{Pg\,C\,K^{-1}}$ in 2100 to $-12.69\ \mathrm{Pg\,C\,K^{-1}}$ in 2300 (Figure 4.6(b) and Table 4.4). However, this same sensitivity increased by a factor of 4 when estimated from the FC and BGC simulations, $\gamma_O^{\mathrm{FC-RAD}}$, changing from $-10.06\ \mathrm{Pg\,C\,K^{-1}}$ at 2100 to $-39.37\ \mathrm{Pg\,C\,K^{-1}}$ at 2300. This difference is attributable to temperature-driven reduction in ocean mixing and reduction in dissolved inorganic carbon (DIC) solubility (i.e., weakening of the solubility pump), which served to limit exchange of carbon with deeper water masses, in the climate change simulation. Tropical to sub-tropical ocean regions, particularly the equatorial Pacific, as well as the Southern Ocean, exhibited the strongest negative sensitivities to increasing temperature (Figure 4.6(d)).

On land, the sensitivity of carbon uptake to increasing atmospheric CO_2 mole fractions calculated directly from the BGC simulation, β_L^{BGC}, declined 19% in the 22$^{\mathrm{nd}}$ century, dropping from $0.42\ \mathrm{Pg\,C\,ppm^{-1}}$ at 2100 to $0.34\ \mathrm{Pg\,C\,ppm^{-1}}$ at 2200, before returning to $0.41\ \mathrm{Pg\,C\,ppm^{-1}}$ at 2300 (Figure 4.7(a) and Table 4.4). During the 23$^{\mathrm{rd}}$ century, the terrestrial biosphere was better able to sequester additional anthropogenic carbon when the growth rate was lower because vegetation and soil carbon pools had more time to adjust to rising CO_2 levels. When derived from the FC and RAD simulations, this sensitivity, $\beta_L^{\mathrm{FC-RAD}}$, was slightly stronger after 2100 as a result of strong ecosystem productivity enhancements under the combined conditions of climate change and elevated atmospheric CO_2. Tropical and sub-tropical forests exhibited the largest positive sensitivity to rising atmospheric CO_2 (Figure 4.7(c)). The climate–carbon feedback sensitivity on land, when calculated from the warming-only simulation, γ_L^{RAD}, strengthened rapidly after 2000, reaching

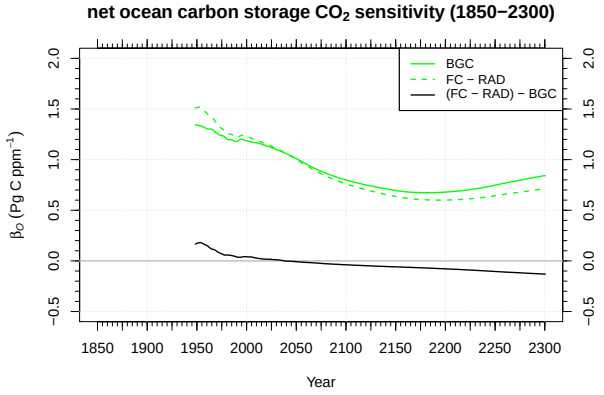

(a) Concentration–carbon sensitivity, β_O

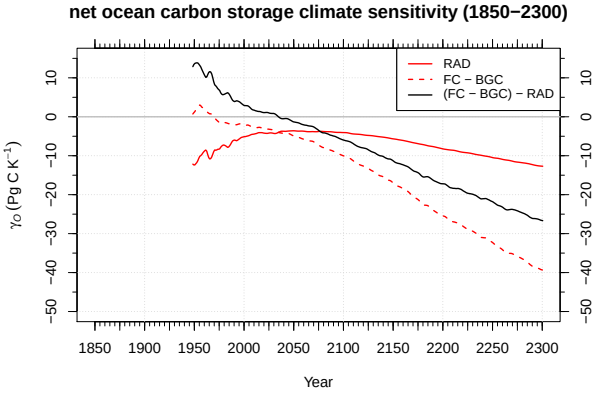

(b) Climate–carbon sensitivity, γ_O

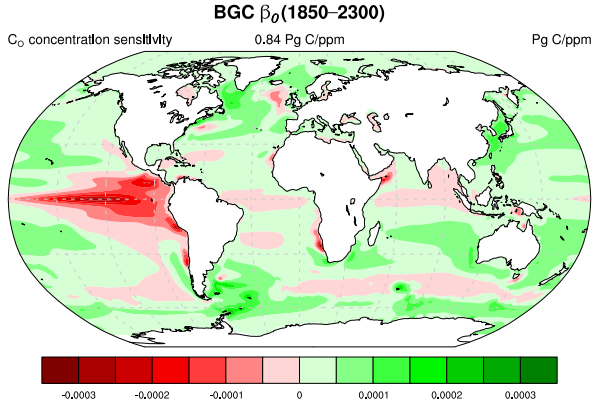

(c) Spatial distribution of the concentration–carbon sensitivity, β_O, in the BGC simulation

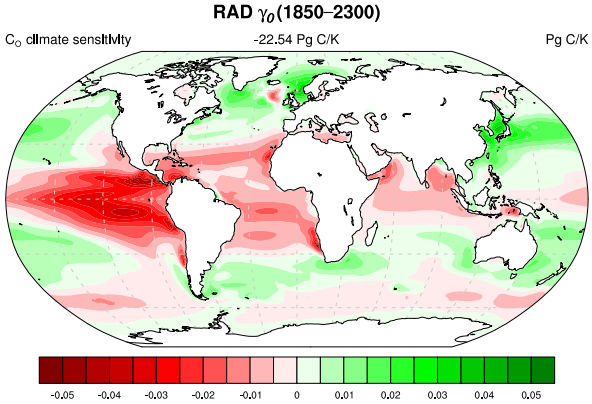

(d) Spatial distribution of the climate–carbon sensitivity, γ_O, in the RAD simulation

Figure 4.6: The ocean concentration–carbon sensitivity, β_O^{BGC}, was 0.84 Pg C ppm^{-1}, and the climate–carbon sensitivity, γ_O^{RAD}, was -12.69 Pg C K^{-1} at the end of the 23$^{\mathrm{rd}}$ century. Global β_O and γ_O values shown above the maps in (c) and (d) may differ from those shown on the plots and reported in Table 4.4 because 1) they are computed as the unweighted mean of the cell-by-cell sensitivities, and 2) temperature changes are calculated as decadal differences in the maps.

Table 4.4: Climate–carbon cycle feedback parameters and gains were calculated for the 20$^{\text{th}}$, 21$^{\text{st}}$, 22$^{\text{nd}}$, and 23$^{\text{rd}}$ centuries, demonstrating the time-varying nonlinearity of land and ocean biogeochemical responses.

	Time Period (years)			
Parameter	**1850–2000**	**1850–2100**	**1850–2200**	**1850–2300**
α ($\mathrm{K\,ppm^{-1}}$)	0.0140	0.0075	0.0052	0.0056
β_O^{BGC} ($\mathrm{Pg\,C\,ppm^{-1}}$)	1.19	0.80	0.68	0.84
$\beta_O^{\mathrm{FC-RAD}}$ ($\mathrm{Pg\,C\,ppm^{-1}}$)	1.23	0.76	0.60	0.71
β_L^{BGC} ($\mathrm{Pg\,C\,ppm^{-1}}$)	0.84	0.42	0.34	0.41
$\beta_L^{\mathrm{FC-RAD}}$ ($\mathrm{Pg\,C\,ppm^{-1}}$)	0.72	0.48	0.39	0.44
γ_O^{RAD} ($\mathrm{Pg\,C\,K^{-1}}$)	−5.10	−4.06	−8.26	−12.69
$\gamma_O^{\mathrm{FC-BGC}}$ ($\mathrm{Pg\,C\,K^{-1}}$)	−2.22	−10.06	−25.47	−39.37
γ_L^{RAD} ($\mathrm{Pg\,C\,K^{-1}}$)	−5.70	−21.09	−36.54	−48.25
$\gamma_L^{\mathrm{FC-BGC}}$ ($\mathrm{Pg\,C\,K^{-1}}$)	−15.00	−14.05	−26.69	−44.77
$g(\beta^{\mathrm{BGC}}, \gamma^{\mathrm{RAD}})$	0.035	0.056	0.075	0.101
$g(\beta^{\mathrm{FC-RAD}}, \gamma^{\mathrm{RAD}})$	0.036	0.056	0.075	0.104
$g(\beta^{\mathrm{BGC}}, \gamma^{\mathrm{FC-BGC}})$	0.057	0.054	0.087	0.139
$g(\beta^{\mathrm{FC-RAD}}, \gamma^{\mathrm{FC-BGC}})$	0.058	0.053	0.087	0.144
$g(E_C^{\mathrm{RAD}}, E_C^{\mathrm{FC}})$	0.056	0.051	0.084	0.143

$-21.09\ \mathrm{Pg\,C\,K^{-1}}$ at 2100, and slowed slightly in the 23rd century, ending at $-48.25\ \mathrm{Pg\,C\,K^{-1}}$ at 2300. (Figure 4.7(b) and Table 4.4). In this experiment, significant temperature increases had a devastating effect on tropical and sub-tropical forests globally after 2100, and drove up autotrophic and heterotrophic respiration until vegetation productivity began to collapse, especially in the 23rd century (Figure 4.7(d)). The temperature sensitivity of land carbon storage, $\gamma_L^{\mathrm{FC-BGC}}$, diverged from that calculated directly from the RAD simulation, and their differences peaked around 2175. This difference was a result of enhanced vegetation productivity under the combined effects of climate change and elevated CO_2 levels, driven by a combination of intensified hydrology and increased nutrient availability. The weakening of the land sensitivity to temperature was diminished by 2300 because of rising maintenance respiration costs at high temperatures that reduced vegetation productivity.

The overall climate–carbon cycle feedback gain, g, was dominated by the temperature sensitivities of terrestrial and marine ecosystems and ocean circulation processes. Although the temperature sensitivity to rising atmospheric CO_2, α, declined by 31% between 2100 and 2200, from $0.0075\ \mathrm{K\,ppm^{-1}}$ to $0.0052\ \mathrm{K\,ppm^{-1}}$, the gain increased by 34–65% over this same time period (Figure 4.8 and Table 4.4). During the 23rd century, the climate sensitivity rose slightly, from $0.0052\ \mathrm{K\,ppm^{-1}}$ to $0.0056\ \mathrm{K\,ppm^{-1}}$, and the gain continued to climb another 35–41%, in response to a slowing growth rate and temperatures that continued to rise, and despite rising sensitivities to atmospheric CO_2, β_L and β_O. We calculated the feedback gain century-by-century, using Equation (4.1), from feedback parameters derived from individual simulations, from pairs of experiments, and combinations of single and paired simulations (Table 4.4). All of these estimates of the feedback gain corresponded well with each other at 2100. However, they diverged after 2150 and clustered around two different values at 2300, depending on whether the temperature sensitivities, γ, were obtained from the RAD or the combination of FC and BGC simulations (Figure 4.8(b)). The gain estimated from compatible emissions, using Equation (4.17), corresponded well with those estimated from the $\gamma^{\mathrm{FC-BGC}}$ parameters (Figure 4.8(b) and Table 4.4).

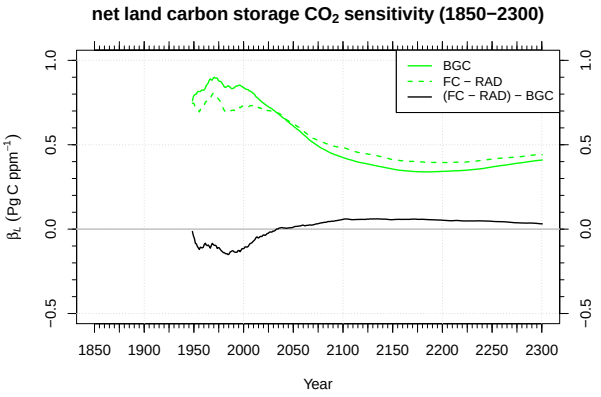

(a) Concentration–carbon sensitivity, β_L

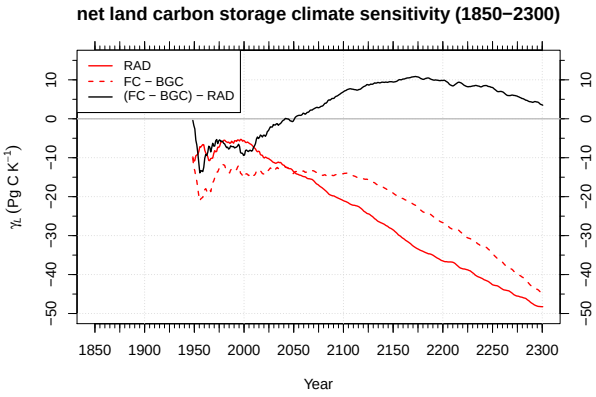

(b) Climate–carbon sensitivity, γ_L

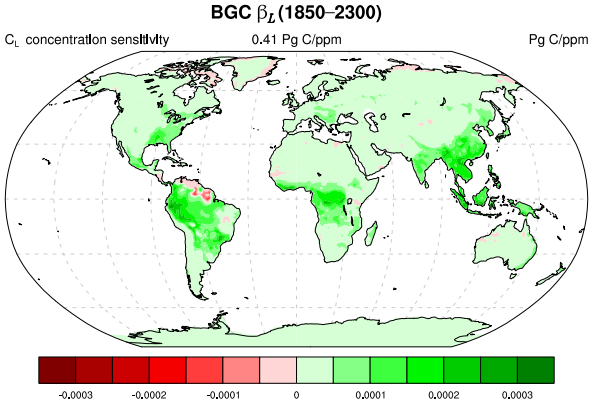

(c) Spatial distribution of the concentration–carbon sensitivity, β_L, in the BGC simulation

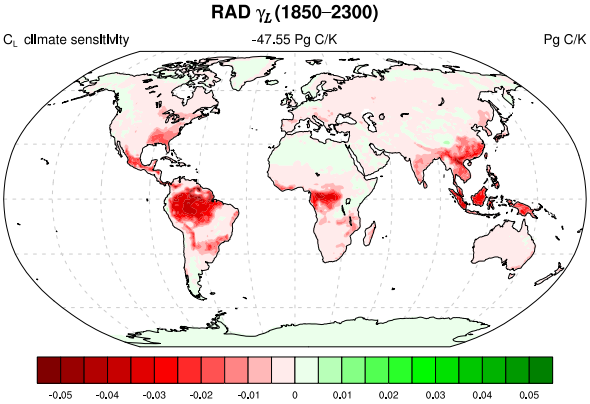

(d) Spatial distribution of the climate–carbon sensitivity, γ_L, in the RAD simulation

Figure 4.7: The land concentration–carbon sensitivity, β_L, was 0.44 Pg C ppm^{-1}, and the land climate–carbon sensitivity, γ_L, was -48.25 Pg C K^{-1} at the end of the 23$^{\text{rd}}$ century. Global β_L and γ_L values shown above the maps in (c) and (d) may differ from those shown on the plots and reported in Table 4.4 because 1) they are computed as the unweighted mean of the cell-by-cell sensitivities, and 2) temperature changes are calculated as decadal differences in the maps.

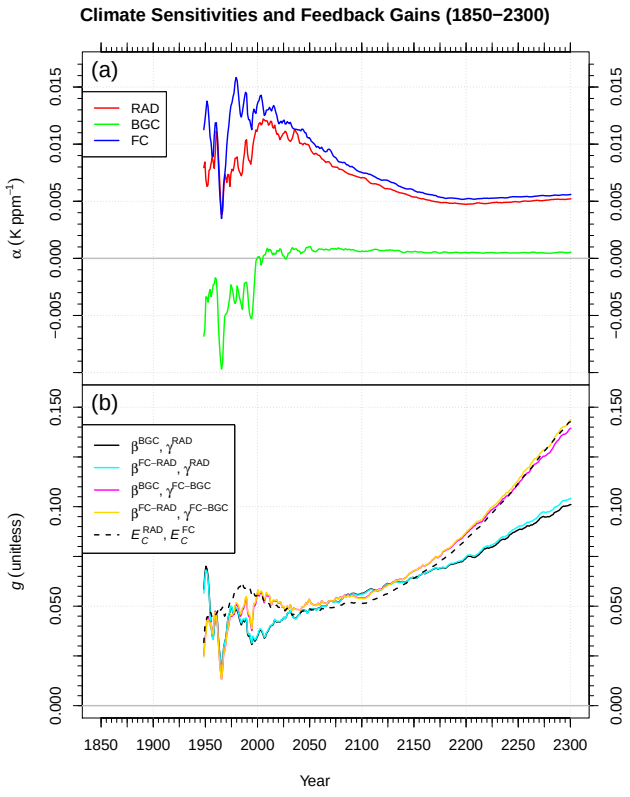

Figure 4.8: (a) The climate sensitivity, α, for the FC simulation was about 0.0056 K ppm^{-1} at the end of the 23$^{\text{rd}}$ century. (b) The climate–carbon cycle gain, g, clustered around two different values, depending on the method and experiments used to calculate it.

4.3.3 Driving mechanisms of nonlinear ocean and land responses

The growing difference between the increasing sensitivities of ocean carbon flux to climate after 2100 was a consequence of reduced exchange between surface and intermediate and deep waters, including weakening of the Atlantic meridional overturning circulation (AMOC). *Randerson et al.* (in press) quantified the AMOC weakening in similar FC and BGC simulations of CESM1(BGC) that included land use change. The AMOC decreased primarily during the 22$^{\text{nd}}$ century and stabilized around 5 Sv by 2300, consistent with long-term simulations that employed other CESM configurations that followed the RCP 8.5 scenario (*Meehl et al.*, 2012, 2013). *Randerson et al.* (in press) estimated a climate–carbon sensitivity for the ocean that was 7% weaker than derived here from the combination of FC and BGC simulations, $\gamma_O^{\text{FC}-\text{BGC}}$, suggesting a similar degree of stratification between the two fully coupled simulations. In the warming-only simulation presented here, exchange between surface and intermediate and deep waters was significantly reduced, resulting in a γ_O^{RAD} that was 68% weaker than $\gamma_O^{\text{FC}-\text{BGC}}$ at 2300. This climate change-induced circulation change, partially due to temperature-induced weakening of the solubility pump (*Long et al.*, 2013), was the source of nonlinear marine responses that grew as temperatures increased in the 22$^{\text{nd}}$ and 23$^{\text{rd}}$ centuries, consistent with the nonlinear ocean feedbacks reported by *Schwinger et al.* (2014) from their analysis of seven CMIP5 models.

After year 2000, gross primary production (GPP) on land increased more rapidly under the combined effect of climate change and elevated CO_2 than under the effect of elevated CO_2 alone, and ended 8% higher at 2300, having increased globally by 84% (Figures 4.9(a) and 4.10(a)). This acceleration of production rates in the FC simulation was fueled by increased precipitation and N mineralization, in response to climate change, and stomatal closure, in response to elevated CO_2. The nonlinearity metric was 0.25, indicating that the change in GPP expected from the combination of the RAD and BGC simulations was 25% lower than that exhibited by the FC simulation. Ecosystem respiration (ER) in all

three simulations exhibited behavior similar to GPP and produced the same nonlinearity metric (Figure 4.9(b)). Net primary production (NPP) increased less dramatically due to soil respiration increases, which were driven up by increased temperatures and precipitation; surging litter inputs; and plant growth and maintenance respiration that were driven up by rising temperatures (Figure 4.9(c)). Most regions saw gains in NPP, particularly in the tropics (Figure 4.9(d)), with notable exceptions being northeast South America, south Central America, and west sub-Saharan Africa, which experienced persistent and increasing dryness due to large scale atmospheric circulation responses to rising temperature.

To investigate the regional contributions to nonlinear responses in GPP, we produced maps of GPP change from single and combined experiments in a 3×3 arrangement, shown in Figure 4.10. The first column of maps—identified as Figures 4.10(a), 4.10(d), and 4.10(g)—are identical and indicate the GPP changes under simultaneous climate change and elevated CO_2 at year 2300. Figures 4.10(b) shows the GPP changes for the warming-only experiment, indicating widespread production declines primarily in tropical and subtropical forests. Figure 4.10(h) shows the GPP changes for the elevated CO_2-only experiment, exhibiting widespread increases in annual production rates. The GPP changes from the RAD simulation, combined with those from the BGC simulation, are shown in Figure 4.10(e). Subtracting the second column of maps from the first column of maps yields the third column of maps. Therefore, Figure 4.10(c) ($\Delta\text{FC} - \Delta\text{RAD}$) shows primarily very large GPP increases, since the losses from the RAD simulation were subtracted from the large gains in the FC simulation. Likewise, Figure 4.10(i) ($\Delta\text{FC} - \Delta\text{BGC}$) shows a mixed set of GPP changes globally, since GPP gains were often larger in the FC simulation than in the BGC simulation. Finally, Figure 4.10(f) ($\Delta\text{FC} - (\Delta\text{RAD} + \Delta\text{BGC})$) shows the regions where GPP gains and losses resulted from nonlinear responses in the FC simulation. In this map, we observed strong nonlinear increases in rates of production in the tropics, particularly in the Central Amazon Basin, and moderate increases in subtropical forests. Nonlinear GPP losses were moderate, with the greatest declines occurring in western coastal South America, parts

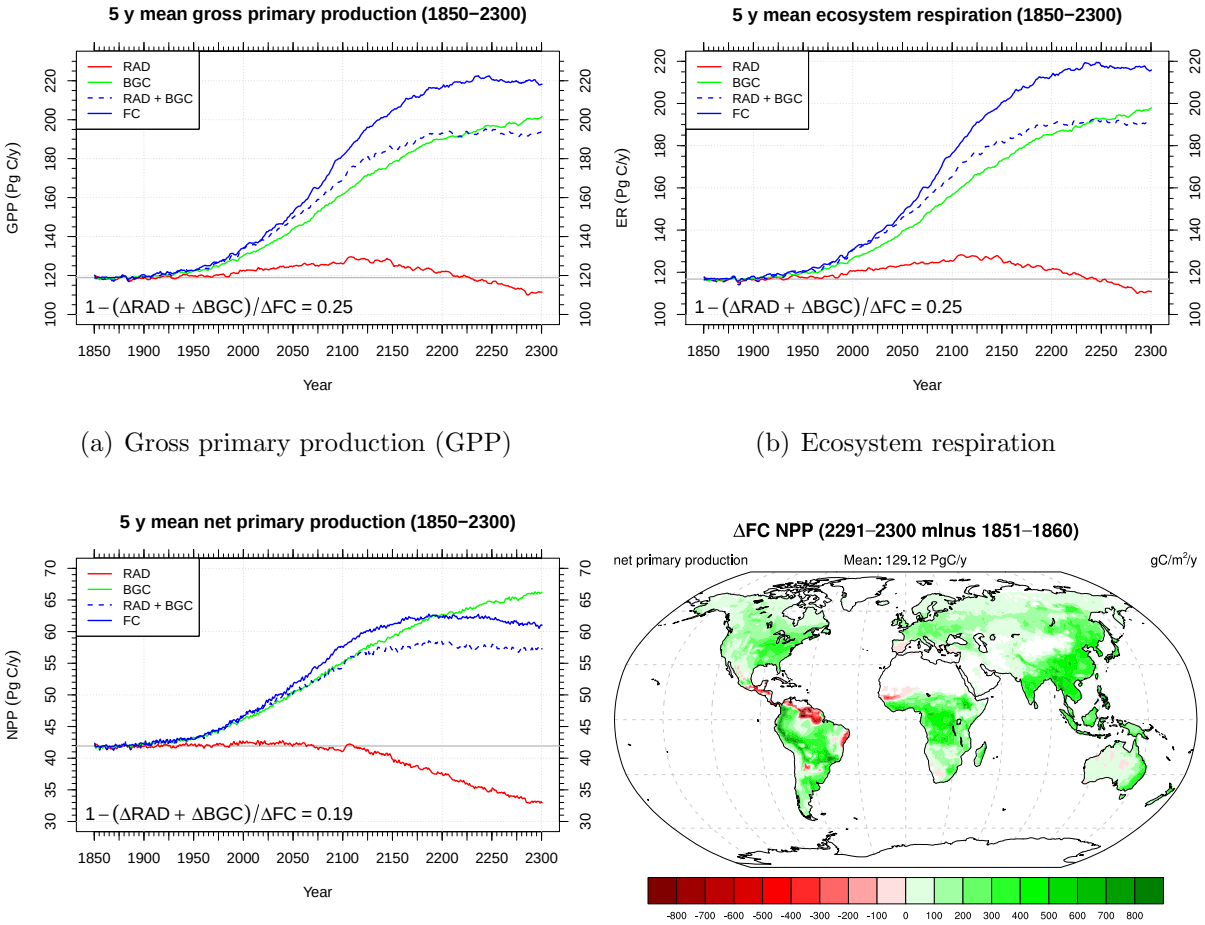

(a) Gross primary production (GPP)

(b) Ecosystem respiration

(c) Net primary production (NPP)

(d) Change in NPP for the FC simulation at 2300

Figure 4.9: (a) The gross primary production (GPP) of the FC simulation exhibited larger than expected gains under the combined conditions of increasing temperature and elevated CO_2. (b) The trajectories of ecosystem respiration (ER) for all three simulations correspond well with and were slightly lower than GPP. (c) The net primary production (NPP) for the FC simulation cross that of the BGC simulation just before 2200 due primarily to hydrological imbalances in regions where strong drying was expected to occur. (d) NPP losses by 2300 were largest where drought stress was induced by strong circulation changes in the 22nd and 23rd centuries.

of South Africa, and northern India.

The nonlinear response in GPP was driven by a variety of interacting energy, water, and nutrient factors, many of which strengthened after 2100. Chief among these factors was a large increase in global precipitation as a consequence of climate change (Figure 4.11(a)). While global precipitation increased by less than 1% in response to elevated CO_2, climate change and the consequent atmospheric circulation changes induced a 20% increase in precipitation globally. After 2100, precipitation increased more rapidly in response to climate change and elevated CO_2, likely due to additional precipitation recycling as a consequence of the positive feedback with GPP that enhanced leaf area. By the late 20^{th} century, divergent responses in evapotranspiration (ET) due to warming and to increasing atmospheric CO_2 were already evident (Figure 4.11(b)). In the RAD simulation, increasing heat stress drove up ET in the 21^{st} and 22^{nd} centuries. It continued to rise slightly in the 23^{rd} century, for a total increase of 14%, due primarily to ground evaporation because of the dramatic loss of vegetation in this simulation. In contrast, increasing atmospheric CO_2 pushed up the water use efficiency of vegetation, as a consequence of stomatal closure due to the improved carbon assimilation efficiency with elevated CO_2, driving ET down by 17% at 2300. When climate change and increasing CO_2 acted together, ET had increased by less than 1% by 2300, yet the combination of the RAD and BGC simulations suggested it should have decreased by 2% instead, resulting in a large nonlinear metric value because of the sign difference. The divergence of ET in the FC simulation from its expected trajectory at 2100 was a consequence of increased canopy evaporation and increased transpiration due to enhanced leaf area.

To investigate the regional distribution of nonlinear responses in precipitation, we produced maps of precipitation differences from single and combined experiments in a 3×3 arrangement, shown in Figure 4.12. Strong increases in precipitation due to elevated CO_2 under simultaneous climate change occurred in western tropical South America, central tropical Africa, and the Indo-Pacific region; while the largest precipitation declines were in eastern

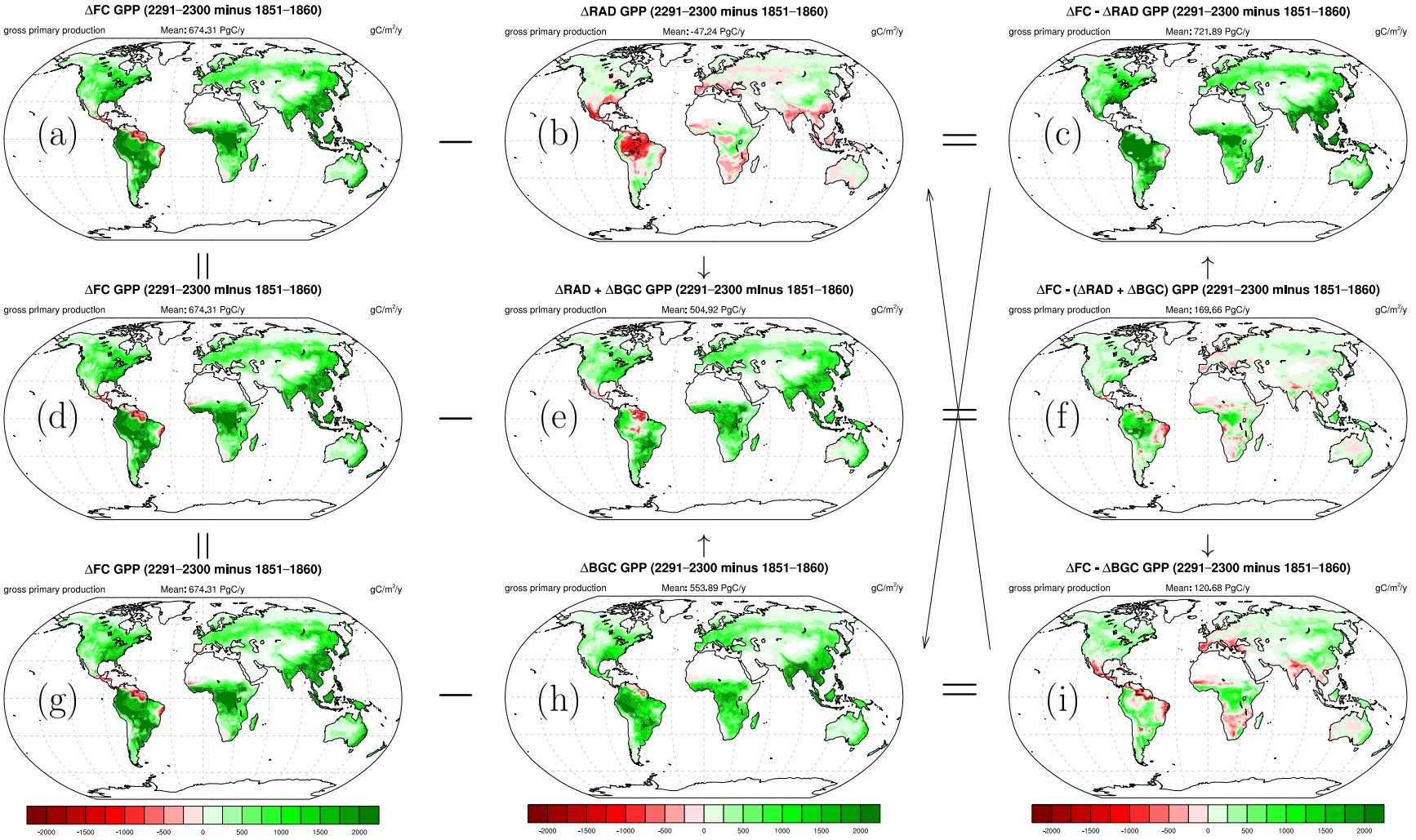

Figure 4.10: The contributions of the radiatively coupled (RAD) and biogeochemically coupled (BGC) changes in gross primary production (GPP) do not add up to the fully coupled (FC) change in GPP at 2300. Biosphere responses to the combined effects of increasing atmospheric CO_2 levels and climate change in the FC simulation resulted in higher GPP than that exhibited by the BGC simulation.

equatorial South America, as shown in Figure 4.12(c). The spatial distribution of nonlinear precipitation change anomalies under climate change and elevated CO_2 conditions is shown in Figure 4.12(f). Precipitation declines occurred in eastern South America, southeast Asia, and northwestern Australia, while the largest increases were observed in inland tropical South America, central tropical Africa, and the Indo-Pacific, further suggesting that these positive anomalies may be due to precipitation recycling in or around dense tropical forests.

We estimated net water availability as the difference between precipitation and evapotranspiration, $P - ET$, and found that the nonlinearities in these two factors counteracted, although not perfectly (Figure 4.11(c)). While only a negligible precipitation increase was exhibited under elevated CO_2, its trajectory of $P - ET$ was higher than that of the warming-only simulation until the end of the 23rd century due to the strong stomatal closure effect. At 2300, $P - ET$ had increased by about 34% in the RAD and BGC simulations, while it had increased by about 65% in the FC simulation. The largest increases in $P - ET$ occurred in the western half of South America, the middle of tropical Africa, the Indo-Pacific region, and the southern edge of the Tibetan Plateau (Figure 4.11(d)). Sensible heat rose due to a repartitioning from latent heat as a consequence of stomatal closure under elevated CO_2, while overall temperatures increased as a result of climate change (Figure 4.13(a)). In the FC simulation, the effects of rising temperature and stomatal closure combined, resulting in a 48% increase in sensible heat globally by 2300. However, the change expected from the combination of the RAD and BGC simulations was 9% greater than that produced by the FC simulation due to enhanced leaf area that resulted in increased canopy evaporation and transpiration. Trajectories of latent heat exhibited the same pattern as trajectories of ET (Figure 4.13(b)). Soil moisture, integrated down to 1 m, decreased due to climate change in the 21st and early 22nd centuries, despite increases in precipitation, due to increasing heat stress on global vegetation (Figure 4.13(c)). Under elevated CO_2, soil moisture increased after 2000 and was 2% larger by 2300. Under the combined conditions of climate change and elevated CO_2, soil moisture increased with a trajectory similar to that of the BGC simula-

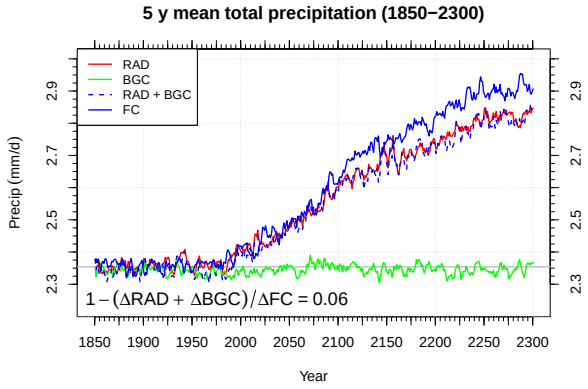

(a) Trajectories of precipitation over land for the RAD, BGC, and FC simulations

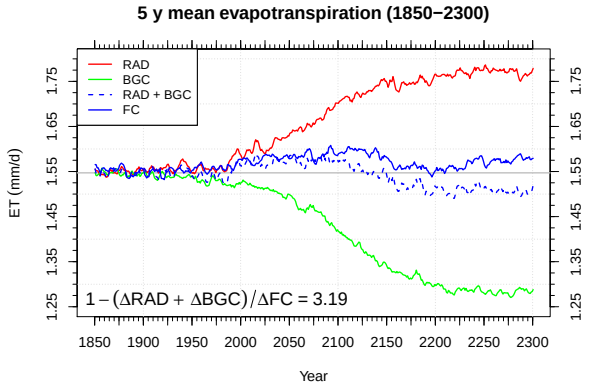

(b) Trajectories of evapotranspiration for the RAD, BGC, and FC simulations

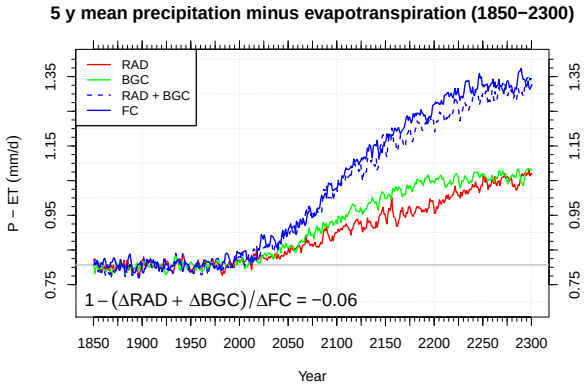

(c) Trajectories of precipitation minus evapotranspiration (P − ET) for the RAD, BGC, and FC simulations

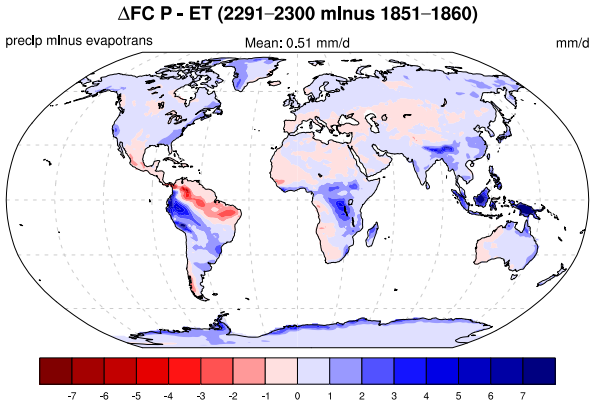

(d) Spatial pattern of P − ET for the FC simulation at 2300

Figure 4.11: (a) Precipitation over land increased as a result of strong temperature increases in the RAD and FC simulations, with no appreciable change seen in the BGC simulation. After 2100, the FC simulation exhibited higher than expected precipitation, likely driven by increases in recycling attributable to gains in canopy evaporation.(b) Correspondingly, the FC simulation exhibited larger than expect evapotranspiration. (c) Despite the lack of increasing precipitation in the BGC simulation, net P − ET was slightly above that of the RAD simulation. (d) The regions of significant drying in northern South America exhibited the largest declines in P − ET.

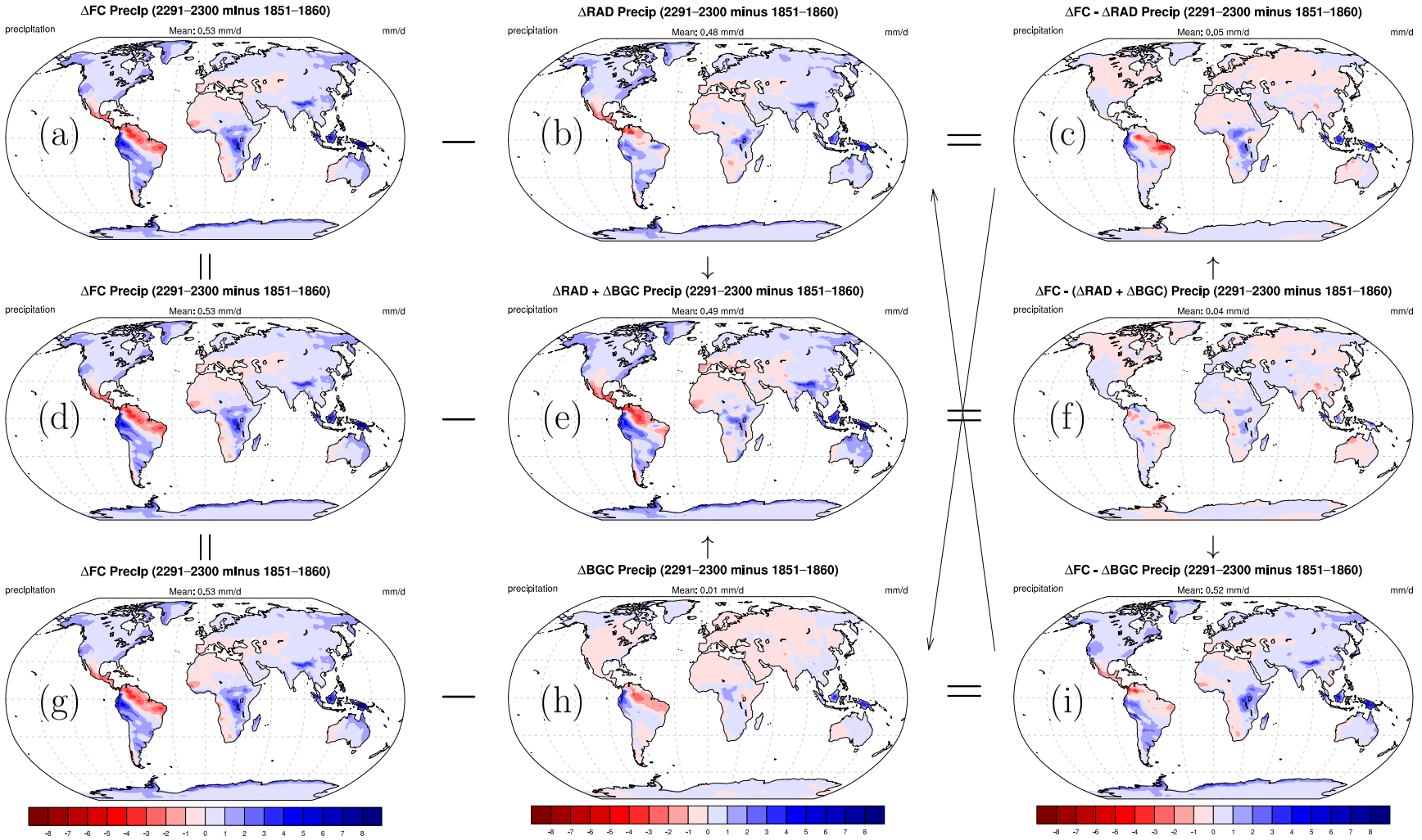

Figure 4.12: Contributions of radiatively coupled (RAD) and biogeochemically coupled (BGC) changes in precipitation to the fully coupled (FC) precipitation.

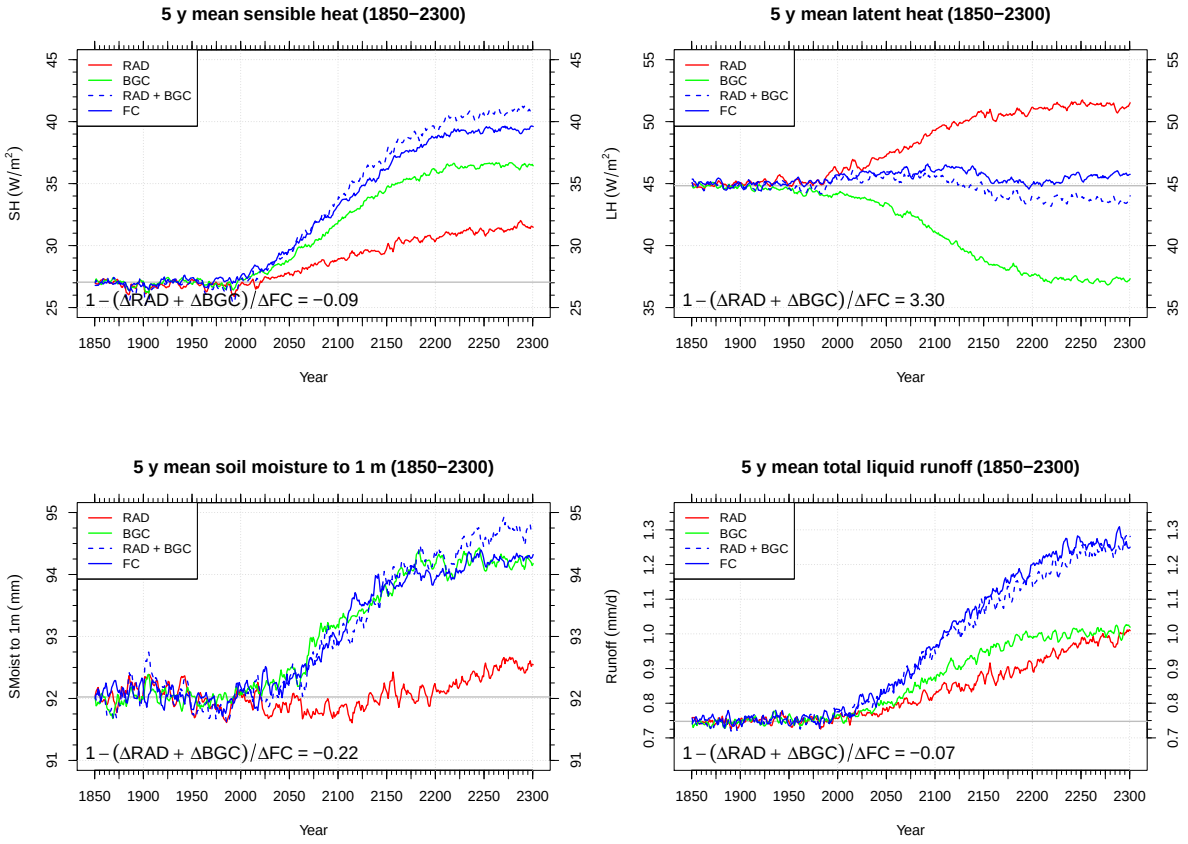

Figure 4.13: (a) Sensible heat increased in all three simulations. (b) The trajectories of latent heat corresponded well with the trajectories of ET (Figure 4.11(b)). (c) The FC and BGC simulations exhibited similar trajectories of soil moisture to 1 m depth. (d) Trajectories of total liquid runoff corresponded well with trajectories of P − ET (Figure 4.11(c)).

tion, which, by 2300, was about 0.5% lower than expected from the combination of the RAD and BGC simulations due to rising maintenance respiration in the 23rd century. Since soil moisture increases were modest globally, the trajectories of total liquid runoff for all three simulations were very similar to the trajectories of P − ET, described above (Figure 4.13(d)).

In addition to the hydrology–GPP feedback that drove nonlinear terrestrial biosphere responses, increased soil nitrogen availability also played a significant role in fueling growing rates of primary production. Under climate change, rising soil temperatures and rainfall rates increased rates of N mineralization since microbial fixation is temperature and moisture dependent (Figure 4.14(a)). Rates of N mineralization increased almost linearly under

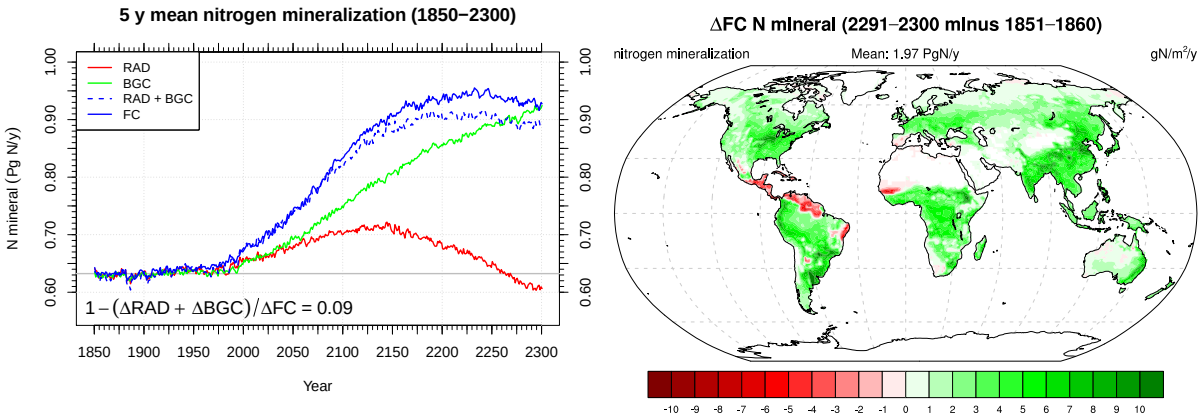

(a) Trajectories of global net nitrogen mineralization for the RAD, BGC, and FC simulations

(b) Spatial distribution of change in net nitrogen mineralization in the FC simulation

Figure 4.14: (a) Increases in net nitrogen mineralization were widespread in the FC simulation, driven by increases in nitrogen deposition forcing and rising soil temperatures. (b) The spatial pattern of N mineralization reductions by 2300 in the FC simulation correspond well with the corresponding NPP losses shown in Figure 4.9(d).

elevated atmospheric CO_2 conditions, rising 46% by 2300 due to substantial increases in litter inputs from rising rates of primary production With both climate change and increasing CO_2 acting together, N mineralization was driven up rapidly until the middle of the 22nd century, when it began to stabilize before slightly decreasing by the middle of the 23rd century. By 2300, rates of N mineralization in the FC simulation had dropped to those exhibited in the BGC simulation. As with GPP, the trajectory of N mineralization for the FC simulation began to diverge from its expected trajectory at 2100 due to higher-than-expected precipitation increases, resulting from intensified precipitation recycling and due to enhanced GPP that yielded increased litter substrate, intensifying soil decomposition. The spatial pattern of changes in rates of N mineralization suggests a strong relationship with both productivity and precipitation changes (Figure 4.14(b)). Rates increased in tropical and subtropical regions, except those areas dominated by significant drying due to atmospheric circulation changes.

The feedbacks between hydrology, productivity, and nutrient availability under warming-induced climate change and rising anthropogenic atmospheric CO_2 mole fractions were the

source of nonlinear terrestrial ecosystem responses. The most significant drivers of the hydrological and ecological changes from all three simulations were quantified for the 451 y simulation time period in Figure 4.15 and Table 4.3. The climate change contributions, ΔRAD, and the elevated CO_2 change contributions, ΔBGC, to the changes in the fully coupled simulation, ΔFC, are shown in red, green, and blue, respectively, in the table and figure. The nonlinear metric for each variable is listed in Table 4.3, and is colored either in red, if climate change was the dominant driver, or in green, if elevated CO_2 was the dominant driver. In the upper panel of Figure 4.15, the relative strengths of the contributing influences of climate change or elevated CO_2 are shown, with the remaining gray bar representing the nonlinear component in the variable, constituting 100% of the FC simulation result. The lower panel shows the relative size and direction of the changes in each variable from the RAD, BGC, and FC simulations at 2300, summarizing the results discussed above.

4.4 Discussion

4.4.1 Comparison of climate–carbon cycle feedback parameters with prior studies

Arora et al. (2013) analyzed idealized 1% y^{-1} increasing CO_2 simulations for nine CMIP5 models, including the model used here, that were run for 140 y. They calculated concentration–carbon sensitivities from BGC simulations and chose to use climate–carbon sensitivities calculated from RAD simulations. *Arora et al.* (2013) reported the multi-model mean (and standard deviation) of β_L to be 0.92 (0.44) $Pg\,C\,ppm^{-1}$, respectively. They found CESM1(BGC) to have the second weakest land sensitivity to elevated CO_2, β_L, estimated at 0.24 $Pg\,C\,ppm^{-1}$, which was only slightly stronger than the other model that incorporated terrestrial N limitation. That value is 43% weaker than the 0.42 $Pg\,C\,ppm^{-1}$ estimated from

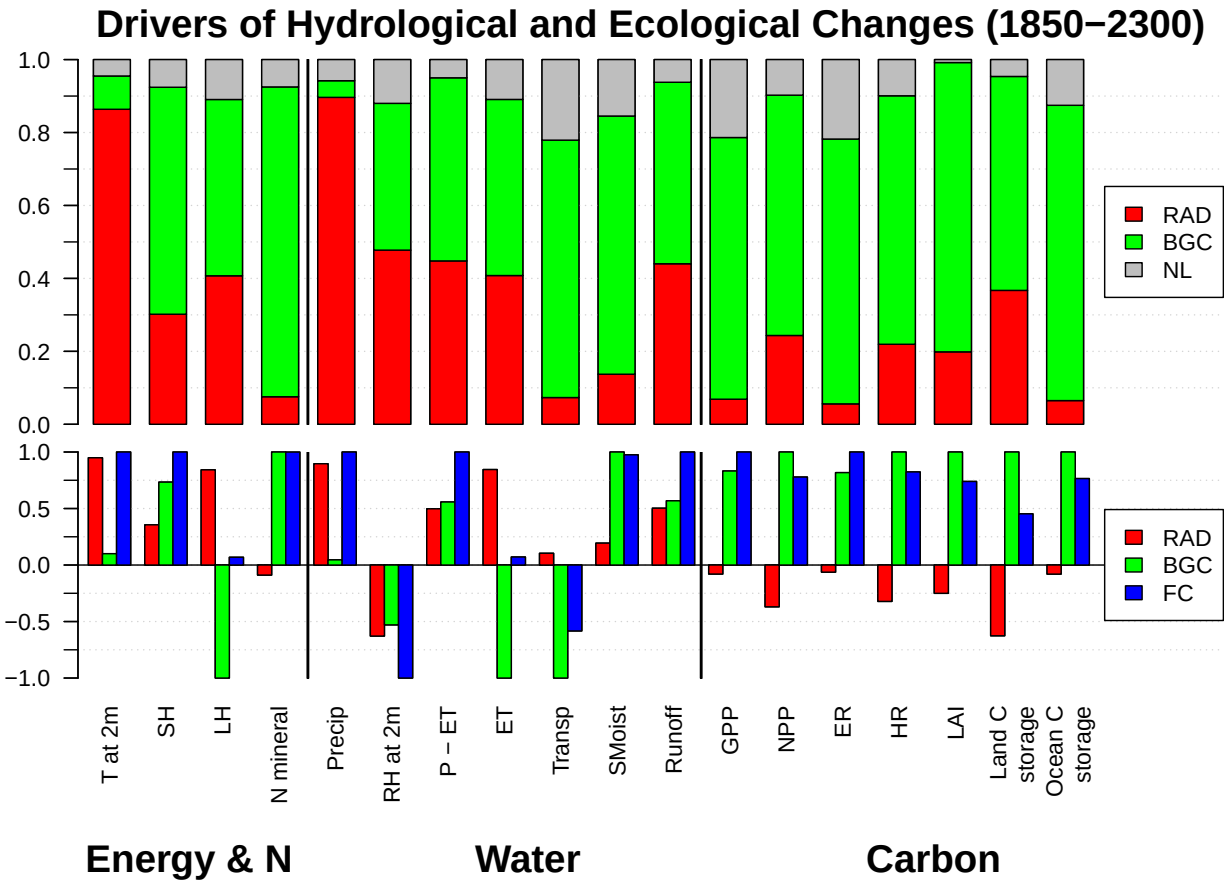

Figure 4.15: Shown are the most significant drivers of hydrological and ecological changes exhibited by the RAD, BGC, and FC simulations. The upper panel shows the strength of the RAD and BGC results for each variable in the FC simulation, with the difference attributed to nonlinear effects (NL). The lower panel shows the strengths of each driving variable relative to that of the strongest contributor, both positively and negatively. The variables listed as labels along the x-axis are defined in Table 4.3.

the BGC simulation of RCP 8.5 at 2100 found here. This weak response, relative to most other CMIP5 models is likely caused by N limitation in the CESM1(BGC) land model, which serves to constrain the productivity-enhancing effects of CO_2 fertilization. Due to large uncertainties regarding the effective strength of CO_2 fertilization on the terrestrial biosphere and the extent to which nutrient limitation regulates carbon uptake, it is not clear that this weaker β_L is the result of a model bias. Moreover, recent work suggested that lack of nutrient limitation in most CMIP5 models led to projections that overestimated the strength of land carbon uptake in response to elevated atmospheric CO_2 (*Wieder et al.*, 2015). *Wieder et al.* (2015) further postulated that phosphorus limitation may ultimately constrain NPP, especially in tropical ecosystems. For the land carbon uptake sensitivity to temperature, γ_L, *Arora et al.* (2013) calculated the multi-model mean (and standard deviation) from the RAD simulations to be -58.4 (28.5) $\mathrm{Pg\,C\,K^{-1}}$, respectively. For CESM1(BGC) they found γ_L to be -21.3 $\mathrm{Pg\,C\,K^{-1}}$, which is very close to the -21.09 $\mathrm{Pg\,C\,K^{-1}}$ value at 2100 we calculated from the RAD simulation of RCP 8.5 at 2100.

Arora et al. (2013) estimated the CESM1(BGC) ocean concentration–carbon sensitivity, β_O, to be 0.72 $\mathrm{Pg\,C\,ppm^{-1}}$, as compared to a value of 0.80 $\mathrm{Pg\,C\,ppm^{-1}}$, which was exhibited by the BGC simulation of RCP 8.5 at 2100. The multi-model mean (and standard deviation) of β_O they computed were 0.80 (0.07) $\mathrm{Pg\,C\,ppm^{-1}}$, respectively. For the ocean climate–carbon sensitivity, γ_O, they estimated the multi-model mean (and standard deviation) as -7.8 (2.9) $\mathrm{Pg\,C\,K^{-1}}$, respectively, and for CESM1(BGC) as -2.4 $\mathrm{Pg\,C\,K^{-1}}$, weaker than any other model in their study. That value was also 41% weaker than the γ_O estimate of -4.06 $\mathrm{Pg\,C\,K^{-1}}$ found for the RAD simulation of RCP 8.5 at 2100. This weak response is likely caused by biases in the CESM1(BGC) ocean model that result in weak intermediate water formation and North Atlantic Deep Water (NADW) and Antarctic Bottom Water (AABW) formation (*Long et al.*, 2013). The similarity of the feedback parameters found here with those *Arora et al.* (2013) found for the 1% $\mathrm{y^{-1}}$ increasing CO_2 simulations suggests that the feedback analysis methodology can be reasonably applied to scenario simulations

that incorporate transient non-CO_2 greenhouse gas mole fractions, aerosol loadings, and N deposition.

4.4.2 Reducing effects of nonlinearity on feedback gains

Despite nonlinear ocean and land model responses exhibited by these simulations, the gain, g, of the climate–carbon cycle feedback increases as temperatures rise in response to radiative forcing. At 2100, the nonlinear ocean and land responses among the RAD, BGC, and FC simulations resulted in γ_O^{RAD} and γ_L^{RAD} differences that nearly compensated for each other ($\pm$6–7 $\mathrm{Pg\,C\,K^{-1}}$), producing a climate–carbon cycle feedback gain (Equations (4.9) and (4.10)) that corresponded well with the gain computed from compatible emissions (Equation (4.17)) or computed using climate–carbon sensitivities derived from FC and BGC simulations, $\gamma_O^{\mathrm{FC-BGC}}$ and $\gamma_L^{\mathrm{FC-BGC}}$ (Equation (4.16)). Because of compensating short-term ocean and land responses to climate change, these results appear to confirm the conclusion of *Gregory et al.* (2009) that γ may be estimated consistently from either a radiatively coupled simulation or the combination of a biogeochemically coupled and a fully coupled simulation. Their reasoning is that γ is less sensitive to scenario differences than is β since both global temperature and carbon uptake lag the radiative and atmospheric CO_2 forcing. However, nonlinear response characteristics are likely to interact and grow over time, as demonstrated by the bifurcating gains in Figure 4.8(b) and Table 4.4, which led to rather different climate–carbon cycle feedback gains in the long term.

At 2300, the overall climate–carbon cycle feedback gain was 28% lower when estimated from climate–carbon sensitivities derived from the RAD simulation than when derived from the difference between the FC and BGC simulations. Since nonlinear ocean and land responses led to the lower gain and the gain estimated from compatible emissions calculations corresponded well with the gain estimated from FC$-$BGC climate–carbon sensitivity parameters,

we suggest that the larger gain is valid. This difference has direct implications for carbon management and energy policies because underestimating the climate–carbon cycle feedback gain would result in allowable emissions estimates that would be too low to meet climate change targets. These results suggest that useful and comparable estimates of the climate–carbon cycle feedback gain should be calculated from temperature sensitivity parameters derived from the combination of FC and BGC simulations to best account for nonlinear responses of the ocean and land in the feedback analysis framework. An important next step is to derive the climate–carbon feedback sensitivities, $\gamma_O^{\mathrm{FC-BGC}}$ and $\gamma_L^{\mathrm{FC-BGC}}$, for the CMIP5 ESMs previously analyzed by *Arora et al.* (2013) to determine the strength of any nonlinear responses in those models that were expressed over the relatively shorter 140 y time period and to minimize the effects of those nonlinearities on estimates of the climate–carbon cycle feedback gains. Alternative feedback gains calculated using these sensitivities should provide for a more rigorous comparison between C^4MIP, CMIP5, and CMIP6 carbon cycle simulations.

4.4.3 Nonlinearity in terrestrial uptake responses

These simulation experiments showed that terrestrial carbon sinks were more efficient when exposed to the combined effect of climate change and elevated CO_2 than to the two effects separately. In contrast, *Zickfeld et al.* (2011) found reduced land uptake under the combined conditions of elevated CO_2 and climate change than in the sum of the responses from the two effects applied separately for their EMIC simulations. Differences in modeled vegetation responses to climate change are likely the cause of these contrasting results. *Zickfeld et al.* (2011) allowed dynamic conversion of vegetation types in their model, and observed that climate change, in the absence of the ameliorating effects of CO_2 fertilization, induced a dieback of tropical forests and replacement by C_4 grasses. While these tropical grasslands stored less carbon as biomass than the forests they replaced, they were more productive

and associated with higher soil carbon. To avoid confounding effects of land use change, we enforced a static, pre-industrial distribution of vegetation and found that climate change effects in isolation caused a collapse of tropical forests.

In the fully coupled simulation presented here, an unexpectedly large increase in gross primary production was fueled by the interactions of rising water availability and increasing N mineralization in soil under the combined effects of increased atmospheric CO_2 and consequent climate change. Increased N mineralization was driven by a transient and globally increasing N deposition forcing and accelerated decomposition due to rising temperatures and water availability, resulting from the net radiative forcing of increasing atmospheric CO_2, other greenhouse gases, and aerosols. Increased water availability was the result of rising precipitation due to atmospheric circulation changes and increased evaporation from the oceans that were driven by increasing temperatures, and a strong reduction in canopy transpiration, resulting from stomatal closure under elevated atmospheric CO_2 levels. Throughout the 22$^{\text{nd}}$ and the early 23$^{\text{rd}}$ centuries, excess plant productivity moderately intensified positive feedbacks in N mineralization through additional substrate inputs and in precipitation through additional moisture recycling that was driven by larger than expected transpiration and canopy evaporation resulting from a larger leaf area. These mechanisms formed a positive feedback that served to drive up overall net land carbon storage in the FC simulation after 2100. However, as the atmospheric CO_2 mole fraction stabilized and temperatures continued to rise during the latter half of the 23$^{\text{rd}}$ century, heat and water stress began to set in, driving up maintenance respiration and weakening this positive feedback. Nevertheless, net land carbon storage in the FC simulation was 309 Pg C by the end of the 23$^{\text{rd}}$ century, as opposed to the 257 Pg C expected from a linear combination of the RAD and BGC simulation results.

4.4.4 Symbiosis of experiments and modeling

Improving our knowledge of carbon cycle feedbacks with Earth's climate system and reducing ESM uncertainties associated with land and ocean responses requires a coordinated program of *in situ* measurements, remote sensing observations, and manipulative field experiments; modular and extensible model development; carefully crafted simulation experiments designed to mimic historical conditions and manipulative field experiments; and comprehensive and routine model assessment. Laboratory and manipulative field experiments have been conducted in an attempt to disentangle terrestrial and marine ecosystem responses to climate change and elevated atmospheric CO_2, together and in isolation, and the influence of nutrient availability on those responses (e.g., *Reich and Hobbie*, 2013). Free Air CO_2 Enrichment (FACE) experiments, designed to measure the response of vegetation to elevated atmospheric CO_2 in isolation from any changes in climate, have been conducted in a variety landscapes, hosting different vegetation types with various soil, water, and nutrient constraints (*Norby et al.*, 2005, 2010). Corresponding model experiments, employing a suite of state-of-the-art terrestrial ecosystem models, have been performed to synthesize observational results and determine how well models capture vegetation responses to elevated atmospheric CO_2 with the objective of reducing model uncertainties (*Walker et al.*, 2014; *Zaehle et al.*, 2014; *Walker et al.*, 2015). However, large-scale FACE experiments have all been carried out at mid-latitudes, while responses of tropical ecosystems are likely to have the largest implications for the global carbon cycle. Fortunately, a new Amazon FACE experiment has been designed and is under construction in a tropical forest site near Manaus, Brazil (*Tollefson*, 2013). Similarly, air and soil warming experiments have been widely conducted, but only recently have these been extended to high and low latitudes, where the largest terrestrial carbon stores are located (*Natali et al.*, 2012; *Cavaleri et al.*, 2015).

Ocean manipulation experiments are more difficult to perform; however, iron fertilization experiments and ongoing long-term geochemical monitoring campaigns, designed to gauge

the response of the solubility pump and the biological pump to climate change, have produced valuable data for constraining ocean carbon cycle models (*Coale et al.*, 1996; *Buesseler et al.*, 2004; *Boyd et al.*, 2007; *Buesseler et al.*, 2008; *Smith et al.*, 2009). More extensive coordination between the modeling and experimental communities is needed to facilitate design of measurement campaigns that best inform model development and to maximize the utility of observations for assessing model performance. In addition, continued development of free and open databases of observations is required to advance our scientific understanding, drive improvement of process representations in models, and support detailed evaluation of model results for informing mitigation and adaptation decision-making and planning.

4.5 Conclusions

Standard sensitivities of feedbacks between the global carbon cycle and Earth's climate system assume the response of carbon uptake to changes in atmospheric CO_2 (the concentration–carbon feedback or β) and changes in climate (the climate–carbon feedback or γ) combine linearly for the ocean and land. Our long-term simulations from the CESM1(BGC) Earth system model indicated that the degree to which these two feedback sensitivities combine linearly is dependent upon how they are derived from simulation experiments. Radiatively coupled (RAD) simulations produced a net ocean carbon storage climate sensitivity (γ_O) that is weaker and a net land carbon storage climate sensitivity (γ_L) that is stronger than those diagnosed from the fully coupled (FC) minus the biogeochemically coupled (BGC) simulations. For the ocean, this nonlinearity was associated with warming-induced weakening of ocean circulation and mixing that limited exchange of carbon between surface and deeper water masses, consistent with the results of *Schwinger et al.* (2014). For the land, this nonlinearity was associated with strong gains in vegetation productivity in the FC simulation that were driven by enhancements in the hydrological cycle and increased nutrient

availability. We developed a nonlinearity metric for individual variables, which can be used to rank nonlinear responses and drivers in a suite of radiatively coupled, biogeochemically coupled, and fully coupled simulations.

Our experimental design enabled an assessment of nonlinear responses of ocean and land carbon uptake to increasing temperature and elevated CO_2, following the CMIP5 historical, RCP 8.5, and ECP 8.5 protocol. Analysis of these experiments demonstrates that climate–carbon cycle feedback analysis can be successfully applied to non-idealized climate change scenario simulations that include transient non-CO_2 greenhouse gases, aerosols, and N deposition. For these simulations, the overall climate–carbon cycle feedback gain at 2300 was 28% lower when estimated from climate–carbon sensitivities derived from the RAD simulation than when derived from the difference between the FC and BGC simulations. The gain estimated from compatible emissions calculations corresponded well with the gain estimated from FC − BGC climate–carbon sensitivity parameters, confirming the validity of the larger gain. This difference has direct implications for carbon management and energy policies because underestimating the climate–carbon cycle feedback gain would result in allowable emissions estimates that would be too low to meet climate change targets.

Our results suggest that comparable estimates of the climate–carbon cycle feedback gain should be calculated from temperature sensitivity parameters, γ, derived from the combination of fully coupled and biogeochemically coupled simulations to best account for nonlinear marine and terrestrial responses. In order to further reduce uncertainties associated with these responses, coordinated campaigns of observations, modeling, and systematic assessment—involving close collaboration between the modeling, measurements, and data management communities—are required. Next steps include assessment of nonlinear responses in CMIP5 models and derivation of climate–carbon feedback sensitivities to estimate climate–carbon cycle feedback gains for a more rigorous comparison between C^4MIP, CMIP5, and CMIP6 carbon cycle simulations.

4.6 Acknowledgements

This research was supported by the Biogeochemistry–Climate Feedbacks Scientific Focus Area (SFA), which is sponsored by the Regional and Global Climate Modeling (RGCM) Program in the Climate and Environmental Sciences Division (CESD) of the Biological and Environmental Research (BER) Program in the U. S. Department of Energy Office of Science. This research used resources of the Oak Ridge Leadership Computing Facility (OLCF) at Oak Ridge National Laboratory (ORNL), which is managed by UT-Battelle, LLC, for the U. S. Department of Energy under Contract No. DE-AC05-00OR22725. The United States Government retains and the publisher, by accepting the article for publication, acknowledges that the United States Government retains a non-exclusive, paid-up, irrevocable, world-wide license to publish or reproduce the published form of this manuscript, or allow others to do so, for United States Government purposes.

Chapter 5

Conclusions

5.1 Computational Climate Research

The research presented here demonstrated the utility of rigorous statistical methods and computational experiments designed to elucidate differences between models and across model configurations. I found a powerful emergent constraint on atmospheric CO_2 and used it to remove biases from a collection of model results, thereby reducing uncertainty in future projections. To reduce biases in individual models, a systematic and rigorous campaign of extensive and multi-faceted model assessment must be routinely performed. Community-based benchmarking, employing open source community-developed software like that created for the International Land Model Benchmarking (ILAMB) activity, is one promising direction for improving model structure and optimizing model parameters.

Similarly, systematic sampling strategies are useful for understanding ecosystem responses to climate change and informing model improvements. This is particularly important in harsh, often under-sampled environments like the Arctic and the tropics, where climate change is most likely to have the strongest effects. In order for models to capture important

processes and feedbacks, a rich body of unbiased and representative observational data is required for parameterizing and evaluating model structures. Large-scale analytical methods, like multivariate spatiotemporal clustering, offer a quantitative means for optimizing sampling networks and characterizing the representativeness of measurements across space and through time at multiple scales. If performed correctly with adequate data, domains stratified in this way provide a framework for up-scaling and extrapolating measurements to regions within and beyond sampling locations, and they supply a quantitative measure of uncertainty. Resulting data products can be used to initialize models, to constrain model projections, or to evaluate model fidelity.

Long-term coupled climate–carbon cycle simulation experiments, incorporating different coupling strategies, are useful for isolating individual processes and for quantifying feedbacks between the global carbon cycle and Earth's climate system. As shown here, slowly changing carbon cycle processes may not express the impacts of climate change or elevated CO_2 in simulations that extend only for 100 years into the future, like those commonly performed for Intergovernmental Panel on Climate Change (IPCC) Assessment Reports. Moreover, nonlinear biosphere and ocean responses to increasing temperature and rising atmospheric CO_2 levels challenge traditional methods for disentangling and quantifying individual feedback effects. Such feedback nonlinearities can lead to errors in estimates of terrestrial and marine carbon sequestration potentials, affecting emissions and energy policies.

5.2 Future Research

The analytical tools and methods developed and applied in the studies presented here have wide applicability for computational Earth science research. The emergent constraint approach applied here to reduce model spread in future projections by removing contemporary biases in atmospheric CO_2 predictions is not expected to apply for arbitrary model vari-

ables or processes. However, a key objective of future research is to evaluate where and to what degree emergent constraints may be usefully applied to reduce uncertainties in future model projections. This assessment is likely to be connected with on-going research to identify metrics of land and ocean model fidelity that will support the development of an open source benchmarking software system, which will be deployed to evaluate the performance of the next generation of ESMs contributing to the sixth phase of the Coupled Model Intercomparison Project (CMIP6). This research will draw upon a growing body of *in situ* and remotely sensed data. Data originating from the U.S. Department of Energy's Next Generation Ecosystem Experiments (NGEE) for the Arctic and the tropics, locations already noted as under-sampled and carbon-rich critical environments, are expected to provide unique constraints for model parameters and projections. Step change experiments, designed to mimic field manipulations, will be designed and performed to test the transient behavior of models while perturbing a small number of variables. For example, doubling or quadrupling atmospheric CO_2 mole fractions will mimic Free Air CO_2 Enrichment experiments; increasing N or P deposition in simulations will replicate field N or P addition experiments that have been conducted under a variety of environmental conditions.

The representativeness methodology developed here helped inform site selection for the NGEE Arctic project, which is presently making *in situ* measurements in the Barrow Environmental Observatory. Field studies in the second phase of the project will transition to the Seward Peninsula partially because this study indicated that current conditions on the Seward Peninsula are likely to be representative of conditions on the coastal North Slope in the future. The same approach was used to characterize the representativeness of the Center for Tropical Forest Science CTFS-ForestGEO network (*Anderson-Teixeira et al.*, 2015) and will be further developed to inform site selection for the NGEE Tropics project. Since existing CTFS-ForestGEO, RAINFOR, and Fluxnet monitoring sites may be candidates for future NGEE Tropics sampling locations, an initial analysis was performed to show their multi-network representativeness globally (Figure 5.1). Additional research is needed to

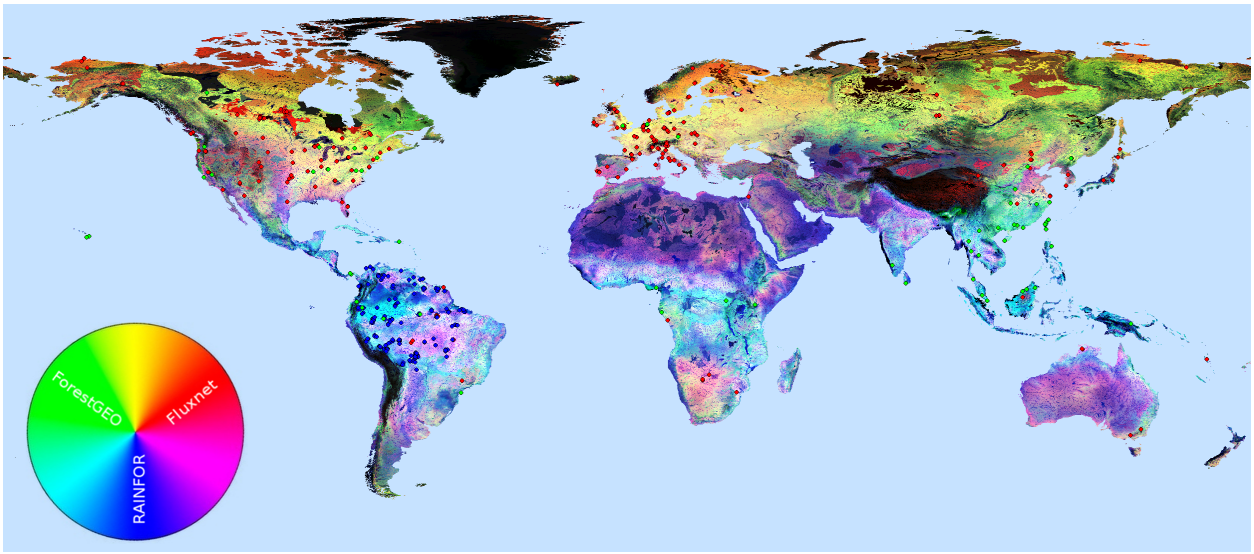

Figure 5.1: This map indicates which sampling network offers the most representative coverage at any location on Earth. Every location is made up of a combination of three primary colors for Fluxnet (red), CTFS-ForestGEO (green), and RAINFOR (blue). Light-colored regions are well represented and dark-colored regions are poorly represented by one or more of these sampling networks.

make maps of partitioned gradients like this useful for specific applications. For example, some measure of ecoregion importance, represented by vegetation productivity or biodiversity or biomass, may be used to adjust the weighting or to scale the color intensity to better identify areas that warrant additional sampling sites. The multivariate spatiotemporal clustering method used for defining ecoregions can also be applied to evaluate and compare model results. An initial study comparing temperature, precipitation, and soil moisture from 500-y business as usual simulation ensemble members was previously conducted and published (*Hoffman et al.*, 2005). Future research will extend this method by adding more variables and introducing observational data sets into the analysis. These same techniques may be applied to explore how landscapes are expected to transition as existing ecoregions shift or vanish and as alternative ecoregions immigrate under climate change scenarios. One possible next step is to investigate how zones disappear over time as a function of area within the ECP 8.5 scenario out to 2300. Is there a predictable relationship between temperature increase and areal extent for individual biomes?

The third study presented here identified mechanisms in the terrestrial biosphere and in ocean circulation that drove nonlinear ESM responses to increasing temperature and elevated CO_2. In the 22nd and 23rd centuries, these nonlinearities were expressed in feedback parameters calculated from different simulations, leading climate–carbon cycle feedback gain trajectories to diverge over time. This study showed, in particular, that using the RAD simulation to calculate climate–carbon feedback sensitivities yielded lower carbon cycle gains due primarily to the underestimate of land carbon sequestration potential from increased GPP, driven by hydrological changes and increased nitrogen mineralization. Since *Arora et al.* (2013) employed RAD simulations in the characterization of feedback responses for CMIP5 models, one important next step is to derive the climate–carbon feedback sensitivities, γ_L and γ_O, from the FC and BGC simulations instead. This will enable a more rigorous comparison between C^{4}MIP, CMIP5, and CMIP6 model results. While the differences in gain may not be large at 2100, particularly if nonlinear responses in the ocean and on land compensate for each other in the short term as they did here, this research indicated a preferred approach for deriving γ for long-term carbon cycle simulations.

Bibliography

Anav, A., P. Friedlingstein, M. Kidston, L. Bopp, P. Ciais, P. Cox, C. Jones, M. Jung, R. Myneni, and Z. Zhu (2013), Evaluating the land and ocean components of the global carbon cycle in the CMIP5 Earth System Models, *J. Clim.*, *26*(18), 6801–6843, doi:10.1175/JCLI-D-12-00417.1.

Anderson-Teixeira, K. J., S. J. Davies, A. C. Bennett, E. B. Gonzalez-Akre, H. C. Muller-Landau, S. J. Wright, K. Abu Salim, A. M. Almeyda Zambrano, A. Alonso, J. L. Baltzer, Y. Basset, N. A. Bourg, E. N. Broadbent, W. Y. Brockelman, S. Bunyavejchewin, D. F. R. P. Burslem, N. Butt, M. Cao, D. Cardenas, G. B. Chuyong, K. Clay, S. Cordell, H. S. Dattaraja, X. Deng, M. Detto, X. Du, A. Duque, D. L. Erikson, C. E. N. Ewango, G. A. Fischer, C. Fletcher, R. B. Foster, C. P. Giardina, G. S. Gilbert, N. Gunatilleke, S. Gunatilleke, Z. Hao, W. W. Hargrove, T. B. Hart, B. C. H. Hau, F. He, F. M. Hoffman, R. W. Howe, S. P. Hubbell, F. M. Inman-Narahari, P. A. Jansen, M. Jiang, D. J. Johnson, M. Kanzaki, A. R. Kassim, D. Kenfack, S. Kibet, M. F. Kinnaird, L. Korte, K. Kral, J. Kumar, A. J. Larson, Y. Li, X. Li, S. Liu, S. K. Y. Lum, J. A. Lutz, K. Ma, D. M. Maddalena, J.-R. Makana, Y. Malhi, T. Marthews, R. Mat Serudin, S. M. McMahon, W. J. McShea, H. R. Memiaghe, X. Mi, T. Mizuno, M. Morecroft, J. A. Myers, V. Novotny, A. A. de Oliveira, P. S. Ong, D. A. Orwig, R. Ostertag, J. den Ouden, G. G. Parker, R. P. Phillips, L. Sack, M. N. Sainge, W. Sang, K. Sri-ngernyuang, R. Sukumar, I.-F. Sun, W. Sungpalee, H. S. Suresh, S. Tan, S. C. Thomas, D. W. Thomas, J. Thompson, B. L. Turner, M. Uriarte, R. Valencia, M. I. Vallejo, A. Vicentini, T. Vrška, X. Wang, X. Wang, G. Weiblen, A. Wolf, H. Xu, S. Yap, and J. Zimmerman (2015), CTFS-ForestGEO: A worldwide network monitoring forests in an era of global change, *Global Change Biol.*, *21*(2), 528–549, doi:10.1111/gcb.12712.

Andres, R. J., J. S. Gregg, L. Losey, G. Marland, and T. A. Boden (2011), Monthly, global emissions of carbon dioxide from fossil fuel consumption, *Tellus B*, *63*(3), 309–327, doi:10.1111/j.1600-0889.2011.00530.x.

Andres, R. J., T. A. Boden, F.-M. Bréon, P. Ciais, S. Davis, D. Erickson, J. S. Gregg, A. Jacobson, G. Marland, J. Miller, T. Oda, J. G. J. Olivier, M. R. Raupach, P. Rayner, and K. Treanton (2012), A synthesis of carbon dioxide emissions from fossil-fuel combustion, *Biogeosci.*, *9*(5), 1845–1871, doi:10.5194/bg-9-1845-2012.

Anisimov, O. A., D. G. Vaughan, T. V. Callaghan, C. Furgal, H. Marchant, T. D. Prowse, H. Vilhjálmsson, and J. E. Walsh (2007), Polar regions (Arctic and Antarctic), in *Cli-*

mate Change 2007: Impacts, Adaptation and Vulnerability, edited by M. L. Parry, O. F. Canziani, J. P. Palutikof, P. J. van der Linden, and C. E. Hanson, pp. 653–685, Cambridge University Press, Cambridge.

Arora, V. K., and G. J. Boer (2005), A parameterization of leaf phenology for the terrestrial ecosystem component of climate models, *Global Change Biol.*, *11*(1), 39–59, doi:10.1111/j.1365-2486.2004.00890.x.

Arora, V. K., J. F. Scinocca, G. J. Boer, J. R. Christian, K. L. Denman, G. M. Flato, V. V. Kharin, W. G. Lee, and W. J. Merryfield (2011), Carbon emission limits required to satisfy future representative concentration pathways of greenhouse gases, *Geophys. Res. Lett.*, *38*(5), L05,805, doi:10.1029/2010GL046270.

Arora, V. K., G. J. Boer, P. Friedlingstein, M. Eby, C. D. Jones, J. R. Christian, G. Bonan, L. Bopp, V. Brovkin, P. Cadule, T. Hajima, T. Ilyina, K. Lindsay, J. F. Tjiputra, and T. Wu (2013), Carbon-concentration and carbon-climate feedbacks in CMIP5 Earth system models, *J. Clim.*, *26*(15), 5289–5314, doi:10.1175/JCLI-D-12-00494.1.

Arp, C. D., and B. M. Jones (2009), Geography of Alaska lake districts: Identification, description, and analysis of lake-rich regions of a diverse and dynamic state, *Scientific Investigations Report 2008-5215*, U.S. Geological Survey, 4210 University Dr., Anchorage, Alaska 99508.

Baccini, A., S. J. Goetz, W. S. Walker, N. T. Laporte, M. Sun, D. Sulla-Menashe, J. Hackler, P. S. A. Beck, R. Dubayah, M. A. Friedl, S. Samanta, and R. A. Houghton (2012), Estimated carbon dioxide emissions from tropical deforestation improved by carbon-density maps, *Nature Clim. Change*, *2*(3), 182–185, doi:10.1038/nclimate1354.

Bailey, R. G. (2009), Ecoregions of the United States, in *Ecosystem Geography*, Statistics for Social and Behavioral Sciences, pp. 93–114, Springer New York, doi:10.1007/978-0-387-89516-1_7.

Bailey, R. G., and H. C. Hogg (1986), A world ecoregions map for resource reporting, *Environ. Conserv.*, *13*(3), 195–202, doi:10.1017/S0376892900036237.

Ballantyne, A. P., C. B. Alden, J. B. Miller, P. P. Tans, and J. W. C. White (2012), Increase in observed net carbon dioxide uptake by land and oceans during the past 50 years, *Nature*, *488*(7409), 70–72, doi:10.1038/nature11299.

Bao, Q., P. Lin, T. Zhou, Y. Liu, Y. Yu, G. Wu, B. He, J. He, L. Li, J. Li, Y. Li, H. Liu, F. Qiao, Z. Song, B. Wang, J. Wang, P. Wang, X. Wang, Z. Wang, B. Wu, T. Wu, Y. Xu, H. Yu, W. Zhao, W. Zheng, and L. Zhou (2013), The Flexible Global Ocean-Atmosphere-Land System model, spectral version 2: FGOALS-s2, *Adv. Atmos. Sci.*, *30*(3), 561–576, doi:10.1007/s00376-012-2113-9.

Bentsen, M., I. Bethke, J. B. Debernard, T. Iversen, A. Kirkevåg, Ø. Seland, H. Drange, C. Roelandt, I. A. Seierstad, C. Hoose, and J. E. Kristjánsson (2013), The Norwegian Earth System Model, NorESM1-M – Part 1: Description and basic evaluation of the physical climate, *Geosci. Model Dev.*, *6*(3), 687–720, doi:10.5194/gmd-6-687-2013.

Boer, G. J., and V. K. Arora (2013), Feedbacks in emission-driven and concentration-driven global carbon budgets, *J. Clim.*, *26*(10), 3326–3341, doi:10.1175/JCLI-D-12-00365.1.

Boucher, O., and M. S. Reddy (2008), Climate trade-off between black carbon and carbon dioxide emissions, *Energ. Policy*, *36*(1), 193–200, doi:10.1016/j.enpol.2007.08.039.

Boyd, P. W., T. Jickells, C. S. Law, S. Blain, E. A. Boyle, K. O. Buesseler, K. H. Coale, J. J. Cullen, H. J. W. de Baar, M. Follows, M. Harvey, C. Lancelot, M. Levasseur, N. P. J. Owens, R. Pollard, R. B. Rivkin, J. Sarmiento, V. Schoemann, V. Smetacek, S. Takeda, A. Tsuda, S. Turner, and A. J. Watson (2007), Mesoscale iron enrichment experiments 1993–2005: Synthesis and future directions, *Science*, *315*(5812), 612–617, doi:10.1126/science.1131669.

Bradley, P. S., and U. M. Fayyad (1998), Refining initial points for k-means clustering, in *ICML '98: Proceedings of the Fifteenth International Conference on Machine Learning*, pp. 91–99, Morgan Kaufmann Publishers Inc., San Francisco, CA, USA.

Brovkin, V., T. Raddatz, C. H. Reick, M. Claussen, and V. Gayler (2009), Global biogeophysical interactions between forest and climate, *Geophys. Res. Lett.*, *36*(7), L07,405, doi:10.1029/2009GL037543.

Buesseler, K. O., J. E. Andrews, S. M. Pike, and M. A. Charette (2004), The effects of iron fertilization on carbon sequestration in the Southern Ocean, *Science*, *304*(5669), 414–417, doi:10.1126/science.1086895.

Buesseler, K. O., S. C. Doney, D. M. Karl, P. W. Boyd, K. Caldeira, F. Chai, K. H. Coale, H. J. W. de Baar, P. G. Falkowski, K. S. Johnson, R. S. Lampitt, A. F. Michaels, S. W. A. Naqvi, V. Smetacek, S. Takeda, and A. J. Watson (2008), Ocean iron fertilization–moving forward in a sea of uncertainty, *Science*, *319*(5860), 162, doi:10.1126/science.1154305.

Caldeira, K., and M. E. Wickett (2003), Oceanography: Anthropogenic carbon and ocean pH, *Nature*, *425*(6956), 365, doi:10.1038/425365a.

Cavaleri, M. A., S. C. Reed, W. K. Smith, and T. E. Wood (2015), Urgent need for warming experiments in tropical forests, *Global Change Biol.*, *21*(6), 2111–2121, doi:10.1111/gcb.12860.

Chapin, F. S., A. D. McGuire, R. W. Ruess, T. N. Hollingsworth, M. C. Mack, J. F. Johnstone, E. S. Kasischke, E. S. Euskirchen, J. B. Jones, M. T. Jorgenson, K. Kielland, G. P. Kofinas, M. R. Turetsky, J. Yarie, A. H. Lloyd, and D. L. Taylor (2010), Resilience of Alaska's boreal forest to climatic change, *Can. J. Forest Res.*, *40*(7), 1360–1370, doi:10.1139/X10-074.

Ciais, P., C. Sabine, G. Bala, L. Bopp, V. Brovkin, J. Canadell, A. Chhabra, R. DeFries, J. Galloway, M. Heimann, C. Jones, C. Le Quéré, R. B. Myneni, S. Piao, and P. Thornton (2013a), Carbon and other biogeochemical cycles, in *Stocker et al.* (2013b), pp. 465–570.

Ciais, P., C. Sabine, G. Bala, L. Bopp, V. Brovkin, J. Canadell, A. Chhabra, R. DeFries, J. Galloway, M. Heimann, C. Jones, C. Le Quéré, R. B. Myneni, S. Piao, and P. Thornton (2013b), Carbon and other biogeochemical cycles, in *Climate Change 2013: The Physical Science Basis. Contribution of Working Group I to the Fifth Assessment Report of the Intergovernmental Panel on Climate Change*, edited by T. F. Stocker, D. Qin, G.-K. Plattner, M. Tignor, S. K. Allen, J. Boschung, A. Nauels, Y. Xia, V. Bex, and P. M. Midgley, pp. 465–570, Cambridge University Press, Cambridge, United Kingdom and New York, NY, USA.

Coale, K. H., K. S. Johnson, S. E. Fitzwater, R. M. Gordon, S. Tanner, F. P. Chavez, L. Ferioli, C. Sakamoto, P. Rogers, F. Millero, P. Steinberg, P. Nightingale, D. Cooper, W. P. Cochlan, M. R. Landry, J. Constantinou, G. Rollwagen, A. Trasvina, and R. Kudela (1996), A massive phytoplankton bloom induced by an ecosystem-scale iron fertilization experiment in the equatorial Pacific Ocean, *Nature*, *383*(6600), 495–501, doi: 10.1038/383495a0.

College of Global Change and Earth System Science (2012), Beijing Normal University-Earth System Model, URL: http://esg.bnu.edu.cn/BNU_ESM_webs/htmls/index.html.

Collins, W. J., N. Bellouin, M. Doutriaux-Boucher, N. Gedney, P. Halloran, T. Hinton, J. Hughes, C. D. Jones, M. Joshi, S. Liddicoat, G. Martin, F. O'Connor, J. Rae, C. Senior, S. Sitch, I. Totterdell, A. Wiltshire, and S. Woodward (2011), Development and evaluation of an Earth-System model – HadGEM2, *Geosci. Model Dev.*, *4*(4), 1051–1075, doi:10.5194/gmd-4-1051-2011.

Committee on Designing an Arctic Observing Network, N. R. C. (2006), *Towards an Integrated Arctic Observing Network*, The National Academies Press.

Conway, T. J., P. P. Tans, L. S. Waterman, K. W. Thoning, D. R. Kitzis, K. A. Masarie, and N. Zhang (1994), Evidence for interannual variability of the carbon cycle from the National Oceanic and Atmospheric Administration/Climate Monitoring and Diagnostics Laboratory Global Air Sampling Network, *J. Geophys. Res.*, *99*(D11), 22,831–22,855, doi: 10.1029/94JD01951.

Cox, P. M., R. A. Betts, M. Collins, P. P. Harris, C. Huntingford, and C. D. Jones (2004), Amazonian forest dieback under climate-carbon cycle projections for the 21st century, *Theor. Appl. Climatol.*, *78*(1–3), 137–156, doi:10.1007/s00704-004-0049-4.

Cox, P. M., D. Pearson, B. B. Booth, P. Friedlingstein, C. Huntingford, C. D. Jones, and C. M. Luke (2013), Sensitivity of tropical carbon to climate change constrained by carbon dioxide variability, *Nature*, *494*(7437), 341–344, doi:10.1038/nature11882.

Dai, Y., X. Zeng, R. E. Dickinson, I. Baker, G. B. Bonan, M. G. Bosilovich, A. S. Denning, P. A. Dirmeyer, P. R. Houser, G. Niu, K. W. Oleson, C. A. Schlosser, and Z.-L. Yang (2003), The common land model, *Bull. Am. Meteorol. Soc.*, *84*(8), 1013–1023, doi: 10.1175/BAMS-84-8-1013.

Dai, Y., R. E. Dickinson, and Y.-P. Wang (2004), A two-big-leaf model for canopy temperature, photosynthesis, and stomatal conductance, *J. Clim.*, *17*(12), 2281–2299, doi: 10.1175/1520-0442(2004)017<2281:ATMFCT>2.0.CO;2.

Danabasoglu, G., and J. Marshall (2007), Effects of vertical variations of thickness diffusivity in an ocean general circulation model, *Ocean Model.*, *18*(2), 122–141, doi: 10.1016/j.ocemod.2007.03.006.

Danabasoglu, G., R. Ferrari, and J. C. McWilliams (2008), Sensitivity of an ocean general circulation model to a parameterization of near-surface eddy fluxes, *J. Clim.*, *21*(6), doi: 10.1175/2007JCLI1508.1.

Danabasoglu, G., S. C. Bates, B. P. Briegleb, S. R. Jayne, M. Jochum, W. G. Large, S. Peacock, and S. G. Yeager (2012), The CCSM4 ocean component, *J. Clim.*, *25*(5), 1361–1389, doi:10.1175/JCLI-D-11-00091.1.

Davidson, E. A., and I. A. Janssens (2006), Temperature sensitivity of soil carbon decomposition and feedbacks to climate change, *Nature*, *440*(7081), 165–173, doi: 10.1038/nature04514.

Denman, K. L., G. Brasseur, A. Chidthaisong, P. Ciais, P. M. Cox, R. E. Dickinson, D. Hauglustaine, C. Heinze, E. Holland, D. Jacob, U. Lohmann, S. Ramachandran, P. L. da Silva Dias, S. C. Wofsy, and X. Zhang (2007), Couplings between changes in the climate system and biogeochemistry, in *Solomon et al.* (2007), pp. 499–588.

Doney, S. C., K. Lindsay, K. Caldeira, J.-M. Campin, H. Drange, J.-C. Dutay, M. Follows, Y. Gao, A. Gnanadesikan, N. Gruber, A. Ishida, F. Joos, G. Madec, E. Maier-Reimer, J. C. Marshall, R. J. Matear, P. Monfray, A. Mouchet, R. Najjar, J. C. Orr, G.-K. Plattner, J. Sarmiento, R. Schlitzer, R. Slater, I. J. Totterdell, M.-F. Weirig, Y. Yamanaka, and A. Yool (2004), Evaluating global ocean carbon models: The importance of realistic physics, *Global Biogeochem. Cycles*, *18*(3), GB3017, doi:10.1029/2003GB002150.

Doney, S. C., V. J. Fabry, R. A. Feely, and J. A. Kleypas (2009a), Ocean acification: The other CO_2 problem, *Annu. Rev. Mar. Sci.*, *1*(1), 169–192, doi: 10.1146/annurev.marine.010908.163834.

Doney, S. C., I. Lima, J. K. Moore, K. Lindsay, M. J. Behrenfeld, T. K. Westberry, N. Mahowald, D. M. Glover, and T. Takahashi (2009b), Skill metrics for confronting global upper ocean ecosystem-biogeochemistry models against field and remote sensing data, *J. Mar. Syst.*, *76*(1–2), 95–112, doi:10.1016/j.jmarsys.2008.05.015.

Downes, S. M., A. Gnanadesikan, S. M. Griffies, and J. L. Sarmiento (2011), Water mass exchange in the Southern Ocean in coupled climate models, *J. Phys. Oceanogr.*, *41*(9), 1756–1771, doi:10.1175/2011JPO4586.1.

Dufresne, J.-L., M.-A. Foujols, S. Denvil, A. Caubel, O. Marti, O. Aumont, Y. Balkanski, S. Bekki, H. Bellenger, R. Benshila, S. Bony, L. Bopp, P. Braconnot, P. Brockmann, P. Cadule, F. Cheruy, F. Codron., A. Cozic, D. Cugnet, N. Noblet, J.-P. Duvel, C. Ethé,

L. Fairhead, T. Fichefet, S. Flavoni, P. Friedlingstein, J.-Y. Grandpeix, L. Guez, E. Guilyardi, D. Hauglustaine, F. Hourdin, A. Idelkadi, J. Ghattas, S. Joussaume, M. Kageyama, G. Krinner, S. Labetoulle, A. Lahellec, M.-P. Lefebvre, F. Lefevre, C. Levy, Z. X. Li, J. Lloyd, F. Lott, G. Madec, M. Mancip, M. Marchand, S. Masson, Y. Meurdesoif, J. Mignot, I. Musat, S. Parouty, J. Polcher, C. Rio, M. Schulz, D. Swingedouw, S. Szopa, C. Talandier, P. Terray, N. Viovy, and N. Vuichard (2013), Climate change projections using the IPSL-CM5 Earth System Model: From CMIP3 to CMIP5, *Clim. Dyn.*, *40*(9–10), 2123–2165, doi:10.1007/s00382-012-1636-1.

Dunne, J. P., J. G. John, A. J. Adcroft, S. M. Griffies, R. W. Hallberg, E. Shevliakova, R. J. Stouffer, W. Cooke, K. A. Dunne, M. J. Harrison, J. P. Krasting, S. L. Malyshev, P. C. D. Milly, P. J. Phillipps, L. T. Sentman, B. L. Samuels, M. J. Spelman, M. Winton, A. T. Wittenberg, and N. Zadeh (2012), GFDL's ESM2 global coupled climate-carbon Earth System Models. Part I: Physical formulation and baseline simulation characteristics, *J. Clim.*, *25*(19), 6646–6665, doi:10.1175/JCLI-D-11-00560.1.

Dunne, J. P., J. G. John, E. Shevliakova, R. J. Stouffer, J. P. Krasting, S. L. Malyshev, P. C. D. Milly, L. T. Sentman, A. J. Adcroft, W. Cooke, K. A. Dunne, S. M. Griffies, R. W. Hallberg, M. J. Harrison, H. Levy, A. T. Wittenberg, P. J. Phillips, and N. Zadeh (2013), GFDL's ESM2 global coupled climate-carbon Earth System Models. Part II: Carbon system formulation and baseline simulation characteristics, *J. Clim.*, *26*(7), 2247–2267, doi:10.1175/JCLI-D-12-00150.1.

Dutay, J.-C., J. L. Bullister, S. C. Doney, J. C. Orr, R. Najjar, K. Caldeira, J.-M. Campin, H. Drange, M. Follows, Y. Gao, N. Gruber, M. W. Hecht, A. Ishida, F. Joos, K. Lindsay, G. Madec, E. Maier-Reimer, J. C. Marshall, R. J. Matear, P. Monfray, A. Mouchet, G.-K. Plattner, J. Sarmiento, R. Schlitzer, R. Slater, I. J. Totterdell, M.-F. Weirig, Y. Yamanaka, and A. Yool (2002), Evaluation of ocean model ventilation with CFC-11: Comparison of 13 global ocean models, *Ocean Model.*, *4*(2), 89–120, doi:10.1016/S1463-5003(01)00013-0.

Etheridge, D. M., L. P. Steele, R. L. Langenfelds, R. J. Francey, J.-M. Barnola, and V. I. Morgan (1996), Natural and anthropogenic changes in atmospheric CO_2 over the last 1000 years from air in Antarctic ice and firn, *J. Geophys. Res.*, *101*(D2), 4115–4128, doi:10.1029/95JD03410.

Farquhar, G. D., S. Caemmerer, and J. A. Berry (1980), A biochemical model of photosynthetic CO_2 assimilation in leaves of C_3 species, *Planta*, *149*(1), 78–90, doi:10.1007/BF00386231.

Fitzpatrick, M., and W. Hargrove (2009), The projection of species distribution models and the problem of non-analog climate, *Biodivers. Conserv.*, *18*(8), 2255–2261, doi:10.1007/s10531-009-9584-8.

Flanner, M. G., C. S. Zender, P. G. Hess, N. M. Mahowald, T. H. Painter, V. Ramanathan, and P. J. Rasch (2009), Springtime warming and reduced snow cover from carbonaceous particles, *Atmos. Chem. Phys.*, *9*(7), 2481–2497, doi:10.5194/acp-9-2481-2009.

Friedlingstein, P., G. Joel, C. B. Field, and I. Y. Fung (1999), Toward an allocation scheme for global terrestrial carbon models, *Global Change Biol.*, *5*(7), 755–770, doi:10.1046/j.1365-2486.1999.00269.x.

Friedlingstein, P., J.-L. Dufresne, P. M. Cox, and P. Rayner (2003), How positive is the feedback between climate change and the carbon cycle?, *Tellus*, *55B*(2), 692–700, doi:10.1034/j.1600-0889.2003.01461.x.

Friedlingstein, P., P. M. Cox, R. A. Betts, L. Bopp, W. von Bloh, V. Brovkin, S. C. Doney, M. Eby, I. Fung, B. Govindasamy, J. John, C. D. Jones, F. Joos, T. Kato, M. Kawamiya, W. Knorr, K. Lindsay, H. D. Matthews, T. Raddatz, P. Rayner, C. Reick, E. Roeckner, K.-G. Schnitzler, R. Schnur, K. Strassmann, S. Thompson, A. J. Weaver, C. Yoshikawa, and N. Zeng (2006), Climate-carbon cycle feedback analysis, results from the C^4MIP model intercomparison, *J. Clim.*, *19*(14), 3373–3353, doi:10.1175/JCLI3800.1.

Gallant, A. L., E. F. Binnian, J. M. Omernik, and M. B. Shasby (1995), Ecoregions of Alaska, *Professional paper 1567*, U.S. Geological Survey.

Gent, P. R. (2011), The Gent–McWilliams parameterization: 20/20 hindsight, *Ocean Model.*, *39*(1–2), 2–9, doi:10.1016/j.ocemod.2010.08.002.

Gent, P. R., and J. C. McWilliams (1990), Isopycnal mixing in ocean circulation models, *J. Phys. Oceanogr.*, *20*(1), 150–155, doi:10.1175/1520-0485(1990)020¡0150:IMIOCM¿2.0.CO;2.

Gent, P. R., G. Danabasoglu, L. J. Donner, M. M. Holland, E. C. Hunke, S. R. Jayne, D. M. Lawrence, R. B. Neale, P. J. Rasch, M. Vertenstein, P. H. Worley, Z.-L. Yang, and M. Zhang (2011), The Community Climate System Model version 4, *J. Clim.*, *24*(19), 4973–4991, doi:10.1175/2011JCLI4083.1.

Gillett, N. P., V. K. Arora, D. Matthews, and M. R. Allen (2013), Constraining the ratio of global warming to cumulative CO_2 emissions using CMIP5 simulations, *J. Clim.*, *26*(18), 6844–6858, doi:10.1175/JCLI-D-12-00476.1.

Girod, C. M., G. C. Hurtt, S. Frolking, J. D. Aber, and A. W. King (2007), The tension between fire risk and carbon storage: Evaluating U.S. carbon and fire management strategies through ecosystem models, *Earth Interact.*, *11*(2), 1–33, doi:10.1175/EI188.1.

Gregory, J. M., C. D. Jones, P. Cadule, and P. Friedlingstein (2009), Quantifying carbon cycle feedbacks, *J. Clim.*, *22*(19), 5232–5250, doi:10.1175/2009JCLI2949.1.

Gruber, N., M. Gloor, S. E. Mikaloff Fletcher, S. C. Doney, S. Dutkiewicz, M. J. Follows, M. Gerber, A. R. Jacobson, F. Joos, K. Lindsay, D. Menemenlis, A. Mouchet, S. A. Müller, J. L. Sarmiento, and T. Takahashi (2009), Oceanic sources, sinks, and transport of atmospheric CO_2, *Global Biogeochem. Cycles*, *23*(1), GB1005, doi:10.1029/2008GB003349.

Hall, A., and X. Qu (2006), Using the current seasonal cycle to constrain snow albedo feedback in future climate change, *Geophys. Res. Lett.*, *33*(3), L03,502, doi:10.1029/2005GL025127.

Hansen, J., A. Lacis, D. Rind, G. Russell, P. Stone, I. Fung, R. Ruedy, and J. Lerner (1984), *Climate Sensitivity: Analysis of Feedback Mechanism*, *Geophys. Monogr.*, vol. 29, pp. 130–163, Amer. Geophys. Union.

Hansen, M. C., S. V. Stehman, and P. V. Potapov (2010), Quantification of global gross forest cover loss, *Proc. Nat. Acad. Sci.*, *107*(19), 8650–8655, doi:10.1073/pnas.0912668107.

Hargrove, W. W., and F. M. Hoffman (1999), Using multivariate clustering to characterize ecoregion borders, *Comput. Sci. Eng.*, *1*(4), 18–25, doi:10.1109/5992.774837.

Hargrove, W. W., and F. M. Hoffman (2004), Potential of multivariate quantitative methods for delineation and visualization of ecoregions, *Environ. Manage.*, *34*(Supplement 1), S39–S60, doi:10.1007/s00267-003-1084-0.

Hargrove, W. W., F. M. Hoffman, and T. Sterling (2001), The do-it-yourself supercomputer, *Sci. Am.*, *265*(2), 72–79.

Hargrove, W. W., F. M. Hoffman, and B. E. Law (2003), New analysis reveals representativeness of the AmeriFlux Network, *Eos Trans. AGU*, *84*(48), 529, 535, doi:10.1029/2003EO480001.

Hargrove, W. W., F. M. Hoffman, and P. F. Hessburg (2006), Mapcurves: A quantitative method for comparing categorical maps, *J. Geograph. Syst.*, *8*(2), 187–208, doi:10.1007/s10109-006-0025-x.

Harris, N. L., S. Brown, S. C. Hagen, S. S. Saatchi, S. Petrova, W. Salas, M. C. Hansen, P. V. Potapov, and A. Lotsch (2012), Baseline map of carbon emissions from deforestation in tropical regions, *Science*, *336*(6088), 1573–1576, doi:10.1126/science.1217962.

Hartigan, J. A. (1975), *Clustering Algorithms*, 351 pp., John Wiley & Sons.

Hinzman, L., N. Bettez, W. Bolton, F. Chapin, M. Dyurgerov, C. Fastie, B. Griffith, R. Hollister, A. Hope, H. Huntington, A. Jensen, G. Jia, T. Jorgenson, D. Kane, D. Klein, G. Kofinas, A. Lynch, A. Lloyd, A. McGuire, F. Nelson, W. Oechel, T. Osterkamp, C. Racine, V. Romanovsky, R. Stone, D. Stow, M. Sturm, C. Tweedie, G. Vourlitis, M. Walker, D. Walker, P. Webber, J. Welker, K. Winker, and K. Yoshikawa (2005), Evidence and implications of recent climate change in Northern Alaska and other Arctic regions, *Clim. Change*, *72*(3), 251–298, doi:10.1007/s10584-005-5352-2.

Hoffman, F. M., and W. W. Hargrove (1999), Multivariate geographic clustering using a Beowulf-style parallel computer, in *Proceedings of the International Conference on Parallel and Distributed Processing Techniques and Applications (PDPTA '99)*, vol. III, edited by H. R. Arabnia, pp. 1292–1298, CSREA Press.

Hoffman, F. M., W. W. Hargrove, D. J. Erickson, and R. J. Oglesby (2005), Using clustered climate regimes to analyze and compare predictions from fully coupled general circulation models, *Earth Interact.*, *9*(10), 1–27, doi:10.1175/EI110.1.

Hoffman, F. M., W. W. Hargrove, R. T. Mills, S. Mahajan, D. J. Erickson, and R. J. Oglesby (2008), Multivariate Spatio-Temporal Clustering (MSTC) as a data mining tool for environmental applications, in *Proceedings of the iEMSs Fourth Biennial Meeting: International Congress on Environmental Modelling and Software Society (iEMSs 2008)*, edited by M. Sànchez-Marrè, J. Béjar, J. Comas, A. E. Rizzoli, and G. Guariso, pp. 1774–1781.

Hoffman, F. M., J. Kumar, R. T. Mills, W. W. Hargrove, P. E. Thornton, and S. D. Wullschlegar (2013), A geospatiotemporal analysis method for site selection for Next Generation Ecosystem Experiments (NGEE), *Technical Memorandum ORNL/TM-2013/196*, Oak Ridge National Laboratory.

Hoffman, F. M., J. T. Randerson, V. K. Arora, Q. Bao, P. Cadule, D. Ji, C. D. Jones, M. Kawamiya, S. Khatiwala, K. Lindsay, A. Obata, E. Shevliakova, K. D. Six, J. F. Tjiputra, E. M. Volodin, and T. Wu (2014), Causes and implications of persistent atmospheric carbon dioxide biases in Earth System Models, *J. Geophys. Res. Biogeosci.*, *119*(2), 141–162, doi:10.1002/2013JG002381.

Houghton, R. A., G. R. van der Werf, R. S. DeFries, M. C. Hansen, J. I. House, C. Le Quéré, J. Pongratz, and N. Ramankutty (2012), Chapter G2: Carbon emissions from land use and land-cover change, *Biogeosci. Discuss.*, *9*(1), 835–878, doi:10.5194/bgd-9-835-2012.

Hudson, B. D. (1992), The soil survey as paradigm-based science, *Soil Sci. Soc. Am. J.*, *56*(3), 836–841, doi:10.2136/sssaj1992.03615995005600030027x.

Hunke, E. C., W. H. Lipscomb, A. K. Turner, N. Jeffery, and S. Elliott (2013), CICE: The Los Alamos sea ice model documentation and software user's manual, version 5.0, *Tech. Rep. LA-CC-06-012*, Los Alamos National Laboratory, Los Alamos, New Mexico, USA.

Huntingford, C., P. Zelazowski, D. Galbraith, L. M. Mercado, S. Sitch, R. Fisher, M. Lomas, A. P. Walker, C. D. Jones, B. B. B. Booth, Y. Malhi, D. Hemming, G. Kay, P. Good, S. L. Lewis, O. L. Phillips, O. K. Atkin, J. Lloyd, E. Gloor, J. Zaragoza-Castells, P. Meir, R. Betts, P. P. Harris, C. Nobre, J. Marengo, and P. M. Cox (2013), Simulated resilience of tropical rainforests to CO_2-induced climate change, *Nature Geosci.*, *6*(4), 268–273, doi:10.1038/ngeo1741.

Hurrell, J. W., M. M. Holland, P. R. Gent, S. Ghan, J. E. Kay, P. J. Kushner, J.-F. Lamarque, W. G. Large, D. Lawrence, K. Lindsay, W. H. Lipscomb, M. C. Long, N. Mahowald, D. R. Marsh, R. B. Neale, P. Rasch, S. Vavrus, M. Vertenstein, D. Bader, W. D. Collins, J. J. Hack, J. Kiehl, and S. Marshall (2013), The Community Earth System Model: A framework for collaborative research, *Bull. Am. Meteorol. Soc.*, *94*(9), 1339–1360, doi: 10.1175/BAMS-D-12-00121.1.

Hurrell, J. W., M. M. Holland, P. R. Gent, S. Ghan, J. E. Kay, P. J. Kushner, J.-F. Lamarque, W. G. Large, D. Lawrence, K. Lindsay, W. H. Lipscomb, M. C. Long, N. Mahowald, D. R. Marsh, R. B. Neale, P. Rasch, S. Vavrus, M. Vertenstein, D. Bader, W. D. Collins, J. J. Hack, J. Kiehl, and S. Marshall (in press), The Community Earth System Model: A

framework for collaborative research, *Bull. Am. Meteorol. Soc.*, doi:10.1175/BAMS-D-12-00121.

Hurtt, G. C., S. W. Pacala, P. R. Moorcroft, J. Caspersen, E. Shevliakova, R. A. Houghton, and B. Moore (2002), Projecting the future of the U.S. carbon sink, *Proc. Nat. Acad. Sci.*, *99*(3), 1389–1394, doi:10.1073/pnas.012249999.

Hurtt, G. C., L. P. Chini, S. Frolking, R. A. Betts, J. Feddema, G. Fischer, J. P. Fisk, K. Hibbard, R. A. Houghton, A. Janetos, C. D. Jones, G. Kindermann, T. Kinoshita, K. Klein Goldewijk, K. Riahi, E. Shevliakova, S. Smith, E. Stehfest, A. Thomson, P. Thornton, D. P. van Vuuren, and Y. P. Wang (2011), Harmonization of land-use scenarios for the period 1500–2100: 600years of global gridded annual land-use transitions, wood harvest, and resulting secondary lands, *Clim. Change*, *109*(1–2), 117–161, doi:10.1007/s10584-011-0153-2.

Hutchinson, G. E. (1957), Concluding remarks, in *Cold Spring Harbor Symposia on Quantitative Biology*, vol. 22, pp. 415–427, reprinted in 1991: Classics in Theoretical Biology, *Bull. Math. Biol.* 53:193–213.

IPCC (2007), Summary for policymakers, in *Solomon et al.* (2007).

IPCC (2013), Summary for policymakers, in *Stocker et al.* (2013b).

Iversen, T., M. Bentsen, I. Bethke, J. B. Debernard, A. Kirkevåg, Ø. Seland, H. Drange, J. E. Kristjánsson, I. Medhaug, M. Sand, and I. A. Seierstad (2013), The Norwegian Earth System Model, NorESM1-M – Part 2: Climate response and scenario projections, *Geosci. Model Dev.*, *6*(2), 389–415, doi:10.5194/gmd-6-389-2013.

Jahn, A., K. Sterling, M. M. Holland, J. E. Kay, J. A. Maslanik, C. M. Bitz, D. A. Bailey, J. Stroeve, E. C. Hunke, W. H. Lipscomb, and D. A. Pollak (2012), Late-twentieth-century simulation of Arctic sea ice and ocean properties in the CCSM4, *J. Clim.*, *25*(5), 1431–1452, doi:10.1175/JCLI-D-11-00201.1.

Jensen, M. E., I. A. Goodman, P. S. Bourgeron, N. L. Poff, and C. K. Brewer (2001), Effectiveness of biophysical criteria in the hierarchical classification of drainage basins, *J. Am. Water Resour. Assoc.*, *37*, 1155–1167.

Jones, C., E. Robertson, V. Arora, P. Friedlingstein, E. Shevliakova, L. Bopp, V. Brovkin, T. Hajima, E. Kato, M. Kawamiya, S. Liddicoat, K. Lindsay, C. H. Reick, C. Roelandt, J. Segschneider, and J. Tjiputra (2013), 21st Century compatible CO_2 emissions and airborne fraction simulated by CMIP5 Earth System Models under 4 Representative Concentration Pathways, *J. Clim.*, *26*(13), 4398–4413, doi:10.1175/JCLI-D-12-00554.1.

Jones, C. D., J. K. Hughes, N. Bellouin, S. C. Hardiman, G. S. Jones, J. Knight, S. Liddicoat, F. M. O'Connor, R. J. Andres, C. Bell, K.-O. Boo, A. Bozzo, N. Butchart, P. Cadule, K. D. Corbin, M. Doutriaux-Boucher, P. Friedlingstein, J. Gornall, L. Gray, P. R. Halloran, G. Hurtt, W. J. Ingram, J.-F. Lamarque, R. M. Law, M. Meinshausen, S. Osprey, E. J. Palin, L. Parsons Chini, T. Raddatz, M. G. Sanderson, A. A. Sellar, A. Schurer,

P. Valdes, N. Wood, S. Woodward, M. Yoshioka, and M. Zerroukat (2011), The HadGEM2-ES implementation of CMIP5 centennial simulations, *Geosci. Model Dev.*, *4*(3), 543–570, doi:10.5194/gmd-4-543-2011.

Keller, M., D. Schimel, W. Hargrove, and F. Hoffman (2008), A continental strategy for the National Ecological Observatory Network, *Front. Ecol. Environ.*, *6*(5), 282–284, doi:10.1890/1540-9295(2008)6[282:ACSFTN]2.0.CO;2, special Issue on Continental-Scale Ecology.

Keppel-Aleks, G., J. T. Randerson, K. Lindsay, B. B. Stephens, J. K. Moore, S. C. Doney, P. E. Thornton, N. M. Mahowald, F. M. Hoffman, C. Sweeney, P. P. Tans, P. O. Wennberg, and S. C. Wofsy (2013), Atmospheric carbon dioxide variability in the Community Earth System Model: Evaluation and transient dynamics during the 20$^{\text{th}}$ and 21$^{\text{st}}$ centuries, *J. Clim.*, *26*(13), 4447–4475, doi:10.1175/JCLI-D-12-00589.1.

Khatiwala, S., F. Primeau, and T. Hall (2009), Reconstruction of the history of anthropogenic CO_2 concentrations in the ocean, *Nature*, *462*(7271), 346–349, doi:10.1038/nature08526.

Khatiwala, S., T. Tanhua, S. Mikaloff Fletcher, M. Gerber, S. C. Doney, H. D. Graven, N. Gruber, G. A. McKinley, A. Murata, A. F. Ríos, and C. L. Sabine (2013), Global ocean storage of anthropogenic carbon, *Biogeosci.*, *10*(4), 2169–2191, doi:10.5194/bg-10-2169-2013.

Koven, C. D., B. Ringeval, P. Friedlingstein, P. Ciais, P. Cadule, D. Khvorostyanov, G. Krinner, and C. Tarnocai (2011), Permafrost carbon-climate feedbacks accelerate global warming, *Proc. Nat. Acad. Sci.*, *108*(36), 14,769–14,774, doi:10.1073/pnas.1103910108.

Koven, C. D., D. M. Lawrence, and W. J. Riley (2015), Permafrost carbon–climate feedback is sensitive to deep soil carbon decomposability but not deep soil nitrogen dynamics, *Proc. Nat. Acad. Sci.*, *112*(12), 3752–3757, doi:10.1073/pnas.1415123112.

Krohn, W. B., R. B. Boone, and S. L. Painton (1999), Quantitative delineation and characterization of hierarchical biophysical regions of Maine, *Northeastern Naturalist*, *6*(2), 139–164.

Kumar, J., R. T. Mills, F. M. Hoffman, and W. W. Hargrove (2011), Parallel k-means clustering for quantitative ecoregion delineation using large data sets, in *Proceedings of the International Conference on Computational Science (ICCS 2011)*, *Procedia Comput. Sci.*, vol. 4, edited by M. Sato, S. Matsuoka, P. M. Sloot, G. D. van Albada, and J. Dongarra, pp. 1602–1611, Elsevier, Amsterdam, doi:10.1016/j.procs.2011.04.173.

Lau, W. K. M., and K.-M. Kim (2015), Robust Hadley Circulation changes and increasing global dryness due to CO_2 warming from CMIP5 model projections, *Proc. Nat. Acad. Sci.*, *112*(12), 3630–3635, doi:10.1073/pnas.1418682112.

Lawrence, D. M., K. W. Oleson, M. G. Flanner, C. G. Fletcher, P. J. Lawrence, S. Levis, S. C. Swenson, and G. B. Bonan (2012a), The CCSM4 land simulation, 1850–2005: Assessment of surface climate and new capabilities, *J. Clim.*, *25*(7), 2240–2260, doi:10.1175/JCLI-D-11-00103.1.

Lawrence, P. J., J. J. Feddema, G. B. Bonan, G. A. Meehl, B. C. O'Neill, K. W. Oleson, S. Levis, D. M. Lawrence, E. Kluzek, K. Lindsay, and P. E. Thornton (2012b), Simulating the biogeochemical and biogeophysical impacts of transient land cover change and wood harvest in the Community Climate System Model (CCSM4) from 1850 to 2100, *J. Clim.*, *25*(9), 3071–3095, doi:10.1175/JCLI-D-11-00256.1.

Le Quéré, C., R. J. Andres, T. Boden, T. Conway, R. A. Houghton, J. House, G. Marland, G. Peters, G. van der Werf, A. Ahlström, R. M. Andrew, L. Bopp, J. G. Canadell, P. Ciais, S. C. Doney, C. Enright, P. Friedlingstein, C. Huntingford, A. K. Jain, C. Jourdain, E. Kato, R. F. Keeling, K. Klein Goldewijk, S. Levis, P. Levy, M. Lomas, B. Poulter, M. R. Raupach, J. Schwinger, S. Sitch, B. D. Stocker, N. Viovy, S. Zaehle, and N. Zeng (2013), The global carbon budget 1959–2011, *Earth Syst. Sci. Data*, *5*(1), 165–185, doi:10.5194/essd-5-165-2013.

Lee, K., C. L. Sabine, T. Tanhua, T.-W. Kim, R. A. Feely, and H.-C. Kim (2011), Roles of marginal seas in absorbing and storing fossil fuel CO_2, *Energy Environ. Sci.*, *4*(4), 1133–1146, doi:10.1039/C0EE00663G.

Lin, P., Y. Yu, and H. Liu (2013), Long-term stability and oceanic mean state simulated by the coupled model FGOALS-s2, *Adv. Atmos. Sci.*, *30*(1), 175–192, doi:10.1007/s00376-012-2042-7.

Lindsay, K., G. B. Bonan, S. C. Doney, F. M. Hoffman, D. M. Lawrence, M. C. Long, N. M. Mahowald, J. K. Moore, J. T. Randerson, and P. E. Thornton (2014), Preindustrial-control and twentieth-century carbon cycle experiments with the Earth system model CESM1(BGC), *J. Clim.*, *27*(24), 8981–9005, doi:10.1175/JCLI-D-12-00565.1.

Litton, C. M., J. W. Raich, and M. G. Ryan (2007), Carbon allocation in forest ecosystems, *Global Change Biol.*, *13*(10), 2089–2109, doi:10.1111/j.1365-2486.2007.01420.x.

Liu, H., P. Lin, Y. Yu, and X. Zhang (2012), The baseline evaluation of LASG/IAP Climate system Ocean Model (LICOM) version 2, *Acta Meteor. Sinica*, *26*(3), 318–329, doi:10.1007/s13351-012-0305-y.

Lobell, D. B., W. Schlenker, and J. Costa-Roberts (2011), Climate trends and global crop production since 1980, *Science*, *333*(6042), 616–620, doi:10.1126/science.1204531.

Long, M. C., K. Lindsay, S. Peacock, J. K. Moore, and S. C. Doney (2013), Twentieth-century oceanic carbon uptake and storage in CESM1(BGC), *J. Clim.*, *26*(18), 6775–6800, doi:10.1175/JCLI-D-12-00184.1.

Luo, Y., D. Hui, and D. Zhang (2006), Elevated CO_2 stimulates net accumulations of carbon and nitrogen in land ecosystems: A meta-analysis, *Ecology*, *87*(1), 53–63, doi:10.1890/04-1724.

Luo, Y. Q., J. T. Randerson, G. Abramowitz, C. Bacour, E. Blyth, N. Carvalhais, P. Ciais, D. Dalmonech, J. B. Fisher, R. Fisher, P. Friedlingstein, K. Hibbard, F. Hoffman, D. Huntzinger, C. D. Jones, C. Koven, D. Lawrence, D. J. Li, M. Mahecha, S. L. Niu,

R. Norby, S. L. Piao, X. Qi, P. Peylin, I. C. Prentice, W. Riley, M. Reichstein, C. Schwalm, Y. P. Wang, J. Y. Xia, S. Zaehle, and X. H. Zhou (2012), A framework for benchmarking land models, *Biogeosci.*, *9*(10), 3857–3874, doi:10.5194/bg-9-3857-2012.

Mahinthakumar, G., F. M. Hoffman, W. W. Hargrove, and N. T. Karonis (1999), Multivariate geographic clustering in a metacomputing environment using Globus, in *Supercomputing '99: Proceedings of the 1999 ACM/IEEE conference on Supercomputing (CDROM)*, Supercomputing '99, ACM Press, New York, NY, USA, doi:10.1145/331532.331537.

Maier-Reimer, E., I. Kriest, J. Segschneider, and P. Wetzel (2005), The HAMburg Ocean Carbon Cycle model HAMOCC 5.1 – Technical description, Release 1.1, *Tech. rep.*, Max-Planck Institute for Meteorology.

Manning, A. C., and R. F. Keeling (2006), Global oceanic and land biotic carbon sinks from the Scripps atmospheric oxygen flask sampling network, *Tellus*, *58*(2), 95–116, doi: 10.1111/j.1600-0889.2006.00175.x.

Matsumoto, K., J. L. Sarmiento, R. M. Key, O. Aumont, J. L. Bullister, K. Caldeira, J.-M. Campin, S. C. Doney, H. Drange, J.-C. Dutay, M. Follows, Y. Gao, A. Gnanadesikan, N. Gruber, A. Ishida, F. Joos, K. Lindsay, E. Maier-Reimer, J. C. Marshall, R. J. Matear, P. Monfray, A. Mouchet, R. Najjar, G.-K. Plattner, R. Schlitzer, R. Slater, P. S. Swathi, I. J. Totterdell, M.-F. Weirig, Y. Yamanaka, A. Yool, and J. C. Orr (2004), Evaluation of ocean carbon cycle models with data-based metrics, *Geophys. Res. Lett.*, *31*(7), L07,303, doi:10.1029/2003GL018970.

McGuire, A. D., L. G. Anderson, T. R. Christensen, S. Dallimore, L. Guo, D. J. Hayes, M. Heimann, T. D. Lorenson, R. W. Macdonald, and N. Roulet (2009), Sensitivity of the carbon cycle in the Arctic to climate change, *Ecol. Monogr.*, *79*(4), 523–553, doi: 10.1890/08-2025.1.

McMahon, G., S. M. Gregonis, S. W. Waltman, J. M. Omernik, T. D. Thorson, J. A. Freeouf, A. H. Rorick, and J. E. Keys (2001), Developing a spatial framework of common ecological regions for the conterminous united states, *Environ. Manage.*, *28*(3), 293–316, doi:10.1007/s0026702429.

Meehl, G. A., W. M. Washington, J. M. Arblaster, A. Hu, H. Teng, C. Tebaldi, B. N. Sanderson, J.-F. Lamarque, A. Conley, W. G. Strand, and J. B. White (2012), Climate system response to external forcings and climate change projections in CCSM4, *J. Clim.*, *25*(11), 3661–3683, doi:10.1175/JCLI-D-11-00240.1.

Meehl, G. A., W. M. Washington, J. M. Arblaster, A. Hu, H. Teng, J. E. Kay, A. Gettelman, D. M. Lawrence, B. M. Sanderson, and W. G. Strand (2013), Climate change projections in CESM1(CAM5) compared to CCSM4, *J. Clim.*, *17*(6), 6287–6308, doi:10.1175/JCLI-D-12-00572.1.

Meinshausen, M., S. Smith, K. Calvin, J. Daniel, M. Kainuma, J.-F. Lamarque, K. Matsumoto, S. Montzka, S. Raper, K. Riahi, A. Thomson, G. Velders, and D. P. van Vuuren

(2011), The RCP greenhouse gas concentrations and their extensions from 1765 to 2300, *Clim. Change*, *109*(1), 213–241, doi:10.1007/s10584-011-0156-z.

Moore, J. K., K. Lindsay, S. C. Doney, M. C. Long, and K. Misumi (2013), Marine ecosystem dynamics and biogeochemical cycling in the Community Earth System Model [CESM1(BGC)]: Comparison of the 1990s with the 2090s under the RCP4.5 and RCP8.5 scenarios, *J. Clim.*, *26*(23), 9291–9312, doi:10.1175/JCLI-D-12-00566.1.

Moss, R. H., J. A. Edmonds, K. A. Hibbard, M. R. Manning, S. K. Rose, D. P. van Vuuren, T. R. Carter, S. Emori, M. Kainuma, T. Kram, G. A. Meehl, J. F. B. Mitchell, N. Nakicenovic, K. Riahi, S. J. Smith, R. J. Stouffer, A. M. Thomson, J. P. Weyant, and T. J. Wilbanks (2010), The next generation of scenarios for climate change research and assessment, *Nature*, *463*(7282), 747–756, doi:10.1038/nature08823.

Nakano, H., H. Tsujino, M. Hirabara, T. Yasuda, T. Motoi, M. Ishii, and G. Yamanaka (2011), Uptake mechanism of anthropogenic CO_2 in the Kuroshio Extension region in an ocean general circulation model, *J. Oceanogr.*, *67*(6), 765–783, doi:10.1007/s10872-011-0075-7.

Nakićenović, N., J. Alcamo, G. Davis, B. de Vries, J. Fenhann, S. Gaffin, K. Gregory, A. Grübler, T. Y. Jung, T. Kram, E. L. La Rovere, L. Michaelis, S. Mori, T. Morita, W. Pepper, H. Pitcher, L. Price, K. Riahi, A. Roehrl, H.-H. Rogner, A. Sankovski, M. Schlesinger, P. Shukla, S. Smith, R. Swart, S. van Rooijen, N. Victor, and Z. Dadi (2000), Special report on emissions scenarios, in *A Special Report of Working Group III of the Intergovernmental Panel on Climate Change*, edited by N. Nakićenović and R. Swart, p. 570, Cambridge University Press, Cambridge, United Kingdom.

Natali, S. M., E. A. G. Schuur, and R. L. Rubin (2012), Increased plant productivity in Alaskan tundra as a result of experimental warming of soil and permafrost, *J. Ecol.*, *100*(2), 488–498, doi:10.1111/j.1365-2745.2011.01925.x.

Neale, R. B., J. Richter, S. Park, P. H. Lauritzen, S. J. Vavrus, P. J. Rasch, and M. Zhang (2013), The mean climate of the Community Atmosphere Model (CAM4) in forced SST and fully coupled experiments, *J. Clim.*, *26*(14), 5150–5168, doi:10.1175/JCLI-D-12-00236.1.

Norby, R. J., E. H. DeLucia, B. Gielen, C. Calfapietra, C. P. Giardina, J. S. King, J. Ledford, H. R. McCarthy, D. J. P. Moore, R. Ceulemans, P. De Angelis, A. C. Finzi, D. F. Karnosky, M. E. Kubiske, M. Lukac, K. S. Pregitzer, G. E. Scarascia-Mugnozza, W. H. Schlesinger, and R. Oren (2005), Forest response to elevated CO_2 is conserved across a broad range of productivity, *Proc. Nat. Acad. Sci.*, *102*(50), 18,052–18,056, doi:10.1073/pnas.0509478102.

Norby, R. J., J. M. Warren, C. M. Iversen, B. E. Medlyn, and R. E. McMurtrie (2010), CO_2 enhancement of forest productivity constrained by limited nitrogen availability, *Proc. Nat. Acad. Sci.*, *107*(45), 19,368–19,373, doi:10.1073/pnas.1006463107.

Nowacki, G., and T. Brock (1995), Ecoregions and Subregions of Alaska, EcoMap Version 2.0, *map*, USDA Forest Service, Alaska Region, Juneau, AK, scale 1:5,000,000.

Nowacki, G., P. Spencer, M. Fleming, T. Brock, and T. Jorgenson (2001), Ecoregions of Alaska: 2001, *Open-file report 02-297 (map)*, U.S. Geological Survey.

Obata, A., and K. Shibata (2012), Damage of land biosphere due to intense warming by 1000-fold rapid increase in atmospheric methane: Estimation with a climate–carbon cycle model, *J. Clim.*, *25*(24), 8524–8541, doi:10.1175/JCLI-D-11-00533.1.

Olson, D. M., and E. Dinerstein (2002), The global 200: Priority ecoregions for global conservation, *Annals of the Missouri Botanical Garden*, *89*(2), 199–224.

Omernik, J. M. (1987), Ecoregion of the conterminuous United States, *An. Assoc. Amer. Geog.*, *77*(1), 118–125, doi:10.1111/j.1467-8306.1987.tb00149.x.

Oschlies, A. (2001), Model-derived estimates of new production: New results point towards lower values, *Deep Sea Research Part II: Topical Studies in Oceanography*, *48*(10), 2173–2197, doi:10.1016/S0967-0645(00)00184-3.

Pan, Y., R. A. Birdsey, J. Fang, R. Houghton, P. E. Kauppi, W. A. Kurz, O. L. Phillips, A. Shvidenko, S. L. Lewis, J. G. Canadell, P. Ciais, R. B. Jackson, S. W. Pacala, A. D. McGuire, S. Piao, A. Rautiainen, S. Sitch, and D. Hayes (2011), A large and persistent carbon sink in the world's forests, *Science*, *333*(6045), 988–993, doi:10.1126/science.1201609.

Peters, G. P., R. M. Andrew, T. Boden, J. G. Canadell, P. Ciais, C. Le Quéré, G. Marland, M. R. Raupach, and C. Wilson (2013), The challenge to keep global warming below 2°C, *Nature Clim. Change*, *3*(1), 4–6, doi:10.1038/nclimate1783.

Phillips, O. L., L. E. O. C. Aragão, S. L. Lewis, J. B. Fisher, J. Lloyd, G. López-González, Y. Malhi, A. Monteagudo, J. Peacock, C. A. Quesada, G. van der Heijden, S. Almeida, I. Amaral, L. Arroyo, G. Aymard, T. R. Baker, O. Bánki, L. Blanc, D. Bonal, P. Brando, J. Chave, Á. C. A. de Oliveira, N. D. Cardozo, C. I. Czimczik, T. R. Feldpausch, M. A. Freitas, E. Gloor, N. Higuchi, E. Jiménez, G. Lloyd, P. Meir, C. Mendoza, A. Morel, D. A. Neill, D. Nepstad, S. Patiño, M. C. Peñuela, A. Prieto, F. Ramírez, M. Schwarz, J. Silva, M. Silveira, A. S. Thomas, H. ter Steege, J. Stropp, R. Vásquez, P. Zelazowski, E. A. Dávila, S. Andelman, A. Andrade, K.-J. Chao, T. Erwin, A. Di Fiore, E. H. C., H. Keeling, T. J. Killeen, W. F. Laurance, A. P. Cruz, N. C. A. Pitman, P. N. Vargas, H. Ramírez-Angulo, A. Rudas, R. Salamão, N. Silva, J. Terborgh, and A. Torres-Lezama (2009), Drought sensitivity of the Amazon rainforest, *Science*, *323*(5919), 1344–1347, doi:10.1126/science.1164033.

Plattner, G.-K., R. Knutti, F. Joos, T. F. Stocker, W. von Bloh, V. Brovkin, D. Cameron, E. Driesschaert, S. Dutkiewicz, M. Eby, N. R. Edwards, T. Fichefet, J. C. Hargreaves, C. D. Jones, M. F. Loutre, H. D. Matthews, A. Mouchet, S. A. Müller, S. Nawrath, A. Price, A. Sokolov, K. M. Strassmann, and A. J. Weaver (2008), Long-term climate commitments projected with climate–carbon cycle models, *J. Clim.*, *21*(12), 2721–2751, doi:10.1175/2007JCLI1905.1.

Raddatz, T., C. Reick, W. Knorr, J. Kattge, E. Roeckner, R. Schnur, K.-G. Schnitzler, P. Wetzel, and J. Jungclaus (2007), Will the tropical land biosphere dominate the climate-carbon cycle feedback during the twenty-first century?, *Clim. Dyn.*, *29*(6), 565–574, doi: 10.1007/s00382-007-0247-8.

Ramaswamy, V., O. Boucher, J. Haigh, D. Hauglustaine, J. Haywood, G. Myhre, T. Nakajima, G. Y. Shi, and S. Solomon (2001), Radiative forcing of climate change, in *Climate Change 2001: The Scientific Basis. Contribution of Working Group I to the Third Assessment Report of the Intergovernmental Panel on Climate Change*, edited by J. T. Houghton, Y. Ding, D. J. Griggs, M. Noguer, P. J. van der Linden, X. Dai, K. Maskell, and C. A. Johnson, pp. 350–416, Cambridge University Press, Cambridge, United Kingdom and New York, NY, USA.

Randerson, J. T. (2013), Climate science: Global warming and tropical carbon, *Nature*, *494*(7437), 319–320, doi:10.1038/nature11949.

Randerson, J. T., K. Lindsay, E. Muñoz, W. Fu, J. K. Moore, F. M. Hoffman, N. M. Mahowald, and S. C. Doney (in press), Changing contribution of ocean and land processes to climate–carbon feedbacks after 2100, *Global Biogeochem. Cycles*, in press.

Raupach, M. R., and J. G. Canadell (2010), Carbon and the anthropocene, *Curr. Opin. Environ. Sustainability*, *2*(4), 210–218, doi:10.1016/j.cosust.2010.04.003.

Reich, P. B., and S. E. Hobbie (2013), Decade-long soil nitrogen constraint on the CO_2 fertilization of plant biomass, *Nature Clim. Change*, *3*(3), 278–282, doi:10.1038/nclimate1694.

Riahi, K., S. Rao, V. Krey, C. Cho, V. Chirkov, G. Fischer, G. Kindermann, N. Nakicenovic, and P. Rafaj (2011), RCP 8.5–a scenario of comparatively high greenhouse gas emissions, *Clim. Change*, *109*(1), 33–57, doi:10.1007/s10584-011-0149-y.

Romanovsky, V. E., and S. Marchenko (2009), The GIPL permafrost dynamics model, *Tech. rep.*, University of Alaska, Fairbanks, Alaska.

Russell, J. L., R. J. Stouffer, and K. W. Dixon (2006), Intercomparison of the Southern Ocean circulations in IPCC coupled model control simulations, *J. Clim.*, *19*(18), 4560–4575, doi:10.1175/JCLI3869.1.

Sabine, C. L., R. A. Feely, N. Gruber, R. M. Key, K. Lee, J. L. Bullister, R. Wanninkhof, C. S. Wong, D. W. R. Wallace, B. Tilbrook, F. J. Millero, T.-H. Peng, A. Kozyr, T. Ono, and A. F. Rios (2004), The oceanic sink for anthropogenic CO_2, *Science*, *305*(5682), 367–371, doi:10.1126/science.1097403.

Sallée, J.-B., E. Shuckburgh, N. Bruneau, A. J. S. Meijers, T. J. Bracegirdle, Z. Wang, and T. Roy (2013), Assessment of Southern Ocean water mass circulation and characteristics in CMIP5 models: Historical bias and forcing response, *J. Geophys. Res.*, *118*(4), 1830–1844, doi:10.1002/jgrc.20135.

Saxon, E., B. Baker, W. Hargrove, F. Hoffman, and C. Zganjar (2005), Mapping environments at risk under different global climate change scenarios, *Ecol. Lett.*, *8*, 53–60, doi:10.1111/j.1461-0248.2004.00694.

Schimel, D., W. Hargrove, F. Hoffman, and J. McMahon (2007), NEON: A hierarchically designed national ecological network, *Front. Ecol. Environ.*, *5*(2), 59, doi:10.1890/1540-9295(2007)5[59:NAHDNE]2.0.CO;2.

Schuur, E. A. G., J. Bockheim, J. G. Canadell, E. Euskirchen, C. B. Field, S. V. Goryachkin, S. Hagemann, P. Kuhry, P. M. Lafleur, H. Lee, G. Mazhitova, F. E. Nelson, A. Rinke, V. E. Romanovsky, N. Shiklomanov, C. Tarnocai, S. Venevsky, J. G. Vogel, and S. A. Zimov (2008), Vulnerability of permafrost carbon to climate change: Implications for the global carbon cycle, *Bioscience*, *58*(8), 701–714, doi:10.1641/B580807.

Schwinger, J., J. F. Tjiputra, C. Heinze, L. Bopp, J. R. Christian, M. Gehlen, T. Ilyina, C. D. Jones, D. Salas-Mélia, J. Segschneider, R. Séférian, and I. Totterdell (2014), Nonlinearity of ocean carbon cycle feedbacks in CMIP5 Earth system models, *J. Clim.*, *27*(11), 3869–3888, doi:10.1175/JCLI-D-13-00452.1.

Smith, K. L., H. A. Ruhl, B. J. Bett, D. S. M. Billett, R. S. Lampitt, and R. S. Kaufmann (2009), Climate, carbon cycling, and deep-ocean ecosystems, *Proc. Nat. Acad. Sci.*, *106*(46), 19,211–19,218, doi:10.1073/pnas.0908322106.

Smith, R., P. Jones, B. Briegleb, F. Bryan, G. Danabasoglu, J. Dennis, J. Dukowicz, C. Eden, B. Fox-Kemper, P. Gent, M. Hecht, S. Jayne, M. Jochum, W. Large, K. Lindsay, M. Maltrud, N. Norton, S. Peacock, M. Vertenstein, and S. Yeager (2010), The Paralla Ocean Program (POP) reference manual, *Tech. Rep. LAUR-10-01853*, Los Alamos National Laboratory, Los Alamos, New Mexico, USA.

Solomon, S., D. Qin, M. Manning, Z. Chen, M. Marquis, K. B. Averyt, M. Tignor, and H. L. Miller (Eds.) (2007), *Climate Change 2007: The Physical Science Basis. Contribution of Working Group I to the Fourth Assessment Report of the Intergovernmental Panel on Climate Change*, Cambridge University Press, Cambridge, United Kingdom and New York, NY, USA.

Stocker, T. F., D. Qin, G.-K. Plattner, L. V. Alexander, S. K. Allen, N. L. Bindoff, F.-M. Bréon, J. A. Church, U. Cubasch, S. Emori, P. Forster, P. Friedlingstein, N. Gillett, J. M. Gregory, D. L. Hartmann, E. Jansen, B. Kirtman, R. Knutti, K. K. Kumar, P. Lemke, J. Marotzke, V. Masson-Delmotte, G. A. Meehl, I. I. Mokhov, S. Piao, V. Ramaswamy, D. Randall, M. Rhein, M. Rojas, C. Sabine, D. Shindell, L. D. Talley, D. G. Vaughan, and S.-P. Xie (2013a), Technical summary, in *Climate Change 2013: The Physical Science Basis. Contribution of Working Group I to the Fifth Assessment Report of the Intergovernmental Panel on Climate Change*, edited by T. F. Stocker, D. Qin, G.-K. Plattner, M. Tignor, S. K. Allen, J. Boschung, A. Nauels, Y. Xia, V. Bex, and P. M. Midgley, pp. 33–115, Cambridge University Press, Cambridge, United Kingdom and New York, NY, USA.

Stocker, T. F., D. Qin, G.-K. Plattner, M. Tignor, S. K. Allen, J. Boschung, A. Nauels, Y. Xia, V. Bex, and P. M. Midgley (Eds.) (2013b), *Climate Change 2013: The Physical Science Basis. Contribution of Working Group I to the Fifth Assessment Report of the Intergovernmental Panel on Climate Change*, Cambridge University Press, Cambridge, United Kingdom and New York, NY, USA.

Sturm, M., C. Rachine, and K. Tape (2001), Climate change: Increasing shrub abundance in the Arctic, *Nature*, *411*(6837), 546–547, doi:10.1038/35079180.

Sturm, M., T. Douglas, C. Racine, and G. E. Liston (2005), Changing snow and shrub conditions affect albedo with global implications, *J. Geophys. Res.*, *110*(G1), G01,004, doi:10.1029/2005JG000013.

Tans, P. (2009), An accounting of the observed increase in oceanic and atmospheric CO_2 and an outlook for the future, *Oceanography*, *22*(4), 26–35, doi:10.5670/oceanog.2009.94.

Tape, K., M. Sturm, and C. Racine (2006), The evidence for shrub expansion in Northern Alaska and the Pan-Arctic, *Global Change Biol.*, *12*(4), 686–702, doi:10.1111/j.1365-2486.2006.01128.x.

Taylor, K. E., R. J. Stouffer, and G. A. Meehl (2012), An overview of CMIP5 and the experiment design, *Bull. Am. Meteorol. Soc.*, *93*(4), 485–498, doi:10.1175/BAMS-D-11-00094.1.

The Arctic Climate Impact Assessment (ACIA) (2005), *Arctic Climate Impact Assessment*, Cambridge University Press.

Thompson, M. V., J. T. Randerson, C. M. Malmström, and C. B. Field (1996), Change in net primary production and heterotrophic respiration: How much is necessary to sustain the terrestrial carbon sink?, *Global Biogeochem. Cycles*, *10*(4), 711–726, doi:10.1029/96GB01667.

Thornton, P. E., J.-F. Lamarque, N. A. Rosenbloom, and N. M. Mahowald (2007), Influence of carbon-nitrogen cycle coupling on land model response to CO_2 fertilization and climate variability, *Global Biogeochem. Cycles*, *21*(4), GB4018, doi:10.1029/2006GB002868.

Tjiputra, J. F., C. Roelandt, M. Bentsen, D. M. Lawrence, T. Lorentzen, J. Schwinger, Ø. Seland, and C. Heinze (2013), Evaluation of the carbon cycle components in the Norwegian Earth System Model (NorESM), *Geosci. Model Dev.*, *6*(2), 301–325, doi:10.5194/gmd-6-301-2013.

Todd-Brown, K. E. O., J. T. Randerson, W. M. Post, F. M. Hoffman, C. Tarnocai, E. A. G. Schuur, and S. D. Allison (2013), Causes of variation in soil carbon simulations from CMIP5 Earth system models and comparison with observations, *Biogeosci.*, *10*(3), 1717–1736, doi:10.5194/bg-10-1717-2013.

Tollefson, J. (2013), Experiment aims to steep rainforest in carbon dioxide, *Nature*, *496*(7446), 405–406, doi:10.1038/496405a.

van Vuuren, D., J. Edmonds, M. Kainuma, K. Riahi, A. Thomson, K. Hibbard, G. Hurtt, T. Kram, V. Krey, J.-F. Lamarque, T. Masui, M. Meinshausen, N. Nakicenovic, S. Smith, and S. Rose (2011), The representative concentration pathways: An overview, *Clim. Change*, *109*(1), 5–31, doi:10.1007/s10584-011-0148-z.

Volodin, E., N. Dianskii, and A. Gusev (2010), Simulating present-day climate with the INMCM4.0 coupled model of the atmospheric and oceanic general circulations, *Izv. Atmos. Ocean. Phys.*, *46*(4), 414–431, doi:10.1134/S000143381004002X.

Walker, A. P., P. J. Hanson, M. G. De Kauwe, B. E. Medlyn, S. Zaehle, S. Asao, M. Dietze, T. Hickler, C. Huntingford, C. M. Iversen, A. Jain, M. Lomas, Y. Luo, H. McCarthy, W. J. Parton, I. C. Prentice, P. E. Thornton, S. Wang, Y.-P. Wang, D. Warlind, E. Weng, J. M. Warren, F. I. Woodward, R. Oren, and R. J. Norby (2014), Comprehensive ecosystem model–data synthesis using multiple data sets at two temperate forest free-air CO_2 enrichment experiments: Model performance at ambient CO_2 concentration, *J. Geophys. Res. Biogeosci.*, *119*(5), 2169–8961, doi:10.1002/2013JG002553.

Walker, A. P., S. Zaehle, B. E. Medlyn, M. G. De Kauwe, S. Asao, T. Hickler, W. Parton, D. M. Ricciuto, Y.-P. Wang, D. Wårlind, and R. J. Norby (2015), Predicting long-term carbon sequestration in response to CO_2 enrichment: How and why do current ecosystem models differ?, *Global Biogeochem. Cycles*, *29*(4), doi:10.1002/2014GB004995.

Walsh, J. E., W. L. Chapman, V. Romanovsky, J. H. Christensen, and M. Stendel (2008), Global climate model performance over Alaska and Greenland, *J. Clim.*, *21*(23), 6156–6174, doi:10.1175/2008JCLI2163.1.

Watanabe, S., T. Hajima, K. Sudo, T. Nagashima, T. Takemura, H. Okajima, T. Nozawa, H. Kawase, M. Abe, T. Yokohata, T. Ise, H. Sato, E. Kato, K. Takata, S. Emori, and M. Kawamiya (2011), MIROC-ESM 2010: Model description and basic results of CMIP5-20c3m experiments, *Geosci. Model Dev.*, *4*(4), 845–872, doi:10.5194/gmd-4-845-2011.

Wieder, W. R., C. C. Cleveland, W. K. Smith, and K. Todd-Brown (2015), Future productivity and carbon storage limited by terrestrial nutrient availability, *Nature Geosci.*, doi:10.1038/NGEO2413, in press.

Wigley, T. M. L. (2003), MAGICC/SCENGEN 4.1, *User manual*, National Center for Atmospheric Research, Boulder, CO 80307.

Wigley, T. M. L. (2008), MAGICC/SCENGEN 5.3 (version 2), *User manual*, National Center for Atmospheric Research, Boulder, CO 80307.

Williams, D. N., K. E. Taylor, L. Cinquini, B. Evans, M. Kawamiya, M. Lautenschlager, B. Lawrence, D. Middleton, and Others (2011), The Earth System Grid Federation: Software framework supporting CMIP5 data analysis and dissemination, *CLIVAR Exchanges*, *16*(2), 40–42.

Wu, T., W. Li, J. Ji, X. Xin, L. Li, Z. Wang, Y. Zhang, J. Li, F. Zhang, M. Wei, X. Shi, F. Wu, L. Zhang, M. Chu, W. Jie, Y. Liu, F. Wang, X. Liu, Q. Li, M. Dong, X. Liang,

Y. Gao, and J. Zhang (2013), Global carbon budgets simulated by the Beijing Climate Center Climate System Model for the last century, *J. Geophys. Res. Atmos.*, *118*(10), 4326–4347, doi:10.1002/jgrd.50320.

Yukimoto, S., H. Yoshimura, M. Hosaka, T. Sakami, H. Tsujino, M. Hirabara, T. Y. Tanaka, M. Deushi, A. Obata, H. Nakano, Y. Adachi, E. Shindo, S. Yabu, T. Ose, and A. Kitoh (2011), Meteorological Research Institute-Earth System Model version 1 (MRI-ESM1) – model description, *Tech. Rep. 64*, Meteorological Research Institute.

Yukimoto, S., Y. Adachi, and M. Hosaka (2012), A new global climate model of the Meteorological Research Institute: MRI-CGCM3 – model description and basic performance, *J. Meteorol. Soc. Jpn.*, *90*(A), 23–64, doi:10.2151/jmsj.2012-A02.

Zaehle, S., P. Friedlingstein, and A. D. Friend (2010), Terrestrial nitrogen feedbacks may accelerate future climate change, *Geophys. Res. Lett.*, *37*(1), L01,401, doi: 10.1029/2009GL041345.

Zaehle, S., B. E. Medlyn, M. G. De Kauwe, A. P. Walker, M. C. Dietze, T. Hickler, Y. Luo, Y.-P. Wang, B. El-Masri, P. Thornton, A. Jain, S. Wang, D. Warlind, E. Weng, W. Parton, C. M. Iversen, A. Gallet-Budynek, H. McCarthy, A. Finzi, P. J. Hanson, I. C. Prentice, R. Oren, and R. J. Norby (2014), Evaluation of 11 terrestrial carbon–nitrogen cycle models against observations from two temperate free-air CO_2 enrichment studies, *New Phytol.*, *202*(3), 803–822, doi:10.1111/nph.12697.

Zhou, Y. (1996), An ecological regionalization model based on NOAA/AVHRR data, *International Archives of Photogrammetry and Remote Sensing*, *XXXI, Part B4*, 1001–1006.

Zickfeld, K., M. Eby, H. D. Matthews, A. Schmittner, and A. J. Weaver (2011), Nonlinearity of carbon cycle feedbacks, *J. Clim.*, *24*(16), 4255–4275, doi:10.1175/2011JCLI3898.1.